

Photo-enforced stratification of liquid crystal / monomer mixtures : principle, theory and analysis of a paintable LCD concept

Citation for published version (APA):

Penterman, R. (2005). *Photo-enforced stratification of liquid crystal / monomer mixtures : principle, theory and analysis of a paintable LCD concept*. [Phd Thesis 2 (Research NOT TU/e / Graduation TU/e), Chemical Engineering and Chemistry]. Technische Universiteit Eindhoven. <https://doi.org/10.6100/IR597706>

DOI:

[10.6100/IR597706](https://doi.org/10.6100/IR597706)

Document status and date:

Published: 01/01/2005

Document Version:

Publisher's PDF, also known as Version of Record (includes final page, issue and volume numbers)

Please check the document version of this publication:

- A submitted manuscript is the version of the article upon submission and before peer-review. There can be important differences between the submitted version and the official published version of record. People interested in the research are advised to contact the author for the final version of the publication, or visit the DOI to the publisher's website.
- The final author version and the galley proof are versions of the publication after peer review.
- The final published version features the final layout of the paper including the volume, issue and page numbers.

[Link to publication](#)

General rights

Copyright and moral rights for the publications made accessible in the public portal are retained by the authors and/or other copyright owners and it is a condition of accessing publications that users recognise and abide by the legal requirements associated with these rights.

- Users may download and print one copy of any publication from the public portal for the purpose of private study or research.
- You may not further distribute the material or use it for any profit-making activity or commercial gain
- You may freely distribute the URL identifying the publication in the public portal.

If the publication is distributed under the terms of Article 25fa of the Dutch Copyright Act, indicated by the "Taverne" license above, please follow below link for the End User Agreement:

www.tue.nl/taverne

Take down policy

If you believe that this document breaches copyright please contact us at:

openaccess@tue.nl

providing details and we will investigate your claim.

Photo-enforced stratification of liquid crystal / monomer mixtures

Principle, theory and analysis of a paintable LCD concept

CIP-DATA LIBRARY TECHNISCHE UNIVERSITEIT EINDHOVEN

Penterman, Roel

Photo-enforced stratification of liquid crystal / monomer mixtures : principle, theory and analysis of a paintable LCD concept / by Roel Penterman. – Eindhoven : Technische Universiteit Eindhoven, 2005.

Proefschrift. – ISBN 90-744-4569-1

NUR 913

Subject headings: liquid crystal displays ; LCD / polymer-dispersed liquid crystals / polymer morphology / polymerization kinetics / diffusion / phase separation / phase diagrams / confocal microscopy ; Raman spectroscopy

Cover design: Robert van Uden (CIS-Visuals, Philips Research), Roel Penterman
Printed by University Press Facilities, Eindhoven, The Netherlands

The work described in this thesis has been carried out at the Philips Research Laboratories Eindhoven as part of the Philips Research programme.

Photo-enforced stratification of liquid crystal / monomer mixtures

Principle, theory and analysis of a paintable LCD concept

PROEFSCHRIFT

ter verkrijging van de graad van doctor aan de
Technische Universiteit Eindhoven, op gezag van de
Rector Magnificus, prof.dr.ir. C.J. van Duijn, voor een
commissie aangewezen door het College voor
Promoties in het openbaar te verdedigen
op woensdag 16 november 2005 om 16.00 uur

door

Roel Penterman

geboren te Stad Delden

Dit proefschrift is goedgekeurd door de promotoren:

prof.dr.ing. D.J. Broer

en

prof.dr. P.J. Lemstra

Copromotor:

dr.ing. C.W.M. Bastiaansen

Aan Loes, Gijs en Teun

Contents

Chapter 1

Introduction

1.1	General introduction	1
1.1.1	Liquid crystal displays	1
1.1.2	Polymer/LC composites	2
1.1.3	Spatially-controlled photopolymerization	4
1.1.4	Spatially-controlled photopolymerization-induced phase separation	5
1.1.5	Polymer/LC composite characterization	6
1.1.6	Supporting models for PIPS, spatially-controlled photopolymerization and spatially-controlled PIPS	8
1.2	A new concept: Paintable LCDs	9
1.3	Outline of this thesis	10
1.4	References	12

Chapter 2

Two-step photo-enforced stratification

2.1	Introduction	17
2.2	Experimental section	18
2.2.1	Materials	18
2.2.2	Substrate preparation	19
2.2.3	Doctor blade coating	19
2.2.4	UV exposure procedures	19
2.2.5	Characterization of the stratified LC/polymer morphologies	21
2.2.6	Device preparation and electro-optical characterization	21
2.3	Results and discussion	22
2.3.1	Photo-enforced stratification: Selection of materials and conditions	22
2.3.2	Photo-enforced stratification process	25
2.3.3	Two-step photo-enforced stratification process	29
2.3.4	Location of the phase separation	33
2.3.5	Composition of the phase separated LC material	35
2.3.6	Model system	35
2.3.7	Electro-optical behavior	36
2.4	Conclusions	39
2.5	References and notes	39

Chapter 3

Confocal Raman microscopy of liquid crystal filled polymer capsules made by photo-enforced stratification

3.1	Introduction	43
3.2	Experimental section	44
	3.2.1 Preparation of arrays of LC-filled polymer capsules	44
	3.2.2 Confocal Raman microscope set-up	45
3.3	Results and discussion	48
	3.3.1 Identification of the component specific signals	48
	3.3.2 Method to establish an estimate of the monomer conversion	51
	3.3.3 Data pre-processing	51
	3.3.4 Characterization of the capsule precursors	52
	3.3.5 Characterization of the LC-filled polymer capsules	54
	3.3.6 Raman spectra of anisotropic media	55
	3.3.7 Morphologies as a function of temperature	57
3.4	Conclusions	61
3.5	References	61

Chapter 4

Photo-enforced stratification model

4.1	Introduction	63
4.2	Photo-enforced stratification model	64
	4.2.1 Introduction	64
	4.2.2 Thermodynamics	65
	4.2.3 Reaction-diffusion model	72
	4.2.4 PIPS model	82
4.3	Results and discussion	84
4.4	Conclusions	87
4.5	References and notes	87

Chapter 5

Quantification of the input parameters of the photo-enforced stratification model

5.1	Introduction	89
-----	--------------	----

5.2	Experimental section	93
5.2.1	Chemicals	93
5.2.2	DSC measurements	93
5.2.3	NMR measurements	94
5.3	Results and discussion	95
5.3.1	Input parameters for the polymerization step	95
5.3.2	Input parameters for the chemical potentials	100
5.3.3	Input parameters for the diffusion step	103
5.4	Conclusions	106
5.5	References and notes	107

Chapter 6

Investigation of the photo-enforced stratification process: model vs. experiments

6.1	Introduction	109
6.2	Experimental section	111
6.2.1	Chemicals	111
6.2.2	Combined photo-DSC/turbidity measurements	112
6.2.3	Nematic-isotropic phase transition temperature of the initial LC/monomers mixture	113
6.2.4	In-situ confocal Raman microscopy	113
6.2.5	Photo-enforced stratification experiments	114
6.3	Results and discussion	114
6.3.1	The phase diagram of the initial LC/monomers mixture: experiment and model	114
6.3.2	The phase separation line: Photo-DSC/turbidity measurements and model calculations	116
6.3.3	Polymerization-induced diffusion monitored by confocal Raman microscopy	122
6.3.4	Reaction-diffusion model	124
6.3.5	Photo-enforced stratification: PES model vs. experimental results	126
6.3.6	Morphological phenomena: PES model predictions vs. experimental results	128
6.4	Conclusions	130
6.5	Appendix	131
6.6	References and notes	133

Chapter 7	
Second generation photo-enforced stratification process	
7.1	Introduction 135
7.2	Experimental section 136
7.2.1	Materials 136
7.2.2	Glass substrate preparation 137
7.2.3	Structuring of the alignment layer 137
7.2.4	Doctor blade coating 138
7.2.5	UV exposure step 139
7.2.6	Confocal Raman microscopy 139
7.2.7	Device preparation and electro-optical characterization 139
7.3	Results and discussion 140
7.3.1	The two-step PES process 140
7.3.2	The single-step PES process 141
7.3.3	Characterization of the LC-filled polymer capsules after application of the planarization layer: confocal Raman microscopy 146
7.3.4	Plastic single-step PES LCD demonstrators 147
7.4	Conclusions 150
7.5	References and notes 150
Technology assessment	151
Summary	155
Samenvatting	159
Dankwoord	163
Curriculum Vitae	

Chapter 1

Introduction

1.1 General introduction

1.1.1 Liquid crystal displays

The liquid crystal display (LCD) TV and computer monitor markets have experienced impressive growths during the last decade as a result of the increased demand to thinner and bigger displays. Besides these display applications, LCDs make up for most of the displays that have been integrated in everyday commodities like digital watches, pocket calculators, clocks, mobile phones, and automotive displays. The reason why LCDs are so widely used is that the display is thin, low-weight and has a low power consumption. Furthermore, the underlying electro-optical effect is relatively simple and well understood.

In its basic form, an LCD consists of a thin liquid crystal (LC) layer that is sandwiched between two glass plates. The glass surface facing the LC layer is covered with a transparent electrode layer, which is commonly indium tin oxide (ITO). To induce a unidirectional orientation of the LC molecules in the layer, an additional (rubbed) polyimide alignment layer is deposited on both electrode surfaces. On the outer surface of the glass plates, sheet polarizers are laminated. Depending on the design of the optical stack, the LCD is either switched from a non-transparent state to a transparent state (the so-called normally black mode) or vice versa (normally white mode) by applying a bias over the electrodes. When a voltage is applied over the electrodes, the LC molecules will reorient in the direction of the electric field, which results in a change of the birefringence of the LC layer, and a concomitant change of the light transmission of the polarizer/LC material/polarizer stack. When the electric field is removed the LC relaxes back to its original orientation due to the elastic forces, which are imposed by the alignment layers. In essence the LCD acts as a shutter: depending on the orientation of the LC molecules, the interaction of the polarizer-LC-polarizer stack with the incoming light is such that it is either (partially) transmitted or completely blocked. In transmissive LCDs the light originates from a

backlight that is positioned behind the LCD, whereas reflective LCDs make use of ambient light.

In the early 1970's Schadt and Helfrich reported the electrically induced switching of twisted nematic (TN) liquid crystal materials.¹ In TN-LCDs the orientation layers are rubbed perpendicular, inducing a 90° twist of the LC in the cell. The TN electro-optical effect is characterized by low switching voltages, a good contrast, and the achromatic behavior. On the other hand, the TN electro-optical effect suffers from a poor viewing angle, which was later improved by the application of appropriate optical compensation foils.² The first TN-LCDs were simple direct driven devices with low information content. The information content of LCDs was increased by the introduction of the super twisted nematic (STN) mode, which enabled a passive matrix addressing of the display.³ A further increase of the resolution (and thus the information content) of the LCD required the use of active matrix technology, where each individual pixel is switched by a thin-film transistor (TFT). In addition, the active matrix technology enabled the use of alternative electro-optical effects such as vertically aligned nematic (VAN)⁴ and in-plane switching (IPS),⁵ known for their superior viewing angle. In fact, current LCD TVs are either based on the VAN effect or the IPS effect.

LCDs are currently being made via a production process called cell-technology.⁶ During this process two glass plates, provided with the transparent electrodes, orientation layers and other layers such as a color filter, are accurately coupled. Previously applied spacers keep the two plates at a distance of several microns while they are adhered together. Under vacuum conditions the resulting cell is then filled with a liquid crystal blend by capillary suction, which is a time-consuming process. Recently, an alternative filling process the so-called one-drop-fill technique, has been developed that reduces the filling time considerably.⁷ In this technique an exact amount of LC material is dispensed on one of the substrates, after which the cell is formed by accurately coupling of the two substrates in vacuum. Due to the nature of the processing steps and related substrate handling the use of rectangular glass substrates is required for cell technology.

1.1.2 Polymer/LC composites

Over the past two decades alternative switching principles for application in LCDs and other electro-optical devices have been developed based on polymer/LC composites.⁸ In the mid 1980's polymer-dispersed liquid crystals (PDLCs) were introduced.^{9,10} In PDLC morphologies the LC material is present in the form of micrometer-sized droplets that are randomly dispersed in the polymer matrix. The polymer content in PDLCs is typically in the range of 30 to 50 wt.%. Occasionally,

also lower polymer concentrations are used. In that case the polymer often forms a continuous network in a co-continuous LC phase. The random morphologies of LC droplets or LC phases dispersed in an isotropic matrix can be electrically switched between a strongly scattering 'off' state and a highly transparent 'on' state (see Figure 1.1).⁸ Multiple scattering of the light by the randomly aligned LC in the off state results in a white appearance.¹¹ In the on state the LC director follows the pattern of the electrical field lines and the resulting ordinary refractive index of the LC, as observed by the viewer, matches the isotropic refractive index of the polymers resulting in a transparent appearance.

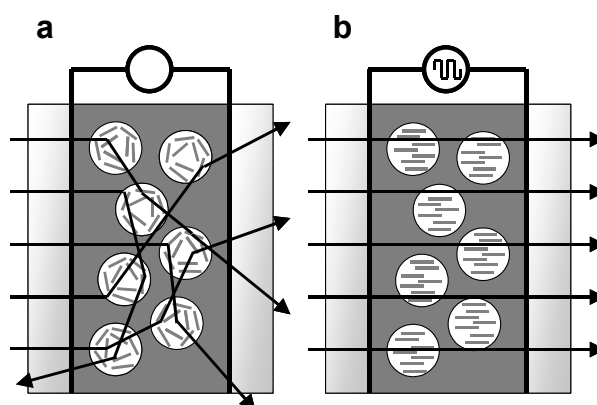


Figure 1.1: Schematic drawing of a polymer-dispersed liquid crystal (PDLC) display. a) The scattering 'off' state. b) The transparent 'on' state.

Composites made from LC and a small amount of mesogenic monomers form a special class. In these systems the mesogenic monomers are polymerized in their liquid crystalline state yielding a continuous LC phase and an anisotropic network morphology with its orientation axis in the same direction as that of the LC.^{12,13,14} When the LC material is dispersed in an anisotropic network it adopts the orientation of the network. Since the ordinary indices and the extraordinary indices of the LC material and polymer are matched, the material is transparent in the off state. By applying an electrical field the LC can be brought to another orientation and the induced refractive index mismatch induces scattering in the on state. Often LC blends with a negative dielectric anisotropy are used to enhance scattering along the principal optical axis of the anisotropic polymer.

The methods that have been used to make PDLCs can be divided into two categories, the first category being the filling of porous matrices with LC material. In these composites the resulting micro-droplets are interconnected. In 1982 Craighead et al. demonstrated electrically controlled light scattering based on such a porous matrix, filled with LC.¹⁵ In the second category, the randomly distributed micro-droplets are isolated and dispersed in a continuous polymer phase. Films with such a

structure can be made through (i) emulsion methods and (ii) various phase separation routes.¹⁶ Emulsion based systems were introduced by Ferguson.¹⁷ In these systems the liquid crystal is dispersed as droplets in an aqueous solution containing a film-forming polymer. The solution is then applied as a thin film and evaporation of the water leads to an LC/polymer composite film. Shrinkage of the film causes flattening of the spherical droplets to oblate ellipsoids. This induces a preferential ‘in-plane’ orientation of the LC. Alternatively, various phase separation routes have been developed to form PDLCs from an initially homogeneous and isotropic mixture. A well-known method is solvent induced phase separation (SIPS), in which phase separation occurs after evaporation of the solvent, or upon the addition of a non-solvent.¹⁸ Another is temperature-induced phase separation (TIPS), where a linear polymer and an LC are fully miscible at higher temperatures but upon lowering the temperature a PDLC morphology is formed.^{19,20}

In polymerization-induced phase separation (PIPS),^{21,22} the monomers in the initial LC/monomer mixture are converted into linear or crosslinked polymers. The increasing polymer fraction results in the separation of an LC phase from the polymeric phase. The polymerization reaction in PIPS can be thermally-induced or photo-initiated. Photo-initiated PIPS is a preferred method, since the processing temperature and rate of polymerization can be chosen independently. This allows a better control of the morphology (e.g. size and to some extent the shape of the droplets) and thus a better control of the electro-optical properties of the final composite.

For the remainder of this chapter the discussion will be mainly focused on PIPS processes, since this technique is the basic principle of photo-enforced stratification (PES), which is the topic of this thesis.

1.1.3 Spatially-controlled photopolymerization

Polymer structures with distinct optical properties have been created via the pattern-wise photopolymerization of multi-component monomer films. For example, mixtures of liquid-crystalline diacrylates and isotropic monoacrylates have been exposed to UV light by means of lithographic or holographic techniques resulting in polymeric gratings with alternating nematic and isotropic lines.²³ The grating preparation was based on the difference in reactivity between the monomers: due to the favored depletion of the more reactive component, i.e. the diacrylate, in the high intensity areas and the resulting diffusion of this component towards these areas, alternating nematic and isotropic regions were formed in the film.

Leewis et al. found that not only a difference in reactivity, but also the difference in monomer size plays a role.²⁴ They showed the preferential incorporation

of small di-functional monomers above larger tetra-functional monomers, which was in correspondence with their reaction-diffusion model based on Flory-Huggins theory of mixing²⁵ extended with an elastic contribution of the forming polymer network.²⁶

Apart from *laterally* induced diffusion by patterned UV-exposure a *transversal* intensity modulation, i.e. an intensity gradient across the layer, can be realized by making use of UV-light absorption of the film. By adding a UV-absorber to a reaction mixture, consisting of a nematic monomer and a chiral-nematic monomer of different reactivity, and subsequent exposure to UV-light, cholesteric films have been made in which the helix has a pitch gradient that provides polarized reflection over the entire visible wavelength spectrum.²⁷ During the polymerization process the more reactive chiral monomer, i.e. the helical twist inducer, diffuses to the high intensity areas near the top of the film. The less reactive nematic monomer, i.e. the helix unwinder, counter-diffuses to the low-intensity areas near the bottom of the film.

1.1.4 Spatially-controlled photopolymerization-induced phase separation

The PIPS process used to produce PDLC devices can be extended further by controlling the photopolymerization spatially using lithography or holographic means or by making use of UV-light absorption, discussed in the previous paragraph.

Holographic PDLCs

Switchable holographic gratings are formed by the photochemical curing of an LC/monomer mixture with a spatially varying intensity profile.^{28,29,30,31} This results in an isotropic polymer matrix in which in the low-intensity areas phase-separated LC droplets are dispersed. An example of such a structure is shown in Figure 1.2. The resulting grating reflects light of a narrow wavelength region in the off state, where the randomly oriented LC in the droplets provides a refractive index modulation that satisfies the Bragg condition for reflection. When aligned in the on state, the refractive index of the droplets matches that of the polymer and the film becomes transparent. These holographic PDLCs (H-PDLCs) have potential application in diverse fields such as reflective flat-panel displays,³² switchable lenses, reflective strain gauge technology,³³ diffractive optical elements²⁹ and many other electro-optical applications. Many basic studies have been performed on the structure, morphology, and properties of H-PDLCs,^{34,35,36,37} and a wide variety of new configurations have been developed.

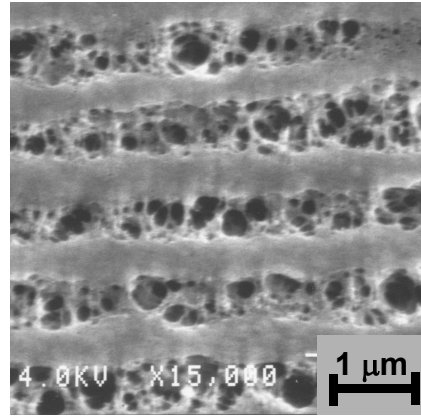


Figure 1.2: Scanning electron microscope picture of a polymer matrix of an H-PDLC, after removal of the LC (courtesy of prof. dr. G.P. Crawford).

In-cell stratification

A way to induce transversal phase separation is by making use of an UV-light intensity gradient. Vorflusev and Kumar used the UV-absorption of a liquid crystal mixture consisting of cyanobiphenyl and cyanoterphenyl derivatives to create a light intensity gradient across the film of an LC/monomer mixture sandwiched between two glass substrates.³⁸ When irradiated with low intensity light the anisotropic polymerization yielded a stratified morphology, i.e. a two-layered structure, the polymer layer being formed at the substrate facing the UV-source and an LC layer at the bottom in which the LC molecules were aligned by the alignment layer on the bottom substrate. This method was used to obtain a thinner LC layer than the initial cell gap as an alternative for using smaller spacers (the use of smaller spacers increases the cell filling time enormously). The experiments were performed with NOA-65 (Norland Optical Adhesive 65) based on thiolene chemistry,⁸ mixed in 60/40 (wt/wt) ratio with the LC blend. They studied the phase separation of nematic LC blends for electrically controlled birefringence (ECB) devices as well as smectic LCs for ferroelectric LC (FLC) devices.

1.1.5 Polymer/LC composite characterization

The electro-optical performance of PDLCs and H-PDLCs is strongly related to the morphology of the LC/polymer composite. Therefore, an understanding of the relationships between processing, morphology, and electro-optic performance is crucial for controlling film properties. It is well known that the formed morphology of PIPS based PDLCs depends on a variety of parameters such as UV-intensity, temperature of polymerization, type and concentration of LC and functionality of the monomers.^{39,40} The morphologies of PDLC,³⁹ H-PDLC^{30,31} and polymer network stabilized LCs⁴¹ have been studied by polarization-optical microscopy (POS) and scanning electron microscopy (SEM). POS gives some insight in the shape and

distribution of the LC phase and provides some information on the molecular orientation. SEM gives a more three-dimensional insight in the morphology, but a main drawback is that the liquid crystal has to be removed. This may seriously affect the polymer morphologies. Alternatively, adding a fluorescent dye that preferentially stays in the polymeric phase enables a non-invasive 3D study of PDLC morphologies with confocal fluorescence microscopy.⁴²

Virtually all polymeric materials used in PDLCs can contain a finite amount of dissolved LC material, i.e. the so-called solubility limit of the LC material in the polymer. The presence of LC in the polymer matrix affects its mechanical and optical properties, and reduces the amount of switchable LC material that is actually available for the electro-optical effect. For example, in the on state of a PDLC device, the remaining LC in the polymer phase may cause an index of refraction mismatch between the polymer matrix and the uniaxially aligned LC in the droplets, thereby reducing the clarity of the PDLC.⁴³ The solubility limit of an LC in a polymer matrix can be determined via various methods.⁴⁴ Examples that can be found in literature among others are

- (i) the determination of the glass-transition temperature of the polymer and nematic-isotropic phase transitions temperature and enthalpies of the LC phase^{45,46} by DSC measurements,
- (ii) the determination of the threshold of light scattering (TLS), by comparing the scattering of LC/polymer composites prepared with different initial LC concentrations,
- (iii) the analysis of the refractive index of the polymer matrix as a function of initial LC concentrations, and
- (iv) the determination of the volumetric number density and the diameter of the droplets with SEM analysis.⁴⁷

For practical applications of LC/polymer composites LC blends consisting of various LC molecules are generally used rather than a single LC molecule. The reason for this arises from the fact that the liquid crystalline phases of LC materials, consisting of one type of molecule, usually have a limited temperature region of existence, often with melting temperatures above room temperature. Therefore eutectic mixtures are generally preferred. As a result of an incomplete phase separation, leaving some of the LC material dissolved in the polymer, the composition of the LC blend may change. Nolan et al. studied the composition of the LC after phase separation in an E7/NOA65 system.⁴⁸ E7 is a four-component blend of three cyanobiphenyl homologues and one cyanoterphenyl derivative (see also Chapter 2, Figure 2.2). They found a preferential phase separation of higher molecular weight compounds. As a result the properties of the phase separated LC (nematic-isotropic

temperature, birefringence) are different from the properties of the initial E7 blend, which will change the electro-optical behavior of the PDLC.

Serbutoviez and co-workers investigated the relations between the photopolymerization parameters, the phase separation behavior and the resulting morphologies.^{49,50} The reaction kinetics of acrylate based PDLC mixtures made by (isothermal) photopolymerization-induced phase separation were studied with the aid of Photo-DSC. Simultaneously with the DSC measurements the light transmission of the reaction mixture was recorded. With these combined so-called photo-DSC/turbidity experiments, the *onset of phase separation* can be established, i.e. the conversion at which a nematic phase in the reaction mixture appears.⁵¹ Additionally, in-situ optical microscopy was performed and a thermodynamic model⁵² was developed that relates the moment of phase separation to the resulting morphologies.

1.1.6 Supporting models for PIPS, spatially-controlled photopolymerization and spatially-controlled PIPS

PIPS models

Many reports have appeared on thermodynamic models that describe the phase separation in PDLC mixtures. It is generally accepted that phase separation occurs as a result of the increasing size of the growing polymer molecules and the corresponding changes in entropy.^{53,54} However, also other driving forces may contribute to the phase separation process: in crosslinking polymerization the Gibbs free energy (ΔG) also changes by the increasing elasticity of the swollen polymer network during polymerization,⁵² and below the clearing point of the LC material the formation of a nematic phase upon phase separation is also a driving force.^{55,56}

The Gibbs free energy describes the thermodynamic state of a mixture at constant temperature and pressure. For each of the contributions to ΔG theoretical models have been developed. The Flory-Huggins theory^{57,58} is generally applied to describe the mixing contribution to the Gibbs free energy. The elastic contribution is the subject of rubber elasticity theory, which originates from Flory and Rehner.^{59,60} The Maier-Saupe theory is frequently used to describe the energy contribution of the nematic ordering.⁶¹

Models for spatially-controlled photopolymerization and spatially-controlled PIPS

One-dimensional diffusion models have been applied to describe holographic recording in photopolymer systems,⁶² two-component isotropic monomer systems²⁴ and two-component monomer systems consisting of an isotropic monoacrylate and a nematic diacrylate.²³ Models of reaction-diffusion kinetics have also been applied to

describe the formation of H-PDLCs^{31,63} and in-cell stratification,⁶⁴ leaving out the issues of phase separation and nematic ordering of LC. Recently, reaction-diffusion models have been combined with phase separation models based on Flory-Huggins free energy of mixing and Maier-Saupe free energy of nematic ordering.^{36,65,66}

1.2 A new concept: Paintable LCDs

To keep pace with customer demand for cost-effective flat panel displays, LCD manufacturing technologies are required that enable the processing of larger substrates with increased production speeds. Moreover, envisioned new display applications such as for example wearable displays and electronic wallpaper will require displays that are curved, non-rectangular in shape and preferably flexible or even rollable. In this thesis a new technology based on a phase separation process is explored that enables the production of *Paintable LCDs*: Instead of using cell technology to produce an LCD,⁶ a Paintable LCD is made by the sequential coating (hence the name Paintable LCD) and UV curing of a stack of organic layers on a *single* substrate.

In Paintable LCDs the LC material is confined between a substrate and a polymer sheet, with the important difference with respect to conventional LCDs that the latter is formed during processing. The *in-situ* polymer sheet formation on top of the LC layer is the result of a spatially-controlled PIPS process starting from a thin film consisting of a blend of LC material and reactive monomers (see Figure 1.3a). The concept has been named *photo-enforced stratification* (PES).⁶⁷ For completion of the LCD, the other necessary optical layers (e.g. the polarizer) can be applied on top of the polymer sheet. Instead of a top-bottom electrode structure, the LC material is switched by in-plane electrical fields originating from interdigitated electrodes (the aforementioned IPS, see Figure 1.3b).⁵ The electrodes are applied on the substrate prior to the PES processing steps.

The Paintable LCD manufacturing technology offers various advantages: the manufacturing process is relatively simple and fast, whereas the resulting LCDs are ultra-thin, flexible, robust and have a free form factor. The use of coating processes makes the Paintable LCD technology potentially suited for the roll-to-roll manufacturing of displays.

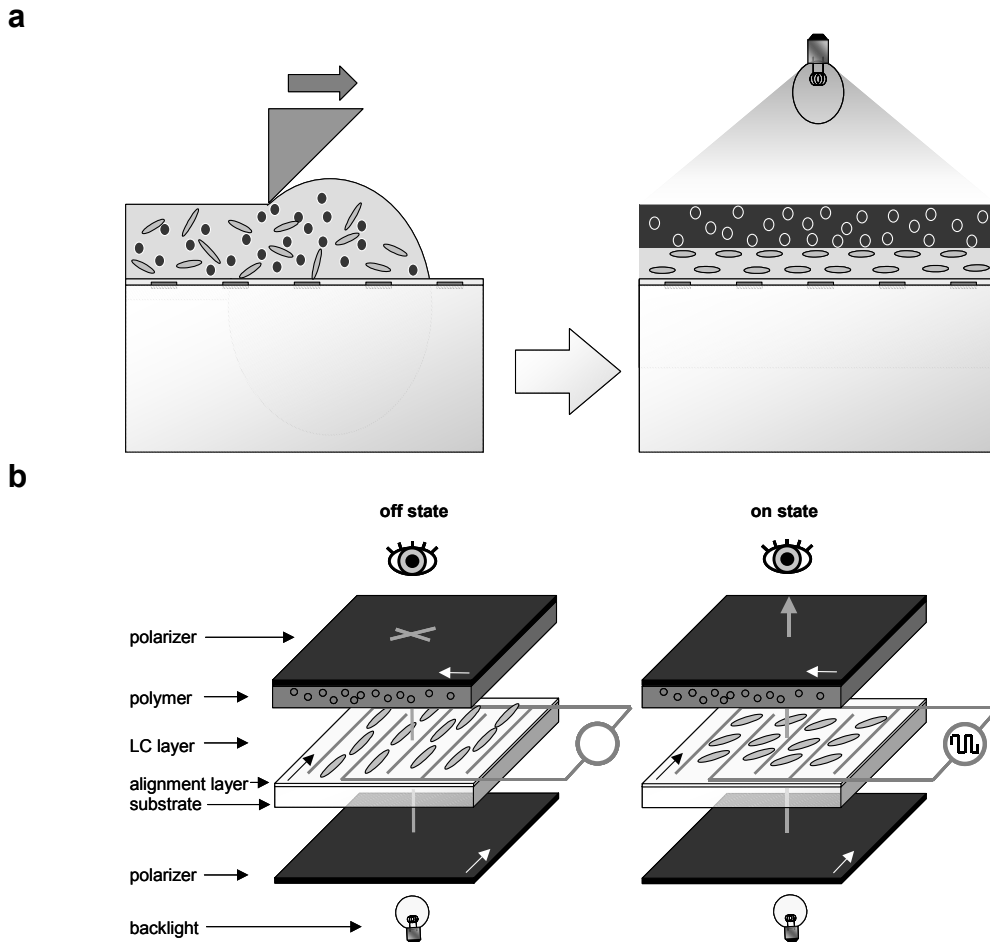


Figure 1.3: a) Schematic representation of the photo-enforced stratification (PES) concept. A thin LC/monomer film is deposited on an appropriate substrate. Upon UV-irradiation, the film phase separates into two discrete layers: a polymer layer on top of an LC layer. b) The LC layer in these so-called Paintable LCDs is switched by in-plane electrical fields originating from interdigitated electrodes. In the off state the LC, which is oriented parallel to the electrodes, has no interaction with the linearly polarized light from the backlight/polarizer combination. It is blocked by the top polarizer of which the transmission axis is oriented perpendicular to that of the bottom polarizer, yielding a dark appearance. In the on state the LC is switched in-plane (parallel to the substrate) by electrical fields between the interdigitated electrodes. The polarization direction of the light is rotated by 90° and transmitted by the second polarizer, resulting in a bright appearance.

1.3. Outline of this thesis

The objective of the research described in this thesis is to demonstrate the PES process on a single substrate. A thorough understanding of the PES process is crucial and will provide a feedback for the process optimization. Therefore, an important part of this thesis is devoted to the development of a physical model based on the integration of existing polymerization-induced diffusion and PIPS models.

In **Chapter 2** a proof of principle of the PES process on a single substrate will be given. It will be shown that the combination of a mask exposure step and a subsequent flood exposure, hence named the *two-step PES* process, of a thin LC/monomer film results in a stratified LC/polymer morphology. The shape of these morphologies is characterized with the aid of polarization microscopy and surface profile measurements. It is also demonstrated that the LC in the stratified morphology can be switched by in-plane electrical fields originating from interdigitated electrodes.

The non-destructive analysis of the LC-filled capsules with Confocal Raman microscopy is described in **Chapter 3**. With this technique information on the spatial composition and the molecular order of the polymer and the LC phase can be obtained. Also further insight in the phase separation process can be acquired by monitoring the temperature dependence of the stratified morphologies.

In **Chapter 4** a numerical PES model is described. The model is based on polymer chain reaction kinetics, diffusion and the thermodynamics of phase separation. The model is a combination of two components: a reaction-diffusion model that provides the evolution of the concentration profiles of the LC, monomer and polymer as a function of depth and time, and a thermodynamic PIPS model that calculates the ternary conversion-phase diagram of the LC/monomer/polymer system. The overall PES model is a one-dimensional model that calculates the position in the film as well as the time at which the phase separation starts.

In **Chapter 5** the input parameters for the model are derived from calculations and measurements on the appropriate LC/monomer mixtures.

In **Chapter 6** the two components of the PES model, the reaction-diffusion model and the PIPS model have independently been compared to experiments. It is shown that the compositional changes (as monitored in-situ with confocal Raman microscopy) in the LC/monomer/polymer layer, irradiated with UV light, are in agreement with the results obtained from the reaction-diffusion model. Photo-DSC (Differential Scanning Calorimetry) was combined with in-situ optical microscopy to investigate the phase separation behavior of the LC/monomer system mixtures. The experimentally determined phase separation lines show a quantitative agreement with the phase separation lines calculated with the PIPS model. The overall PES model qualitatively describes the trends that have been observed in the photo-enforced stratification experiments as a function of the LC fraction in the initial LC/monomer mixture.

In **Chapter 7** an improved PES process is demonstrated showing that regular arrays of polymer capsules filled with liquid crystal can be obtained via a single UV exposure step, hence named the *single-step PES* process. For this improved process, the substrate is modified with an adhesion promoter using offset printing. During the

stratification process, the walls of the capsules are defined by the adhesive patterns as the polymer locally forms chemical bonds with the adhesion promoter. This results in mechanically stable LC-filled polymer capsules, which are very well suited for application in flexible plastic displays.

1.4 References

1. Schadt, M., and Helfrich, W. *Appl. Phys. Lett.* **18**, 127-128 (1971).
2. Mori, H., Itoh, Y., Nishiura, Y., Nakamura, T., and Shinagawa, Y. *Jpn. J. Appl. Phys.* **36**, 143-147 (1997).
3. Scheffer, T.J., and Nehring, J. *Appl. Phys. Lett.* **45**, 1021-1023 (1984).
4. Crandell, K.A., Fisch, M.R., Petschek, R.G., and Rosenblatt, C. *Appl. Phys. Lett.* **65**, 118-120 (1994).
5. Kiefer, R., Weber, B., Windscheid, F., and Baur, G. in: *Proc. 12th IDRC, Japan Display 1992*, 547-550 (1992).
6. Morozumi, S. in: *Liquid Crystals: Application and Uses* (Ed. Bahadur, B.), World Scientific, London, 181 (1990).
7. Kamiya, H., Tajima, K., Toriumi, K., Terada, K., Inoue, H., Yokoue, T., Shimizu, N., Kobahashi, T., Odahara, S., Hougham, G., Cai, C., Glowonia, J. H., Gutfiel, R.J von, John, R., and Lien, S.-C.A. *SID01 Digest Tech. Papers*, 1354 (2001).
8. Drzaic, P.S. *Liquid Crystal Dispersions*, World Scientific, Singapore (1995).
9. Drzaic, P.S. *J. Appl. Phys.* **60**, 2142-2148 (1986).
10. Doane, J.W., Vaz, N.S., Wu, B.G., and Zumer, S. *Appl. Phys. Lett.* **48**, 269-271 (1986).
11. Boots, H.M.J., Neijen, J.H.M., Paulissen, F.A.M.A., Mark, M.B. van der, and Cornelissen, H.J. *Mol. Cryst. Liq. Cryst.* **303**, 37-40 (1997).
12. Hikmet, R.A.M. *J. Appl. Phys.* **68**, 4406-4412 (1990).
13. Hikmet, R. A. M. *J. Mater. Chem.* **9**, 1921-1932 (1999).
14. Rajaram, C.V., Hudson S.D., and Chien, L.C. *Chem. Mater.* **7**, 2300-2308 (1995).
15. Craighead, H.G., Cheng, J., and Hackwood, S. *Appl. Phys. Lett.* **40**, 22-24 (1982).
16. Doane, J.W., Golemme, A., West, J.L., Whitehead Jr., J.B., and Wu, B.-G. *Mol. Cryst. Liq. Cryst.* **165**, 511-532 (1988).
17. Ferguson, J. L. *SID85 Digest Tech. Papers* **16**, 68 (1985).
18. West, J.L., *Mol. Cryst. Liq. Cryst.* **157**, 427-441 (1988).

19. Wu, B.-G., West, J.L., and Doane, J.W. *J. Appl. Phys.* **62**, 3925-3931 (1987).
20. Kim, W.-K., and Kyu, T., *Mol. Cryst. Liq. Cryst.* **250**, 131-141 (1994).
21. Vaz, N.A., Smith, G.W., and Montgomery Jr., G.P., *Mol. Cryst. Liq. Cryst.* **146**, 1-15 (1987).
22. Hirai, Y., Niama, S., Kumain, H., and Gunjima, T. *Proc. SPIE Int. Soc. Opt. Eng.* **1257**, 2-8 (1990).
23. Nostrum, C.F. van, Nolte, R.J.M., Broer, D.J., Fuhrman, T., and Wendorff, J.H. *Chem. Mater.* **10**, 135-145 (1998).
24. Leewis, C.M., Jong, A.M. de, and IJzendoorn, L.J. van, and Broer, D. J. *J. Appl. Phys.* **95**, 4125-4139 (2004).
25. Flory, P. J. *Principles of Polymer Chemistry*, Cornell University Press, Ithaca, New York (1953).
26. Thomas, N. L., and Windle, A. H. *Polymer* **23**, 529 (1982).
27. Broer, D.J., Lub, J., and Mol, G.N., *Nature* **378**, 467 (1995).
28. Margerum, J. D., Lackner, A. M., Ramos, E., Smith, G. W., Vaz, N. A., Kohler, J. L., and Allison, C. R. *US Patent* 4,938,568 (1990).
29. Sutherland, R. L., Tondiglia, V. P., Natarajan, L. V., Bunning, T. J., and Adams, W.W. *Appl. Phys. Lett.* **64**, 1074 (1994).
30. Bunning, T.J., Natarajan, L.V., Tondiglia, V., Sutherland, R.L., Vezie, D.L., and Adams, W.W. *Polymer* **36**, 2699-2708 (1995).
31. Bowley, C.C., and Crawford, G.P. *Appl. Phys. Lett.* **76**, 2235-2237 (2000).
32. Crawford, G.P. (Ed.) in: *Flexible flat panel displays*, John Wiley and Sons, Chichester (UK), 313-330 (2005).
33. Cairns, D. R., Bowley, C. C., Danworaphong, S., Fontecchio, A. K., Crawford, G. P., Li, L., and Faris, S. M. *Appl. Phys. Lett.* **77**, 2677-2679 (2000).
34. Bharadwaj, R. K., Bunning, T. J., and Farmer, B. L. *Liq. Cryst.* **27**, 591 (2000).
35. Jazbinsek, M., Olenik, I. D., Zgonik, M., Fontecchio, A. K., and Crawford, G. P. *J. Appl. Phys.* **90**, 3831 (2001).
36. Kyu, T., Nwabunma, D., and Chiu, H.-W. *Phys. Rev. E* **63**, 061802 (2001).
37. Sarkar, M. de, Gill, N.L., Whitehead, J.B., and Crawford, G.P. *Macromol.* **36**, 630-638 (2003).
38. Vorflusev, V., and Kumar, S. *Science* **283**, 1903-1905 (1999).
39. Lovinger, A.J., Amundsen, K.R., and Davis, D.D. *Chem. Mater* **6**, 1726-1736 (1994)

40. Montgomery Jr., G.P., Smith, G.W., and Vaz, N.A. in: *Liquid crystalline and Mesomorphic Polymers* (Eds. Shibaev, V.P., and Lam, L.), Springer, New York, 149-192 (1994).
41. Rajaram, C.V., Hudson, S.D., and Chien, L.C. *Chem. Mater.* **7**, 2300-2308 (1995).
42. Amundson, K., Blaaderen, A. van, and Wiltzius, P. *Phys. Rev. E* **55**, 1646-1654 (1997).
43. Nolan, P., Tillin, M., and Coates, D. *Liq. Cryst.* **14**, 339-344 (1993).
44. Smith, G.W., and Vaz, N.A. *Mol. Cryst. Liq. Cryst.* **237**, 243-269 (1993).
45. Smith, G.W. *Mol. Cryst. Liq. Cryst.* **241**, 37-53 (1994).
46. Vaz, N.A., Smith, G.W., and Montgomery Jr., G.P. *Mol. Cryst. Liq. Cryst.* **197**, 83-101 (1991).
47. Smith, G.W. *Mol. Cryst. Liq. Cryst.* **180B**, 201-222 (1990).
48. Nolan, P., Tillin, M., and Coates, D. *Mol. Cryst. Liq. Cryst.* **8**, 129-135 (1992).
49. Serbutoviez, C., Kloosterboer, J.G., Boots, H.M.J., and Touwslager, F.J. *Macromol.* **29**, 7690-7698 (1996)
50. Serbutoviez, C., Kloosterboer, J.G., Boots, H.M.J., and Touwslager, F.J. *Liq. Cryst.* **22**, 145-156 (1997).
51. Kloosterboer, J.G., Serbutoviez, C., and Touwslager, F.J. *Polymer* **37**, 5937-5942 (1996).
52. Boots, H.M.J., Kloosterboer, J.G., Serbutoviez, C., and Touwslager, F.J. *Macromol.s* **29**, 7683-7689 (1996).
53. Hirai, Y., Niyama, S., Kumai, H., and Gunijama, T. *S. Rep. Res. Lab. Asahi Glass Co., Ltd.* **40**, 285-296 (1990)
54. Kim, J.Y., Cho, C.H., Palffy-Muhoray, P., Mustafa, M., and Kyu, T. *Phys. Rev. Lett.* **71**, 2232-2235 (1993).
55. Shen, C., and Kyu, T. *J. Chem. Phys* **102**, 556-562 (1995).
56. Benmouna, F., Bedjaoui, L., Maschke, U., Coqueret, X., and Benmouna, M. *Macromol. Theory Simul.* **7**, 599-611 (1998).
57. Flory, J.P. *J. Chem. Phys.* **9**, 660 (1941).
58. Huggins, M.L. *J. Chem. Phys.* **9**, 440 (1941).
59. Flory, P.J., and Rehner, J. *J. Chem. Phys.* **11**, 521-526 (1943).
60. Flory, P.J. *J. Chem. Phys.* **18**, 108-111 (1950).
61. Maier, V.W., and Saupe, A. *Z. Naturforschg.* **14a**, 882-889 (1959).
62. Zhao, G., and Mouroulis, P. *J. Mod. Opt.* **41**, 1929-1939 (1994).
63. Qi, J., DeSarkar, M., Warren, G.T., and Crawford, G.P. *J. Appl. Phys.* **91**, 4795 (2002).

64. Qian, T., Kim, J.-H., Kumar, S., and Taylor, P. L. *Phys. Rev. E* **61**, 4007-4010 (2000).
65. Sutherland, R.L., Tondiglia, V.P., Natarajan, L.V., and Bunning, T.J. *J. Appl. Phys.* **96**, 951-965 (2004).
66. Meng, S., Kyu, T., Natarajan, L.V., Tondiglia, V.P., Sutherland, R.L., and Bunning, T.J. *Macromol.* **38**, 4844-4854 (2005).
67. Penterman, R., Klink, S.I., Koning, H. de, Nisato, G., and Broer, D.J. *Nature* **417**, 55-58 (2002).

Chapter 2

Two-step photo-enforced stratification*

2.1 Introduction

Polymerization-induced phase separation in a mixture containing monomers, a liquid crystalline (LC) material and an increasing fraction of polymers is a well-known technique to create thin composite films with a specific morphology and molecular order for liquid crystal display (LCD) applications and various other electro-optic device applications.^{1,2} For example, phase separation induced by photo initiated polymerization, further denoted as photopolymerization, has been applied to produce ‘random’ morphologies in polymer-dispersed liquid crystal (PDLC) devices^{3,4,5,6,7,8} and in liquid crystal cells containing oriented or liquid crystal polymer networks.⁹ PDLCs are thin films composed of micrometer-sized droplets of LC material homogeneously dispersed in a polymer matrix. They can be electrically switched between a strongly scattering ‘off’ state and a highly transparent ‘on’ state. Although there are several methods to produce PDLCs, UV-induced polymerization of a homogeneous mixture of monomers and LC material is a preferred method. Unlike alternative processes such as solvent-induced (SIPS) or temperature-induced phase separation (TIPS), photopolymerization-induced phase separation allows that the processing temperature and rate of polymerization are chosen independently. This provides a better control of the morphology (e.g. size and to some extent the shape of the droplets) and thus a better control of the electro-optical properties of the film.

Here, the goal is to develop a new LCD manufacturing technology based on a photopolymerization-induced phase separation process. Instead of using cell technology to produce LCDs,¹⁰ the LCD is made by the sequential coating and UV curing of a stack of organic layers on a substrate. The heart of a conventional LCD is a thin LC layer (typically 5 μm) sandwiched between two 0.7 mm thick glass substrates. In coatable (‘Paintable’) LCDs the liquid crystal material is confined

* Part of this chapter has been published in: Penterman, R., Klink, S.I., Koning, H. de, Nisato, G., and Broer, D.J. *Nature* **417**, 55-58 (2002).

between a substrate and a polymer sheet, with the important difference that the latter is formed during processing. This *in-situ* polymer sheet formation is the result of a photopolymerization-induced phase separation and the concept has been named *photo-enforced stratification*.

Since a photo-polymerization reaction is generally started by the (UV)-light-induced dissociation of a photoinitiator into free radicals, the reaction (and thus the final morphology) can be controlled by modulation of the light intensity in the monomer film. Such an intensity modulation can for example be realized *laterally* by exposure of the film through a mask and *transversally* by making use of light absorption of the film.^{11,12,13} In the concept of the present study the polymer sheet formation on top of a layer of LC material is induced by the presence of (a sufficiently high concentration of) a UV-light absorbing monomer in the film. During UV irradiation of the film, an exponentially decreasing UV-light intensity (I) is established in the film due to the presence of the UV-light absorber. This UV-light intensity gradient is translated into a transversal polymerization rate (P) gradient (assuming steady-state conditions, $P \sim I^{1/2}$).¹⁴ The faster consumption of monomers in the top of the film induces an upward diffusion of monomers, and a concomitant downward diffusion of LC material. As a result the bottom of the film becomes enriched with LC material, and at a certain conversion, the LC material phase separates from the polymer gel phase and forms a new LC phase at the bottom of the film.

In this chapter a proof of principle of the photo-enforced stratification concept is demonstrated. It is shown that the combination of a mask exposure step and a subsequent flood exposure (hence the term two-step photo-enforced stratification process) of a thin LC/monomers film of a tailored composition results in a stratified LC/polymer morphology. Furthermore, a qualitative description of the photo-enforced stratification process is given.

2.2 Experimental section

2.2.1 Materials

Structural formulae of the compounds used are shown in Figure 2.2. Isobornylmethacrylate (IBoMA) was purchased from Mitsubishi Chemical (Minatoku, Tokyo, Japan) and used without further purification. 4,4'-di-(6-methacryloyloxyhexyloxy)-3-methylstilbene (*stilbene-dimethacrylate*) was synthesized in-house by Dr. J. Lub and Ing. W. Nijssen at Philips Research (Eindhoven, The Netherlands). The synthesis is described in Ref. 15. E7 and K15

were purchased from Merck (Darmstadt, Germany). Dimethoxyphenylacetophenone (DMPA or Irgacure 651) was purchased from Ciba Specialty Chemicals (Basel, Switzerland). The composition of the LC/monomers mixture is 50 wt.% LC material (E7 or K15), 5 wt.% stilbene-dimethacrylate, 44.5 wt.% IBoMA, and 0.5 wt.% Irgacure 651.

The UV-VIS absorption spectra of stilbene-dimethacrylate, Irgacure 651 and E7 were determined via measurements of their UV-VIS absorption spectra with a Perkin-Elmer Lambda 900 photo-spectrometer. Thereto, 1-cm cuvettes were filled with four solutions containing different concentrations of the respective compounds dissolved in acetonitrile. The extinction coefficient was deduced from a linear fit of the absorbance versus the concentration.

2.2.2 Substrate preparation

The glass substrates (Corning, Japan, 6 x 7 cm²) were cleaned by hand with water and soap (Teepol), subsequently rinsed with water and dried in a cold airflow. A planar alignment layer was deposited from solution (AL3046 from JSR, Japan) via a spin coating process (20 BM spin coater (BLE electronic equipment GmbH, Germany), 5 s at 1000 rpm, followed by 30 s at 4000 rpm). The polyimide-covered substrates were subsequently subjected to two heating steps: 10 minutes at 90°C on a hotplate, and 60 minutes at 180°C in an oven. Finally, the alignment layer was rubbed using a homemade rubbing machine (a rotating drum covered with a velvet cloth, moving with a constant speed over the substrate surfaces).

2.2.3 Doctor blade coating

A thin film of the LC/monomers mixture was applied on the polyimide-covered glass substrate by means of doctor blade coating. An Erichsen 509 MC/1 coater was used for this purpose. A doctor blade with a gap of 60 µm in combination with a blade velocity of 2.5 mm·s⁻¹ was used to obtain a film of 30 µm thickness. Typically 0.2 ml of the LC/monomers mixture was applied.

2.2.4 UV exposure procedures

Stratification step

To prevent oxygen inhibition of the free-radical polymerization,¹⁶ the photopolymerization was conducted in a nitrogen atmosphere. Thereto, the samples were placed in a stainless steel nitrogen-flushed chamber with a UV transparent glass lid (B270 glass). After placing the sample in the chamber, the system was flushed with nitrogen for 5 minutes prior to the UV exposure. During the exposure there is a

constant nitrogen flow through the chamber. The temperature in the chamber was kept constant at 50°C using a hotplate. The experimental set-up is depicted in Figure 2.1a. The phase separation process is monitored with a polarization microscope (Leica MZ-12) equipped with a camera (Leica IC-A). A separate light source (Leica CLS 100) in combination with a UV cut-off filter and a polarization filter illuminates the sample. The reflected light from the sample passes a second polarization filter (the analyzer) and the camera in the microscope captures the image. Internal reflections from and within the sample are utilized rather than a mirror on the bottom of the chamber, since the latter would result in an undesired reflection of UV-light and a consequent decrease of the intensity gradient. The polarization filters are in a crossed configuration, which results in a dark appearance of the (isotropic) films before polymerization. The rubbing direction of the alignment layer was placed at 45° with respect to the transmission axis of the polarizers. Image Pro Plus software (Media Cybernetics) was used to capture images of the sample at time intervals of 10 seconds.

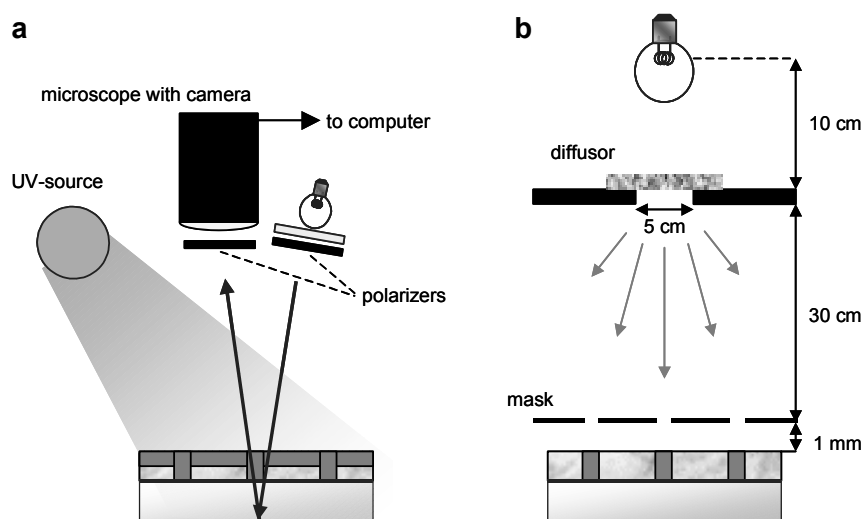


Figure 2.1: a) A schematic drawing of the experimental set-up. The phase separation process is followed in time with a polarization microscope equipped with a camera. A separate UV-filtered polarized light source illuminates the sample. After passing the analyzer the reflected light is collected by a CCD camera. b) The mask exposure set-up for patterned irradiation of the samples.

The samples were exposed to UV-light for 30 minutes. The exposure was conducted with four 4W Philips TL08 lamps, positioned such that a homogeneous intensity of $0.8 \text{ mW}\cdot\text{cm}^{-2}$ was obtained at a distance of 15 cm from the lamps. The intensity of the array of TL08 lamps was measured with an IL1700 radiometer (International Light, Inc.). For this purpose, the photodiode unit contained a W, a QNDS3 and a WBS 320 filter. The presence of the microscope objective at a few centimeters from the sample made UV irradiation of the sample at an angle necessary. This results in an additional intensity gradient in the direction parallel to the substrate. At the sample surface the intensity drops with a factor of two over a distance of 5 cm.

Since the images were taken from only a small area ($2.5 \times 2.5 \text{ mm}^2$) in the center of the sample this lateral intensity gradient can be neglected.

Mask exposure set-up

The mask exposure set-up used for patterned irradiation of the LC/monomers film is illustrated in Figure 2.1b. A high-intensity lamp (Philips UHP 100W) was positioned at a distance of 40 cm from the sample. At 10 cm from the source, the beam passes a diffuser plate to obtain a homogenous light beam and subsequently a hole with a diameter of 5 cm. The mask contains a grid of transparent lines. The line width is 20 μm and the distance between the lines is 480 μm . Spacers keep the mask at a distance of 1 mm from the film. The UV light intensity at the position of the sample was $30 \text{ mW}\cdot\text{cm}^{-2}$ as determined with an IL1700 radiometer (International Light, Inc.) equipped with a photodiode unit that contained a W, a QNDS3 and a WBS 400 filter.

The sample, spacers and mask were placed in a stainless steel chamber with a UV transparent glass lid. After closing the chamber it was flushed with nitrogen for 5 minutes before the sample was exposed to UV light for 3 minutes.

2.2.5 Characterization of the stratified LC/polymer morphologies

A Leica DM-LP microscope equipped with a Leica camera and a Leica MZ-6 microscope with a Leica IC-A camera were used for optical characterization of the structures. Image Pro Plus software (Media Cybernetics) was used to capture the data. Surface profile measurements were performed with a Dektak3ST stylus profiler and a Wyko NT2000 optical profiler, both from Veeco Instruments.

The composition of the phase separated LC-rich phase was determined by HPLC analysis (Waters HPLC system). The measurements were performed using a LichroCart 250-4 Superspher 100RP-18 end capped column (cat.nr.1.16858.0001). The column temperature was adjusted to 50°C . 0.3 mg of sample material was diluted with 4 ml acetonitrile (ACN) and the injection volume was 8 μl . The composition of the eluent was 87%ACN/13% H_2O by volume and the flow rate was 1 ml/min. To detect the signals a 996 photodiode array detector (Waters) was used. A wavelength of 290 nm was selected to quantify the components.

2.2.6 Device preparation and electro-optical characterization

Glass substrates (Corning 1737) covered with 150 nm thick transparent indium-tin-oxide (ITO) were structured by standard photolithography. The photolithography involves subsequently spin-coating of a photoresist (AZ1518, Clariant, Switzerland) at 2000 rpm for 30 s, UV exposure through a mask (Karl Süss

MA-8, $I = 10 \text{ mW}\cdot\text{cm}^{-2}$, $t = 9 \text{ s}$), developing (AZ developer, Clariant, Switzerland), wet chemical etching (etchant: 94 wt% 1N HCl + 6 wt% $\text{FeCl}_3\cdot 6\text{H}_2\text{O}$, $t = 150 \text{ s}$) and stripping (Microstrip 2001, Fujifilm, Japan). The resulting interdigitated ITO electrodes have a width of $9 \mu\text{m}$ and the distance between the electrodes is $9 \mu\text{m}$. A planar polyimide alignment layer is applied on the substrate according to the procedure described in Paragraph 2.2.2. The alignment layer was rubbed at an angle of 10 degrees with respect to the electrode axis to obtain an in-plane pre-tilt of the LC molecules.

After the photo-enforced stratification process the substrate with the array of LC-filled polymer capsules was placed between crossed polarizers, such that the rubbing direction of the alignment layer was parallel to the transmission axis of one of the polarizers. In-plane electrical fields switch the LC material in the formed capsules when a voltage is applied over the interdigitated electrodes. The set-up to measure the transmission-voltage (T - V) curve and the transmission-time (T - t) curve consisted of a Leica polarization microscope (type DM LSP) equipped with a photo-multiplier and a PC. Labview-based software was utilized to control the drive voltage applied on the device via data acquisition hardware (DAQ) in the PC and to collect the signals from the photo-multiplier. The device is driven by a square wave (AC) voltage train.

2.3 Results and discussion

2.3.1 Photo-enforced stratification: Selection of materials and conditions

The LC material that has been used for the photo-enforced stratification process is E7, an LC blend that consists of only four components: three cyano-biphenyls and a cyano-terphenyl (see Figure 2.2). Occasionally, for model experiments, E7 was replaced by the single-component LC material K15 (4-n-pentyl-4'-cyanobiphenyl or 5CB), which is in fact the major component of E7. In Table 2.1 the properties of E7 and K15 are listed.

Table 2.1: Phase transitions and electro-optical properties of E7 and K15.

LC	C-N (°C)*	N-I (°C)*	n_e **	n_o **	$\Delta n (=n_e - n_o)$	ϵ_{\parallel} ***	ϵ_{\perp} ***	$\Delta\epsilon (= \epsilon_{\parallel} - \epsilon_{\perp})$
E7	-10	58.0	1.75	1.52	0.23	19.3	5.2	14.1
K15	23.5	35.5	1.72	1.53	0.19	16	6	10

* C-N and N-I are respectively the crystalline-to-nematic and the nematic-to-isotropic transitions.

** n_e is the extraordinary and n_o is the ordinary index of refraction.

*** ϵ_{\parallel} and ϵ_{\perp} are the dielectric constants parallel and perpendicular to the LC director, respectively.

Nematic ordering of the liquid phase upon phase separation as described by the Maier-Saupe theory^{17,18} can be a driving force for phase separation. Shen and Kyu have combined the Maier-Saupe free energy of nematic ordering with the Flory-Huggins free energy of isotropic mixing to model the thermodynamic phase equilibria of a liquid crystal and a polymer mixture with the ultimate goal to produce PDLCs by temperature-induced phase separation (TIPS).¹⁹ To employ the nematic ordering contribution in the stratification experiments, the processing temperatures will be kept below the nematic-isotropic temperature of the LC material, i.e. below 58.0°C in the case of E7 and below 35.5°C in the case of K15.

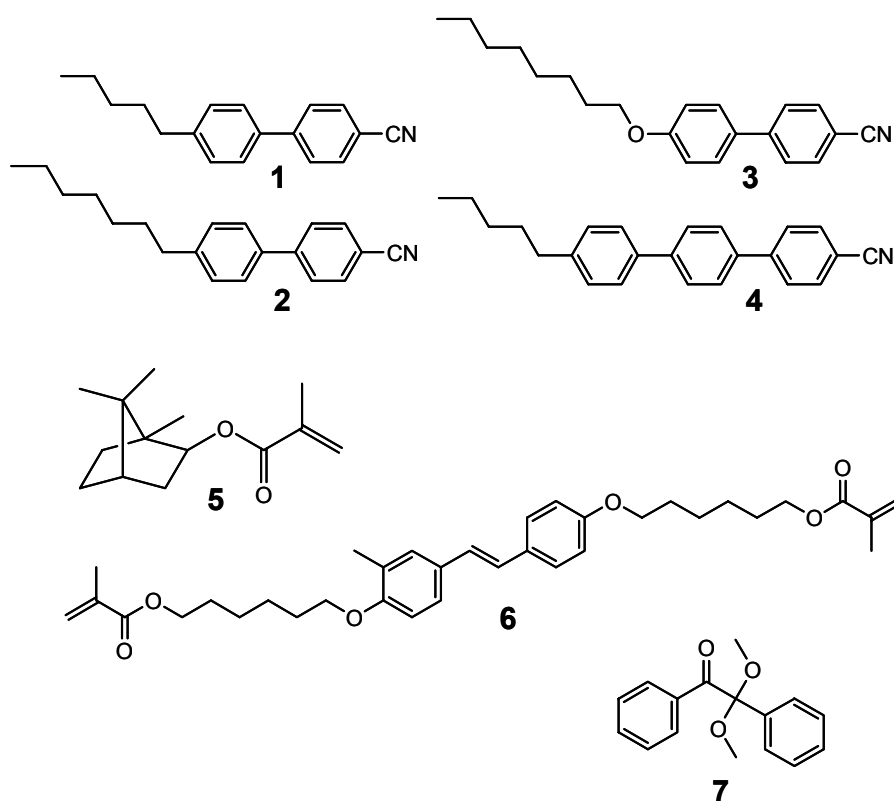


Figure 2.2: The structures of the liquid crystal blend E7 consisting of 3 cyanobiphenyls and a cyanoterphenyl: **1**) 5CB (51 wt%), **2**) 7CB (25wt%), **3**) 8OCB (16wt%), **4**) 5CT (8wt%). The monomer system consists of: **5**) isobornylmethacrylate (IBoMA), **6**) 4,4'-di-(6-methacryloyloxyhexyloxy)-3-methylbibenzyl (stilbene-methacrylate), **7**) photoinitiator DMPA (Irgacure 651).

Isobornylmethacrylate (IBoMA) has been selected as the main component of the monomer mixture, because it is a non-volatile liquid monomer of low viscosity and upon polymerization, poly(IBoMA) is a transparent glassy polymer with a glass transition temperature of 110 °C. The other component of the monomer mixture, stilbene-dimethacrylate, has been designed and synthesized to combine two features: Firstly, it has an intense absorption band that overlaps with the absorption spectrum of the selected photoinitiator dimethoxyphenyl acetophenone (DMPA or Irgacure 651).

In acetonitrile the extinction coefficient of stilbene-dimethacrylate is $25 \times 10^3 \text{ M}^{-1} \text{ cm}^{-1}$ at 340 nm. Secondly, it provides the crosslinks between the poly(IBoMA) chains (the IBoMA/stilbene-dimethacrylate molar ratio was taken as 23:1, see below). Dušek has adapted Flory-Rehner's theory of swelling equilibria and rubber elasticity for polymerizing systems. He has modelled the influence of the increasing crosslink density of the polymer network on phase-separation in a reactive monomer/solvent system.²⁰ Serbutoviez et al. have demonstrated that crosslinks contribute to the phase separation in a PDLC system containing K15 as the LC material and tetraethyleneglycoldiacrylate (TEGDA).²¹

Chemical and physical interactions between the components in the polymerizing mixture as expressed by the respective Flory-Huggins interaction parameters contribute to the driving force for phase separation. The *enthalpic* component of the Flory-Huggins interaction parameter (χ_H) between two components can be obtained via Equation 2.1 once the solubility parameters δ of the components have been estimated.^{22,23}

$$\chi_H = V_1(\delta_1 - \delta_2)^2 / RT \quad (2.1)$$

where V_1 is the molar volume of the component, and δ_1 and δ_2 are the respective solubility parameters of the component and the co-polymer. It should be noted that since the *entropic* contribution to the Flory-Huggins interaction parameter cannot be obtained in this way, χ_H will be used as an approximation of the Flory-Huggins parameter. For a qualitative description of the system, this approximation is sufficient. The solubility parameter of a polymer cannot be determined directly. Therefore the solubility parameters of the polymer and the single components were estimated on the basis of contributions from the various chemical groups, present in the molecular structure.^{22,24} The estimated δ 's and the χ_H 's between the various compounds and the poly(IBoMA-co-stilbene-dimethacrylate) co-polymer are listed in Table 2.2. For the calculation of δ of the co-polymer the IBoMA/stilbene-dimethacrylate ratio has been taken as 23:1, i.e. the initial mole ratio in the starting mixture.²⁵ As can be expected from the structural resemblance of the monomers and the co-polymer, the mutual Flory-Huggins interaction parameters are essentially zero, whereas the interaction parameter is +0.5 for the LC/polymer interaction. Therefore, there will be a much larger driving force for the LC compounds to phase separate from the co-polymer than for the two monomers. As a result an LC rich phase is expected upon phase separation. The LC/monomers ratio has been selected as 50/50 (wt./wt.). The reason for this is straightforward: a large excess of LC material will result in an extremely

thin polymer layer and a large excess of monomer may not result in phase separation upon polymerization.

Table 2.2: Calculated²⁴ solubility parameters (δ) and Flory-Huggins interaction parameters $\chi_{p,c}$ (enthalpic contribution) between poly-(isobornylmethacrylate-stilbene-dimethacrylate) and the various components.

Compound	δ	$\chi_{p,c}$
5CB	21	0.5
7CB	21	0.5
8OCB	21	0.5
5CT	21	0.5
IBoMA	19	0
Stilbene-dimethacrylate	20	0.1
Co-polymer (23:1)	19	0

2.3.2 Photo-enforced stratification process

UV-intensity gradient

In the photo-enforced stratification concept, a thin film of the E7/IBoMA/stilbene-dimethacrylate mixture is irradiated with UV light. Figure 2.3a shows the overlapping absorption spectra of stilbene-dimethacrylate and Irgacure 651 and the emission spectrum of the TL08 lamp. Using Beer's law and by taking into account the absorption spectra of stilbene-dimethacrylate and Irgacure 651 as well as the emission spectrum of the lamp,²⁶ the intensity gradient of UV light absorbed by the photoinitiator across the layer thickness is calculated, see Figure 2.3b. It should be noted that also the absorption spectrum of 5CT (not shown), one of the components of E7, has a partial overlap with that of Irgacure 651 and this small contribution has also been taken into account. It can be seen in Figure 2.3b that towards the bottom of the film the intensity drops to approximately 20% of the initial intensity. This residual intensity is due to the fact that the overlap of the absorption spectra of stilbene-dimethacrylate and Irgacure 651 is not perfect, and as a result the film is transparent to UV light of longer wavelengths than 370 nm, which is also emitted by the TL08 lamps.

Since the absorption spectrum of Irgacure 651 has been taken into account in the calculation of the UV-light intensity (I) gradient, the polymerization rate gradient as a function of depth can also be estimated based on $P \sim I^{1/2}$, see Figure 2.3b.¹⁴ These

profiles only represent the intensity and polymerization rate gradients at the onset of the photopolymerization reaction. The profiles are expected to change during the photopolymerization process as a result of diffusion of the components. Moreover, the stilbene core of stilbene-dimethacrylate exhibits some UV-induced trans-cis isomerization, and the cis-isomer has a lower absorption coefficient than the trans-isomer, effectively resulting in some bleaching.

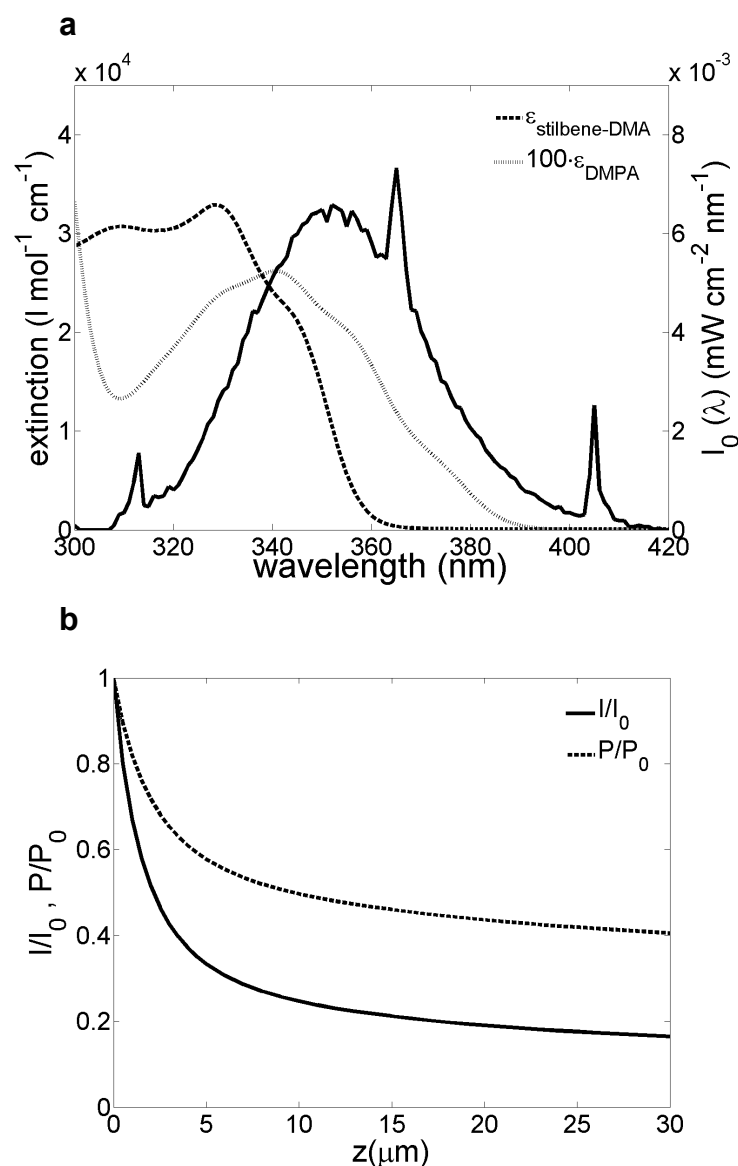


Figure 2.3: a) The extinction curves of the UV-absorber and the photoinitiator and the emission spectrum of the UV source (Philips TL08, measured at 10 cm distance). b) Calculated intensity- and polymerization gradient at the onset of irradiation.

Single-step photo-enforced stratification process

A 30 μm film of the E7/IBoMA/stilbene-dimethacrylate/Irgacure 651 mixture was exposed to UV light of $0.8 \text{ mW} \cdot \text{cm}^{-2}$. The temperature was set to 50°C , below the

nematic–isotropic temperature of E7, and above 40°C at which the stilbene-dimethacrylate monomer tends to precipitate from the mixture during polymerization. The photopolymerization process and in particular the phase-separation process was monitored with a camera mounted on a polarization microscope. Figure 2.4a-d shows four snapshots respectively after 7.5, 8, 10 and 20 minutes of irradiation. At $t = 0$, the isotropic film is dark in the chosen set-up of the polarization microscope with the sample between crossed polarizers (see Paragraph 2.2.4). At a certain conversion (t is approx. 7.5 minutes), the appearance of macroscopic bright nematic droplets can be observed. Since the LC material in these droplets is uniaxially aligned in the direction imposed by the alignment layer, it can be concluded that the droplets are formed at the alignment layer interface. Furthermore, the fact that the growing LC droplets are nematic at the polymerization temperature indicates that the amount of monomers in this LC phase is very low. For a mixture of pure E7 and (unpolymerized) IBoMA it was found that the IBoMA fraction must be lower than 4 wt.% in order to get a nematic phase at 50°C (which is the polymerization temperature). It should be noted that phase separation may lead to compositional drift i.e. the phase separated LC does not necessarily have the same composition as the LC in the starting mixture, which affects the phase behavior. For instance, in literature it is reported that E7/NOA65 (Norland Optical Adhesive 65) based PDLCs made via polymerization-induced phase separation have reduced fractions of the lower molecular weight compounds 5CB and 7CB in the phase separated LC, resulting in a higher nematic to isotropic temperature (T_{NI}).²⁷ This implies that the actual fraction of monomers in the phase separated LC may slightly deviate from the 4 wt.% found for the E7/IBoMA mixture. Compositional drift will be addressed in more detail in Paragraph 2.3.4.

Upon further photopolymerization, the LC droplets grow and coalesce into larger droplets (see Figures 2.4b-d). Although under the present experimental conditions the LC droplets do not coalesce into a continuous layer, the intended stratified morphology is obtained: a polymer layer is formed on top of the LC droplets with the LC in contact with the alignment layer at the substrate surface. The schematic cross-section in Figure 2.4e was deduced from the polarization microscopy pictures and surface profile measurements of the sample. The size of the final droplets ranges from approximately 200 to 500 μm .

It is tempting to describe the appearance of the macroscopic LC droplets at $t = 7.5$ minutes as the nucleation-controlled start of the phase separation process. However, numerous repetitions of this experiment and careful examination of the resulting pictures led to the conclusion that in fact the phase separation has started earlier. As was mentioned before, at $t = 0$ the film is dark in the polarization microscopy pictures. Shortly before the formation of the macroscopic LC droplets, the

entire film becomes bright as a result of incipient light scattering. This has been interpreted as the onset of the phase separation: the nucleation of small, (sub)-micrometer sized LC droplets. These small LC droplets grow and coalesce into larger droplets, which can be seen in Figure 2.4.

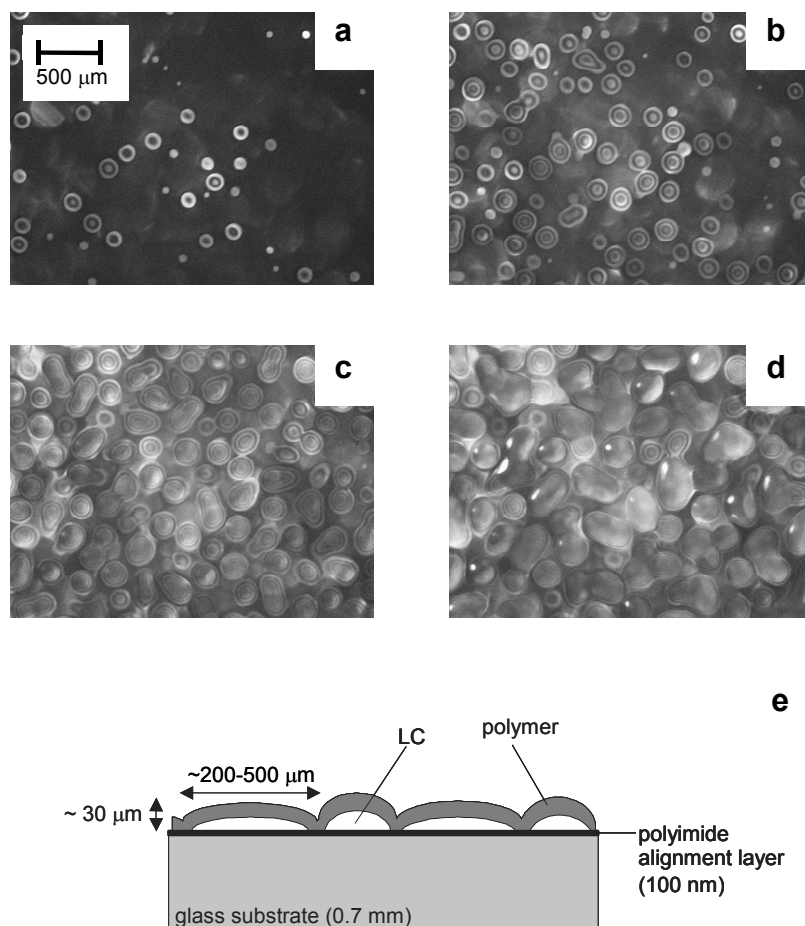


Figure 2.4: The photo-enforced stratification of the thin E7/reactive monomer film seen from the top after: a) 7.5 minutes, b) 8 minutes, c) 10 minutes, d) 20 minutes. After the onset of phase separation the droplets grow and coalesce into randomly distributed LC droplets covered with a polymer topcoat. e) Schematic cross-section of the stratified morphology (note that the dimensions in this drawing are not to scale). The droplets do not coalesce into a continuous and flat LC layer.

The experiment demonstrates that the concept of photo-enforced stratification works for the E7/IBoMA/stilbene-dimethacrylate material system. However, it also shows that under these conditions the droplets do not coalesce into a continuous flat LC layer, despite the homogeneous start of the phase separation. Varying the temperature between 40°C and 60°C, and/or varying the UV irradiation intensity between 0.3 and 0.8 W/cm² in subsequent experiments did not improve on this. In the next paragraph a solution to this problem will be presented.

2.3.3 Two-step photo-enforced stratification process

In the single-step stratification process irregular structures are formed, due to the random growth and coalescence of LC droplets. A possible way to control the growth of the LC droplets (and thus to obtain more uniform structures) is to confine their growth and coalescence. Thereto the strategy was followed to confine the growth and coalescence to small compartments via the prior formation of a grid of polymer walls in the LC/monomers film. Such structures can be obtained by irradiating the film through an appropriate mask with UV light with wavelengths larger than 360 nm, schematically represented in Figure 2.5a. These wavelengths are beyond the absorption region of the stilbene-dimethacrylate monomer, but still at wavelengths which are absorbed by the photoinitiator (see Figure 2.5c). Therefore the light penetrates the layer all the way to the bottom and polymerization in the exposed areas results in the formation of polymer walls by a simultaneous process of localized polymerization and lateral monomer diffusion to the polymerizing areas. A mask with a grid pattern with a 500 μm pitch of was chosen, since these dimensions are of the order of the final droplet sizes found in the single-step stratification process. In a subsequent step, the sample was flood exposed to UV light from the array of TL08 lamps under the same conditions as for the single-step stratification process (Figure 2.5b).

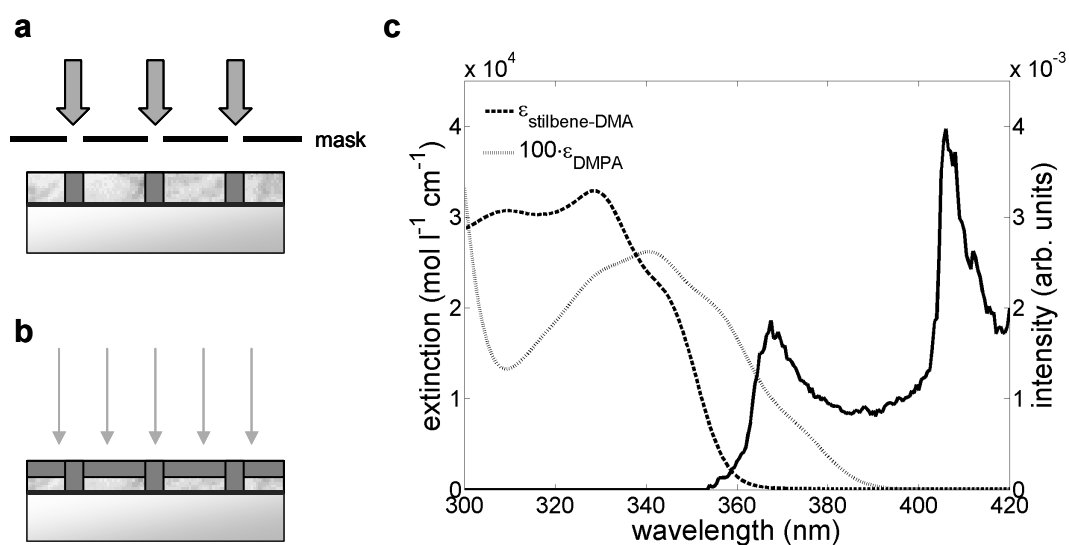


Figure 2.5: The two-step UV exposure process: a) During the first step the polymer walls are formed during mask exposure. b) During the second step (the stratification step) a flood exposure forms a polymer cover on top of a continuous LC layer confined by the polymer walls. c) The absorption spectra of the UV-absorber and the photoinitiator in the monomer/LC mixture and the emission spectrum of the UV source (Philips UHP) used in the mask exposure.

Finding the optimal mask exposure time was done by trial and error. Details of the set-up can be found in Paragraph 2.2.4. As a result of refraction, internal reflections and scattering in the LC/monomers film some polymer is also formed in the unexposed areas. It was found that a mask exposure time of 3 minutes at room temperature, followed by a flood exposure of 30 minutes at 50°C led to the best results: the formation of an array of polymer capsules filled with liquid crystal (see Figure 2.5b for a schematic representation). The capsules consist of polymer walls that were formed during the mask exposure step and a polymer ‘lid’ created during the second polymerization step, i.e. the stratification step. After the mask exposure step, the surface of the sample was probed with an interferometer. It can be seen in Figure 2.6a that an array of polymer walls has been formed, which are a few microns higher than the unexposed areas of the film. This is the result of mass transport of monomers from the unexposed areas to the exposed areas.

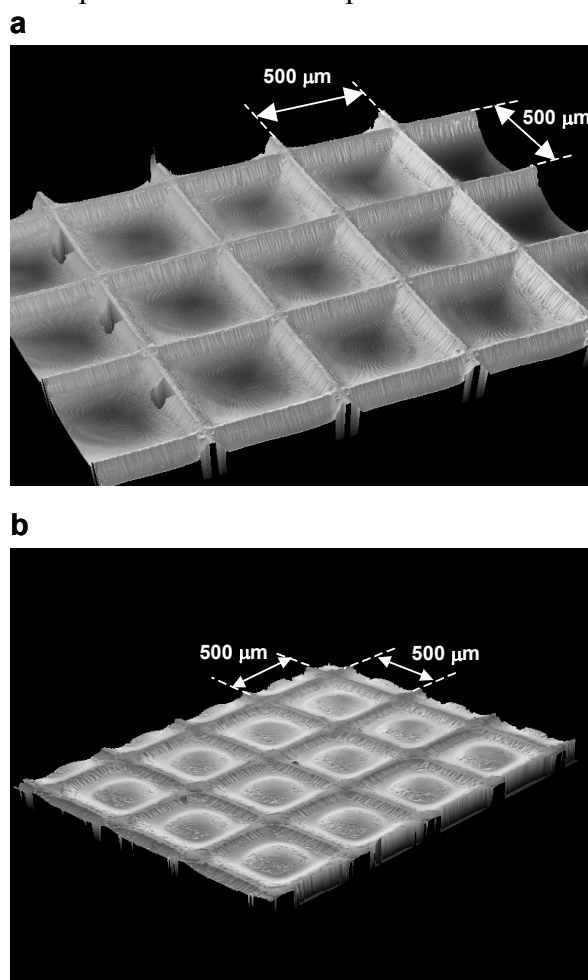


Figure 2.6: a) The surface profile of the structures observed by interferometric microscopy after polymerization of the walls. b) The surface profile after the stratification step. The pictures show an increase of the thickness of the film at the positions of the walls. The polymer on top of the liquid crystal domains has a convex shape. Please note that the vertical dimensions do not scale with the lateral dimensions. The polymer protrusions at the position of the walls are of the order of 5-10 μm high.

The formation of the LC phase in each of the capsules during the stratification step has been followed with the polarization microscope (Figures 2.7a-d). The start of the phase separation, i.e. the characteristic scattering of light by the sample, was observed after 5 minutes. Shortly after the start, macroscopic LC droplets appear in the vicinity of the polymer walls (Figure 2.7a). Subsequently, the droplets grow and coalesce further into a continuous LC domain within several minutes. Although the time for the droplets to grow and coalesce seems to differ from capsule to capsule (Figure 2.7b-c), the final LC domains in each of the capsules have a similar shape and thickness and the layer has a regular optical appearance (Figure 2.7d).

The surface profile of the structures obtained by interferometry is shown in Figure 2.6b. A striking feature is the regularity of the structures over the entire substrate. Besides this, two other features can be recognized in the structures: the protruding polymer walls and the convex shape of the polymer on top of the LC domains.

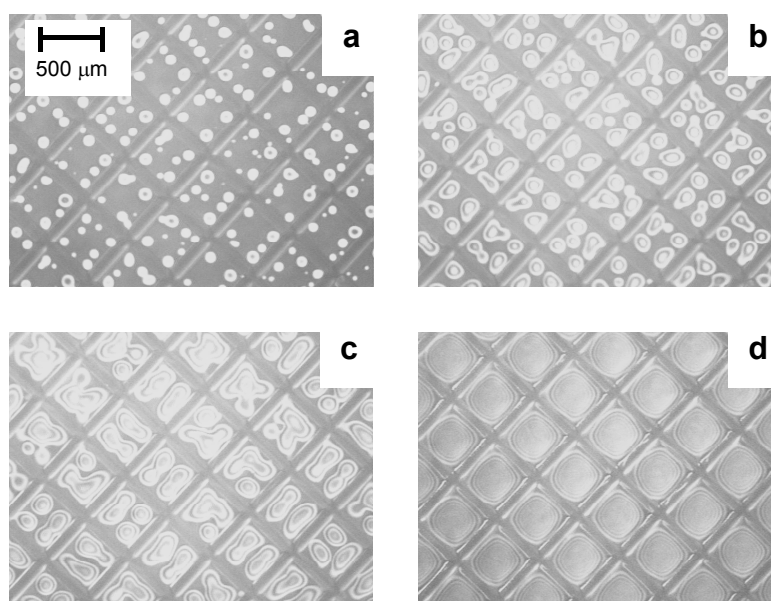


Figure 2.7: Polymerization-enforced stratification localized between the grid of polymer walls, seen from the top after: a) 5.5 minutes, b) 6.5 minutes, c) 7.5 minutes, d) 30 minutes. The polymer walls were made by irradiating the film through a mask for 3 minutes with high intensity UV light. During the subsequent flood exposure within each box the LC droplets coalesce into a (small) continuous LC layer.

Figure 2.8a shows an enlarged polarization microscopy picture of the LC-filled polymer capsules. The transmission axes of the polarizers in the microscope were at 90° with respect to each other, and at 45° with respect to rubbing direction of the alignment layer of the sample. The LC material in the capsules is uniaxially aligned. The fringes in the LC domains indicate a curved shape of the LC-polymer interface. The thickness of the LC layer is at its maximum in the center of the capsule

and drops off to zero at the edges. The dark appearance of the polymer walls confirms that the polymer walls are isotropic.

The height of the capsules was determined with a stylus profiler by making a cut through the stack. Subsequently, the polymer capsules were removed from the substrate and their inner dimensions were probed with a surface profiler. From these measurements, a schematic cross-section of the capsules was deduced (see Figure 2.8b). The capsules are $0.5 \times 0.5 \text{ mm}^2$ wide with walls of approximately $100 \mu\text{m}$ thickness. The polymer layer that covers the LC material is approximately $15 \mu\text{m}$ thick. The thickness of the LC layer in the center of the capsule is approximately $15 \mu\text{m}$. The polymer walls are locally approximately $7 \mu\text{m}$ higher than the polymer top layer.

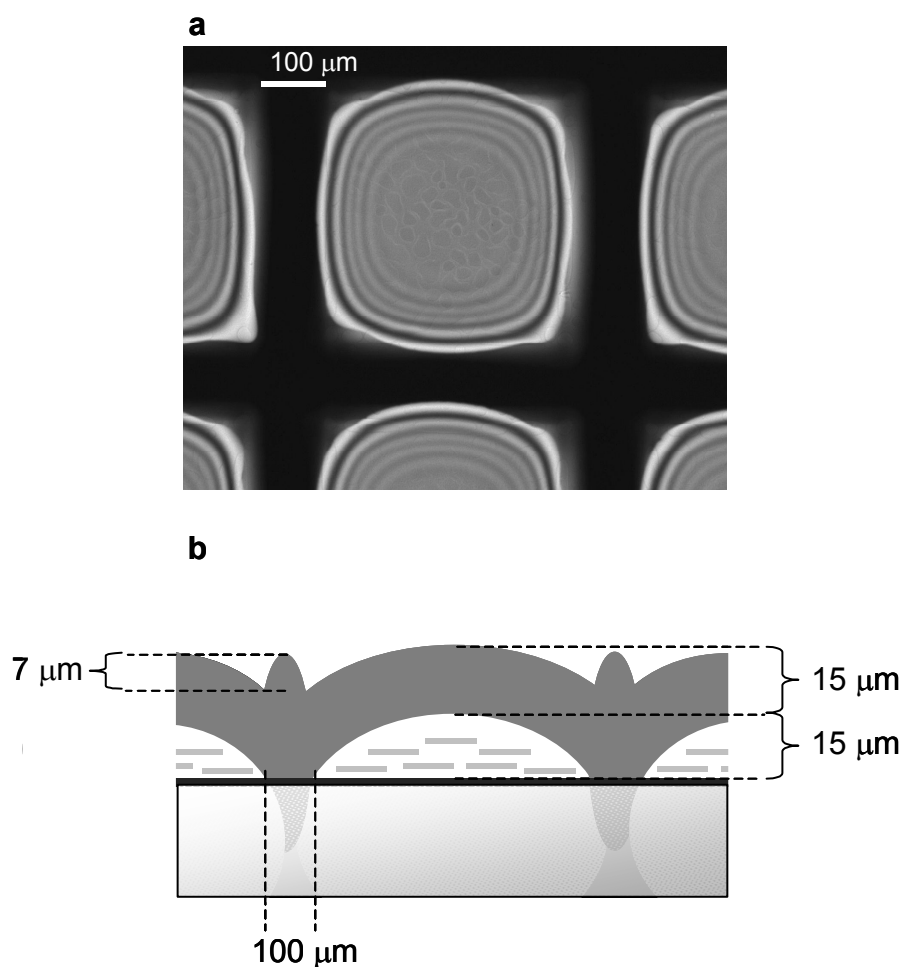


Figure 2.8: a) LC filled polymer capsule observed between crossed polarizers by a polarization microscope (polarizers at 45° with respect to the rubbing direction of the alignment layer; the rubbing direction is parallel to the polymer walls). b) A schematic cross-section deduced from optical and surface profile measurements.

2.3.4 Location of the phase separation

In the concept of photo-enforced stratification, the faster consumption of monomers in the top of the film induces an upward diffusion of monomers, and a concomitant downward diffusion of LC material to the bottom. At a certain conversion, the LC material phase separates and forms a new phase at the bottom of the film. This was indeed observed both in the single-step and two-step photo-enforced stratification experiments. However, under the current experimental conditions phase separation is not only limited to the bottom of the film, but also takes place to some extent at other positions in the film.

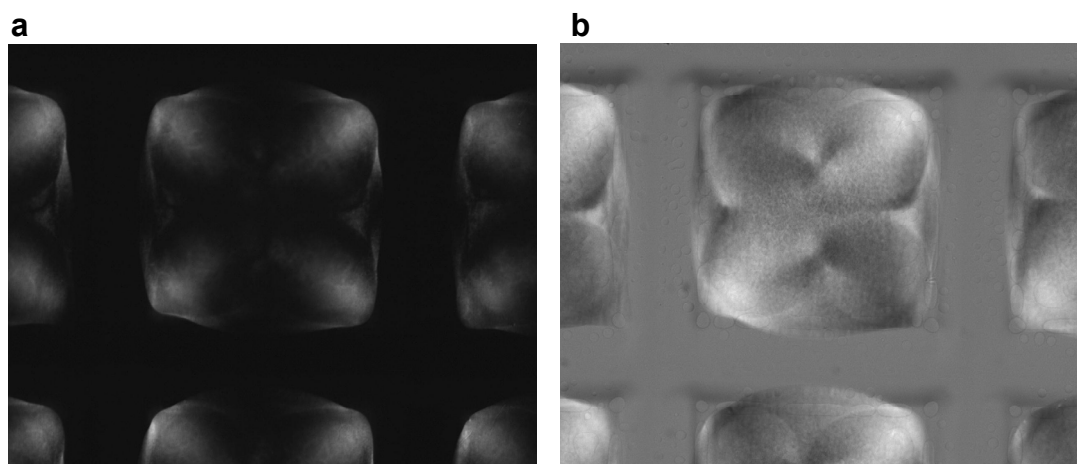


Figure 2.9: a) LC filled polymer capsule between crossed polarizers. b) The same LC capsule when the polarizers are at an angle of 60° . Between the polymer walls (above the LC layer) circular shaped contours are visible. The transmission axis of the entrance polarizer is parallel to rubbing direction of the alignment layer. (The rubbing direction is parallel to the polymer walls).

Figure 2.9a shows a polarization microscopy picture of the LC-filled polymer capsules. This time the transmission axes of the polarizers in the microscope were at 90° with respect to each other, and at 0° with respect to rubbing direction of the alignment layer of the sample. Figure 2.9a shows that the capsules are dark (as one would expect for a uniaxially aligned LC phase), except for the positions near the corners. An explanation for this light ‘leakage’ is depolarization of the light induced by inhomogeneities in the polymer film. There are strong indications that these inhomogeneities are in fact stretched microscopic LC droplets in the polymer located near the polymer/LC interface. During the stratification process spherical microscopic LC droplets are formed in the middle and at the bottom of the film. For reasons that will be explained in Chapter 6 the microscopic LC droplets that are not located directly at the alignment layer interface cannot coalesce, but instead are deformed by anisotropic stresses exerted on the polymer by the expanding LC domains at the bottom of the film. As a result the LC material within each droplet becomes aligned

along the direction of the stress. The mechanism is schematically visualized in Figure 2.10.

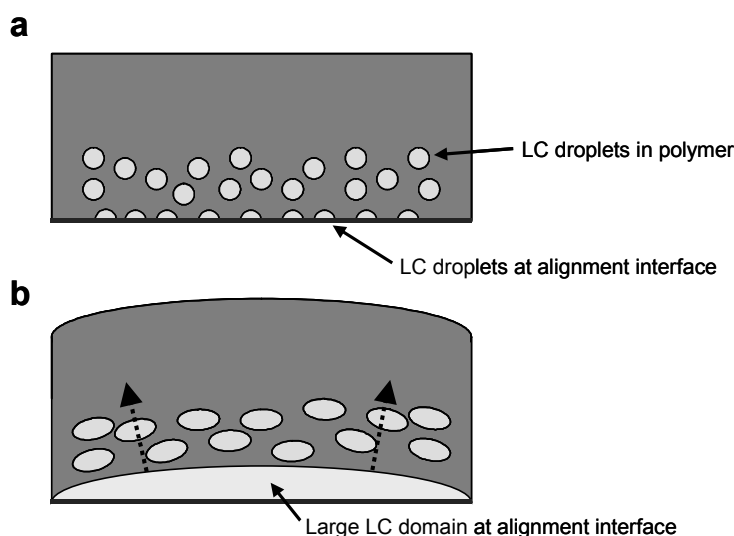


Figure 2.10: a) Schematic representation of the spherical LC droplets formed in the polymer topcoat during the process. b) Due to the expanding LC domain at the bottom of the film and the concomitant lateral stresses on the polymer the droplets deform.

The director pattern of the stretched droplets is macroscopically visible as circular shaped contours in the polymer topcoat, which become more apparent when the capsule is placed between polarization filters, which are at an angle of 60° with respect to each other (Figure 2.9b). The shapes of the circular contours show a remarkable resemblance with the shapes of the LC droplets visible in the snapshots of the process in Figure 2.7b-c. This indicates that the director patterns of the stretched droplets are already being formed during the growth of the LC domains at the bottom of the film before these domains coalesce into a continuous LC layer. The contours disappear when the sample is heated above the nematic-isotropic transition temperature of the LC material (not shown). Upon cooling back to room temperature the contours reappear. The presence of this localized PDLC-like morphology in the polymer film will be discussed more extensively in Chapter 6.

It was also observed that occasionally LC was phase separated on top of the polymer film. This is most likely the result of the presence of low concentrations of oxygen in the sample chamber. Oxygen-inhibition of the polymerization in the top of the layer results in an inverse polymerization gradient and a consequent separation of LC material. This was corroborated by experiments where oxygen was deliberately leaked into the system, which resulted in an increased amount of phase separated LC material on top of the polymer layer.

2.3.5 Composition of the phase-separated LC material

Measurements of the nematic-isotropic transition temperature (T_{NI}) of the LC material in the capsules after the two-step photopolymerization process revealed that the T_{NI} has increased from 58°C (E7) to 68°C. This indicates that the composition of the phase separated LC deviates from the initial composition of E7. HPLC analysis of the phase separated LC confirmed that indeed the composition has drifted: the fractions of the 5CB and 7CB have decreased while the fractions of the larger molecules 8OCB and 5CT have increased (Table 2.3). As mentioned earlier, this has also been found in E7/NOA65 based PDLCs made via polymerization-induced phase separation.²⁷ The components 5CB and 7CB preferentially remain behind in the polymer, which indicates that (chemical and/or physical) interactions between these components with the formed polymer are less repelling than the interactions of the other two with the polymer. The calculated values of the respective Flory-Huggins interaction parameters (see Table 2.2) are too crude to explain this behavior. The altered composition of the LC phase will consequently affect the electro-optical properties of the LC blend such as the switching behavior, and the temperature window of operation. This will have to be taken into account in the optimization of the material system and device properties.

Table 2.3: Mole fractions of the 4 LC components in the liquid crystal blend before and after the two-step photo polymerization process

LC component	Mole fractions in E7	Mole fraction after phase separation
5CB	0.55	0.51
7CB	0.24	0.23
8OCB	0.14	0.16
5CT	0.07	0.10

2.3.6 Model system

In order to simplify the in-depth investigation of the photo-enforced stratification process, both the total number of compounds is decreased and the composition drift is eliminated by exchanging E7 for a single component LC material: K15 (5CB, the main component of E7, see Figure 2.1). Unfortunately, when the two-step photo-enforced stratification process was performed at 50°C (the same temperature that was used for the E7 experiments), no phase-separation was observed. However, when the process was carried out at 30°C, which is 5.5°C below T_{NI} of K15, a stratified morphology was formed. With this formulation, i.e. K15 instead of E7, stilbene-dimethacrylate did not precipitate from the mixture during polymerization at temperatures below 40°C. Figure 2.11 shows polarization microscope pictures of a

sample in the bright (a) and the dark (b) state. The alignment layer uniaxially aligns the LC in the circular LC domains. The light leakage in the dark state is the result of phase separated LC on top of the film, visible through the Schlieren structures near the polymer walls resulting from the multi-domain arrangement of the LC.

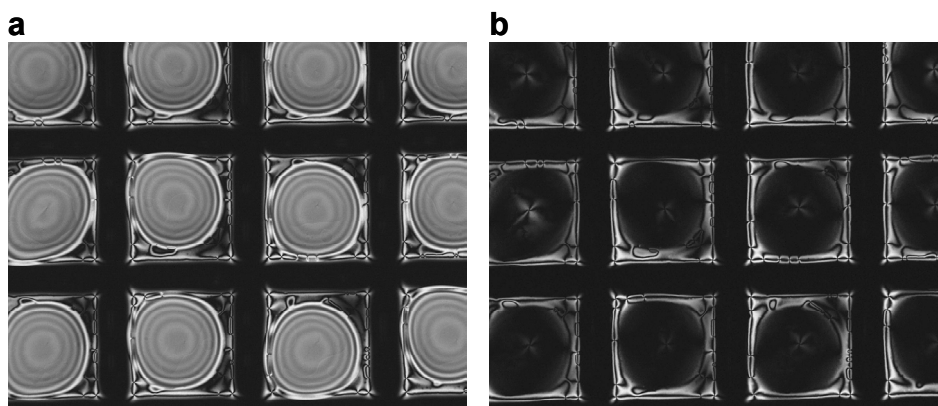


Figure 2.11: Results of the two-step photo-enforced stratification of a material system containing K15 as the LC component (mask exposure: 3 min., flood exposure: 60 min.). a) The bright state shows circular shaped LC domains. b) Light leakage in the dark state is caused by phase separated K15 on top of the polymer top film.

The fact that polymerization at 30°C does give phase separation and polymerization at 50°C not is an important indication that the nematic order of the LC material plays an essential role in the phase separation. Further, the start of the phase separation, i.e the formation of macroscopic nematic LC droplets, was observed after 40 minutes, much later than was observed for the reaction mixture based on E7. The starting time decreased to 15 minutes when the process temperature was further reduced to 22°C, which is expected for phase separation driven by nematic ordering: At a lower temperature the K15 can form a nematic phase in the presence of a larger amount of unreacted monomer. Consequently, the phase separation starts at lower conversions (and thus after shorter irradiation times). The experiments above show that with the materials system consisting of K15, IBoMA and stilbene-dimethacrylate structures can be formed comparable to the initial system containing E7. The reduction of the number of components as well as the elimination of composition drift makes this model system more suitable for further investigation of the photo-enforced stratification process, discussed in the following chapters.

2.3.7 Electro-optical behavior

The LC layers in the polymer capsules are switched with in-plane electrical fields (IPS).²⁸ Thereto, prior to the two-step photo-enforced stratification process, the glass substrate is provided with interdigitated ITO electrodes below the polyimide

alignment layer. Figure 2.12a and 2.12b respectively show a capsule in the off state and driven in the on state (15V). The transmission-voltage curve in Figure 2.12c shows that maximum transmission is obtained at 15V. The overall LC director is then at 45° with respect to the transmission axis of the polarizers. At higher voltages the director angle with respect to the polarizers decreases again and consequently the transmission of the electro-optical stack is reduced, typical for IPS.²⁹ The contrast between the on state and the off state is of the order of 1:20. Switching speeds below 50 ms are obtained: $\tau_{\text{on}} = 5$ ms and $\tau_{\text{off}} = 40$ ms (switched between 0 - 15V, time interval measured between 10 - 90% transmission). The response curves are illustrated in Figure 2.12d.

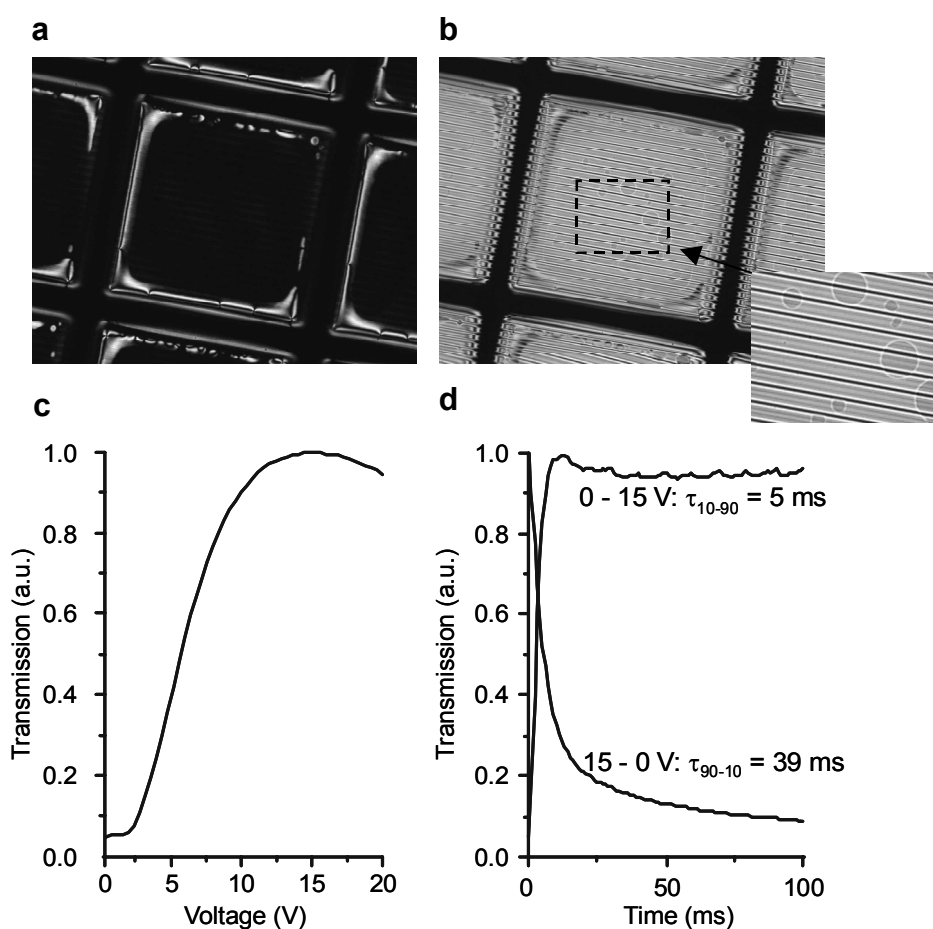


Figure 2.12: The LC is driven by in-plane switching. The interdigitated electrode structure has a pitch of $18 \mu\text{m}$ and a spacing of $9 \mu\text{m}$. a) Polarization microscope picture of a capsule in the off state. b) In the on state the LC is partially switched. Above the electrodes the capsule stays dark. The isotropic walls stay dark as well. c) Normalized transmission-voltage (T - V) curve (crossed polarizers, maximum transmission is 1). d) The off-on and on-off switching (T - t) curves.

In the current example the contrast ratio is mainly limited due to the light leakage at the edges of the capsules in the dark state, see Figure 2.12a. This is caused by undesired phase separation of LC on top of the polymer capsules, concentrated near the polymer walls. The close-up of the capsule in Figure 2.12b clearly shows zero transmission above the center of the electrodes. Maximum transmission of the electro-optical stack takes place near the edges of the electrodes and even in a small region above. This is in line with observations of peak intensities near the electrodes for LCs with positive Δn in standard in-plane switching configurations.³⁰ Variations in the transmittance over the electrode gap are the result of a convex shape of the electrical field: In the center the electrical field lines are in-plane but near the electrode edges they bend towards the electrodes. As a consequence the director varies over the electrode gap yielding a varying optical pathway.

Figure 2.13a shows a photograph of a display produced by the two-step photo-enforced stratification process placed between crossed polarizers.³¹ The device is operated in the so-called transmissive mode (also denoted in literature as normally black, i.e. dark pixels at zero driving voltages). The stack transmits light from the backlight at the location where the LC is addressed by an electrical field. The close-up in Figure 2.13b demonstrates that the shape of the electrodes rather than the shape of the capsules determine the features. The LC in the capsules at the edge of the activated area is partly switched. Hence, the use of a grid pattern of polymer walls does not limit the resolution of the display but lowers the transmission to some extent.

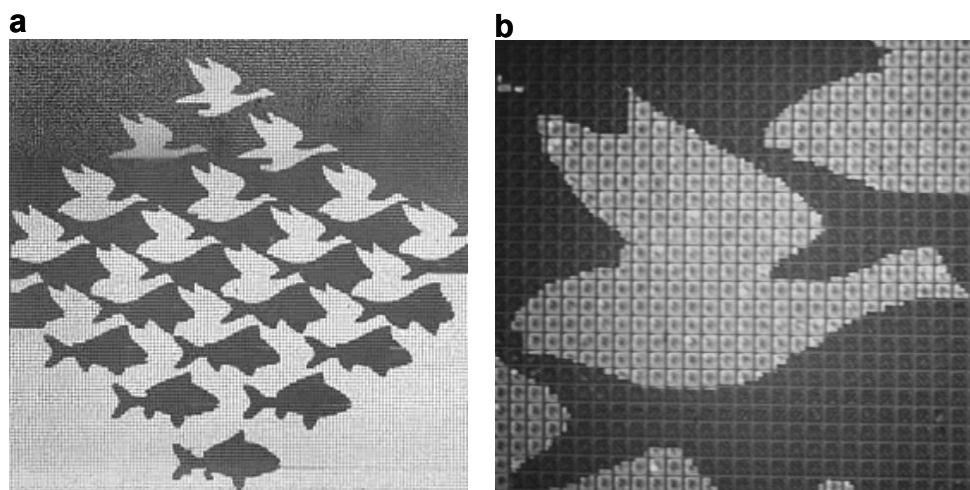


Figure 2.13: A photograph of an LCD produced by the photo-enforced stratification-process (a) and a close-up (b). The device is operated in transmissive mode (normally black) by using a backlight and two crossed polarizers. The stack transmits light from the backlight at the position where the LC is activated by direct addressing.

2.4 Conclusions

This chapter demonstrates the photo-enforced stratification principle, which enables the production of single-substrate LCDs. Due to random growth of LC droplets at the alignment interface a single-UV exposure yields irregular structures, optically insufficient for application in electro-optical devices. Regular structures are obtained when a mask exposure step is performed prior to the stratification process. In this way arrays of LC-filled polymer capsules with a uniform optical appearance were made.

Optical and surface profile measurements give a good insight of the dimensions of the LC-filled polymer capsules and their optical characteristics. Polarization microscopy revealed the presence of small LC droplets dispersed in the polymer. This will be addressed further in Chapter 3, where the structures will be investigated with confocal Raman microscopy, and in Chapter 6, where single-step photo-enforced stratification will be compared to results of the PES model, which will be presented in Chapter 4. For further investigation of the photo-enforced stratification process the use of a single component LC (K15) is preferred, since then composition drift of the LC is eliminated. The large temperature dependence of the process, i.e. no phase separation was observed above T_{NI} of the LC, indicates that for the current material system nematic ordering is an important driving force for phase separation.

2.5 References and notes

1. Drzaic, P.S. *Liquid Crystal Dispersions*, World Scientific, Singapore (1995).
2. Bunning, T.J., Natarajan, L.V., Tondiglia, V., Sutherland, R.L., Vezie, D.L., and Adams, W.W. *Polymer* **26**, 2699-2708 (1995).
3. Ferguson, J. L. *Soc. Information Display Digest Tech. Papers* **16**, 68 (1985).
4. Drzaic, P.S. *J. Appl. Phys.* **60**, 2142-2148 (1986).
5. Doane, J.W., Vaz, N.S., Wu, B.G., and Zumer, S. *Appl. Phys. Lett.* **48**, 269-271 (1986).
6. Vaz, N.A., Smith, G.W., and Montgomery Jr., G.P. *Mol. Cryst. Liq. Cryst.* **146**, 1-15 (1987).
7. Hirai, Y., Niama, S., Kumain, H., and Gunjima, T. *Proc. SPIE Int. Soc. Opt. Eng.* **1257**, 2-8 (1990).
8. Sutherland R. L., Tondiglia V. P., Natarajan L. V., Bunning T. J., and Adams W.W. *Appl. Phys. Lett.* **64**, 1074 (1994).

9. Hikmet, R.A.M. *J. Mater. Chem.* **9**, 1921-1932 (1999).
10. Morozumi, S. in: *Liquid Crystals: Application and Uses* (Ed. Bahadur, B.), World Scientific, London, 181 (1990).
11. Broer, D.J., Lub, J., and Mol, G.N. *Nature* **378**, 467-469 (1995).
12. Vorflusev, V., and Kumar, S. *Science* **283**, 1903-1905 (1999).
13. Qian, T., Kim, J.-H., Kumar, S., and Taylor, P. L. *Phys. Rev. E* **61**, 4007-4010 (2000).
14. Odian, G. *Principles of Polymerization*, John Wiley & Sons, London (1981).
15. Broer, D. J., Penterman, R. *US patent application*, US6818152 B2 (2002).
16. Flory, P.J. *Principles of Polymer Chemistry*, Cornell University Press, Ithaca, New York (1953).
17. Maier, V.W., and Saupe, A. *Z. Naturforschg.* **14a**, 882-889 (1959).
18. Maier, V.W., and Saupe, A. *Z. Naturforschg.* **15a**, 287-292 (1960).
19. Shen, C., and Kyu, T. *J. Chem. Phys.* **102**, 556-562 (1995).
20. Dušek, K. *J. of Pol. Sci.* **C16**, 1289-1299 (1967).
21. Serbutoviez, C., Kloosterboer, J.G., Boots, H.M.J., and Touwslager, F.J. *Macromol.* **29**, 7690-7698 (1996).
22. Brandrup, J., Immergut, E., and Grulke, E. *Polymer Handbook*, John Wiley & Sons, London (1999).
23. Smith, G.W. *Mol. Cryst. Liq. Cryst.* **225**, 113-130 (1993).
24. The solubility parameters are calculated via Hoy's system: Krevelen, D.W. van *Properties of Polymers*, Elsevier, Amsterdam, Chapter 7, Table 7.10 (1990).
25. Composition drift as a result of difference in reactivity between IBoMA and stilbene-dimethacrylate is neglected.
26. The emission spectrum of the UV source is divided in small sections of 1 nm. In each section the average intensity emitted by the UV source is multiplied with the average absorption of the photoinitiator. The result is called the wavelength dependent effective intensity (of the UV source/photoinitiator combination). Then in each section the effective intensity gradient is calculated with Beer's law by taking the absorption of E7 and stilbene-dimethacrylate into account. The overall effective intensity gradient is obtained by adding up the effective intensity gradients of all sections. In the calculations of the effective intensity gradient, equal quantum efficiency for initiation of the polymerization by Irgacure 651 for this wavelength region is assumed.

27. Nolan, P., Tillin, M. and Coates, D. *Mol. Cryst. Liq. Cryst. Lett.* **8**, 129-135 (1992).
28. Kiefer, R., Weber, B., Windscheid, F., and Baur, G. *Proc. 12th IDRC, Japan Display 1992*, 547-550 (1992).
29. Oh-e, M. and Kondo, K. *Appl. Phys. Lett.* **67**, 3895-3897 (1995).
30. Oh-e, M., Yoneya, M. and Kondo, K. *J. Appl. Phys.* **82**, 528-535 (1997).
31. In-plane switching electrodes were structured, inspired by the Dutch artist M.C. Escher, woodcut 'Sky and water' (1938).

Chapter 3

Confocal Raman microscopy of liquid crystal filled polymer capsules made by photo-enforced stratification*

3.1 Introduction

The two-step photo-enforced stratification enables the fabrication of regular arrays of liquid crystal-filled capsules of micrometer dimensions from a thin liquid crystal/monomer film.¹ The liquid crystal (LC) material in the capsules is switched by in-plane electrical fields. Therefore these arrays of capsules can be applied as the electro-active layer in a liquid crystal display (LCD) device as was demonstrated in the previous chapter. In Chapter 2, the morphological features of the arrays of capsules were studied by optical (polarization) microscopy and interference microscopy. In this chapter the capsules will be investigated in more detail, for example the chemical composition of the polymer phase and the morphology of the polymer-LC interface. Depth profiling of the LC-filled polymer capsules with micrometer resolution would provide valuable information, but is only possible by using a non-contact technique. Most analytical techniques cannot be applied without seriously affecting the morphology of the system. For example, polymer-dispersed liquid crystal (PDLC),^{2,3,4} holographic polymer dispersed liquid crystal (H-PDLC)^{5,6} and polymer network stabilized LC^{7,8} morphologies have been studied by scanning electron microscopy (SEM). Since the preparation of the samples for this analysis requires the removal of the LC material from the sample, this is not likely to be a characterization of the actual morphology.

For a detailed investigation of the capsules confocal Raman microscopy was selected since it enables a non-destructive analysis. With regard to the spatial resolution, the capabilities of Raman microscopy fit much better with the dimensions

* Part of this chapter has been published in: Mank, A.J.G., Vorstenbosch, I., Penterman, R., Vogels, J.P.A., Klink, S.I., and Broer, D.J. *Appl. Spectrosc.* **59**, 965-975 (2005).

and characteristics of the polymer capsules (with typical dimensions of the capsules being 500 x 500 x 20 μm) than other non-invasive molecular analysis techniques such as IR spectroscopy. In addition, confocal Raman microscopy enables the real-time characterization of the temperature dependence of the morphology and phase compositions of the LC-filled polymer capsules. The limited sensitivity of the technique has always been the biggest challenge of Raman microscopy. However, data pre-processing in combination with a classical-least-squares approach (CLS)⁹ has overcome this problem. In addition, the use of such methods instead of simple band integration makes it possible to reduce analysis times enabling real-time studies of the response of the polymer morphologies to changes in external conditions.

In this chapter the information that is deduced from Raman spectra of the array of LC-filled polymer capsules is discussed. Firstly, since the monomer blend used in the photo-enforced stratification process consists of two monomers, Raman spectroscopy also offers the possibility of studying the *spatial homogeneity* of the copolymer with respect to the two monomer repeat units. Secondly, the composition of the phases can be determined, i.e. the presence of LC material in the polymer phase, and the presence of polymer and/or monomer fractions in the LC phase can be detected. Thirdly, the degree of polymerization i.e. the *monomer double bond conversion* can be established. Fourthly, besides to their difference in chemical composition, the polymer layer can be distinguished from the LC phase because of the difference in *the molecular order* in both phases: the polymer phase is isotropic, whereas the LC phase is anisotropic. Finally, monitoring the temperature dependence of the morphology gives a further insight in the phase separation process.

3.2 Experimental section

3.2.1 Preparation of arrays of LC-filled polymer capsules

For ease of characterization of the structures, the single component LC material K15 has been selected as the LC material instead of the four component LC material E7 that was used for the standard device manufacturing. Therefore, the LC/monomers mixture consists of 50 wt.% of K15, 44.5 wt.% of isobornylmethacrylate (IBoMA), 5 wt.% of 4,4'-di-(6-methacryloyloxyhexyloxy)-3-methylbiphenyl (*stilbene-dimethacrylate*) and 0.5 wt.% of Irgacure 651 (see Figure 3.1). Detailed information on the processing steps can be found in Chapter 2 (Paragraph 2.2.2 to 2.2.4).

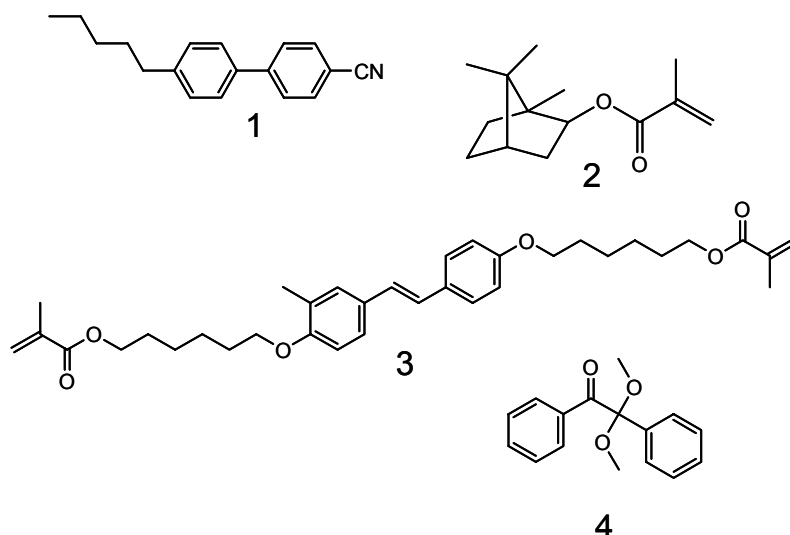


Figure 3.1: Chemical structures of the compounds in the LC/monomer mixture: 1) the liquid crystal material K15 (50 wt.%), 2) isobornylmethacrylate (IBoMA, 44.5 wt.%), 3) stilbene-dimethacrylate (5 wt.%), 4) the photoinitiator Irgacure 651 (0.5 wt.%).

3.2.2 Confocal Raman microscope set up

Equipment

A dedicated confocal LabRam Raman microscope (Jobin Yvon, Lille, France) has been configured for laser excitation at 633 nm. For the quantitative analysis of the capsules the spectrometer has been equipped with an 1800 lines/mm grating, unless mentioned otherwise. For a fast overview analysis (400-3300 cm^{-1}) of the samples a 600 lines/mm grating was selected. In order to cover the entire 800-3300 cm^{-1} spectral region, two spectral regions have been measured with a small overlap (800-2300 cm^{-1} and 2000-3300 cm^{-1}). Since the two overlapping regions contain the strong nitrile $\text{C}\equiv\text{N}$ stretching band around 2220 cm^{-1} when LC material is present, alignment of spectra during pre-processing is straightforward. The spectra were not stitched before analysis. Signal collection has been performed using a Spectrum One CCD detector (1024 pixels, N_2 cooled). The confocal hole in the system was set at 300 μm as a standard. With this diameter of the confocal hole the resolution (approximately 2 μm at the surface of the layer) is as good as with smaller diameters, while the signal intensity is still 60% of what would be available without a confocal hole. Unless stated otherwise, a quarter-wavelength plate is present in the excitation beam and a scrambler is placed in the Raman beam to avoid spectral variations due to orientation effects of the material. Depth profiling was performed using a closed-loop piezo-driven Z-stage (Physik Instrumente, Karlsruhe, Germany) with a maximum range of 100 μm and a step-resolution of 0.1 μm .

Selection of objective.

In the literature it has been shown that with *metallurgic objectives* only limited depth resolution is available.^{10,11,12,13} The depth resolution of high numerical aperture (NA) metallurgic objectives was compared to *oil immersion objectives* for depth profiling.^{14,15} In the case of metallurgic objectives, Everall has studied the effect of refraction on the depth resolution and showed that the depth resolution (DR) deteriorates linearly with depth (Δ) according to the following equation:¹⁴

$$DR = \Delta \sqrt{\left(\frac{NA^2(n^2 - 1)}{1 - NA^2} + n^2 \right)} - n \quad (3.1)$$

where n is the refractive index of the material and NA the numerical aperture of the objective (see also Figure 3.2a). On the other hand, the theoretical DR for oil immersion objectives (see Figure 3.2b) is independent of depth and proportional to NA^2 following the equation:

$$DR = \frac{n\lambda}{4NA^2} \quad (3.2)$$

where n is the refractive index of the material, NA the numerical aperture of the objective and λ the wavelength of the excitation source. Theoretical studies show that for metallurgic objectives it is possible to predict and partly circumvent the loss in resolution inherent to the refractive index changes that occur in the medium between the objective and the sample.¹⁴ However, when compared to the depth resolution of oil immersion objectives the resolution of the latter will always be better.

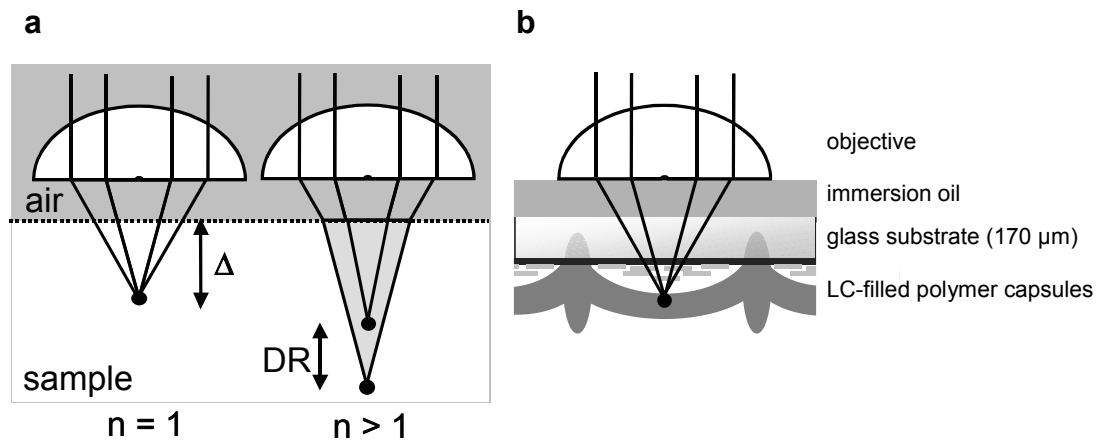


Figure 3.2: a) Visualization of loss of depth resolution in a sample with $n > 1$ using a metallurgic objective in air. b) Measurement configuration for depth profiling through the substrate of LC-filled polymer capsules using immersion oil avoiding the air gap between lens and substrate.

To determine whether the superior depth resolution of an oil-immersion objective is required for the current application, a layered test sample was examined with various metallurgic and oil-immersion objectives (see Table 3.1). The sample consisted of 25 μm low-density polyethylene (LDPE), 10 μm polyamide and 25 μm of LDPE. The thickness of these layers and those found in the capsules are of the same order, making this a representative test sample.

Table 3.1: Specifications of the metallurgic and oil immersion objectives that have been used to measure the test sample stack (a 10 μm polyamide layer sandwiched between two 25 μm of LDPE layers).

Objective type	magnification	WD*	NA**	Brand
Metallurgic	50x	long	0.50	Olympus
Metallurgic	100x	long	0.80	Olympus
Oil immersion	100x	standard	1.25	Olympus
Oil immersion***	100x	long 360 μm	1.30	Zeiss

* working distance; ** numerical aperture; *** this objective has been selected to study the polymer capsules

A classical-least-squares approach (see also Paragraph 3.3.3) was used to separate the signals from glass, oil, LDPE and polyamide. The first two metallurgic objectives gave a resolution that was at least a factor of two worse than the results that have been obtained with the oil immersion objectives and in fact no pure spectrum of the polyamide layer could be obtained. It could therefore be concluded that the metallurgic objectives are unsuitable for the study of the polymer capsules. A depth profile of the test sample taken with an oil-emersion objective is shown in Figure 3.3. All layers can be distinguished and the interfaces between the layers can be localized accurately (within 2 μm). The loss of resolution over the sample depth is very limited. The signal drop as a function of depth is due to scattering of the laser light by the sample.

The confocal Raman analysis of the array of LC-filled polymer capsules is complicated by the fact that liquid immersion objectives cannot be applied on top of the structures as both water and various types of immersion oil were found to penetrate into the polymer capsules. To avoid disturbing the sample properties, the measurements were performed from the back of the sample i.e. from the glass substrate side. Thin glass substrates of 170 μm were used to be able to position the polymer capsules within the working distance of the microscope (see Figure 3.2b). The 100x oil immersion objective from Zeiss (Oberkochen, Germany) is used for the

remainder of this study. This long working distance objective was found to give exactly the same concentration profiles for the multi-layer test material as the standard Olympus oil immersion objective, even when the multi-layer was measured through a 170 μm thick glass substrate.

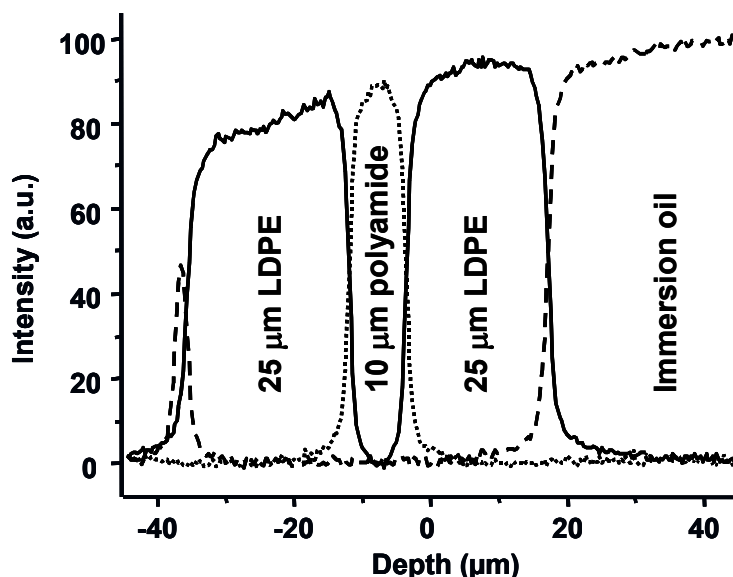


Figure 3.3: Depth profile of a multi-layer sample obtained using 633nm excitation with 100x oil immersion objective ($NA = 1.30$). Data was collected with 0.2- μm steps in depth. The small peak between a relative depth of -30 and -40 originates from a thin layer of immersion oil, present on the side of the sample far from the objective.

Temperature scan

A thermal hot stage was utilized to study the temperature dependence the samples. To prevent direct contact of the capsules with the hot stage a 1 mm thick copper spacer was placed in between. The metal spacer served also as a conductor of the heat generated by the hot stage. The temperature of the sample at the measurement position was checked with the aid of a thermo-couple on the back of the substrate.

3.3 Results and discussion

3.3.1 Identification of the component specific signals

Raman spectra were collected for the LC/monomer mixture as well as for the individual compounds K15, IBoMA and stilbene-dimethacrylate. The reference spectra of the compounds are shown in Figure 3.4. Due to its low concentration, the signal contribution of the photoinitiator in the mixture is negligible. No spectral

changes were found to result from interactions between the compounds in the mixture. In Table 3.2 the bands that are most specific for each of the individual components are given. Overlap between bands of different components is always present except for the K15 signal at 2220 cm^{-1} ($\text{C}\equiv\text{N}$ stretch).

Table 3.2: Spectral bands characteristic for the individual components.

Compound	wt. %	Band position (cm^{-1})
K15	50	1591 - 1621*
		1257 - 1315
		2216 - 2243
IBoMA	44.5	2942 - 2999*
		1423 - 1512
		1696 - 1742
Stilbene-dimethacrylate	5	1621 - 1647*

* Preferred band for quantification independent of conversion.

In order to study the influence of polymerization on the reference spectra, thin films of IBoMA, stilbene-dimethacrylate and IBoMA/stilbene-dimethacrylate (molar ratio 23:1) were photopolymerized. The films contained 1 wt.% Irgacure 651 and were irradiated with UV light ($\lambda = 340\text{-}420\text{ nm}$, $\lambda_{\text{max}} = 367\text{ nm}$, $I = 1\text{ mW}\cdot\text{cm}^{-2}$) for 30 minutes. The intensity of the component specific Raman signals of IBoMA and stilbene-dimethacrylate were found to stay constant within 5%, independent of the polymerization. Moreover, at the positions of the component specific signals, the spectrum of the polymerized IBoMA/stilbene-dimethacrylate was found to be a linear combination of the spectra of the polymerized IBoMA and the polymerized stilbene-dimethacrylate samples. This demonstrates that there are no interaction-related fitting problems. To determine the composition of the structures the aromatic C-C signal of K15 (1600 cm^{-1}), the C-H signals of IBoMA (2950 cm^{-1}) and the C=C signal of the central core in stilbene-dimethacrylate (1630 cm^{-1}) are used (all marked in Table 3.2).

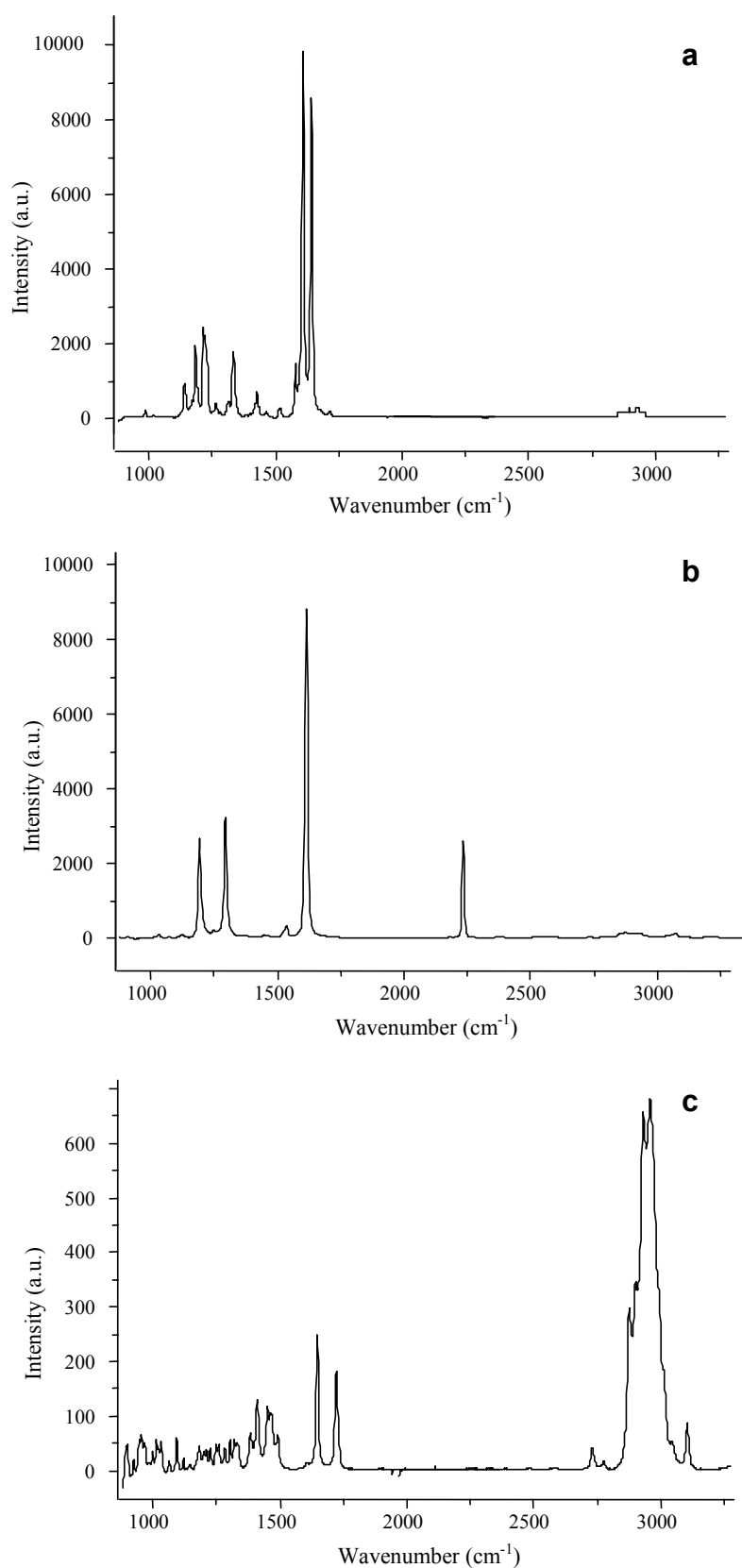


Figure 3.4: Raman spectra of the various starting compounds: a) LC material K15, b) isobornylmethacrylate, c) stilbene-dimethacrylate.

3.3.2 Method to establish an estimate of the monomer conversion

A direct measurement of the double bond conversion by monitoring the decay of the Raman signal, specific for conjugated C=C signal in the methacrylate group would be preferred. Unfortunately, direct measurement is impossible due to spectral overlap with the intense aromatic C-C signals of K15. However, a rough estimate of the conversion is obtained by measuring the intensity decrease of the 1718 cm^{-1} Raman band, specific for the conjugated C=O functionality. From a series of experiments in which samples of pure IBoMA have been exposed to different doses of UV light, the intensity decrease of this Raman band was observed to be close to linear with the Raman signal, specific for conjugated C=C signal in the methacrylate group. The ratio of this Raman band versus a reference Raman band at 2950 cm^{-1} for IBoMA and the 1630 cm^{-1} band for stilbene-dimethacrylate has therefore been used to estimate the monomer conversion. CLS fitting is required (see Paragraph 3.3.3) to remove the K15 signal before the double bond conversion of the individual monomers can be determined as significant spectral overlap is present.

3.3.3 Data pre-processing

The K15 signals are dominating the Raman spectra at almost all positions of the capsule. It is therefore necessary to accurately subtract the K15 signals from the spectra and a reliable method to achieve this is via the Classical Least Squares approach (CLS).¹⁶ A simple procedure has been followed for all spectral analyses. A newly developed pre-processing routine in MatLab (MathWorks, Massachusetts, USA) has been used to remove spikes and the background signal.⁹ Subsequently, CLS is used to remove the K15 spectrum (Figure 3.5). After the removal of the K15 signal from the Raman spectrum of the total mixture, the IBoMA and stilbene-dimethacrylate concentration profiles are determined by simple band integration (at 2950 cm^{-1} for IBoMA and at 1630 cm^{-1} for stilbene-dimethacrylate, respectively). IBoMA and stilbene-dimethacrylate contribute both to the Raman signal at 2950 cm^{-1} , representing C-H vibrations. But since IBoMA and stilbene-dimethacrylate are present in a 23:1 ratio, the stilbene-dimethacrylate contribution is marginal and therefore the band at 2950 cm^{-1} can be used to monitor the IBoMA concentration.

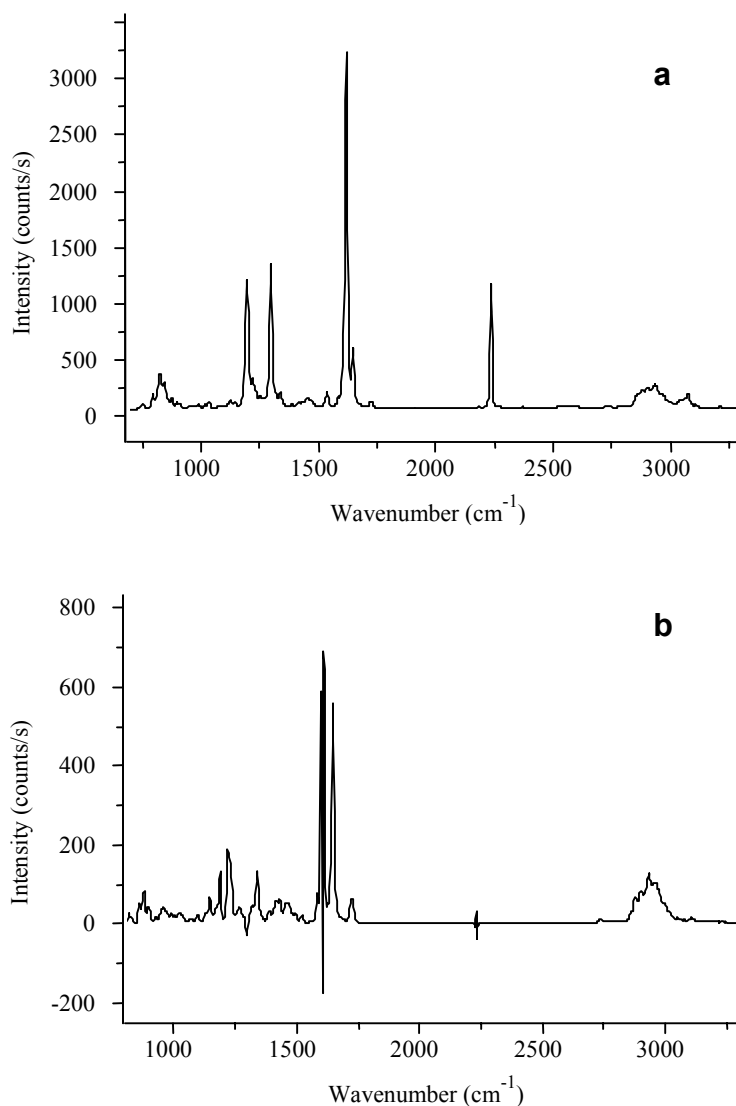


Figure 3.5: a) Typical Raman spectrum of a capsule-wall before CLS removal of the K15 spectrum. b) The spectrum after the CLS removal. The bands most suitable for quantifying the total amount of stilbene-dimethacrylate and IBoMA after this correction are located at 1630 cm^{-1} and 2950 cm^{-1} , respectively.

3.3.4 Characterization of the capsule precursors

In Chapter 2 it was shown by interferometric microscopy that after the mask exposure step the resulting polymer walls in the capsule precursors have become significantly higher than the rest of the film. Moreover, undesired gelation of the LC/monomer mixture (i.e. polymerization) was observed in the regions between the polymer walls that were shielded by the mask. These observations were studied in further detail with the aid of confocal Raman microscopy. To determine the distribution of the various components in the film after the mask exposure, spatially resolved Raman spectra have been measured following a vertical cross section through the center of a capsule precursor, i.e. on an equidistant line between two neighboring polymer walls. In the X-direction of the plane 5- μm steps were used,

while in the Z-direction of the plane 1- μm steps were used during the measurement. With an integration time of 120 seconds per point, the distribution of the K15 and IBoMA can be determined with sufficient accuracy and the corresponding CLS-based concentration profiles are shown in Figure 3.6. For the concentration profiles of IBoMA no distinction was made between unreacted monomers and the monomer units already chemically bonded to the polymer matrix.

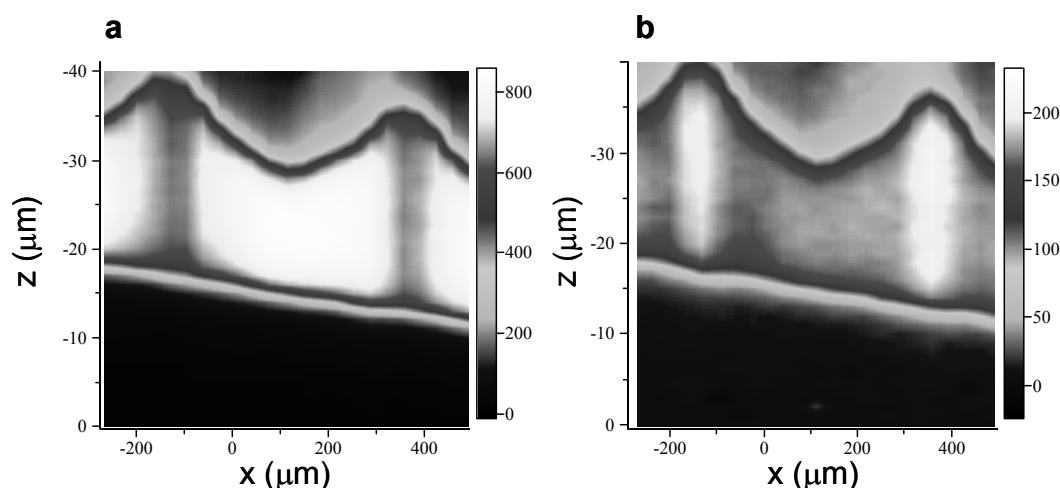


Figure 3.6: X-Z Raman signal intensity profiles for a single capsule precursor after the mask exposure step in the two-step photo-enforced stratification step of (a) K15 and (b) IBoMA. The X-Z graphs are slightly slanted due to a small tilt of the sample with respect to the microscope objective. The gray scale level is a measure for the concentration. The black areas at the bottom of the graphs represent the glass substrate. The surface undulations are the result of the patterned irradiation. The film is elevated at the positions of the polymer walls. (For colored images of similar structures, see Ref. 17)

The X-Z concentration profiles of IBoMA and K15 in the capsule precursor are in agreement with the surface profile measurements described in Chapter 3: the polymer walls have become approximately 10 μm higher than the regions between the walls. The X-Z concentration profiles further show that the polymer walls contain a significantly higher concentration of IBoMA, while the concentration of K15 is significantly lower than in the rest of the film. In contrast, the stilbene-dimethacrylate concentration profile (not shown) displayed a homogeneous distribution of this monomer over the capsule precursor structure. For future modeling of the system, it is important to note that in the areas between the polymer walls the composition LC/monomer mixture has changed due to lateral photo-diffusion and polymerization, in particular with respect to the IBoMA and K15 content.

Images of the polymer conversion as a function of the position are difficult to obtain, as they require even longer integration times to obtain sufficient signal-to-noise levels. However, by integration over the entire depth of the layer an indication of the conversion can be obtained using the method described in Paragraph 3.3.2. The

methacrylate conversion of IBoMA and stilbene-dimethacrylate in the polymer walls is roughly 80 %. The relevant Raman signals of IBoMA and stilbene-dimethacrylate in the areas between the walls indicate that only a limited amount of monomers (<10%) has been converted into polymer, but precise quantification is not possible due to the nature of the method and insufficient signal-to-noise ratios.

3.3.5 Characterization of the LC-filled polymer capsules

In the two-step photo-enforced stratification process, the mask exposure step is followed by a flood exposure using UV light of wavelengths at which the stilbene chromophore exhibits a high extinction. During this flood exposure the actual stratification takes place: the formation of LC-filled polymer capsules from the capsule precursors. The composition of the LC-filled polymer capsules was determined by measuring XZ-intensity profiles through the center. The spectra have been collected at 20 μm intervals in the X-direction and 1 μm intervals in the Z-direction using an integration time of 60 s per point. Figure 3.7 shows the resulting concentration profiles for K15, IBoMA and stilbene-dimethacrylate. K15 is present in both the LC- and the polymer phase (Figure 3.7a). The major part of the LC phase is present as a large drop with a maximum thickness of about 10 μm and located at the bottom of the structure. A small amount is present on top of the capsules in the ridge between the wall and the convex-shaped top of the capsule. The presence of LC material in the polymer phase is not unexpected. After the start of the polymerization-induced phase separation, the LC concentration in the polymer phase is lowered until it reaches the solubility limit of the LC material in the polymer network i.e. the LC concentration that the polymer network can contain without exhibiting phase separation. The solubility limit depends on the properties of the polymer network and the LC phase as well as the conditions (e.g. the temperature). Figures 3.7b-c indicate that both IBoMA and stilbene-dimethacrylate are only present in the polymer phase. No signal of either IBoMA or stilbene-dimethacrylate was found in the LC phase. The lateral concentration gradients observed for IBoMA and stilbene-dimethacrylate are attributed to the scattering of the Raman excitation light by the nematic LC phase. Scattering results in a decrease of the Raman signals of the components in the topcoat above the K15 phase. However, it will be shown in Paragraph 3.3.7 that a clearer picture of the composition of the polymer is obtained, when the sample is measured at temperatures well above the nematic-isotropic temperature of the K15.

Spectra of the final capsules have been taken at a large number of positions. The shape and relative intensities of respectively the IBoMA signal and the stilbene-dimethacrylate signal were found to be constant throughout the polymer. From this

data was concluded that the double bond conversion is roughly 80 %, independent of the position in the polymer.

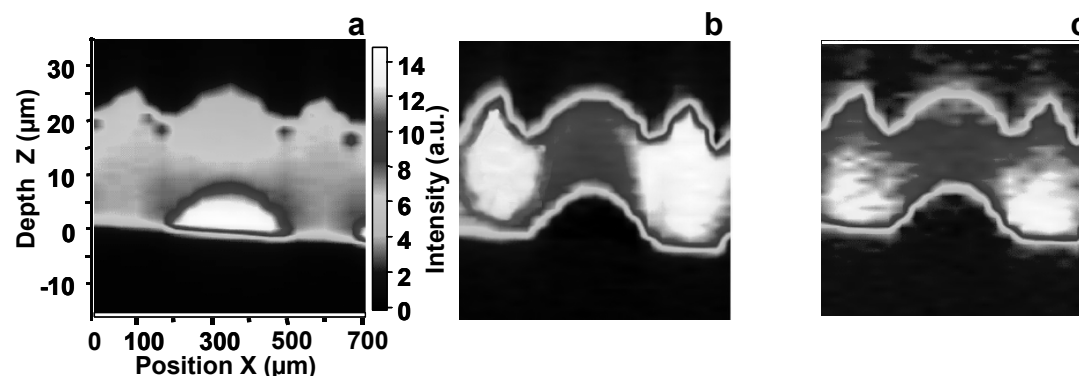


Figure 3.7: X-Z Raman intensity profiles of a single capsule of (a) K15 (b) IBoMA and (c) stilbene-dimethacrylate. The gray scale level is a measure for the concentration, with black representing a zero concentration. The high intensity area (color: white) in the K15 profile (a) represents the LC droplet in the center of the capsule between the polymer walls. The IBoMA (b) and stilbene-dimethacrylate profiles (c) show the shape of the polymer phase covering the LC droplet in the center of the capsule. (see Ref. 17 for colored versions of the X-Z profiles).

3.3.6 Raman spectra of anisotropic media

The orientation of molecules with respect to the polarization direction of the excitation light influences their relative Raman signal intensities. Especially when the molecules are uniaxially aligned, spectral and intensity variations occur for particular Raman bands as a function of the angle between the respective vibrational moments within the molecules and the polarization direction of the laser light. This effect allows the study of the molecular order of the material by comparing the spectra obtained with *linear* and *circular* polarized excitation light. Reference measurements on a thin film of uniaxially aligned K15 confirmed that specific signal intensities (e.g. the $-C\equiv N$ vibration at 2220 cm^{-1}) can differ as much as a factor of five in intensity upon changing the polarization direction of the laser with respect to the director of the LC material from parallel to perpendicular. When these measurements were repeated with circularly polarized light, the spectra were identical. With a circularly polarized excitation source, the intensities of the Raman bands of a molecule are independent of its orientation in the plane of the film. While traveling through the birefringent medium circularly polarized light subsequently becomes converted into elliptically, linearly, elliptically and again into circularly polarized light. As a result of this repeated chain of events, the electrical field vector by definition becomes oriented at an angle of 45° with the average in-plane orientation of the molecules and thus with the average direction of for example the CN dipole, which makes the signal independent of the in-plane orientation of the molecules.

Figure 3.8a shows the intensity profiles of the K15 signal measured in the Z-direction in the center of the capsule at 20°C with respectively linearly polarized light, parallel to the rubbing direction of the alignment layer, and circularly polarized excitation light. The intensity profile in the case of linearly polarized light is significantly higher in the LC region (between a relative depth of 17 and 8 μm) than in the case of circularly polarized light, indicating a uniaxially aligned nematic LC phase. When the linearly polarized light was oriented perpendicular to the rubbing direction, the intensity profile was significantly lower (not shown). The profiles are similar in the polymer region (from 33 to 17 μm), demonstrating that the polymer contains molecularly dissolved LC material and that the molecular orientation of the dissolved LC is random. The nematic to isotropic transition temperature (T_{NI}) of K15 is 35°C. When the sample was heated above this temperature, the measured concentration profiles are perfectly identical, which indicates that the LC material was no longer in its nematic state (Figure 3.8b). However, the profiles also show that the morphology of the structure had changed: the pure LC layer at the bottom of the film has become thinner while a higher concentration of LC is observed at the top (from 33 to 28 μm). The increase of the signal at the top is the result of redistribution of pure LC initially present near the polymer walls. Upon increasing temperature the initially convex polymer topcoat becomes flatter enabling the LC to spread over the surface. The temperature effects and the (ir)reversibility of thermal treatment will be discussed in more detail in the next paragraph.

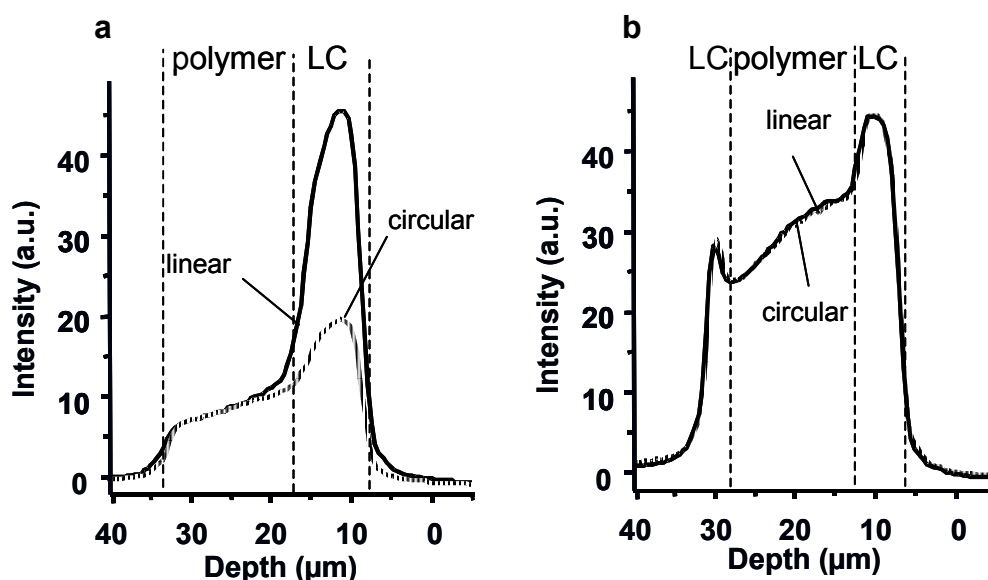


Figure 3.8: a) Effect of the polarization (linear, circular) of the incident laser beam on the K15 Raman signal at the center of a capsule at 20°C. b) K15 Raman signal measured under the same circumstances at 40°C.

3.3.7 Morphologies as a function of the temperature

High resolution depth profiles measured at 25°C in the center and in a wall of the capsule clearly show the composition: a pure K15 phase which is in an uniaxially aligned nematic state, while the polymer phase contains molecularly dissolved LC material which is isotropic (Figure 3.9a). For these measurements, data were collected at a relatively long integration time of 300 s per point, over a range of 40 μm using 0.5 μm depth intervals, using circular polarized excitation light.

The Raman intensity profiles clearly confirm the expected structure of the capsules. The LC depth profile in the center of the capsule exhibits a large increase of the signal at about 2/3rd of the layer thickness measured from the top, indicating the interface between polymer- and LC phase. The LC concentration in the polymer phase shows a slight increase in the direction towards the interface. Close to the polymer surface IBoMA seems to be present at a somewhat higher level than the stilbene-dimethacrylate, both in the center and in the walls. No corrections have been made for the limited scattering of the laser light by the nematic K15 phase. It should be noted that this effect does not influence the ratio of the signals from the various components.

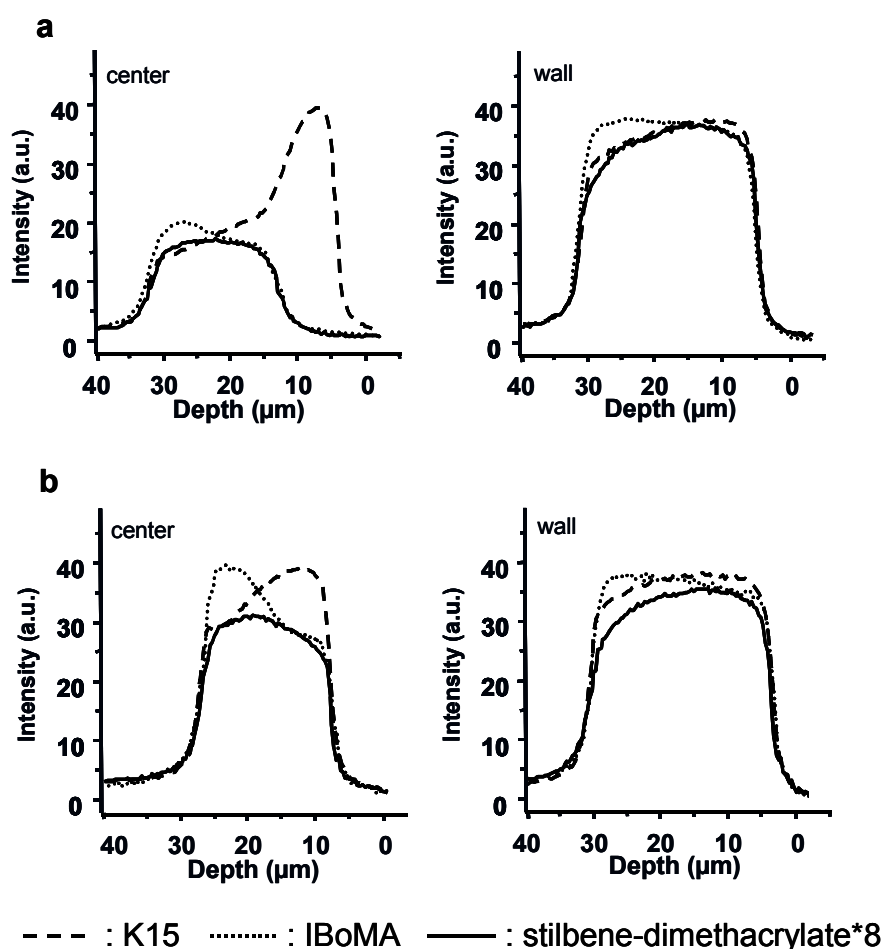


Figure 3.9: High resolution depth profiles for the various components in the center of a capsule and in a capsule wall at two temperatures: a) $T = 25^\circ\text{C}$, b) $T = 45^\circ\text{C}$.

Figure 3.9b depicts the intensity profiles of the three components at the center and wall position of the same capsule recorded at 45°C. The K15 distribution in the walls has remained the same, while the distribution in the center of the capsule changed completely: No pure LC phase can be distinguished anymore and the polymer phase is present across whole layer thickness. The ratio of the IBoMA and stilbene-dimethacrylate signals in the polymer is independent of the temperature, both in the center and in the wall of the capsule. To investigate the temperature dependence further, XZ-intensity profiles were measured through the center of a capsule at 25°C, 35°C and 45°C. The corresponding results are presented in Figure 3.10. Data are collected at 20- μm intervals in the X-direction and every 1 μm in depth, using an integration time of 60 s per point. The data demonstrate that upon raising the temperature, the LC droplet in the capsule gradually disappears as the polymer becomes more and more swollen with K15 (Figures 3.10a-d-g). At 45°C, which is above its nematic to isotropic transition (T_{NI}), the K15 is completely dissolved in the polymer and the morphology of the capsules changes completely. Apparently, the nematic nature of the K15 stabilizes the formed structures. As was mentioned in Chapter 2, nematic ordering of the liquid phase upon phase separation is one of the driving forces for phase separation. It was shown that upon conducting the polymerization process above T_{NI} no stratification was obtained (Chapter 2, Paragraph 2.3.6) The current experiments show that after stratification nematic ordering of the LC phase still plays an important role with respect to the temperature dependence of the morphologies. Changes in the chemical and physical interactions between LC and polymer might also add to the temperature dependence (see Chapter 2, Paragraph 2.3.1). But since the temperature intervals are small these are assumed to have a minor contribution.

The intensity profile of K15 at 45°C still indicates a higher concentration of LC near the bottom than in the rest of the polymer (Figure 3.10g). An explanation for the higher LC concentration is the local existence of small, micrometer-sized, LC droplets in the polymer (PDLC morphology), which was already postulated earlier in Chapter 2 (Paragraph 2.3.4) based on polarization microscope observations. The free energy of the system is lowered by absorption of the isotropic liquid crystal in the capsule into the polymer top layer and the corresponding macroscopic change in shape of the polymer. However the small LC-filled droplets in the polymer appeared to be relatively stable despite the fact that the isotropic LC above T_{NI} is highly attracted by the polymer. The polymer matrix is relatively rigid (80% conversion), requiring large elastic energies to avoid the formation of thermodynamically unfavorable free surface should the LC become dissolved in the polymer matrix. Moreover, the uptake of LC by the polymer and the corresponding swelling exerts a

force on the droplets that leads to their elongation rather than to a minimization of their dimensions. As a result, part of the LC remains in the PDLC-like area while the LC in the capsule becomes dissolved. Following this explanation, according to Figure 3.10g PDLC morphology seems to be formed in about the bottom half of the polymer layer. The fact that the polymer is locally less dense is confirmed by a lower intensity of the IBoMA signal at this position (Figure 3.10h). The local existence of PDLC morphology also explain the elevated LC concentrations near the polymer-LC interface observed at temperatures below T_{NI} (Figure 3.9a).

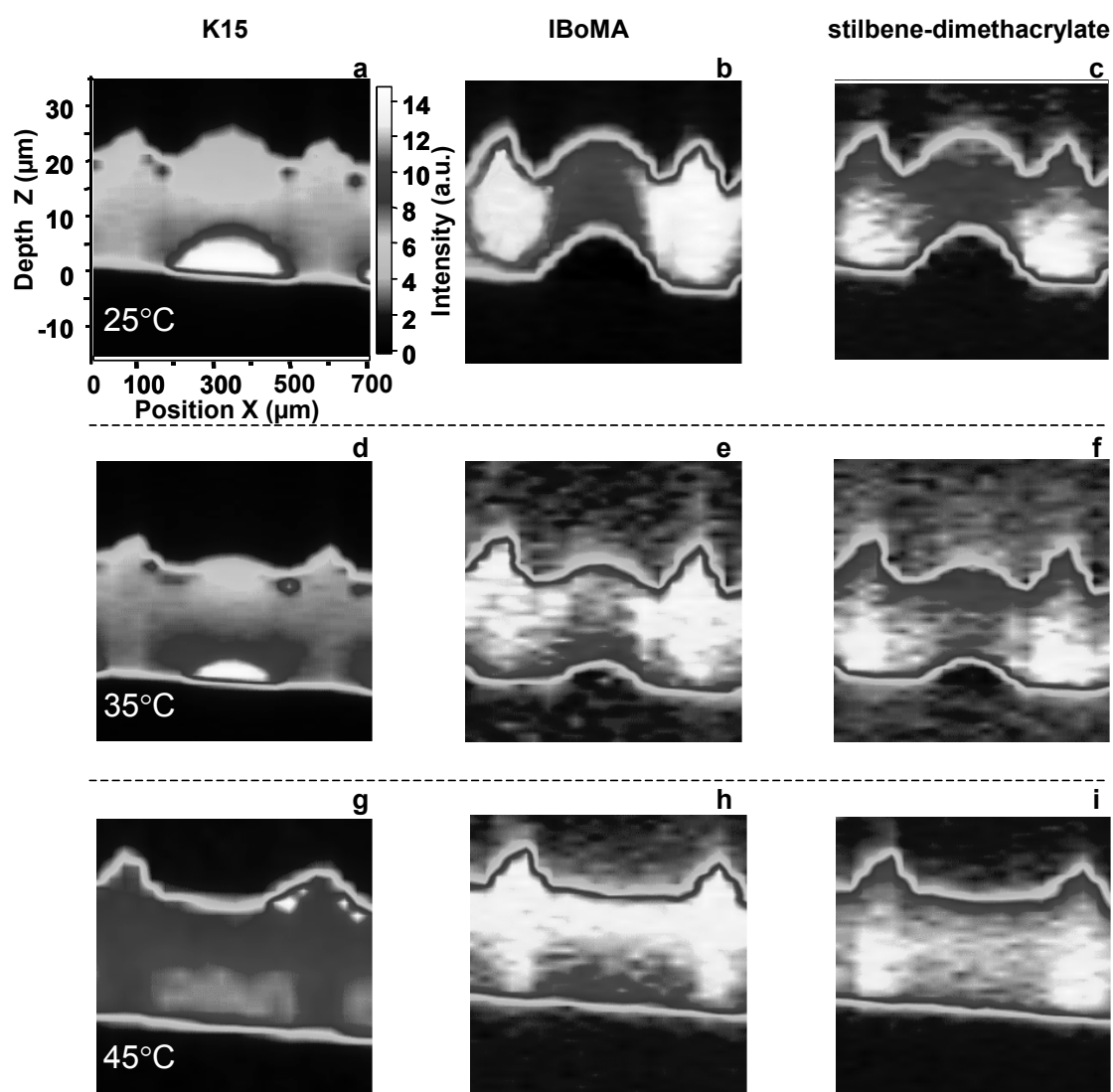


Figure 3.10: X-Z concentration profiles of the various components in a capsule at different temperatures: 25°C (a-c), 35°C (d-f), 45°C (g-i). All profiles are taken through the center of a capsule (see Ref. 17 for colored versions of the X-Z profiles).

Below T_{NI} the XZ-profiles of IBoMA and stilbene-dimethacrylate (Figures 3.10b-c) are influenced by the nematic nature of the K15 droplet but at higher temperatures, when the LC droplet has disappeared, the lateral distribution of the IBoMA and stilbene-dimethacrylate in the polymer becomes more apparent (Figures 3.10h-i).

Subsequently, Raman microscopy was used to follow the change of the morphology upon cooling back to room temperature. The sample was cooled from 45°C to 25°C in 2.5 h measuring the X-Z intensity profile of K15 each 30 minutes (Figure 3.11). The profiles were established using intervals of respectively 20 and 2 μm in X-direction and Z-direction and an integration time of 10 s per point. The figures show how again phase separation occurs. In this case the phase separation is not induced by a polymerization reaction as it was during the formation of the capsules, but now *temperature induced phase separation* (TIPS) takes place. A large drop of LC material is formed again at the bottom of the layer in the center of the capsule. However, a larger amount of LC is separated out towards the top of the structure than initially was the case after the stratification process. This shows that the thermally induced change upon first heating of the sample is irreversible. Further cyclic heating and cooling proved to be reversible.

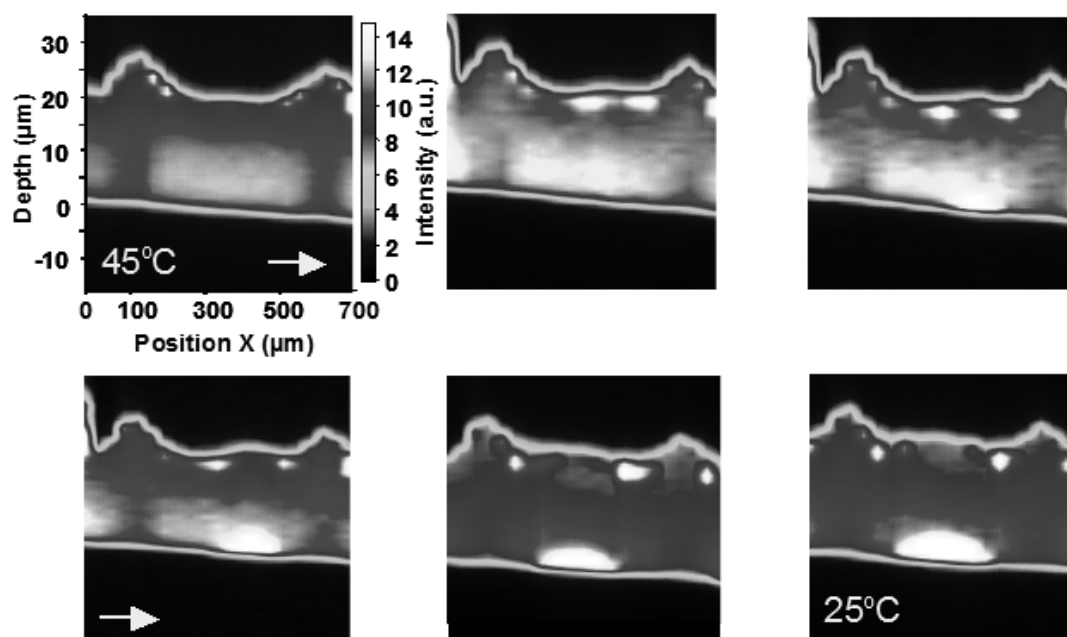


Figure 3.11: X-Z concentration profiles of K15 in a capsule during cool down. All profiles are taken through the center of a capsule. Images are taken at time intervals of 30 min, going from 45°C to 25°C in about 2.5 h (see Ref. 17 for colored versions of the X-Z profiles).

3.4 Conclusions

Confocal Raman microscopy provides detailed information about local composition, conversion, LC orientation and phase separation behavior of the LC-filled polymer capsules obtained via two-step photo-enforced stratification. Measurements after the mask exposure step revealed a composition drift as a result of photo-induced diffusion – the areas between the polymer walls are enriched with LC. In these areas also preliminary polymerization is observed. After stratification the polymer phase still contains a significant amount of liquid crystal, which because of its diluted nature has a random orientational distribution.

Investigation of the temperature dependency of the structures provides insight in the phase separation behavior of the current material system. The nematic nature of the K15 phase largely contributes to the stability of the capsules – above T_{NI} the K15 droplet becomes completely dissolved in the polymer and the capsule shape changes dramatically. From this can be concluded that in order to obtain structures that will be more stable under temperature variations, an LC material should be used with a significantly higher T_{NI} .

The LC gradient in the polymer phase indicates the existence of small LC droplets dispersed in the polymer, which is in line with earlier findings obtained via polarization microscopy (see Chapter 2). From the temperature-induced phase separation upon subsequent heating and cooling of the structures it can be concluded that the polymer does not possess strong chemical (composition) or physical (crosslink) gradients that push the LC in the desired direction in order to recover the structures. This indicates that the gradient in the polymerization rate and consequently a gradient in the conversion *during formation* of the structures play a major role to obtain a stratified morphology. In our set-up PES produces a metastable structure.

3.5 References

1. Penterman, R., Klink, S.I., Koning, H. de, Nisato, G., and Broer, D.J. *Nature* **417**, 55-58 (2002).
2. Vaz, N.A., Smith, G.W., and Montgomery Jr., G.P. *Mol. Cryst. Liq. Cryst.* **197**, 83-101 (1991).
3. Noh, C.H., Jung, J.E., Kim, J.Y., Sakong, D.S., and Choi, K.S. *Mol. Cryst. Liq. Cryst.* **237**, 299-309 (1993).
4. Lovinger, A.J., Amundsen, K.R., and Davis, D.D. *Chem. Mater.* **6**, 1726-1736 (1994).

5. Bunning, T.J., Natarajan, L.V., Tondiglia, V., Sutherland, R.L., Vezie, D.L., and Adams, W.W. *Polymer* **26**, 2699-2708 (1995).
6. Bowley, C.C., and Crawford, G.P. *Appl. Phys. Lett.* **16**, 2235-2237 (2000).
7. Hikmet, R.A.M. *Liq. Cryst.* **9**, 405-416 (1991).
8. Rajaram, C.V., Hudson, S.D., and Chien, L.C. *Chem. Mater.* **7**, 2300-2308 (1995).
9. Stanimirovic, O., Boelens, H.F.M., Mank, A.J.G., Hoefsloot, H.C.J., and Smilde, A.K. *Appl. Spectrosc.* **59**, 267-274 (2005).
10. Baia, L., Gigant, K., Posset, U., Petry, R., Schottner, G., Kiefer, W., and Popp, J. *Vibrational Spectrosc.* **29**, 245-249 (2002).
11. Baia, L., Gigant, K., Posset, U., Schottner, G., Kiefer, W., and Popp, J. *Appl. Spectrosc.* **56**, 536-540 (2002).
12. Vyorykka, J., Paaso, J., Tenhunen, M., Tenhunen, J., Iitti, H., Vuorinen, T., and Stenius, P. *Appl. Spectrosc.* **57**, 1123-1128 (2003).
13. Froud, C.A., Hayward, I.P., and Laven, J. *Appl. Spectrosc.* **57**, 1468-1474 (2003).
14. Everall, N.J. *Appl. Spectrosc.* **54**, 773-782 (2000).
15. Everall, N.J. *Appl. Spectrosc.* **54**, 1515-1520 (2000).
16. Martens, H., and Naes, T. *Multivariate Calibration*, John Wiley & Sons, New York (1989).
17. Mank, A.J.G., Vorstenbosch, I., Penterman, R., Vogels, J.P.A., Klink, S.I., Broer, D.J. *Appl. Spectrosc.* **59**, 965-975 (2005).

Chapter 4

Photo-enforced stratification model

4.1 Introduction

In Chapter 2 the photo-enforced stratification (PES) process has been experimentally demonstrated and qualitatively described in terms of simultaneously occurring photopolymerization-induced diffusion^{1,2} and phase separation^{3,4} processes. A key component in the PES process is the presence of a UV-absorber in the LC/monomer, which results in a predominant monomer consumption in the top of the layer. The local monomer depletion leads to diffusion of monomers towards the top and a concomitant diffusion of LC to the bottom of the layer. At a certain moment during this process, the conditions in terms of LC concentration and monomer conversion, have changed such that phase separation sets in at the bottom of the layer and LC droplets form at the interface with the alignment layer. The growth of nematic LC droplets shortly after the start of the phase separation and the coalescence into bigger LC domains was recorded with an optical polarization microscope provided with a video camera.

Many reports have appeared in the literature on thermodynamic phase separation models for polymer dispersed liquid crystal (PDLC) morphologies.^{5,6,7,8,9,10} Special attention has been paid to the influence of network elasticity in the case of polymerization-induced phase separation (PIPS),⁷ and nematic ordering in temperature-induced phase separation (TIPS) of a polymer/LC blend.^{8,9} Conventional reaction diffusion equations have been applied to model spatially controlled phase separation in holographic PDLCs (H-PDLCs)¹¹ and processes similar to the photo-enforced stratification process.¹² However, phase separation and the influence of the network and nematic ordering of the LC were not addressed in these latter models. In fact, there is very limited literature on the combination of reaction-diffusion equations with a thermodynamic approach to describe spatially controlled phase separation processes. Recently, a number of papers have appeared where phase separation and reaction diffusion are combined to model H-PDLCs.^{13,14} By incorporating the time

dependent Ginzburg-Landau (TDGL) equations, the influence of the spatially controlled phase separation process on the morphological details in the alternating layers and the resulting optical characteristics were calculated.

In this chapter the development of a numerical PES model based on polymer chain reaction kinetics, diffusion and the thermodynamics of phase separation is presented. The model is a combination of two distinct components: The first component is a reaction-diffusion model that calculates the evolution of the concentration profiles of the liquid crystal (LC), monomer and polymer as a function of depth and time. The second component is a thermodynamic polymerization-induced phase separation (PIPS) model that calculates the contribution of the entropic and enthalpic mixing (Flory-Huggins theory of mixing),¹⁵ elasticity of the polymer network (Flory-Rehner)¹⁶ and nematic ordering (Maier-Saupe)¹⁷ to the Gibbs free energy of a given LC/monomer/polymer composition. The overall PES model is a one-dimensional model, which calculates the location and the time (conversion) at which the phase separation sets in. A simulation experiment will illustrate how the model works in practice and the generated results will be discussed.

4.2 Photo-enforced stratification model

4.2.1 Introduction

The PES model is based on a layer consisting of a three-component (ternary) system of monomer (M), liquid crystal (LC), polymer (P) in which the polymer is formed via the conversion of monomers into polymeric repeat units. Two alternatives will be investigated: (i) the monomer is an organic entity with a single vinyl functional group (mono-vinyl; functionality $f = 2$) or (ii) the monomer has two polymerizable groups (di-vinyl; functionality $f = 4$). In the model, the volume and mass of the system are maintained constant; hence possible volume shrinkage due to polymerization and evaporation of the components is not taken into account. For the polymerization kinetics steady state kinetics is assumed, therefore non-linear effects as auto-acceleration and oxygen inhibition of the polymerization are excluded. In addition, the polymerization rate is assumed to be proportional to the double bond fraction, regardless of the functionality of the monomer. The PES model is a one-dimensional model: there is a UV light intensity gradient and materials transport in the z -direction of the layer excluding diffusion in lateral directions. The intensity gradient is assumed to stay constant through the process irrespective of the compositional changes in the layer. Initially, the diffusion coefficients of the monomer and the LC are taken constant, independent of the conversion. In Chapter 6

this approximation will be refined to conversion dependent diffusion coefficients (established by diffusion weighted NMR experiments that will be discussed in Chapter 5). Due to its high molecular weight and early gelation for $f = 4$, diffusion of the formed polymer is neglected in the model: the polymer is fixed at the position where it emerges. Diffusion of the photo-initiator is also neglected.

4.2.2 Thermodynamics

The Gibbs free energy (G) describes the thermodynamic state of a mixture at constant temperature, pressure and the number of particles. ΔG refers to the difference between the actual Gibbs free energy of the mixture and the average of the Gibbs free energies of the pure components at the same temperature and pressure. Mixing, elasticity and nematic ordering are assumed to contribute independently to the Gibbs free energy:

$$\Delta G = \Delta G^{mix} + \Delta G^{el} + \Delta G^{nem} \quad (4.1)$$

where ΔG^{mix} is the mixing term (isotropic order) and is described by the Flory-Huggins lattice theory, ΔG^{el} is the elastic contribution of the polymer network, described by Flory-Rehner and ΔG^{nem} is the nematic term, which is described using the Maier-Saupe free energy model. The monomer chemical potential is obtained by differentiation of ΔG with respect to the number N_M of monomer molecules at constant pressure, temperature and numbers of polymer and solvent molecules:

$$\frac{\Delta\mu_M}{k_B T} = \frac{\partial}{\partial N_M} \left(\frac{\Delta G}{k_B T} \right)_{p, T, N_P, N_{LC}} \quad (4.2)$$

where k_B is Boltzmann's constant, T is the absolute temperature. Similarly the chemical potential of the liquid crystal component ($\Delta\mu_{LC}$) is obtained.

Mixing contribution

The isotropic mixing of the monomer, liquid crystal (LC), and polymer is described by the Flory-Huggins lattice model¹⁵ with the concentration independent interaction parameters χ_{ij} . For the three-component mixture, the Flory-Huggins term is given by

$$\frac{\Delta G^{mix}}{N k_B T} = \frac{\phi_M}{r_M} \ln \phi_M + \frac{\phi_{LC}}{r_{LC}} \ln \phi_{LC} + \frac{\phi_P}{r_P} \ln \phi_P + \sum_{i < j} \chi_{ij} \phi_i \phi_j \quad (4.3)$$

where ϕ_M , ϕ_{LC} and ϕ_P are the volume fractions of the three components: monomer (M), liquid crystal (LC) and polymer (P) and r_i the number of lattice sites occupied by component i . χ_{ij} is the Flory-Huggins interaction parameter between particle i and j ; $(i,j) = (M,LC), (M,P), (LC,P)$. If N_i is the number of molecules of component i , then $N = r_M N_M + r_{LC} N_{LC} + r_P N_P$ is the total number of sites in the system. By using Eq. 4.2 the mixing contribution to the monomer chemical potential becomes

$$\begin{aligned} \frac{\Delta\mu_M^{mix}}{k_B T} = & \ln \phi_M + \left(1 - \frac{r_M}{r_{LC}}\right) \phi_{LC} + \left(1 - \frac{r_M}{r_P}\right) \phi_P \\ & + r_M \left(\chi_M (1 - \phi_M)^2 + \chi_{LC} \phi_{LC}^2 + \chi_P \phi_P^2 \right) \end{aligned} \quad (4.4)$$

and correspondingly the mixing contribution to the liquid crystal chemical potential ($\Delta\mu_{LC}^{mix}$) is obtained. The χ parameters are given by

$$\chi_M = \frac{1}{2} (\chi_{M-LC} + \chi_{M-P} - \chi_{LC-P}) \quad (4.5)$$

and in the same way χ_{LC} and χ_P are obtained.

For simplicity of notation some assumptions are made. The size of monomer molecules, LC molecules and monomer repeat units in the polymer are taken to be equal to unity. Furthermore, r_P will be taken infinite throughout: In radical chain polymerization the chains rapidly grow to a large size. Almost instantaneously, the size of the polymer is orders of magnitude larger than the sizes of the monomer and the LC. Moreover, in crosslinking polymerization of di-vinyl monomers the gel-point generally is found at low conversions.¹⁸ So, early in the reaction the number of monomer repeat units will be infinite.

The chemical structures of the monomer molecules and the monomer repeat units in the polymer are almost identical. Therefore, χ_{M-P} , the interaction parameter between the monomer and the polymer, is approximated equal to zero. Also based on the structural resemblance of monomer and monomer repeat units, the interaction parameter between the monomer and the LC (χ_{M-LC}) and the interaction parameter between the LC and the polymer (χ_{LC-P}) are taken equal: $\chi_{M-LC} = \chi_{LC-P} = \chi$. Consequently, using Eq. 4.5, $\chi_{LC} = \chi$ and $\chi_M = \chi_P = 0$. The chemical potentials of mixing for respectively the monomer and the LC then become

$$\frac{\Delta\mu_M^{mix}}{k_B T} = \ln \phi_M + \phi_P + \chi \phi_{LC}^2 \quad (4.6)$$

and

$$\frac{\Delta\mu_{LC}^{mix}}{k_B T} = \ln \phi_{LC} + \phi_P + \chi(1 - \phi_{LC})^2 \quad (4.7)$$

Elastic contribution

The PES model will be used to evaluate the influence of the elasticity of the polymer network to the Gibbs free energy of the system. Thereto, the difference in phase separation behavior will be investigated between a reaction mixture containing di-functional monomers ($f = 2$, mono-vinyl) and a reaction mixture based on tetra-functional monomers ($f = 4$, di-vinyl). The standard expression for the elastic contribution to the Gibbs free energy per molecule is given by (Flory-Rehner)¹⁶

$$\frac{\Delta G^{el}}{Nk_B T} = \frac{\phi_P}{m_c} \left(\frac{3}{2} A \Phi_P^{2/3} (\phi_P^{1/3} - 1) + B \ln \phi_P \right) \quad (4.8)$$

where m_c is the network chain length (measured in repeat units) between crosslinks. Φ_P is the polymer fraction ϕ_P at the moment of crosslinking. In the case of crosslinking polymerization, Φ_P is equal to ϕ_P . A and B are network model parameters. Here, the Flory affine network model was employed in the calculations:¹⁹

$$A = 1 \quad ; \quad B = \frac{2}{f} \quad (4.9)$$

where f is the functionality of the cross-links; in this case $f = 4$. The network model, which assumes a ring-free network of Gaussian chains, is more accurate for vulcanization of linear chains than for cross-linking polymerization. In chain reactions of di-vinyl monomers it has been found that densely crosslinked microgel particles are formed, containing many closed rings that do not contribute to the elasticity. Moreover, due to the high crosslink density the chains between the crosslinks will not follow a Gaussian distribution. Nevertheless the above network model is applied in the model calculations and the errors that are introduced may be corrected for by an effective value of m_c .

Since in the experimental reaction mixtures it is not possible to determine the average of m_c^{-1} for the polymerization of a reaction mixture based on tetra-functional monomers ($f = 4$, di-vinyl), a crude mean field estimate was used⁷

$$m_c^{-1} = \rho_{XL} = \frac{x^2}{\alpha} = \frac{2 - \alpha - 2\sqrt{1 - \alpha}}{\alpha} \quad (4.10)$$

where α is the monomer conversion (the fraction of monomer molecules converted into polymer repeat units), x is the conversion of reactive groups and x^2 is the probability for a unit to be a crosslink, so that $x^2/\alpha = \rho_{XL}$ is the fraction of crosslinks among reacted units. Dilution of the system, however, causes intramolecular crosslinking (microgels) and a decrease in the number of elastically effective crosslinks.²⁰ The length of the monomer can also have a negative effect on the elastic contribution; when the monomer is more compact it is more likely that cyclization will take place. To account for this specific cyclization character an overall efficiency factor ($\varepsilon \leq 1$) is introduced. This term expresses the fraction of elastically effective network chains. Differentiation of Eq. 4.8 and using Eqs. 4.9 and 4.10 yields the elastic contributions to the chemical potentials of the monomer and the LC:

$$\frac{\Delta\mu_M^{el}}{k_B T} = \frac{\Delta\mu_{LC}^{el}}{k_B T} = \varepsilon \rho_{XL} \phi_P \quad (4.11)$$

Nematic ordering of a liquid crystal

The nematic phase has properties intermediate to the solid and liquid state of matter. Molecules in the nematic phase are arranged in such a manner that there is a long-range orientational order but no positional order of their center of mass. The molecules tend to orient on the average along a preferred direction within a large cluster of molecules, called the director. A frequently used theory in literature²¹ for describing the nematic ordering contribution to the Gibbs free energy is the Maier-Saupe theory.^{17,22} This phenomenological theory is a simplified mean field theory where the details of the molecular structure are ignored. The order parameter S is introduced to represent the state of order in the nematic phase. This parameter is non-zero in the nematic phase but vanishes, for symmetry reasons, in the isotropic phase. The orientational order parameter S is defined as follows:

$$S = \frac{1}{2} \langle 3 \cos^2 \theta - 1 \rangle = \int f(\theta) \frac{1}{2} (3 \cos^2 \theta - 1) d\Omega \quad (4.12)$$

where θ is the angle between a reference axis of a liquid crystal molecule and the director and $f(\theta)$ the equilibrium distribution function. $f(\theta)$ gives the probability of finding rods in a small solid angle $d\Omega = 2\pi \sin \theta d\theta$ around the direction θ . So the distribution function has to satisfy the following constraint:

$$\int f(\theta) d\Omega = 1 \quad (4.13)$$

If the distribution function is entirely random (independent of θ , e.g. isotropic), then S becomes zero, if $f(\theta)$ is strongly peaked around $\theta = 0$ and $\theta = \pi$ (parallel alignment) then S becomes 1. Maier and Saupe stated that the pure nematic contribution to the Gibbs free energy contains two terms:

$$\Delta G^{nem} = k_B T \int f(\theta) \ln(4\pi f(\theta)) d\Omega - \frac{1}{2} US^2 \quad (4.14)$$

where the first term reflects the decrease in entropy due to an anisotropic angular distribution. The second term describes the effects of intermolecular interactions. U is called the potential of a director orientation (pseudo-potential), and Maier and Saupe assumed that U is entirely determined by van der Waals forces and is temperature-independent.

To get an expression for the distribution function, Eq. 4.14 is minimized for all variations of f that satisfy the constraint 4.13. This gives:

$$f(\theta) = \frac{e^{(m \cos^2(\theta))}}{4\pi Z} \quad (4.15)$$

with the mean field parameter m ,

$$m = \frac{3US}{2k_B T} \quad (4.16)$$

and the normalization constant Z ,

$$Z = \int e^{m \cos^2 \theta} d(\cos \theta) \quad (4.17)$$

The behavior of the distribution is shown in Figure 4.1a for various values of the mean field parameter m . Re-writing of Eq. 4.12 using Eq. 4.15 and 4.17 gives

$$S = -\frac{1}{2} + \frac{3}{2} \frac{\partial Z}{Z \partial m} \quad (4.18)$$

The simultaneous solution of Eq. 4.16 and 4.18 can be found via numerical calculations and gives the local minima in $\Delta G(S)$. Apart from the solution $S = 0$, which corresponds to an isotropic phase, the set of equations provides a solution that corresponds to a nematic phase. To establish which of the solutions is realized

physically the resulting values of ΔG^{nem} are compared. When T is below the nematic-isotropic transition temperature of the pure liquid crystal T_{NI} defined by²³

$$\frac{U}{k_B T_{NI}} = 4.54 \quad (4.19)$$

the nematic phase is the stable one, i.e. $\Delta G_{nem}(S) < 0$. For higher temperatures, the isotropic fluid is stable ($S = 0$); there is a first-order transition at $T = T_{NI}$.

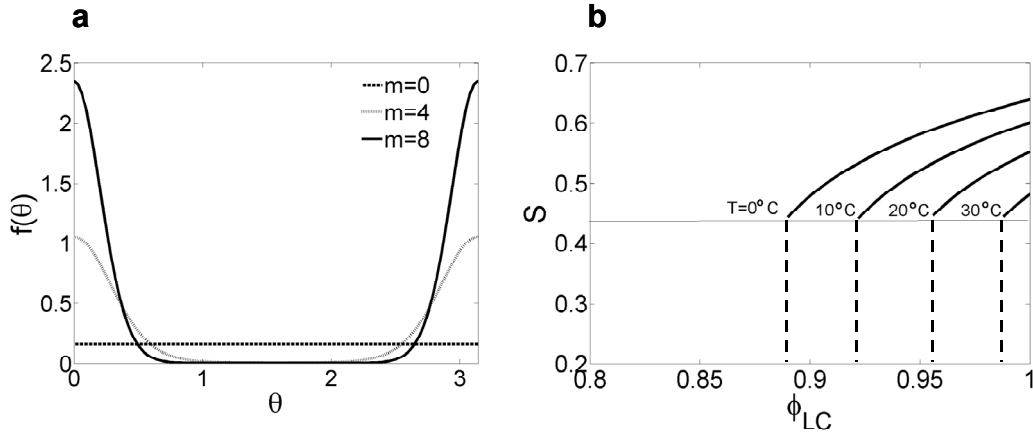


Figure 4.1: a) The distribution function $f(\theta)$ for different mean field parameters m ; increasing m means decreasing temperatures; θ is given in radians. b) The variation of the orientational order parameter S as function of LC fraction ϕ_{LC} in a binary mixture of monomers and K15 for various temperatures.

Nematic ordering contribution to the Gibbs free energy and the chemical potentials in the phase separated liquid phase

After phase separation, the liquid phase formed consists of monomer and liquid crystal molecules (the volume fraction of the polymer will be assumed zero as will be discussed further in Paragraph 4.2.3). To describe the nematic ordering contribution to the Gibbs free energy of the system, the Maier-Saupe theory is modified to couple with the Flory-Huggins equation by incorporating the volume fraction of the LC. The Gibbs free energy due to nematic ordering then becomes:⁸

$$\frac{\Delta G^{nem}}{Nk_B T} = \phi_{LC} \left(\int f(\theta) \ln(4\pi f(\theta)) d\Omega - \frac{1}{2} \frac{U \phi_{LC} S^2}{k_B T} \right) \quad (4.20)$$

The anisotropic driving forces for nematic ordering are non-zero only if the order parameter S is non-zero, which is the case if temperature and composition satisfy the conditions

$$T \leq T_{NI} \quad \phi_{LC} \leq \phi_{NI} \quad (4.21)$$

where ϕ_{NI} is the critical LC fraction, which is directly proportional to the temperature:

$$\phi_{NI} = T / T_{NI} \quad (4.22)$$

In Figure 4.1b the order parameter S in a binary mixture consisting of monomer and liquid crystal molecules (K15, $T_{NI} = 35.5^\circ\text{C}$) is given as function of the volume fraction of the LC material for various temperatures. The critical LC fraction decreases as temperature decreases. For mixtures where the LC fraction is below the critical LC fraction there will be an isotropic phase ($S = 0$) and the nematic term of the Gibbs energy becomes zero.

The nematic ordering contributions to the chemical potentials of the monomer and the liquid crystal, respectively, can be deduced from Eq. 4.20 using Eqs. 4.2 and 4.19:

$$\frac{\Delta\mu_M^{nem}}{k_B T} = 2.27 \frac{T_{NI}}{T} \phi_{LC}^2 S^2 \quad (4.23)$$

$$\frac{\Delta\mu_{LC}^{nem}}{k_B T} = -\ln Z + 2.27 \frac{T_{NI}}{T} \phi_{LC}^2 S^2 \quad (4.24)$$

Chemical potentials

The chemical potentials of M and LC based on the contributions described above will be used as input for the reaction-diffusion model as well as the PIPS model. For a system consisting of di-vinyl monomers and liquid crystals of equal size, in which $\chi_{M-P} = 0$ and $\chi_{M-LC} = \chi_{LC-P} = \chi$, the respective chemical potentials of M and LC, taking the contributions of mixing, elasticity of the network and nematic ordering into account, are

$$\frac{\Delta\mu_M}{k_B T} = \ln \phi_M + \phi_P + \chi \phi_{LC}^2 + \varepsilon \rho_{XL} \phi_P + 2.27 \frac{T_{NI}}{T} \phi_{LC}^2 S^2 \quad (4.25)$$

$$\frac{\Delta\mu_{LC}}{k_B T} = \ln \phi_{LC} + \phi_P + \chi(1 - \phi_{LC})^2 + \varepsilon \rho_{XL} \phi_P - \ln Z + 2.27 \frac{T_{NI}}{T} \phi_{LC}^2 S^2 \quad (4.26)$$

where the crosslink density ρ_{XL} is provided by Eq. 4.10 in which α represents the fraction of monomer molecules converted into polymer repeat units. α is given by:

$$\alpha = \frac{\phi_P}{\phi_M + \phi_P} \quad (4.27)$$

In the case of mono-vinyl monomers the terms representing the elasticity of the network in Eqs. 4.25 and 4.26 are omitted.

4.2.3 Reaction-diffusion model

In this paragraph the reaction-diffusion model will be discussed. The differences in the polymerization kinetics across the layer induce gradients in the chemical potentials of the monomer and the liquid crystal.²⁴ This leads to a change of the composition due to chemical-potential-driven diffusion. The polymerization kinetics is described with a steady state model. The changes of the respective concentration profiles in the layer are calculated with the aid of the general diffusion equation.

Steady state model

The type of polymerization employed in the photo-enforced stratification process is called *free radical chain-addition polymerization*. Radical chain polymerization is a chain addition reaction consisting basically of a sequence of four steps: dissociation, initiation, propagation and termination. These steps are illustrated in Figure 4.2. The process is started by dissociation of the photo-initiator into two primary radicals after the absorption of a UV-photon i.e. photo-initiated polymerization (Fig. 4.2a). These two radicals may or may not have the same molecular structure. The advantage of this photo-initiated polymerization is that the polymerization can be spatially directed, for example by adding a UV-absorber in the case of the PES process. The reaction of the primary radical with a monomer unit is called the initiation step (Fig. 4.2b). Addition of a monomer unit to the growing (macro)-radical is referred to as propagation (Fig. 4.2c). Further growth of two macro-radicals is terminated when combination (Fig. 4.2d) or disproportionation (Fig. 4.2e) occurs. This is called the termination step.

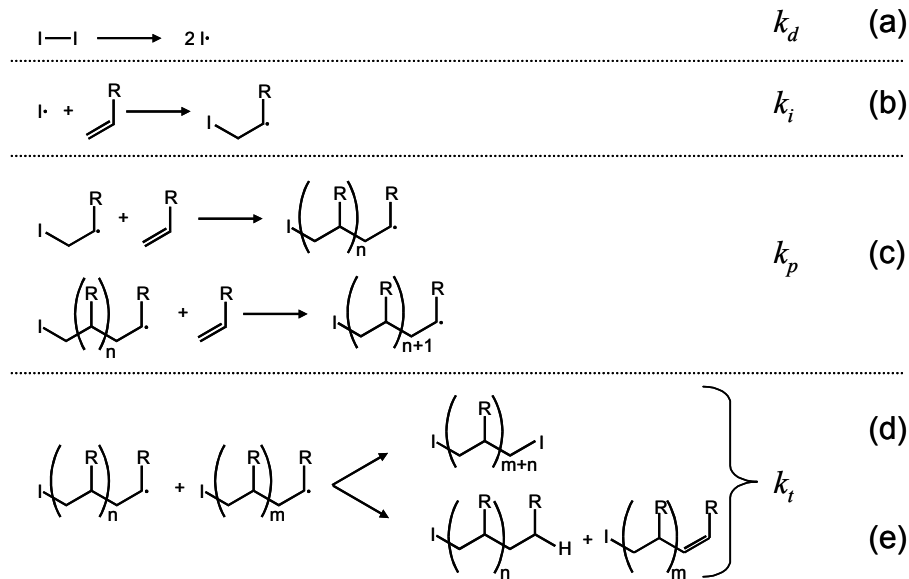


Figure 4.2: The various steps in free radical chain polymerization and their respective rate constants: a) dissociation, b) initiation, c) propagation. There are two termination mechanisms: d) combination, e) disproportionation.

For mono-vinyl monomers the rate of monomer depletion is proportional to the rate of polymerization and is given by

$$-\frac{d[M]}{dt} = R_i + R_p \quad (4.28)$$

where $[M]$ is the monomer concentration in moles per liter and R_i and R_p are rates of initiation and propagation ($\text{mol}\cdot\text{l}^{-1}\cdot\text{s}^{-1}$), respectively. However, in a process producing high molecular weight polymer the initiator concentration is usually small. Therefore, the number of monomer molecules reacting in the initiation step is far less than the number of molecules reacting in the propagation step. So the rate of propagation can be approximated by

$$-\frac{d[M]}{dt} = R_p \quad (4.29)$$

The rate constants for all the propagation steps are considered to be equal. This means that they do not depend on chainlength. Consequently the polymerization rate can be expressed by

$$R_p = k_p [M\cdot][M] \quad (4.30)$$

where $[M\cdot]$ is the total concentration of all chain radicals, i.e. all radicals of size $[M_1\cdot]$ and larger; k_p is the propagation constant in $(\text{l}\cdot\text{mol}^{-1}\cdot\text{s}^{-1})$.

In order to eliminate $[M\cdot]$ the *steady-state assumption* is made: The concentration of radicals is assumed to be constant.²⁵ Hence, the rates of initiation R_i and termination R_t of radicals are taken equal:

$$R_i = R_t = 2k_t[M\cdot]^2 \quad (4.31)$$

where k_t the termination constant $(\text{l}\cdot\text{mol}^{-1}\cdot\text{s}^{-1})$. The use of the factor of 2 in the termination rate equation follows the generally accepted convention that termination includes two macro-radicals. Rearrangement of 4.31 and substitution into 4.30 yields

$$R_p = k_p[M]\sqrt{\frac{R_i}{2k_t}} \quad (4.32)$$

for the rate of polymerization. The rate of photochemical initiation is given by

$$R_i = 2\varphi_{ini}I_a \quad (4.33)$$

where I_a is the intensity of absorbed light in moles of photons per liter-second (called Einsteins in photochemistry) and φ_{ini} is the number of propagating chains initiated per light photon absorbed (quantum yield for initiation). An expression for the polymerization rate is obtained by combining 4.32 and 4.33 to yield

$$R_p = k_p[M]\sqrt{\frac{\varphi_{ini}I_a}{k_t}} \quad (4.34)$$

Calculation of the polymerization gradient

In the photo-enforced stratification process a UV-intensity gradient is created across the layer by adding a UV-absorber to the reaction mixture. The samples are irradiated with a frequency range. By using Beer's law the absorbed light $I_a(z)$ is obtained via

$$I_a(z) = \int_{\lambda} \varepsilon_{PI}(\lambda)I_0(\lambda)10^{-\varepsilon_S(\lambda)[S]z} d\lambda[PI] \quad (4.35)$$

where $\varepsilon_{PI}(\lambda)$ and $\varepsilon_S(\lambda)$ respectively are the extinction coefficients $(\text{l}\cdot\text{mol}^{-1}\cdot\text{cm}^{-1})$ of the photo-initiator and the UV-absorber and $[PI]$ and $[S]$ are their respective

concentrations ($\text{mol}\cdot\text{l}^{-1}$). $I_0(\lambda)$ is the spectrum of the UV source ($\text{Einsteins}\cdot\text{m}^{-2}\cdot\text{s}^{-1}\cdot\text{nm}^{-1}$) at the surface of the layer facing the UV-source, λ the wavelength of the light (nm) and z the distance from the surface (cm). The (insignificant) absorption contribution of the photo-initiator to the intensity gradient will be neglected. The polymerization rate at depth z is obtained by rewriting Eq. 4.34 to

$$R_p(z,t) = k_p[M] \sqrt{\frac{\varphi_{ini} I_a(z)}{k_t}} \quad (4.36)$$

By combining Eqs. 4.35 and 4.36 the polymerization rate $R_p(z,t)$ becomes

$$R_p(z,t) = k_p[M] \sqrt{\frac{\varphi_{ini} \int_{\lambda} \varepsilon_{PI}(\lambda) I_0(\lambda) 10^{-\varepsilon_s(\lambda)[S]z} d\lambda [PI]}{k_t}} \quad (4.37)$$

in which the quantum efficiency of the photo-initiator φ_{ini} is assumed to be wavelength independent.

Chemical-potential-driven diffusion

According to Fick's law, diffusion will arise due to a gradient in the concentration. For one-dimensional diffusion, Fick's (first) law gives de flux J of component x by

$$J_x = -D_x \frac{\partial c_x}{\partial z} \quad (4.38)$$

where D_x is its diffusion coefficient, c_x its concentration and z the z -coordinate in the layer. This empirical law is in fact a derivation from a more universe law in which the flux is caused by a gradient in the chemical potential μ ,²⁶

$$J = -\frac{Dc}{k_B T} \frac{\partial \mu}{\partial z} \quad (4.39)$$

Chemical potential gradients act as the driving force for the movement of molecules. While neglecting convection and chemical reactions, the general diffusion equation is calculated by using conservation of mass:

$$\frac{\partial c}{\partial t} = \frac{\partial}{\partial z} \left(\frac{Dc}{k_B T} \frac{\partial \mu}{\partial z} \right) \quad (4.40)$$

In the case of an ideal solution, e.g. hard spherical non-interacting particles, the chemical potential is given by $\mu = kT \ln c$ and Eq. 4.40 will convert into Fick's law. However, when treating monomer/LC/polymer systems, the chemical potentials are not simply given as the logarithm of a concentration as can be seen in Eqs. 4.25 and 4.26 and the general diffusion equation should be applied.

Differential equations

It is convenient to express the diffusion Equation 4.40 in terms of volume fractions instead of concentrations. The relations for each component are given by:

$$\varphi_i = \frac{c_i M_i}{\rho_i} \quad (4.41)$$

where ρ_i is the density in $\text{g}\cdot\text{cm}^{-3}$ of component i , M_i its the molecular weight in $\text{kg}\cdot\text{mol}^{-1}$ and c_i the concentration of component i in $\text{mol}\cdot\text{l}^{-1}$. The differential equations expressed in volume fractions become:

$$\frac{\partial \phi_M}{\partial t} = \frac{\partial}{\partial z} \left(D_M \phi_M \frac{\partial}{\partial z} \frac{\Delta \mu_M(\phi_M(z,t), \phi_{LC}(z,t), \phi_P(z,t))}{k_B T} \right) - R_P(z,t) \quad (4.42)$$

$$\frac{\partial \phi_{LC}}{\partial t} = \frac{\partial}{\partial z} \left(D_{LC} \phi_{LC} \frac{\partial}{\partial z} \frac{\Delta \mu_{LC}(\phi_M(z,t), \phi_{LC}(z,t), \phi_P(z,t))}{k_B T} \right) \quad (4.43)$$

where t is time, D_M and D_{LC} ($\text{m}^2\cdot\text{s}^{-1}$) are the diffusion coefficients of the monomer and the liquid crystal, respectively. The functions $\Delta \mu_M(\phi_M(z,t), \phi_{LC}(z,t), \phi_P(z,t))/k_B T$ and $\Delta \mu_{LC}(\phi_M(z,t), \phi_{LC}(z,t), \phi_P(z,t))/k_B T$ are the chemical potentials of the monomer and the liquid crystal formulated in Eqs. 4.25 and 4.26. $R_P(z)$ is the polymerization rate, given by Eq. 4.37 for a mono-vinyl monomer. The polymerization rate equation for a di-vinyl monomer will be given later.

The polymer is assumed to be immobilized at the position where it is formed. This is obvious in the case of crosslinking polymerization, but also for linear polymers the diffusion coefficient D_P will be much smaller than D_M and D_{LC} . Then, the conversion of the polymer volume fraction becomes:

$$\frac{\partial \phi_P}{\partial t} = R_P(z,t) \quad (4.44)$$

The material balance states that $\frac{\partial \phi_M}{\partial t} + \frac{\partial \phi_{LC}}{\partial t} + \frac{\partial \phi_P}{\partial t} = 0$, which implies that the first terms behind the equality signs in Eqs. 4.42 and 4.43 must cancel each other out. This is the case when the monomer flux is equal and opposite to the LC flux, $J_M = -J_{LC}$. However, the volume fractions as well as the derivatives of the chemical potentials of the two components will be different throughout the process and therefore this requirement will not be fulfilled with the current set of differential equations. The material balance was made correct deliberately by adjusting the set of differential equations. Thereto, the chemical potentials of one of the components were made *dominant* i.e. the flux of one of the components is calculated and subsequently the flux of other component is taken equal with opposite sign. When the chemical potentials of the monomer are made dominant, the LC volume fraction is calculated via

$$\frac{\partial \phi_{LC}}{\partial t} = -\frac{\partial}{\partial z} \left(D_M \phi_M \frac{\partial \Delta \mu_M(\phi_M(z,t), \phi_{LC}(z,t), \phi_P(z,t))}{\partial z} \frac{1}{k_B T} \right) \quad (4.45)$$

This is called monomer-chemical-potential-driven diffusion, because the gradient in the monomer chemical potential, which arises from the polymerization process is taken as the driving force for diffusion. The term monomer-chemical-potential-driven diffusion will be abbreviated further to monomer-driven diffusion. When gradient in the LC chemical potential is taken as the driving force for diffusion, it will be called LC-driven diffusion. To examine the influence of the assumptions made both alternatives will be compared.

Diffusion model: numerical scheme

The partial differential equations are solved using a Forward in Space Center in Time (FSCT) numerical method with Neumann boundary conditions. The one-dimensional layer with thickness d is divided into N segments of equal lengths Δz . The polymerization and the diffusion are calculated in subsequent steps. The functions (J, ϕ or μ) are denoted as follows

$$X_{Y,n}^m = X_Y(m\Delta t, n\Delta z) \quad (4.46)$$

where X represents a function of component Y . Δt is the grid step for the time and m and n are integers between respectively, 0 and $m_t (= t_{max}/\Delta t)$, and 1 and $n_d (= d/\Delta z)$. The value of a function before the polymerization step will be denoted as $X_{Y,n}^m$,

between the polymerization and the diffusion step as $X_{Y,n}^{m*}$ and after the diffusion step as $X_{Y,n}^{m+1}$.

Prior to the diffusion step the change in the monomer- and polymer volume fractions due to polymerization are calculated. The change in the monomer volume fraction after polymerization during time step Δt can be described in discretized form by

$$\frac{\phi_{M,n}^{m*} - \phi_{M,n}^m}{\Delta t} = -k_p \phi_{M,n}^m \sqrt{\frac{\phi I_a(n)}{k_t}} \quad (4.47)$$

where $I_a(n)$ is the intensity of absorbed light in moles of photons per liter-second in segment n . The reactivity, i.e. the capture probability of an unreacted monomer, of di-vinyl monomers is twice the reactivity of a mono-vinyl monomer, assuming equal capture probabilities of the primary reacted and the pendant double bonds. Thus, for a di-vinyl the change in monomer volume fraction will be twice as fast:

$$\frac{\phi_{M,n}^{m*} - \phi_{M,n}^m}{\Delta t} = -2k_p \phi_{M,n}^m \sqrt{\frac{\phi I_a(n)}{k_t}} \quad (4.48)$$

Consequently, after calculating the new monomer fractions via Eqs. 4.47 or 4.48, depending on whether mono-vinyls or di-vinyls are used, the polymer fraction is calculated via

$$\phi_{P,n}^{m*} - \phi_{P,n}^m = -(\phi_{M,n}^{m*} - \phi_{M,n}^m) \quad (4.49)$$

The monomer conversion is given by

$$\alpha_n^{m*} = \frac{\phi_{P,n}^{m*}}{\phi_{M,n}^{m*} + \phi_{P,n}^{m*}} \quad (4.50)$$

In the case of di-vinyls the crosslink density ρ_{XL} is calculated with a discretized version of Eq. 4.10:

$$\rho_{XL,n}^{m*} = \frac{2 - \alpha_n^{m*} - 2\sqrt{1 - \alpha_n^{m*}}}{\alpha_n^{m*}} \quad (4.51)$$

The above equation is intended for ‘closed’ systems i.e. systems in which the sum of monomer units and monomer repeat units in the polymer remains constant. However,

in the PES process the segments are ‘open’ and the number of monomer units in the segments varies due to diffusion. Simulations have shown that the errors, introduced by describing the evolution of the crosslink density in the ‘open’ segments with Eq. 4.51, are small. Therefore, this equation can be used as a good approximation. During polymerization the LC fraction stays constant:

$$\phi_{LC,n}^{m*} = \phi_{LC,n}^m \quad (4.52)$$

After the polymerization step, the chemical potentials of the dominant component are calculated. In the case of monomer-driven diffusion

$$\frac{\Delta\mu_{M,n}^{m*}}{k_B T} = \ln \phi_{M,n}^{m*} + \phi_{P,n}^{m*} + \chi(\phi_{LC,n}^{m*})^2 + \varepsilon\rho_{XL}\phi_{P,n}^{m*} \quad (4.53)$$

or the case of LC-driven diffusion

$$\frac{\Delta\mu_{LC,n}^{m*}}{k_B T} = \ln \phi_{LC,n}^{m*} + \phi_{P,n}^{m*} + \chi(1 - \phi_{LC,n}^{m*})^2 + \varepsilon\rho_{XL}\phi_{P,n}^{m*} \quad (4.54)$$

Until the onset of phase separation the reaction mixture is isotropic and therefore the nematic contributions are omitted. Subsequently, the flux of the dominant component Y through the interface $n-1/2$ between segments n and $n-1$ is calculated by

$$J_{Y,n-1/2}^{m*} = \frac{D_Y(\phi_{Y,n-1}^{m*} + \phi_{Y,n}^{m*})(\mu_{Y,n}^{m*} - \mu_{Y,n-1}^{m*})}{2k_B T \Delta z} \quad (4.55)$$

It is assumed that there is no polymerization-induced volume shrinkage, so the thickness of the layer remains constant. As discussed before, the flux of the dominant component is counterbalanced by the other component and therefore also the segment size stays constant. The volume and the mass of the system stay constant; hence the fluxes at the boundaries are zero:

$$J_0 = -\frac{D_Y \phi_Y}{k_B T} \frac{\partial \mu_0}{\partial z} = 0 \quad (4.56)$$

$$J_d = -\frac{D_Y \phi_Y}{k_B T} \frac{\partial \mu_d}{\partial z} = 0 \quad (4.57)$$

The change of the volume fractions of component Y in segment n as a result of diffusion in time step Δt is calculated by an explicit numerical method:

$$\begin{aligned}
\phi_{Y,n}^{m+1} - \phi_{Y,n}^{m*} &= -\Delta t \frac{J_{Y,n+1/2}^{m*} - J_{Y,n-1/2}^{m*}}{\Delta z} \\
&= -\frac{\Delta t}{(\Delta z)^2} \frac{D}{2k_B T} \left\{ \begin{aligned} & \left(\phi_{Y,n-1}^{m*} + \phi_{Y,n}^{m*} \right) \left(\mu_{Y,n}^{m*} - \mu_{Y,n-1}^{m*} \right) - \\ & \left(\phi_{Y,n}^{m*} + \phi_{Y,n+1}^{m*} \right) \left(\mu_{Y,n+1}^{m*} - \mu_{Y,n}^{m*} \right) \end{aligned} \right\} \\
&= -\frac{\Delta t}{(\Delta z)^2} \frac{D}{2k_B T} \left\{ \begin{aligned} & \phi_{Y,n-1}^{m*} \left(\mu_{Y,n}^{m*} - \mu_{Y,n-1}^{m*} \right) + \\ & \phi_{Y,n}^{m*} \left(-\mu_{Y,n-1}^{m*} + 2\mu_{Y,n}^{m*} - \mu_{Y,n+1}^{m*} \right) - \\ & \phi_{Y,n+1}^{m*} \left(\mu_{Y,n+1}^{m*} - \mu_{Y,n}^{m*} \right) \end{aligned} \right\} \tag{4.58}
\end{aligned}$$

The discretized equations at the boundaries $n = 1$ and $n = n_d$ become

$$\phi_{Y,1}^{m+1} - \phi_{Y,1}^{m*} = -\frac{\Delta t}{(\Delta z)^2} \frac{D}{2k_B T} \left(\left(\phi_{Y,1}^{m*} + \phi_{Y,2}^{m*} \right) \left(\mu_{Y,2}^{m*} - \mu_{Y,1}^{m*} \right) \right) \tag{4.59}$$

$$\phi_{Y,n_d}^{m+1} - \phi_{Y,n_d}^{m*} = -\frac{\Delta t}{(\Delta z)^2} \frac{D}{2k_B T} \left(\left(\phi_{Y,n_d-1}^{m*} + \phi_{Y,n_d}^{m*} \right) \left(\mu_{Y,n_d}^{m*} - \mu_{Y,n_d-1}^{m*} \right) \right) \tag{4.60}$$

In a monomer-driven diffusion simulation the volume fractions and the chemical potentials in the above equations represent the monomer volume fractions and the monomer chemical potentials, respectively ($Y = M$). In that case the change in the LC volume fractions is subsequently calculated via

$$\phi_{LC,n}^{m+1} - \phi_{LC,n}^{m*} = -\left(\phi_{M,n}^{m+1} - \phi_{M,n}^{m*} \right) \tag{4.61}$$

No polymer flux is assumed, thus

$$\phi_{P,n}^{m+1} = \phi_{P,n}^{m*} \tag{4.62}$$

The calculated monomer, LC and polymer volume fractions are used as input parameters in the next program cycle.

Flowchart

Summarized, the numeric reaction-diffusion model contains three main building blocks: The calculations of the polymerization, the chemical potentials and the diffusion, respectively. In Figure 4.3 a flow chart is depicted, containing the main building blocks and the equations that are subsequently solved during a single time step Δt . It shows an example of a monomer-driven diffusion simulation for the case of a reaction mixture containing di-vinyl monomers. For stability of the numerical simulations, the time steps Δt have to be chosen sufficiently small with respect to Δz .

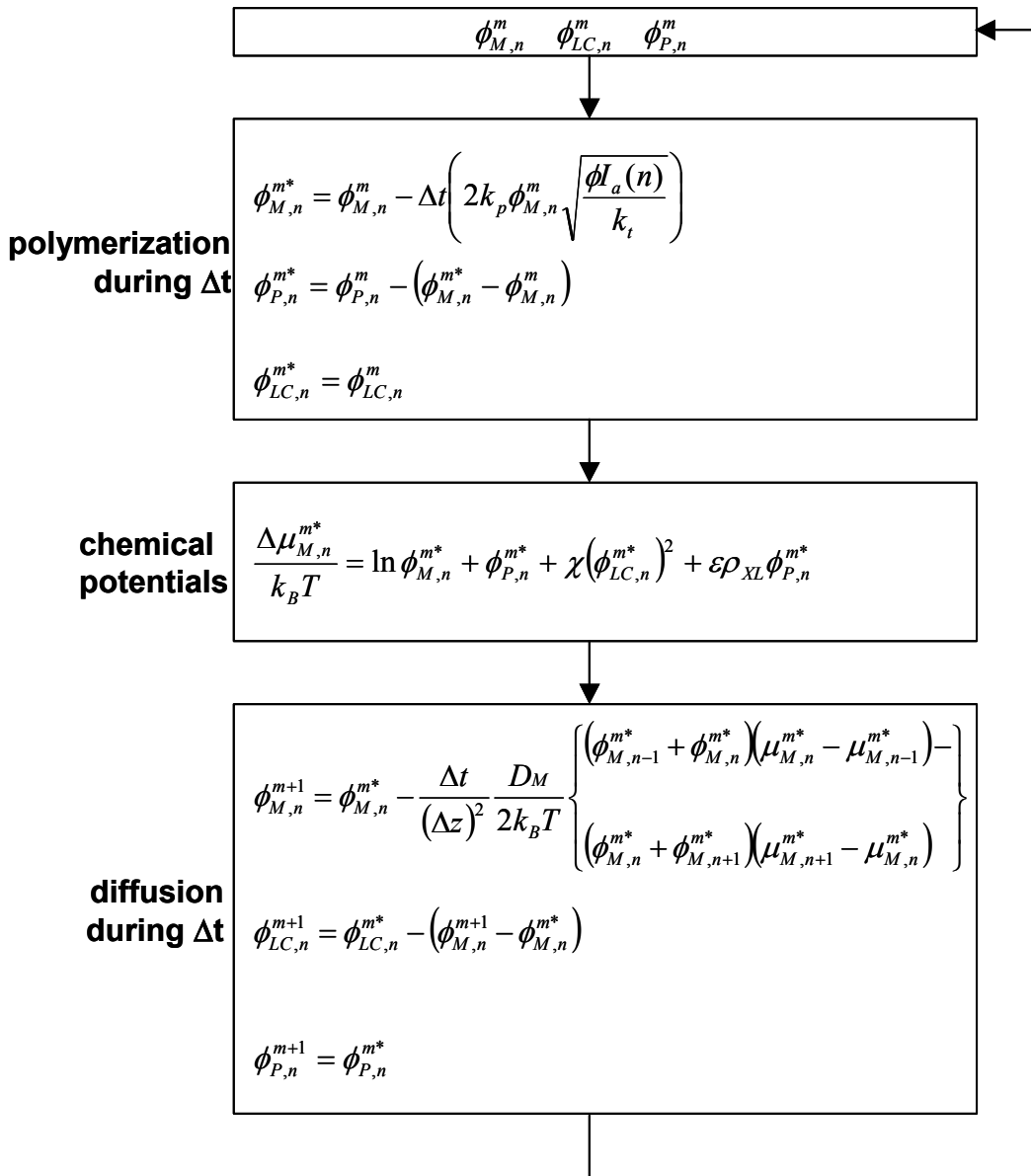


Figure 4.3: The flow chart of a monomer-driven diffusion simulation for the case of a reaction mixture containing di-vinyl monomers.

4.2.4 PIPS model

Phase separation occurs when the polymer rich phase (*I*) and the liquid phase (*II*) are in thermodynamic equilibrium i.e. the chemical potential of the monomer as well as the chemical potential of the liquid crystal has the same value in both phases. The volume fractions, ϕ_M and ϕ_{LC} , in both phases *I* and *II* at the onset of phase separation, are calculated numerically by solving the following non-linear equations:

$$\Delta\mu_M^I = \Delta\mu_M^{II} \quad (4.63)$$

$$\Delta\mu_{LC}^I = \Delta\mu_{LC}^{II} \quad (4.64)$$

The polymer fraction in the liquid phase, ϕ_P^{II} , is taken zero. In the case of a di-vinyl monomer the gel-point will be reached at early conversion. In a gelled system all the reacting monomers are almost immediately attached to the network. At the onset of phase separation only one phase contains the polymer network while the liquid phase is a network-free phase. Tompa²⁷ showed that also for ternary systems consisting of a solvent, a non-solvent and a linear polymer with $r_P > 100$ (which is the case for free-radical chain polymerization), the liquid phase is virtually polymer-free. Applying the material balance to the two phases gives the following equations:

$$\phi_M^I + \phi_{LC}^I + \phi_P^I = 1 \quad (4.65)$$

$$\phi_M^{II} + \phi_{LC}^{II} = 1 \quad (4.66)$$

Calculation of the volume fractions of the monomer and the LC in both phases, $\phi_M^{I,II}$ and $\phi_{LC}^{I,II}$, at the onset of phase separation as function of ϕ_P^I yields the phase separation curve, which connects all compositions for which the polymer rich phase is in thermodynamic equilibrium with the liquid phase. Thereto, Eqs. 4.25 and 4.26 are combined with Eqs. 4.65 and 4.66. Figure 4.4 shows the resulting chemical potentials of the monomer and the LC in phase *I* and phase *II*. After including Eq. 4.10 and Eq. 4.27, the chemical potentials are inserted in Eq. 4.63 and 4.64, which are solved numerically. The model contains 4 system dependent parameters (χ, ε, T and T_{NI}) and 5 variables ($\phi_M^I, \phi_{LC}^I, \phi_P^I, \phi_M^{II}, \phi_{LC}^{II}$).

PIPS model

M

I: $\frac{\Delta\mu_M^I}{k_B T} = \ln \phi_M^I + \phi_P^I + \chi(\phi_{LC}^I)^2 + \varepsilon\rho_{XL}\phi_P^I$

=

II: $\frac{\Delta\mu_M^{II}}{k_B T} = \ln \phi_M^{II} + \chi(\phi_{LC}^{II})^2 + 2.27 \frac{T_{NI}}{T} (\phi_{LC}^{II})^2 S^2$

and

LC

I: $\frac{\Delta\mu_{LC}^I}{k_B T} = \ln \phi_{LC}^I + \phi_P^I + \chi(1 - \phi_{LC}^I)^2 + \varepsilon\rho_{XL}\phi_P^I$

=

II: $\frac{\Delta\mu_{LC}^{II}}{k_B T} = \ln \phi_{LC}^{II} + \chi(1 - \phi_{LC}^{II})^2 - \ln Z + 2.27 \frac{T_{NI}}{T} (\phi_{LC}^{II})^2 S^2$

Figure 4.4: The PIPS model calculates the volume fractions of the monomer (ϕ_M) and the LC (ϕ_{LC}) in the polymer-rich (I) and in the liquid phase (II) at the onset of phase separation for a given polymer fraction ϕ_P^I . At the onset of phase separation the phases are in thermodynamic equilibrium: the chemical potentials of the monomer are equal in both phases as well as the chemical potentials of the LC.

The phase separation curves will be plotted in a ternary conversion phase diagram. A ternary conversion phase diagram is a way to visualize the dependence of the onset of phase separation on the initial composition of the reaction mixture.⁷ A conversion phase diagram differs from the conventional phase diagram in the fact that the polymer component does not only change in amount, but also in molecular size and distribution and/or molecular structure with increasing conversion. Figure 4.5 shows a ternary conversion phase diagram describing an imaginary bulk polymerization process in the presence of LC. The polymerization is described as a line of constant LC fraction represented by line AB. The polymerization starts at the left axis and upon increasing conversion it follows a horizontal line from left to right. In the beginning of the polymerization there is one phase containing monomers and liquid crystals and polymer. The phase separation line is represented by line CD. At the left hand side of this curve the system exhibits a single phase (I). At the right hand side the system exhibits two phases (I+II). Point X, where the polymerization line AB intersects the phase separation line CD is the *onset of phase separation*. At the onset of phase separation the polymer rich phase with composition X is in thermodynamic equilibrium with a liquid phase with composition Y. The thermodynamic equilibrium is visualized by the tie line XY, linking the compositions in both phases. The monomer, LC and polymer fractions in the polymer rich phase, respectively, can be

deduced via translation of X on the three axes: m , B and p . The intersection of the bottom axis with a straight line through the top corner of the diagram and point X , point α , yields the conversion at the onset of phase separation. Point D will be called the *solubility limit* of the LC in the polymer and gives the LC fraction, which the fully polymerized material can contain without exhibiting phase separation.

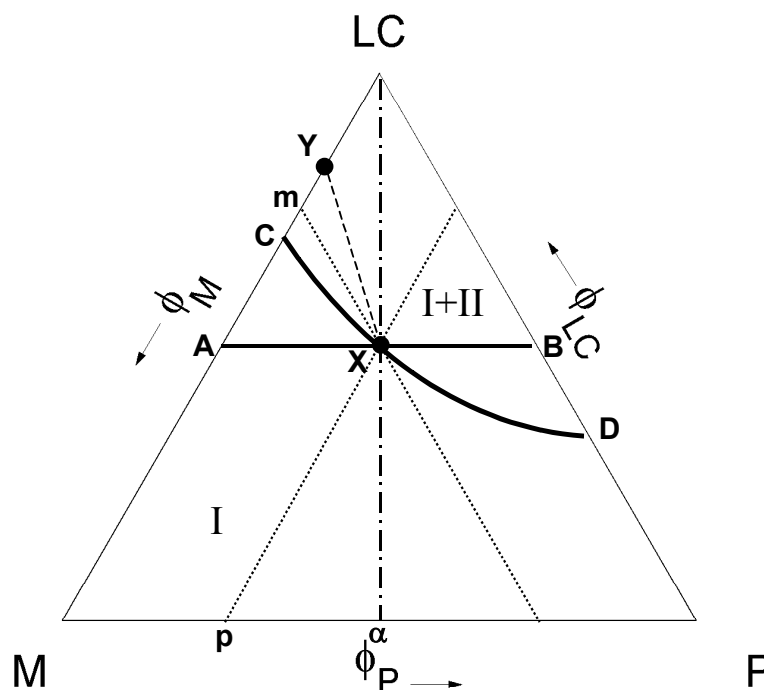


Figure 4.5: Ternary conversion phase diagram of the polymerization of monomer M to polymer P in the presence of liquid crystal LC . CD is the phase separation curve. The regions at the left hand side (I) and the right hand side ($I+II$) of CD , respectively, refer to a single- and a two-phase system. A polymerization line AB at constant LC fraction $\phi_{LC} = 0.5$ is drawn. It intersects the phase separation curve CD in X at monomer conversion $\alpha = 0.5$. X and Y are the compositions of the (isotropic) polymer rich phase and the new (isotropic) liquid phase at the onset of phase separation. The composition of X can be read from the axes: m , B and p give the monomer fraction, the liquid crystal fraction, and the polymer fraction, respectively.

4.3 Results and discussion

The PES model is a combination of the reaction-diffusion model and the PIPS model. In this paragraph the PES model will be explained with the aid of an example. In this example the photopolymerization of a 25- μm layer consisting of a 50/50 LC/mono-vinyl monomer mixture is modeled. The values of the respective input parameters are given in Table 4.1.

Table 4.1: Input parameters of the PES model

	Parameter	Value / calculated via
LC fraction	ϕ_{LC}	0.5
Layer thickness (μm)	d	25
Incident intensity ($\text{mW}\cdot\text{cm}^{-2}$)	I_0	0.8
Effective intensity gradient* ($\text{Einsteins}\cdot\text{m}^{-2}\cdot\text{s}^{-1}$)	$I_a(z)$	Equation 4.35*
Quantum efficiency photo-initiator	ϕ_{mi}	0.4
Propagation / termination constants ($\sqrt{\text{l}\cdot\text{mol}^{-1}\cdot\text{s}^{-1}}$)	$\frac{k_p}{\sqrt{k_t}}$	1.5
Interaction parameter	χ	0.6
Mono-vinyl monomer, polymerization kinetics		Equation 4.47
Mono-vinyl monomer, no crosslinks	ρ_{XL}	0
Monomer-driven diffusion; monomer diffusion coefficient ($\text{m}^2\cdot\text{s}^{-1}$)	D_M	$1*10^{-10}$
Nematic-isotropic temperature LC ($^{\circ}\text{C}$)	T_{NI}	35.5
Temperature ($^{\circ}\text{C}$)	T	20

* $I_0(\lambda)$ intensity profile of the TL08 UV source, $\varepsilon_p(\lambda)$ and $\varepsilon_s(\lambda)$ the extinction curves of the photo-initiator Irgacure 651 (concentration $[P] = 1.95*10^{-5} \text{ mol}\cdot\text{l}^{-1}$) and the UV-absorber stilbene-dimethacrylate ($[S] = 8.87*10^{-5} \text{ mol}\cdot\text{l}^{-1}$), which are all shown Chapter 2, Figure 2.3.

In the ternary conversion phase diagram (Figure 4.5a) the phase separation lines as well as the polymerization lines at six different z -positions in the layer are plotted (0 - 25 μm with 5 μm intervals). The highest and the lowest polymerization line respectively represent the development of the composition in the bottom and in the top of the layer upon increasing conversion (bottom of the layer $z = 0 \mu\text{m}$, top: $z = 25 \mu\text{m}$). Two phase separation lines which have been calculated with the phase separation model split the ternary diagram into three regions: A large region in which the reaction mixture exhibits a single isotropic phase (I), a region at the top right of the diagram in which the system de-mixes in a nematic phase and an isotropic polymer phase (N-I) and a smaller region at the top left in which both phases are isotropic (I-I). The phase separation lines are valid for all z values, hence the intersections of the polymerization lines with the phase separation line give an impression of the region of the layer in which phase separation might occur. The diagram shows that the 15, 20 and 25 μm polymerization lines do not intersect the N-I phase separation line, which implies that in the top of the film no phase separation will take place and will be limited to the lowest region of the film. To determine the time to the onset of phase separation as well as the location of the onset of phase separation, an additional plot is constructed to depict the time-of-intersection of the

respective polymerization lines and the phase separation line. In Figure 4.5b the z -position where the corresponding polymerization line intersects the phase separation line is plotted as a function of time. The time-of-intersection plot shows that after 11 minutes the phase separation line is crossed first at the bottom of the layer. This is the onset of the phase separation.

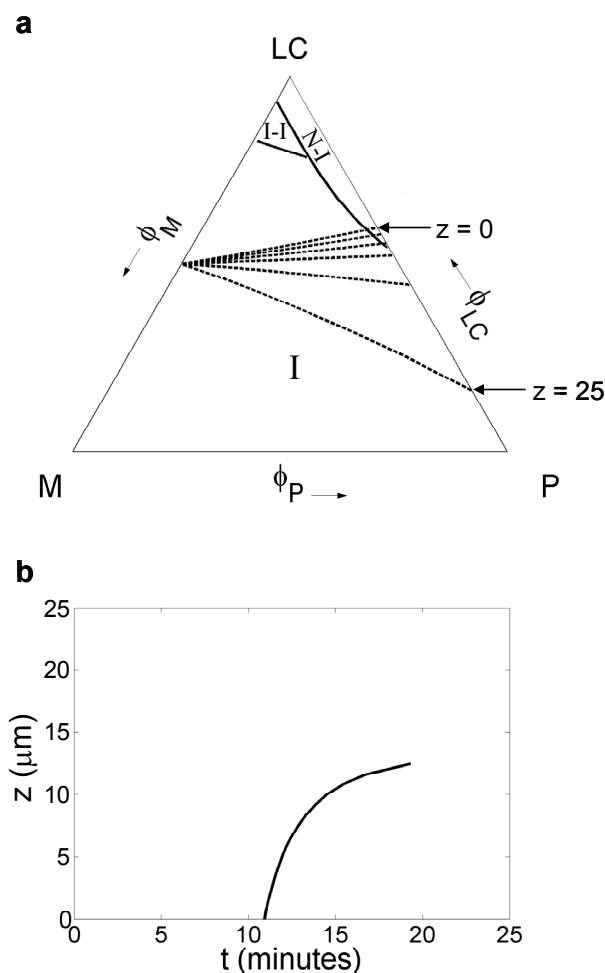


Figure 4.5: a) Ternary phase diagram providing the phase separation lines (I-I- and N-I de-mixing line), calculated with the phase separation model, as well as six polymerization lines at different z -positions (dotted lines; top line: $z = 0$ μm , bottom line: $z = 25$ μm , 5- μm intervals), calculated with the (monomer-driven) reaction-diffusion model. b) The time-of-intersection plot shows the z -position where the corresponding polymerization line intersects the N-I phase separation line as a function of time.

Formally, after the onset of the phase separation the model is not longer valid; after separation into a two-phase system new parameters should be introduced.¹⁹ Polymerization, for example, will continue in the nematic phase (which will contain a small amount of unreacted monomer). Also, the diffusion model is only valid for a single isotropic phase. Therefore, the times-of-intersection calculated in the other regions of the film do not have a physical meaning. However, the shape of the time-of-intersection curve gives an indication of the morphology that will be formed. For example, if the curve shows intersections equally in time across the entire layer, the

phase separation process will be basically similar to the polymerization-induced phase separation in a PDLC i.e. micrometer-sized LC droplets randomly distributed in the polymer phase will be formed. If the curve shows that intersection mainly takes place in the bottom half of the film as in Figure 4.5b, the top of the polymer film will be free of LC droplets but PDLC morphology formation in the bottom cannot be excluded. When the intersection occurs solely at the very bottom of the layer, the polymer film will be essentially free of LC droplets.

4.4 Conclusions

A photo-enforced stratification model for a ternary LC/monomer/polymer system has been developed, based on the combination of two distinct models: a reaction-diffusion model and a polymerization-induced phase separation model. The predictions of each model i.e. the polymerization lines and the phase separation line can be plotted in a ternary phase diagram. The overall model gives the start and the starting position of the phase separation in the layer. It does not describe whether stratification takes place i.e. formation of a polymer covered liquid crystal layer, since the model is only valid until the start of the phase separation. However, the PES model may help to predict trends in the formation of for instance the undesired PDLC morphology in the layer, and will be useful for the optimization of process and material parameters.

4.5 References and notes

1. Nostrum, C., Nolte, R.J.M., Broer, D.J., Fuhrman, T., and Wendorff, J.H. *Chem. Mater.* **10**, 135-145 (1998).
2. Bowley, C.C., and Crawford, G.P. *Appl. Phys. Lett.* **16**, 2235-2237 (2000).
3. Drzaic, P.S. *J. Appl. Phys.* **60**, 2142-2148 (1986).
4. Doane, J.W., Vaz, N.S., Wu, B.-G., and Zumer, S. *Appl. Phys. Lett.* **48**, 269-271 (1986).
5. Hirai, Y., Niyama, S., Kumai, H., and Gunijama, T. *S. Rep. Res. Lab. Asahi Glass Co., Ltd.* **40**, 285-296 (1990).
6. Kim, J.Y., Cho, C.H., Palffy-Muhoray, P., Mustafa, M., and Kyu, T. *Phys. Rev. Lett.* **71**, 2232-2235 (1993).
7. Boots, H.M.J., Kloosterboer, J.G., Serbutoviez, C., and Touwslager, F.J. *Macromol.* **29**, 7683-7689 (1996).
8. Shen, C., and Kyu, T. *J. Chem. Phys.* **102**, 556-562 (1995).

9. Benmouna, F., Bedjaoui, L., Maschke, U., Coqueret, X., and Benmouna, M. *Macromol. Theory Simul.* **7**, 599-611 (1998).
10. Nwabunma, D., Chiu, H.-W., and Kyu, T. *J. Chem. Phys.* **113**, 6429-6436 (2000).
11. Sarkar, M. D., Gill, N.L., Whitehead, J.B., and Crawford, G.P. *Macromol.* **36**, 630 (2003).
12. Qian, T., Kim, J.-H., Kumar, S., and Taylor, P. L. *Phys. Rev. E* **61**, 4007-4010 (2000).
13. Kyu, T., Nwabunma, D., and Chiu, H.-W. *Phys. Rev. E* **63**, 061802 (2001).
14. Meng, S., Kyu, T., Natarajan, L.V., Tondiglia, V.P., Sutherland, R.L., and Bunning, T.J. *Macromol.* **38**, 4844-4854 (2005).
15. Flory, P.J. *J. Chem. Phys.* **9**, 660 (1941); Huggins, M.L. *J. Chem. Phys.* **9**, 440 (1941).
16. Flory, P.J. *Principles of Polymer Chemistry*, Cornell University Press, Ithaca, New York (1953).
17. Maier, V.W., and Saupe, A. *Z. Naturforschg.* **14a**, 882-889 (1959).
18. Kloosterboer, J.G., Hei, G.M.M. van de, and Boots, H.M.J. *Polym. Commun.* **25**, 354-357 (1984).
19. Dušek, K. *J. Polym. Sci.* **C16**, 1289-1299 (1967).
20. Elliott, J., Anseth, J.W., and Bowman, C.N. *Chem. Eng. Sci.* **56**, 3173-3184 (2001).
21. Gennes, P. de, and Prost, J. *The physics of Liquid Crystals*, Oxford University Press, Oxford (1995).
22. Maier, V.W., and Saupe, A. *Z. Naturforschg.* **15a**, 287-292 (1960).
23. Brochard, F., Jouffroy, J., and Levinson, P. *J. Physique* **45**, 1125-1136 (1994).
24. Leewis, C.M., Jong, A.M. de, IJzendoorn, L.J. van, and Broer, D. J. *J. Appl. Phys.* **95**, 4125-4139 (2004).
25. More precisely: in the pseudo steady state approximation the rate of change of the radical concentration is much smaller than the rate of change of the monomer concentration.
26. Atkins, P. *Physical Chemistry*, Oxford University Press, Oxford (1990).
27. Tompa, H. *Polymer solutions*, Butterworth, London (1956).

Chapter 5

Quantification of the input parameters of the photo-enforced stratification model

5.1 Introduction

The photo-enforced stratification (PES) process is a complex process in which the combination of photopolymerization-induced diffusion^{1,2} and polymerization-induced phase separation^{3,4} ultimately results in the formation of stratified LC/polymer morphologies. In Chapter 4, the thermodynamic and kinetic equations of these processes have been combined into a numerical model. In this chapter, the fine-tuning of the model equations on the K15/IBoMA/stilbene-dimethacrylate system will be presented, as well as the determination of the model input parameters. The final comparison between the PES model calculations and a set of experiments based on the K15/IBoMA/stilbene-dimethacrylate material system will be described and discussed in Chapter 6.

The PES model consists of two distinct components, a reaction-diffusion model and a polymerization-induced phase separation (PIPS) model. Figure 5.1 shows the flow chart of the reaction-diffusion model and Figure 5.2 shows the equations that are solved by the PIPS model. The required input parameters are also indicated in Figures 5.1 and 5.2. Based on their nature, the input parameters can be divided into four categories:

1. The variable input parameters:

These are the material independent input parameters that can be chosen freely, which are the temperature (T), the initial composition of the LC/monomers mixture, i.e. $\phi_{M,n}^0$ and $\phi_{LC,n}^0$ and the thickness of the layer d .

2. The physical input parameters that can be determined by measurement:

The polymerization rate constants for propagation k_p and termination k_t do not require to be determined individually. Instead the overall value for the term $k_p/\sqrt{k_t}$ can be determined by photo-DSC experiments. The monomer diffusion constant D_M as a function of the conversion can be determined by NMR spectroscopy. The light absorbed by the photo-initiator as a function of the position n in the layer ($I_a(n)$) can be calculated once the emission spectrum of the UV source and the absorption spectra of the photo-initiator and UV absorber have been established.

The determination of the nematic-isotropic transition temperature (T_{NI}) of the LC/monomers mixture as a function of the LC fraction will be treated in detail in Chapter 6.

3. The material related input parameters:

These input parameters can be obtained by calculation or from the literature. The Flory-Huggins interaction parameters (χ) can be calculated via the solubility parameters of the components, which in turn can be obtained via Hoy's system. The monomer volume (r_M), the LC volume (r_{LC}), and the monomer functionality (f) are material properties. In polymerization chain reactions, the volume of the polymer (r_P) can in general be taken as infinitely large with respect to r_M and r_{LC} . The initiation quantum yield of the photo-initiator (ϕ_{mi}) can be found in the literature.

The efficiency factor ε expresses the fraction of elastically effective network chains. The determination and relevance of this factor will be treated in Chapter 6.

4. The variable input parameters related to the mathematics of the calculations:

These are the segment size (Δz) and the time-steps (Δt) in the numerical calculations. These input parameters have been discussed in Chapter 4.

In this chapter the focus will be on the physical and material related input parameters. Alternatively, the input parameters can be grouped according to the equations describing the physical processes in which they play a role. For a better overview, the determination of the physical and material related input parameters and the resulting fine-tuning of the equations will be treated in this way.

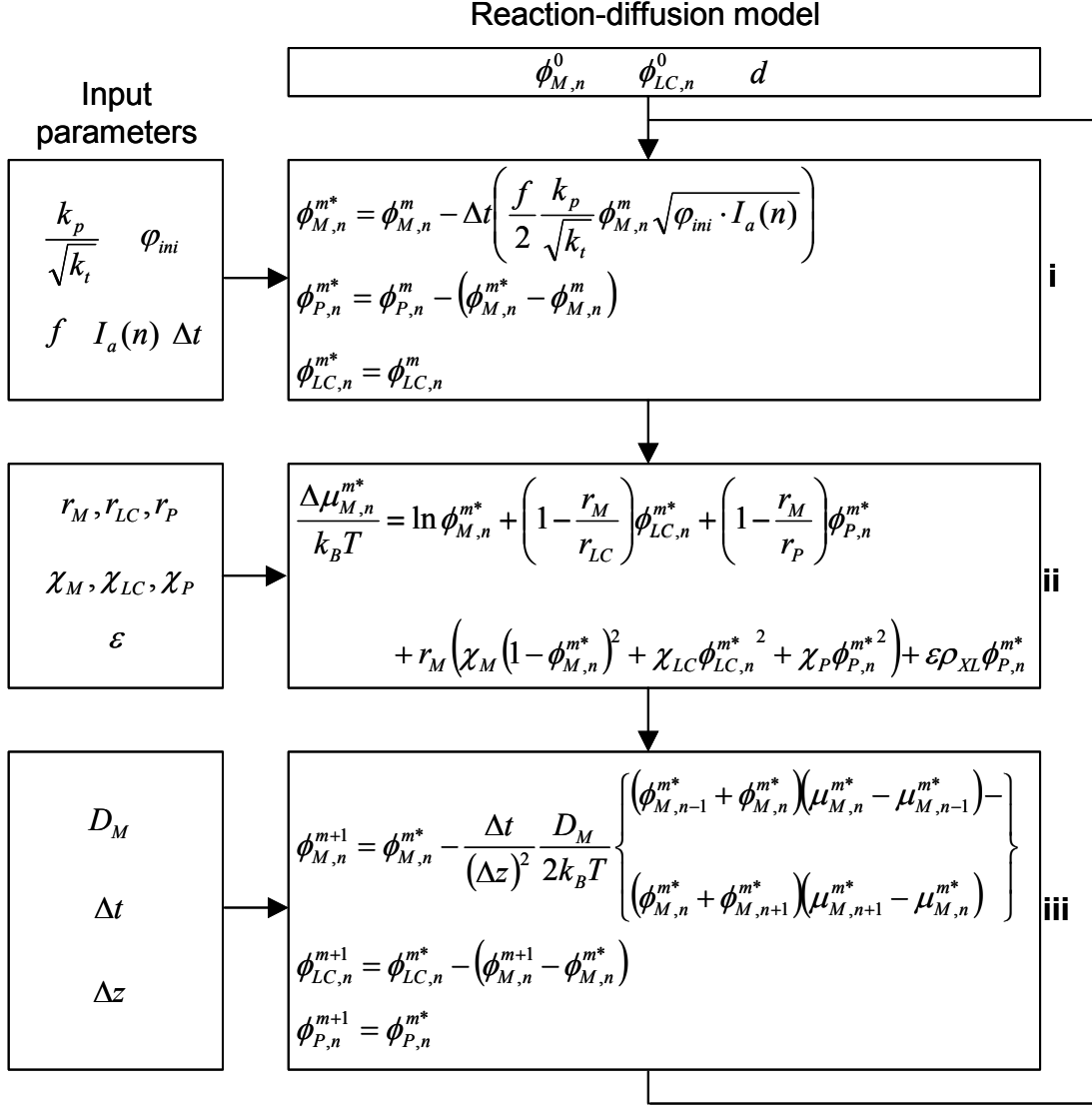


Figure 5.1: Flow chart of the numerical reaction-diffusion model (monomer-chemical-potential-driven, see Chapter 4). The variable input parameters are the initial volume fractions of the monomer (ϕ_M) and the LC (ϕ_{LC}) at $t = 0$ and the layer thickness d . The model contains three main building blocks: (i) The polymerization step, (ii) calculation of the chemical potentials and (iii) the diffusion step. For each of the building blocks the required input parameters are indicated. (i) k_p and k_t are polymerization rate constants, ϕ_{ini} is the quantum efficiency of the photoinitiator, f is the monomer functionality, $I_a(n)$ is the intensity gradient of absorbed UV-light by the photoinitiator and Δt is the time step (ii) r_i are the component sizes, χ_i are the Flory-Huggins interaction parameters and ε is the fraction of effective crosslinks. (iii) D_M is the diffusion coefficient and Δz is the segment thickness.

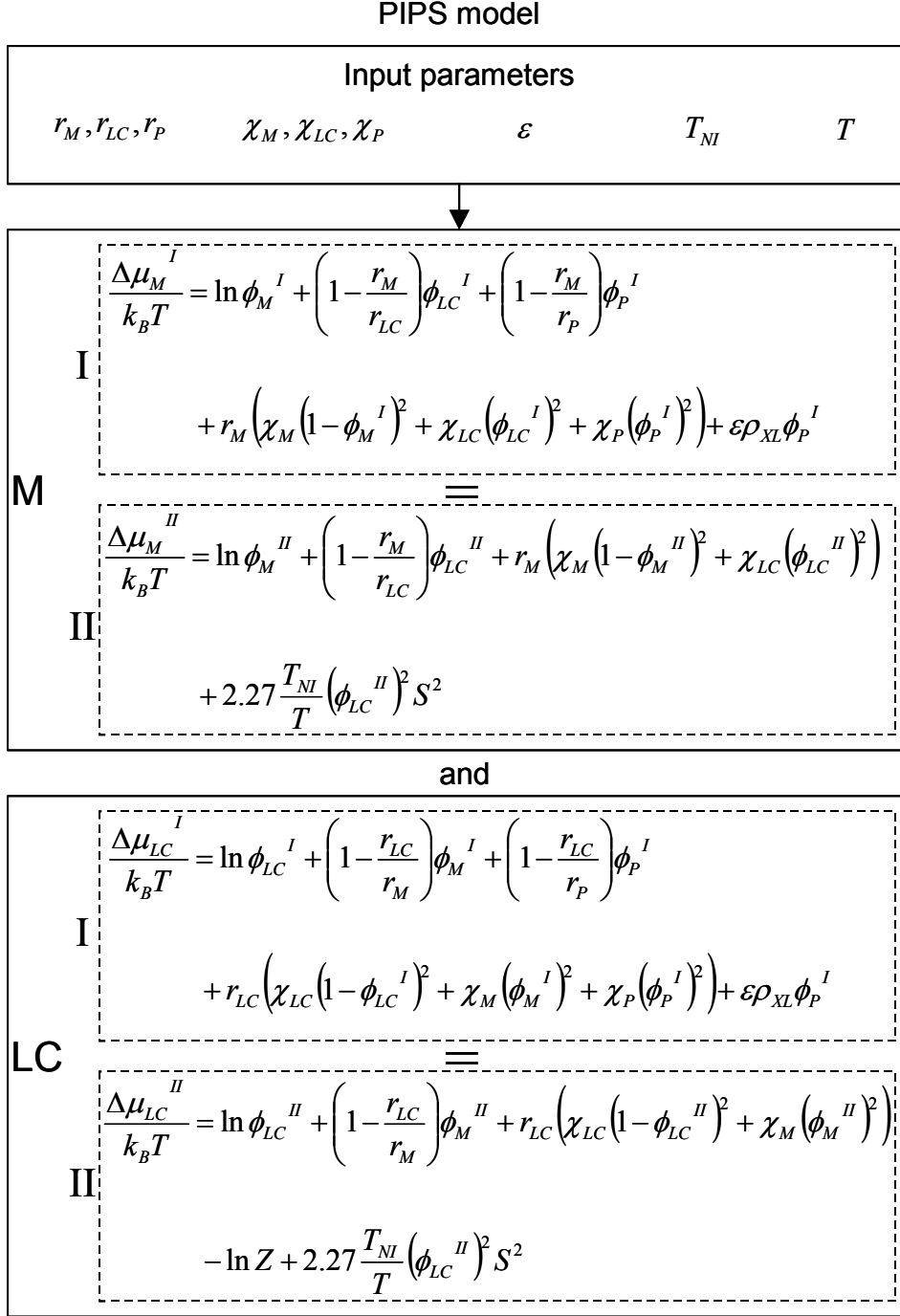


Figure 5.2: PIPS model. Chemical potentials of the monomer and the LC in the polymer-rich (I) and in the liquid phase (II). Also the required input parameters are indicated: r_i are the component sizes, χ_i are the Flory-Huggins interaction parameters, ε is the fraction of effective crosslinks, T_{NI} the nematic-isotropic temperature of the pure LC and T the process temperature.

5.2 Experimental section

5.2.1 Chemicals

n-Pentylcyanobiphenyl (K15) was purchased from Merck (Darmstadt, Germany). Isobornylmethacrylate (IBoMA) was purchased from Mitsubishi Chemicals (Japan) and used without further purification. Dimethoxyphenylacetophenone (DMPA, Irgacure 651), used as the photo-initiator, was obtained from Ciba Specialty Chemicals (Basel, Switzerland). 4,4'-di-(6-methacryloyloxyhexyloxy)-3-methylstilbene (*stilbene-dimethacrylate*) and bisphenol-A-di-(6-methacryloyloxyhexyloxy)-ether (*bisphenol-A-dimethacrylate*) were synthesized in-house by Dr. J. Lub and Ing. W. Nijssen at Philips Research (Eindhoven, The Netherlands). The structural formulas of the compounds are depicted in Figure 5.3.

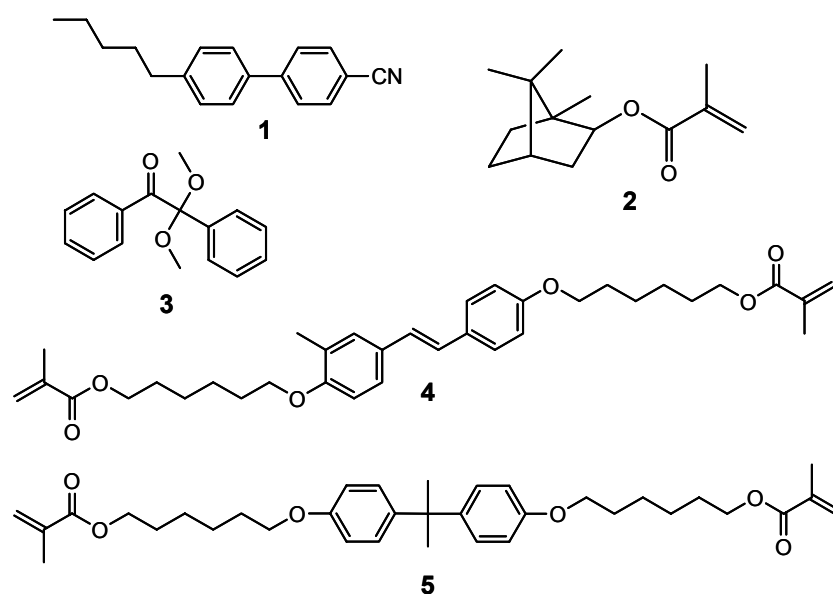


Figure 5.3: (1) *n*-Pentylcyanobiphenyl, (2) isobornylmethacrylate, (3) dimethoxyphenylacetophenone (DMPA, Irgacure 651) photo-initiator, (4) stilbene-dimethacrylate, (5) bisphenol-A-dimethacrylate.

5.2.2 DSC measurements

Various blends of monomers and LC were photopolymerized in a differential scanning calorimeter (DSC 7, Perkin Elmer). A 4W Philips TL08 (0.3 mW·cm⁻²) UV lamp is used. The double bond conversion as function of time is calculated via the following procedure: Integration of the heat flux over the whole irradiation period provides the total heat of reaction. The achieved end conversion can be derived by dividing the total heat of reaction by the heat potentially generated when all double (C=C) bonds would have reacted. The latter is calculated via multiplication of the

total number of double bonds initially present in the sample with the molar heat of C=C bonds, which is 56 kJ for methacrylates.⁵ Via multiplication of the end conversion with the partial integral of the heat flux as function of time (taking the integral over the whole irradiation period 1) the conversion versus time is obtained.

5.2.3 NMR measurements

The samples were prepared by transferring approximately 0.5 ml of the reaction mixture into an NMR-tube (Aldrich) with a diameter of 5 mm. For locking purposes a coaxial insert with deuterated tetrachloroethane (C₂D₂Cl₄) was brought into the NMR-tube, which was subsequently sealed (Parafilm, SPI supplies). The preparation of the samples was performed in a glove box to avoid oxygen being present in the tube. The presence of oxygen would inhibit the polymerization.

The reaction mixture was exposed to UV-light for subsequent short periods of approximately 30 s (4W Philips TL08, 1 mW·cm⁻²). Between the exposure steps, the conversion and the diffusion coefficients (*D*) of the liquid crystal and the monomers were determined with NMR. From the collected data a plot was made of the diffusion coefficients as a function of the degree of polymerization in the sample.

All samples were measured at 303 K on a 7 Tesla Bruker Avance 300-MHz spectrometer, making use of a 5 mm Inverse Broad Band probe, equipped with a Z-gradient with a maximum gradient strength of 54 G·cm⁻¹. The field gradient was calibrated using a 99.9% D₂O sample. At 25°C the diffusion coefficient of H₂O was measured to be 1.9·10⁻⁹ m²·s⁻¹, which corresponds to values reported in literature.⁶ For the determination of the conversion of the sample, a ¹H-spectrum with 16 averages and a delay-time of 5 seconds was recorded. To determine the diffusion coefficients, diffusion weighted NMR measurements were performed.⁷ A stimulated echo sequence using bipolar gradients was used.⁶ The amount of diffusion weighting was varied by increasing the gradient strength from 2% to 95% of the maximum strength in 16 linear increments. The component specific signal intensities decay upon increasing gradient strength. The respective diffusion coefficients can be deduced by fitting these decay curves with the Stejskal-Tanner equation.^{6,7}

5.3 Results and discussion

5.3.1 Input parameters for the polymerization step

In this paragraph the input parameters will be determined for the polymerization step in the reaction-diffusion model. In the model, the monomer volume fraction is calculated via

$$\frac{\phi_{M,n}^{m*} - \phi_{M,n}^m}{\Delta t} = -\frac{f}{2} \frac{k_p}{\sqrt{k_t}} \phi_{M,n}^m \sqrt{\phi_{ini} I_a(n)} \quad (5.1)$$

The input parameters are the monomer functionality (f), rate constants k_p and k_t , the quantum efficiency of the photoinitiator (ϕ_{ini}) and the intensity gradient of absorbed UV-light ($I_a(n)$).

Determination of $k_p/\sqrt{k_t}$ and ϕ

The polymerization kinetics of the K15/IBoMA/bisphenol-A-dimethacrylate/DMPA system was studied by means of photo-DSC. Bisphenol-A-dimethacrylate (see Figure 5.3) was used as the crosslinking component, which is a non-absorbing substitute for stilbene-dimethacrylate. In this way the photopolymerization behavior of the PES mixture was mimicked in the absence of a UV gradient. This provides a homogeneous polymerization of the reaction mixtures, while the overall chemical composition of the mixture hardly changes. The solubility parameters of stilbene-dimethacrylate and bisphenol-A-dimethacrylate, calculated from group contributions,¹⁹ are almost equal: 19.6 versus 19.3 J^{1/2}·cm^{3/2}. Therefore, the intermolecular interactions in the reaction mixture are expected to be unchanged.

The DSC measures the exothermic heat flux of the polymerization reaction, which is proportional to the reaction rate. In order to mimic the PES process conditions as much as possible, the experiments were conducted with the same TL08 UV light source. The intensity of this lamp (0.3 mW·cm⁻²) was chosen within the range of intensities applied in the PES experiments (0.15-0.8 mW·cm⁻²). The influence of the LC concentration was investigated by mixing K15 and the monomers in various ratios while keeping the ratio between IBoMA and bisphenol-A-methacrylate constant at 23:1. In this way the overall chemical composition of the resulting polymer is equal for each of the mixtures provided that the same end conversion and the same crosslink density is reached. All mixtures contained 0.5 wt.% DMPA photo-initiator and were photopolymerized at 20°C.

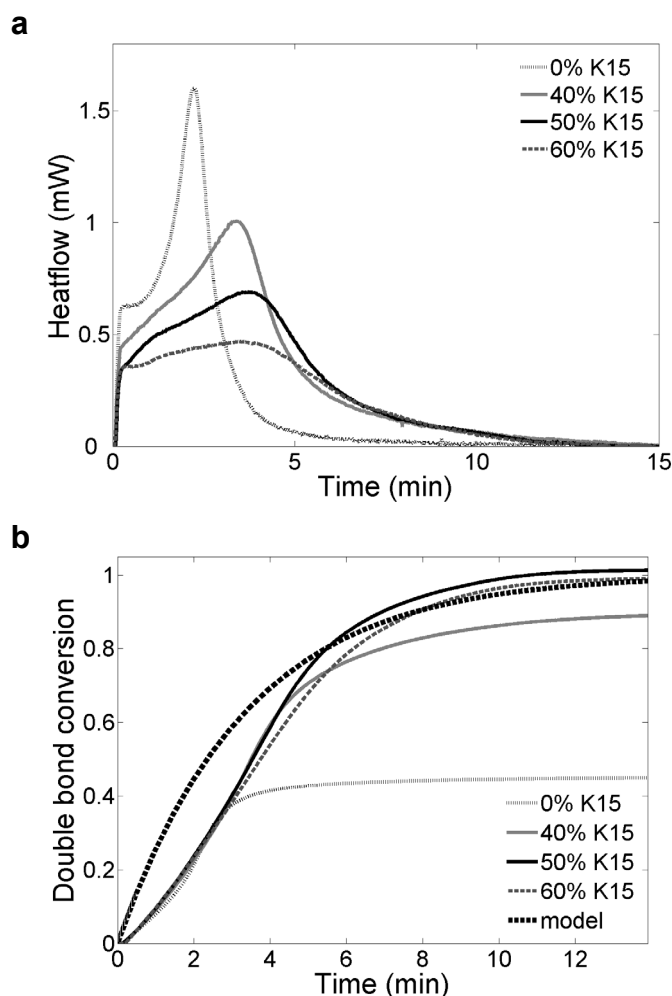


Figure 5.4: a) DSC curves after baseline correction of K15/IBoMA/bisphenol-A-dimethacrylate for various K15 concentrations. b) The double bond conversion versus time as derived from the DSC curves and a calculated model curve assuming steady-state conditions.

Figure 5.4a shows the DSC curves after baseline correction for different mixtures containing between 0 wt.% and 60 wt.% K15. The pure blend of monomers (0% K15) shows a rapid increase of the polymerization rate soon after the start of the reaction. This is a typical behavior for chain-addition crosslinking polymerization of undiluted monomers.⁸ The rapid increase is referred to as the auto-acceleration effect (also known as the Tromsdorff- or gel-effect). It occurs due to mobility limitations of the growing polymer radicals. Because of vitrification and an increased viscosity, termination is suppressed. Since monomer diffusion is much less hindered, the radical population is increased, which results in an enhancement of the polymerization rate. Upon a further increase of the viscosity, also the monomer mobility drops, limiting the diffusion of the double bonds to the reactive chain ends. As a result of this so-called auto-deceleration of the polymerization reaction usually a final conversion of less than 100% is reached. Through integration of the DSC curves the development of

the conversion can be obtained, which is depicted in Figure 5.4b. For the pure monomer blend a conversion of approximately 40% is observed, signifying that still 60% of unreacted double bonds is present in the polymer matrix. When 40 wt.% K15 is added to the reaction mixture a reduced auto-acceleration effect is observed. K15 acts as a solvent and in a later stage of the polymerization as a plasticizer, which lowers the viscosity of the reaction mixture and enhances the diffusional mobility of the monomer, also at higher conversions. It has been shown in the literature that a lower viscosity leads to an increase of termination rate^{9,10} and a consequent suppression of the auto-acceleration peak.^{11,12} Adding more K15 results in a further suppression of the auto-acceleration effect. It also affects the end conversion: Figure 5.4b shows that increasing the K15 fraction to 50 wt.% or above (typically used in the photo-enforced stratification process) leads to end conversions near 100 % after approximately 15 minutes. Determining the end conversion by the integration of the relatively low DSC-signals (below 1 mW) yields an error of $\pm 5\%$, because of the large influence of the baseline-correction on the result. The polymerization behavior is modeled assuming steady state conditions,¹³ see Chapter 4. The polymerization rate R_p is given by

$$R_p = \frac{k_p}{\sqrt{k_t}} [C=C] \sqrt{\varphi_{ini} \int_{\lambda} \varepsilon_{PI}(\lambda) I_0(\lambda) d\lambda [PI]} \quad (5.2)$$

where k_p and k_t are the rate constants for propagation and the termination in $\text{l}\cdot\text{mol}^{-1}\cdot\text{s}^{-1}$, $[C=C]$ is the double bond concentration ($\text{mol}\cdot\text{l}^{-1}$), φ_{ini} the quantum yield for initiation, $\varepsilon_{PI}(\lambda)$ the extinction of the DMPA photo-initiator in $\text{l}\cdot\text{mol}^{-1}\cdot\text{cm}^{-1}$ (see Figure 5.6a) and $[PI]$ its concentration in ($\text{mol}\cdot\text{l}^{-1}$). $I_0(\lambda)$ is the light intensity profile of the UV-source in $\text{Einsteins}\cdot\text{m}^{-2}\cdot\text{s}^{-1}$ (see Figure 5.6a). The value for φ_{ini} ($= 0.4$) was obtained from the literature¹⁴ and assumed independent of the wavelength λ . The double bond conversion as function of time is calculated via integration of Eq. 5.2 and is depicted in Figure 5.4b. The value of $k_p\sqrt{k_t}$ used in these calculations is not based on experimentally determined values for k_p and k_t but it is chosen such that beyond 5 minutes polymerization time the calculated curve is close to the experimental curves for the reaction mixtures containing 40 – 60 wt.% K15. The calculated curve is optimized for the region beyond 5 minutes because this is the region of interest: In Chapter 2 it was already shown that in PES under similar exposure conditions phase separation occurs at times well above 5 minutes. The resulting value for $k_p\sqrt{k_t}$ is $1.5\sqrt{\text{l}\cdot\text{mol}^{-1}\cdot\text{s}^{-1}}$, which will be implemented in the reaction diffusion model. As a result of the fitting, the double bond conversion is overestimated at times below 5 minutes. Taking into account polymerization effects such as volume relaxation¹⁵ and the auto-

acceleration-effect¹⁶ would lead to a more precise description. However, it would require extensive experimental effort to quantify the necessary input parameters.

Determination of f

The experimental K15/IBoMA/stilbene-dimethacrylate and K15/IBoMA/bisphenol-A-dimethacrylate systems contain mono-vinyls *and* di-vinyls in a 23:1 molar ratio. In the model the monomer mixture has to be approximated by a single monomer system with one functionality. In this case the monomer system has to be approximated by either a mono-vinyl monomer ($f = 2$) or a di-vinyl monomer ($f = 4$). For both types there is a different relation between the monomer conversion and the double bond conversion: For a mono-vinyl monomer the monomer conversion α into polymer is equal to the double bond conversion x , i.e. $\alpha = x$. For a di-vinyl the development of the monomer conversion as function of the double bond conversion is generally approximated with a mean field estimate, which results in $\alpha = 1 - (1 - x)^2$. To determine which of these relations is the best approximation of the experimental system, the relation between monomer conversion and double bond conversion has been calculated for mono-vinyl/di-vinyl mixtures containing various di-vinyl fractions (ϕ_{XL}) via

$$\alpha = x(1 - \phi_{XL}) + x(2 - x)\phi_{XL} \quad (5.3)$$

The results have been plotted in Figure 5.5. The figure shows that for mono-vinyl/di-vinyl mixtures containing less than 10 mol% di-vinyl the monomer conversion is close to linear with the double-bond conversion. The IBoMA:stilbene-dimethacrylate ratio in the K15/IBoMA/stilbene-dimethacrylate system is 23:1 (4 mol% stilbene-dimethacrylate), a linear dependence between monomer conversion and double-bond conversion ($f = 2$) will be implemented in the model calculations.

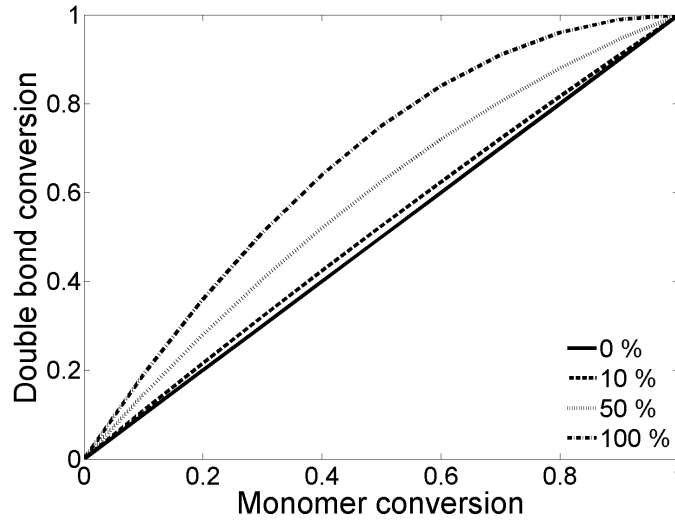


Figure 5.5: Relation between monomer conversion and double bond conversion for various percentages of di-vinyl monomer in a mono-vinyl/di-vinyl mixture.

Determination of $I_a(n)$

The absorbed light intensity $I_a(n)$ as function of position n at the onset of irradiation is calculated for the K15/IBoMA/stilbene-dimethacrylate/DMPA mixture. The absorbed light intensity $I_a(z)$ is obtained by taking the intensity profile of the UV source $I_0(\lambda)$ as well as the extinction curves $\varepsilon_{PI}(\lambda)$ and $\varepsilon_S(\lambda)$ of the photo-initiator and the UV absorber into account via

$$I_a(z) = \int_{\lambda} \varepsilon_{PI}(\lambda) I_0(\lambda) 10^{-\varepsilon_S(\lambda)[S]z} d\lambda [A] \quad (5.4)$$

See Figure 5.6a for the absorption spectra of DMPA (Irgacure 651) and stilbene-dimethacrylate and the intensity profile of the UV-source ($I_0 = \int I_0(\lambda) d\lambda = 0.3 \text{ mW}\cdot\text{cm}^{-2}$). The calculated normalized intensity gradient $I_a(z)/I_a(0)$ is depicted in Figure 5.6b. The intensity gradient is assumed to stay unchanged during the process irrespective of the compositional changes in the layer. In the calculation of the intensity gradient $I_a(z)$ in the stratification experiments ($I_0 = 0.8 \text{ mW}\cdot\text{cm}^{-2}$), $I_0(\lambda)$ is given by the intensity profile in Figure 5.6a multiplied with a factor of $0.8/0.3$. $I_a(n)$ is the discretized version of $I_a(z)$.

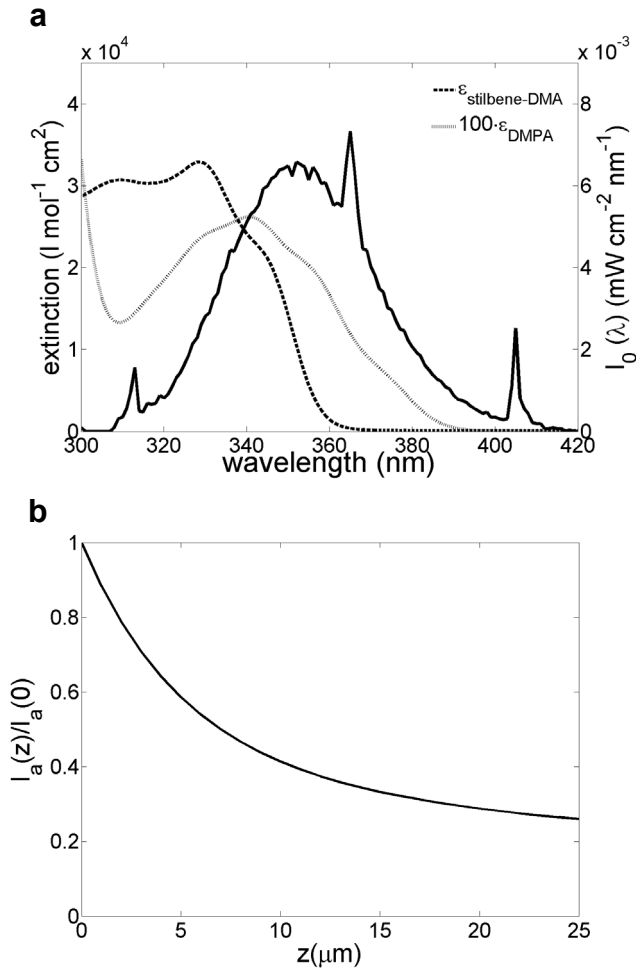


Figure 5.6: a) Absorption spectra of stilbene-dimethacrylate and DMPA ($\epsilon * 100$) and the intensity distribution of the UV source at approximately 10 cm from the lamp. b) The normalized intensity gradient in a 25- μm layer at the onset of irradiation

5.3.2 Input parameters for the chemical potentials

The chemical potentials consist of a mixing term, an elastic term and a nematic term (see Chapter 4). The mixing term requires input of the component sizes r_M , r_{LC} and r_P as well as the Flory-Huggins interaction parameters χ_M , χ_{LC} and χ_P . The mixing contribution to the monomer chemical potential is given by

$$\frac{\Delta\mu_M^{mix}}{k_B T} = \ln \phi_M + \left(1 - \frac{r_M}{r_{LC}}\right) \phi_{LC} + \left(1 - \frac{r_M}{r_P}\right) \phi_P + r_M (\chi_M (1 - \phi_M)^2 + \chi_{LC} \phi_{LC}^2 + \chi_P \phi_P^2) \quad (5.5)$$

and correspondingly the mixing contribution to the liquid crystal chemical potential ($\Delta\mu_{LC}^{mix}$) is obtained. The χ parameters are given by

$$\chi_M = \frac{1}{2}(\chi_{M-LC} + \chi_{M-P} - \chi_{LC-P}) \quad (5.6)$$

and in the same way χ_{LC} and χ_P are obtained. The sizes of the monomer molecules and the LC in the experimental system are derived with the aid of space filling models and the interaction parameters are calculated using the estimated solubility parameters of the various components. The input for the elastic and nematic terms in the chemical potentials will be discussed in Chapter 6.

Molecular dimensions

Figure 5.7 depicts the space filling models of K15, IBoMA and stilbene-dimethacrylate in their minimized free-energy conformation. Some typical dimensions are shown in Table 5.1. It shows that the main components in the mixture, K15 and IBoMA, have a similar size. The size of stilbene-dimethacrylate is significantly larger than that of K15 and IBoMA, but since the stilbene-dimethacrylate:IBoMA ratio is only 1:23 its contribution to the mixing term in the chemical potentials is neglected. Therefore, as a first approximation in the model, the sizes of the monomer and the LC will be chosen equal: $r_M = r_{LC} = 1$.

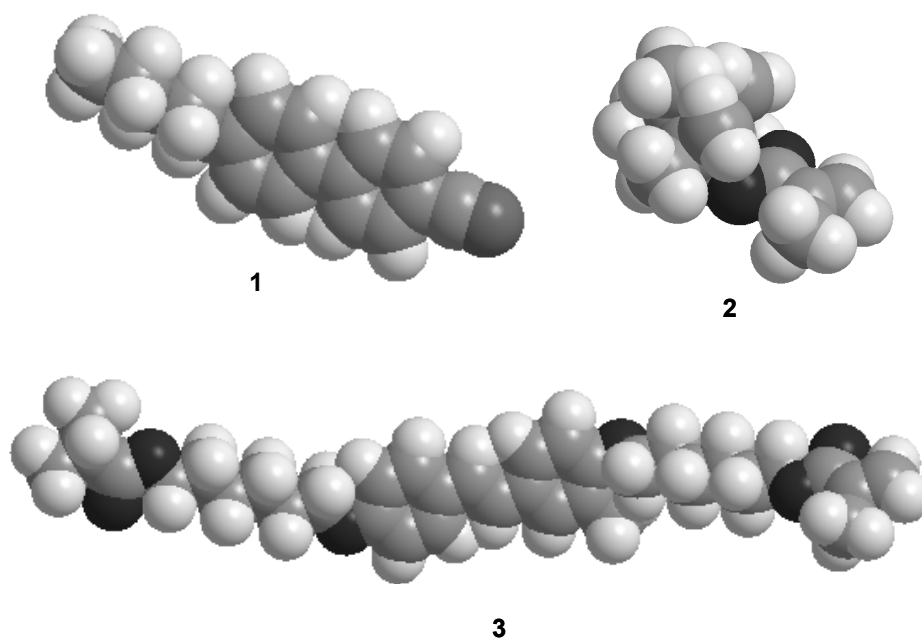


Figure 5.7: Space filling models: (1) K15, (2) IBoMA, (3) stilbene-dimethacrylate.

Table 5.1: Molecular dimensions of K15, IBoMA and stilbene-dimethacrylate.

	Molecular volume (nm ³)	Connolly molecular area ¹⁷ (nm ²)
K15	1.6	2.8
IBoMA	1.3	2.2
Stilbene-dimethacrylate	3.5	6.2

Flory-Huggins interaction parameters

The *enthalpic* component of the Flory Huggins interaction parameter (χ_H) between the components in the reaction-mixture is obtained via Equation 5.7 once the solubility parameters δ of the components are estimated.^{5,18}

$$\chi_H = \frac{V_1}{RT}(\delta_1 - \delta_2)^2 \quad (5.7)$$

where V_1 is the molar volume of the component, and δ_1 and δ_2 are the respective solubility parameters of the component and the co-polymer. χ_H is used as an approximation of the Flory Huggins parameter χ . In Table 5.2 the δ 's¹⁹ of K15, the monomers and the poly(IBoMA-co-stilbene-dimethacrylate) are listed. For the calculation of δ of the co-polymer the IBoMA/stilbene-dimethacrylate ratio has been taken as 23:1, i.e. the initial mole ratio in the starting mixture.²⁰ Based on the calculations of the respective χ_H 's, the mutual Flory Huggins interaction parameters between the monomers and the co-polymer will be taken zero, $\chi_{M-P} = 0$, whereas the respective interaction parameters for the LC/polymer interaction and the LC/monomer interaction will be taken $\chi_{LC-M} = \chi_{LC-P} = 0.5$.

Table 5.2: Calculated¹⁹ solubility parameters (δ) and Flory Huggins interaction parameters $\chi_{p,c}$ (enthalpic contribution) between and poly-(isobornylmethacrylate-co-stilbene-dimethacrylate) and the various components

Compound	δ	$\chi_{p,c}$
K15	21	0.5
IBoMA	19	0
Stilbene-dimethacrylate	20	0.1
Co-polymer (23:1)	19	0

Based on the calculations above the mixing terms for the monomer and LC chemical potentials become

$$\frac{\Delta\mu_M^{mix}}{k_B T} = \ln\phi_M + \phi_P + 0.5\phi_{LC}^2 \quad (5.8)$$

and

$$\frac{\Delta\mu_{LC}^{mix}}{k_B T} = \ln\phi_{LC} + \phi_P + 0.5(1 - \phi_{LC})^2 \quad (5.9)$$

5.3.3 Input parameters for the diffusion step

For input in the reaction-diffusion model conversion resolved diffusion coefficients (D) were established with NMR. Figure 5.8 shows the proton spectra of the mixture (50 wt.% K15, 44.5 wt.% IBoMA, 5 wt.% bisphenol-A-dimethacrylate, 0.5 wt.% photoinitiator) and the individual components. The component specific proton signals (H1-H6) that are used in the measurements are indicated in the spectra and correlated to the proton positions in the molecules. For the determination of the conversion the signals of H1 and H2 (double-bond signals) were integrated using the integral of H6 (K15) as an internal reference.

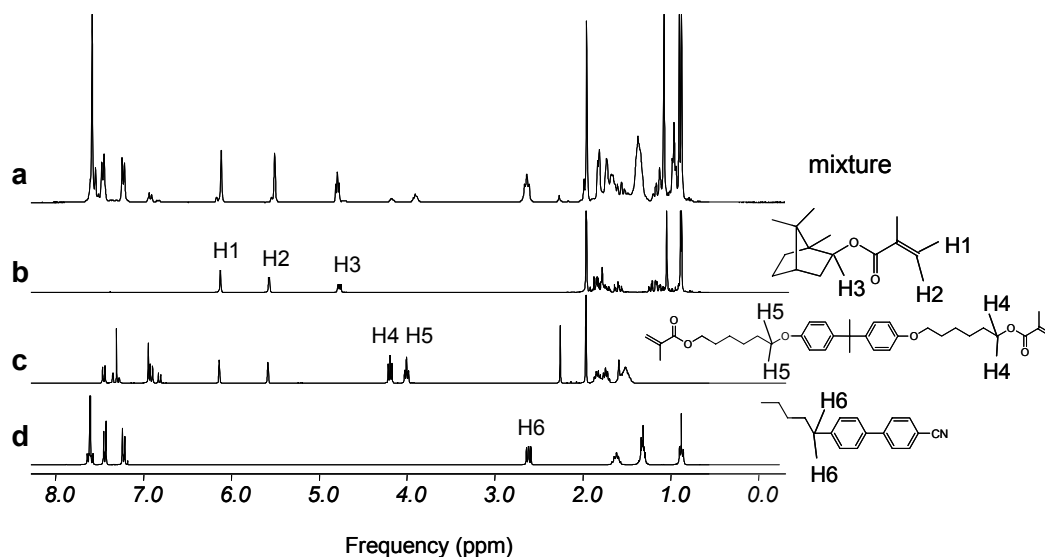


Figure 5.8: Proton spectra: a) mixture (50 wt.% K15, 44.5wt.% IBoMA, 5wt.% bisphenol-A-dimethacrylate, 0.5 wt.% photoinitiator). b) IBoMA. c) bisphenol-A-dimethacrylate. d) K15. The component specific proton signals (H1-H6) as well as the position of the involved protons in the molecules are also indicated.

The diffusion coefficients of the components in the initial K15/IBoMA/stilbene-dimethacrylate system as well as in the initial K15/IBoMA/bisphenol-A-dimethacrylate system were measured. The results are shown in Table 5.3. It can be seen that the diffusion coefficients of K15 and IBoMA are similar ($\approx 7 \cdot 10^{-11} \text{ m}^2 \cdot \text{s}^{-1}$ at 303 K). Also the diffusion coefficients stilbene-dimethacrylate and bisphenol-A-dimethacrylate in both mixtures are equal ($3 \cdot 10^{-11} \text{ m}^2 \cdot \text{s}^{-1}$) which is a further indication of the similarity of the two components.

Table 5.3: Diffusion constants of K15, IBoMA, stilbene-dimethacrylate and bisphenol-A-dimethacrylate in various reaction mixtures at 303 K.

Component	K15/IBoMA/ stilbene- dimethacrylate*, 50wt.% K15 D (*10 ⁻¹¹ m ² ·s ⁻¹)	K15/IBoMA/ bisphenol-A- dimethacrylate*, 50wt.% K15 D (*10 ⁻¹¹ m ² ·s ⁻¹)	K15/IboMA/ bisphenol-A- dimethacrylate**, 40wt.% K15 D (*10 ⁻¹¹ m ² ·s ⁻¹)	K15/IBoMA/ bisphenol-A- dimethacrylate**, 60wt.% K15 D (*10 ⁻¹¹ m ² ·s ⁻¹)
K15	6.9	7.3	8.5	6.2
IBoMA	6.4	7.4	8.5	6.3
stilbene- dimethacrylate	2.9	--	--	--
bisphenol- dimethacrylate	--	3.0	not measured	not measured

* IBoMA:crosslinker ratio 23:1 (mol/mol), ** 0.5 wt.% DMPA, IBoMA:crosslinker ratio 23:1 (mol/mol)

The diffusion coefficients of the main components in the K15/IBoMA/bisphenol-A-dimethacrylate/DMPA mixture, K15 and IBoMA, were measured as a function of the conversion. As was mentioned earlier, the absorption of the bisphenol-A-dimethacrylate does not overlap with the absorption spectrum of the DMPA photoinitiator and therefore a homogeneous UV irradiation of the sample was obtained. Figure 5.9 depicts the diffusion coefficient of IBoMA. The diffusion coefficient of K15 was found to be equal to that of IBoMA (within $1 \cdot 10^{-12} \text{ m}^2 \cdot \text{s}^{-1}$), independent of the conversion. The error in the measured value of the conversion increases at higher conversions due to peak broadening in the NMR signals. An explanation for this is the increase of the viscosity of the reaction mixture.²¹ The error in the values of the diffusion coefficient is estimated based on duplicate measurements. Below 40% conversion the error is $\pm 0.2 \text{ m}^2 \cdot \text{s}^{-1}$. At conversions above 40% the error becomes larger: $\pm 0.4 \text{ m}^2 \cdot \text{s}^{-1}$ due to a decrease of signal-to-noise-ratios (SNR). The decay of the diffusion coefficient is not dramatic (less than two decades), which is attributed to the presence of LC in the reaction mixture. The LC lowers the

viscosity of the mixture such that the diffusion rates stay relatively high with respect to polymerized pure monomers. As a reference it was attempted to measure the diffusion coefficients of pure IBoMA. However, already after conversions of a few percent the diffusion coefficients could not be measured due to low SNR, which indicates a much steeper decay of the diffusion coefficient.

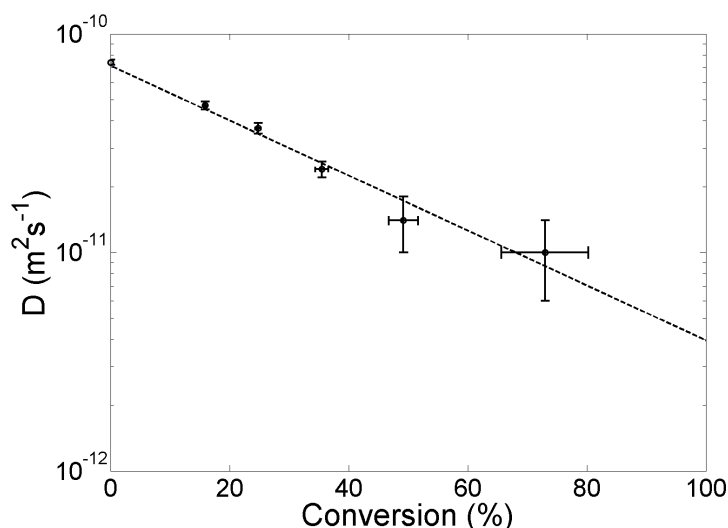


Figure 5.9: The conversion resolved diffusion coefficient of IBoMA fitted with a mono-exponential. The diffusion coefficients of K15 were identical to the diffusion coefficients of IBoMA (within $1 \cdot 10^{-12} \text{ m}^2 \text{ s}^{-1}$).

The influence of the initial composition was investigated further. It was found that the diffusion coefficients of K15 and IBoMA become lower upon higher K15 fractions (compare mixtures with 40, 50 and 60 wt.% K15 in Table 5.3). Although a trend was observed that upon higher LC fractions the decay of the diffusion coefficients on increasing conversion becomes less steep, the differences were marginal. Therefore, as a first approximation in the reaction-diffusion model, the diffusion coefficient will be considered independent of the LC fraction in the 40-60 wt.% K15 region.

Figure 5.9 shows an exponential fit of the diffusion coefficients of IBoMA in the 50 wt.% K15 sample as function of the double bond conversion. Using the approximation that in the K15/IBoMA/bisphenol-A-dimethacrylate system due to the low crosslinker fraction the monomer conversion is linear with the double bond conversion (see Par. 5.3.1), the following relation between the diffusion coefficient and the polymer fraction is entered into the model calculations:

$$D_n^m = D_0 e^{-\frac{\phi_{P,n}^m}{C}}, \quad D_0 = 7 \cdot 10^{-11} \text{ m}^2 \text{ s}^{-1}, C = 0.35 \quad (5.10)$$

In which D_0 is the diffusion coefficient at zero polymer fraction and C a constant.

5.4 Conclusions

To enable the comparison of the numerical PES model with experiments, input parameters of the K15/IBoMA/stilbene-dimethacrylate/DMPA and the K15/IBoMA/bisphenol-A-dimethacrylate/DMPA systems were established via calculations and experiments. Bisphenol-A-dimethacrylate is used as a non-absorbing substitute for stilbene-dimethacrylate in the DSC and NMR experiments to provide for a homogeneous polymerization in the samples.

Although the steady-state model does not account for the auto-acceleration found in the DSC experiments, it is more practical to use than the more sophisticated polymerization models and will not influence the qualitative nature of the PES model results. Input parameter $k_p \sqrt{k_t}$ was chosen such that above 5 minutes polymerization time, which is the region of interest, the calculated double bond conversion is close to experimental results. NMR was found to be a suitable technique to measure conversion resolved diffusion coefficients in the current reaction mixture. The NMR data could be fitted with an exponential, which will be implemented in the reaction-diffusion model.

In both the DSC and NMR measurements a large effect of adding K15 to the monomer mixture is found. It results in a reduction of the auto-acceleration, while the decay of the diffusion coefficients of K15 and IBoMA upon increasing conversions becomes less dramatic. Above 40 wt.% the effect of varying the K15 fraction on the reaction kinetics and the diffusion constants is significantly smaller. Consequently, the derived input parameters for the PES model from DSC and NMR measurements are only valid for K15 fractions above 40 wt.%. Caution has to be taken when experimental mixtures containing lower K15 fractions are modeled, since then the behavior of the system may strongly deviate.

5.5 References and notes

1. Nostrum, C., Nolte, R.J.M., Broer, D.J., Fuhrman, T., and Wendorff, J.H. *Chem. Mater.* **10**, 135-145 (1998).
2. Bowley, C.C., and Crawford, G.P. *Appl. Phys. Lett.* **16**, 2235-2237 (2000).
3. Drzaic, P.S. *J. Appl. Phys.* **60**, 2142-2148 (1986).
4. Doane, J.W., Vaz, N.S., Wu, B.-G., and Zumer, S. *Appl. Phys. Lett.* **48**, 269-271 (1986).
5. Brandrup, J., Immergut, E., and Grulke, E. *Polymer Handbook*, John Wiley & Sons, London (1999).

6. Antalek, B. *Concepts in Magn. Reson.* **14**, 225-258 (2002).
7. Stejskal, E.O., and Tanner, J.E. *J. Chem. Phys.* **42**, 288-292 (1965).
8. Kloosterboer, J.G., and Lippits, G.J.M. *J. Rad. Cur.* **11**, 10 (1984).
9. Benson, S.W., and North, A.M. *J. Am. Chem. Soc.* **81**, 1339 (1959).
10. Kamachi, M., Satoh, J., Liaw, D.J., and Nozakura S.-I *Macromol.* **10**, 501-502 (1977).
11. Schultz, G.V., and Harborth, G. *Macromol. Chem.* **1**, 169, (1947).
12. Louie, B. M., Carratt, G.M., and Soong, D.S. *J. Appl. Pol. Sci.* **30**, 3985-4012 (1985).
13. Odian, G. *Principles of polymerization*, John Wiley & Sons, New York, (1981).
14. Groenenboom, J.C., Hageman, H.J., Overeem, T., and Weber, A.J.M. *Makromol. Chem.* **183**, 281 (1982).
15. Bowman, C.N., and Peppas, N.A. *Macromol.* **24**, 1914-1920 (1991).
16. Goodner, M.D., and Bowman C.N. *Macromol.* **32**, 2491-2499 (1999).
17. Connoly, M.L. *J. Appl. Crystallogr.* **16**, 548-558 (1983).
18. Smith, G.W. *Mol. Cryst. Liq. Cryst.* **225**, 113-130 (1993).
19. The solubility parameters are calculated via Hoy's system: Krevelen, D.W. van, *Properties of Polymers*, Elsevier, Amsterdam, Chapter 7, Table 7.10, (1990).
20. Composition drift as a result of difference in reactivity between IBoMA and stilbene-demethacrylate is neglected.
21. Sanders, J.K.M., and Hunter, B.K. *Modern NMR Spectroscopy*, Oxford University Press, Oxford (1993).

Chapter 6

Investigation of the photo-enforced stratification process: model vs. experiments

6.1 Introduction

The numerical model of the photo-enforced stratification process (PES), described in Chapter 4, is a combination of a reaction-diffusion model and a polymerization-induced phase separation (PIPS) model. The model is based on standard, unperturbed free radical polymerization,¹ diffusion equations,² and equations that were derived by Flory and Huggins (lattice theory),³ Flory, Rehner and Dušek (elasticity of the polymer network),^{4,5} and Maier and Saupe (liquid crystalline behavior of the solvent).⁶ Based on a set of input parameters, such as the initial composition of the LC/monomers mixture, the temperature, and the UV intensity gradient across the layer, the model yields a so-called phase separation line and various polymerization lines which can be plotted in a ternary phase diagram (see Figure 6.1a). The phase separation line denotes the compositions of the LC/monomer/polymer mixture for which two phases, i.e. the polymer-rich phase and the liquid phase, are in equilibrium. The polymerization lines for various z/d positions in the layer (with z being the transversal distance in the layer and d the thickness of the layer; $z/d = 0$ at the bottom of the layer and $z/d = 1$ at the top) represent the local composition of the mixture as a function of the conversion. For polymerization-induced phase separation to occur at a given z/d position in the layer, the corresponding polymerization line must intersect the phase separation line, which can be read in the ternary conversion phase diagram. The diagram shows that the conversion at the intersection decreases with decreasing z/d . An additional plot is constructed to depict the time-of-intersection of the respective polymerization lines and the phase separation line. It shows the z/d position where the corresponding polymerization line intersects the phase separation line as a function of time (see Figure 6.1b). From this plot the onset of phase separation i.e. starting time as well as the position where the phase separation starts can be deduced.

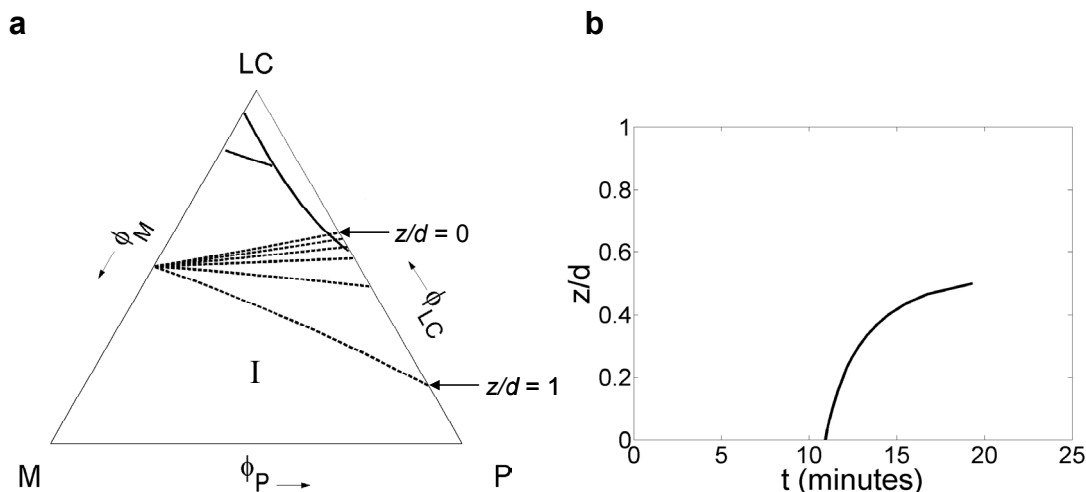


Figure 6.1: a) Results of a PES model simulation, the phase separation line (solid lines enclosing an isotropic-nematic (upper right) and an isotropic-isotropic phase separation area (upper left)) and the polymerization lines for various z/d positions (dashed lines), in a ternary conversion phase diagram. b) The time-of-intersection plot shows the z/d position where the corresponding polymerization line intersects the phase separation line as a function of time. The onset of phase separation takes place in the bottom ($z/d = 0$) of the film, since there the polymerization line intersects the phase separation line first.

In this chapter, the two basic components of the PES model, the reaction-diffusion model and the PIPS model will be checked independently from each other with a set of specific experiments. The model input parameters for the photopolymerization kinetics ($k_p/\sqrt{k_t}$) and diffusion behavior of the LC and the monomers in the system, as well as the interaction parameters (χ 's) have been determined in Chapter 5.

The calculated phase diagram of the initial LC/monomers mixture will be discussed in relation to the experimentally determined nematic-isotropic temperature as function of LC fraction in the initial mixture. Furthermore, the phase separation lines calculated for two different temperatures will be compared to the experimentally determined phase separation lines of the K15/IBoMA/bisphenol-A-dimethacrylate model system. Since in the literature photo-DSC/turbidity measurements have proven to be a useful tool to investigate the phase separation behavior of LC/monomer mixtures,^{7,8} this method will be used to determine the phase separation lines.

Next, the polymerization lines in the ternary diagram, calculated with the reaction-diffusion model, will be compared to the measured concentration profile of K15 as function of time and depth during UV polymerization of the K15/IBoMA/stilbene-dimethacrylate system under PES conditions. This profile will be measured real-time by confocal Raman microscopy.⁹ Confocal Raman microscopy has already proven to be a good and non-evasive method to characterize the stratified morphologies made by the PES process (Chapter 3).

Finally, the PES model will be refined with the input parameters obtained in the preceding experiments and the subsequent simulations will be compared to the photo-enforced stratification behavior of the K15/IBoMA/stilbene-dimethacrylate system as function of the initial K15 fraction.

Formally, the model only describes the PES process until the onset of phase separation and provides the starting time as well as the position where the phase separation starts. After the separation into a two-phase system the model is not longer valid and the times-of-intersection calculated in the other regions of the film do not have a physical meaning. However, comparison of the simulation and experiments will show that the time-of-intersection plot profile provides the utmost important information whether the conditions for stratification have been met and/or that PDLC morphology¹⁰ may arise.

6.2 Experimental section

6.2.1 Chemicals

K15 (n-pentylcyanobiphenyl) was purchased from Merck (Darmstadt, Germany). Isobornylmethacrylate (IBoMA) was purchased from Mitsubishi Chemicals (Japan), and used without further purification. Dimethoxyphenyl acetophenone (DMPA, Irgacure 651), used as the photo-initiator, was obtained from Ciba Specialty Chemicals (Basel, Switzerland). 4,4'-di-(6-methacryloyloxyhexyloxy)-3-methylstilbene (*stilbene-dimethacrylate*) and bisphenol-A-di-(6-methacryloyloxyhexyloxy)-ether (*bisphenol-A-dimethacrylate*) were provided by Johan Lub and Wim Nijssen from Philips Research (Eindhoven, The Netherlands). The chemical structures of the compounds are depicted in Figure 6.2.

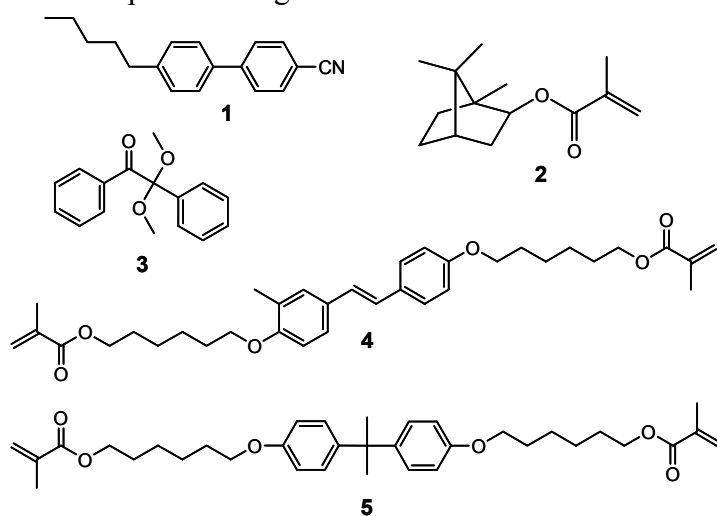


Figure 6.2: The chemical structures of (1) K15, (2) isobornylmethacrylate (IBoMA), (3) dimethoxyphenyl acetophenone (Irgacure 651), (4) stilbene-dimethacrylate, and (5) bisphenol-A-dimethacrylate.

6.2.2 Combined photo-DSC/turbidity measurements

Various LC/monomers mixtures were isothermally photopolymerized in a differential scanning calorimeter (DSC 7, Perkin Elmer, Wellesley, USA). The samples were prepared by applying a droplet of 2 mg in an aluminum DSC cup (Perkin Elmer 0219-0062), normally used as sample lid. The bottom of the cup has two levels: The center area with a diameter of 0.5 cm is deeper than the outer ring. The height difference prevents undesired spreading of the liquids and reproducible circular droplets are obtained with a maximum height of approximately 100 μm . The DSC set-up has been extended with a microscope (Leica Z16, Leica microsystems AG, Wetzlar, Germany) equipped with a camera (Sony DFW-X700, Sony, Japan). The camera was connected to a computer to monitor the onset of turbidity of the sample. Streampix software (Norpix, Montreal, Canada) was used to capture images at 1 s time intervals. Figure 6.3 shows the experimental set-up.

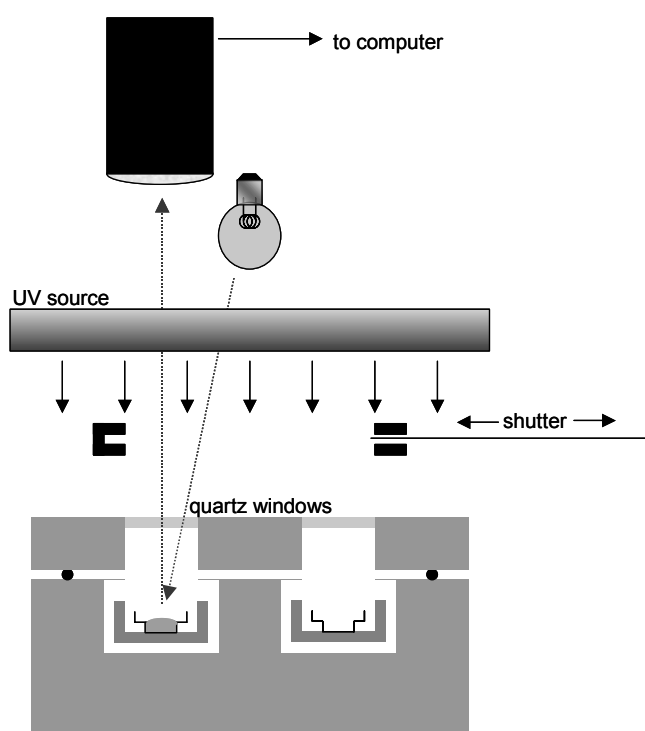


Figure 6.3: Schematic representation of the set-up used for the photo-DSC/turbidity measurements. A standard photo-DSC set-up has been extended with an optical microscope and a light source for probing the onset of the turbidity of the sample.

A 4W Philips TL08 source was centered above the sample and reference cup at a distance of approximately 10 cm resulting in an intensity of 0.3 mWcm^{-2} at the sample position. The white light source for probing the onset of the turbidity of the sample was equipped with a UV cut-off filter, and illuminates both the sample and the

reference cup. Reflection of the light at the bottom of aluminum cup containing the LC/monomers mixture resulted in a bright appearance of the sample. As soon as the sample became turbid due to the formation of nematic droplets in a polymer matrix, the intensity of reflected light drops because of the aperture of the optical set up and the sample appeared darker. Combination of the conversion versus time plot derived from the DSC data (see Chapter 5) and the onset of turbidity detected with the microscope set-up yielded the conversion at the moment of phase separation.

6.2.3 Nematic-isotropic phase transition temperature of the initial LC/monomers mixture

The nematic-isotropic phase transition temperatures (T_{NI}) of K15/IBoMA/bisphenol-A-dimethacrylate mixtures as a function of the K15 weight fraction have been determined. Samples were prepared containing K15 mixed in various ratios with the IBoMA/bisphenol-A-dimethacrylate monomer system (the IBoMA:bisphenol-A-dimethacrylate molar ratio has been kept constant at 23:1). No DMPA was added. The influence of the photo-initiator DMPA on the phase behavior has been neglected, since it is only present in a small amount in the photo-enforced stratification mixture (0.5 wt.%). The samples were placed in the photo-DSC/microscope set-up, described in Paragraph 6.2.2. A linear polarization filter was placed between the microscope and the sample to improve the discrimination between the isotropic and the nematic phase of the sample. The samples were heated in the DSC, applying a heating rate of $1^{\circ}\text{C}\cdot\text{min}^{-1}$. With the aid of the microscope the temperature T_{NI} was determined at which the samples exhibited a nematic to isotropic phase transition.

6.2.4 In-situ confocal Raman microscopy

In-situ confocal Raman microscopy measurements have been performed to study the diffusion behavior of K15 in the K15/IBoMA/stilbene-dimethacrylate system during photopolymerization under PES conditions. Thereto a confocal LabRam Raman microscope (Jobin Yvon, Lille, France) has been configured for laser excitation at 633 nm. The Raman signals were detected by a Spectrum One CCD detector (1024 pixels, N_2 -cooled). Depth profiling was performed by using a closed-loop piëzo-driven Z-stage (Physik Instrumente, Karlsruhe, Germany). With a confocal hole of 300 μm an optimum in the compromise between the Raman signal intensity and depth resolution was achieved. With these settings the excitation laser spot size was smaller than 5 μm (as determined by the width of the Raman signal intensity profile at half-maximum of a Si-air interface, obtained via depth profiling of a silicon wafer).

Samples were prepared by sandwiching a droplet of the LC/monomers mixture between two glass substrates, which were kept at a constant distance of 30 μm with spacers made from Mylar foil. The top glass substrate of the sample (which faced the microscope) was only 100 μm thick, which was required to position the LC/monomers layer within the working distance of the 100x oil immersion objective (Zeiss, Oberkochen, Germany). The UV source (4W Philips TL08, $0.8 \text{ mW}\cdot\text{cm}^{-2}$) was placed at the opposite side of the sample. The experiments were conducted at room temperature. Further details on confocal Raman microscopy have been given in Chapter 3.

6.2.5 Photo-enforced stratification experiments

For the PES experiments glass substrates covered with a rubbed AL3046 alignment layer were used. Various mixtures of K15/IBoMA/stilbene-dimethacrylate in which the K15 fraction has been varied were applied on the substrate by means of a doctor blade. An Erichsen 509 MC-1 doctor blade coater (Erichsen, Rueil-Malmaison, France) was used for this purpose. The blade was set to a spacing of 60 μm and the blade velocity to $2.5 \text{ mm}\cdot\text{s}^{-1}$. The samples were exposed to UV light (4W Philips TL08, $0.8 \text{ mW}\cdot\text{cm}^{-2}$) in a N_2 -atmosphere at 22°C . The phase separation process was monitored by taking pictures of the sample every 10 s. A polarization microscope equipped with a camera was used for this purpose. After the process the samples were analyzed with a surface profiler and by polarization microscopy. See the experimental section of Chapter 2 for a more detailed description of the experimental steps described above.

6.3 Results and discussion

6.3.1 The phase diagram of the initial LC/monomers mixture: experiment and model

Before the polymerization-induced phase separation of the K15/IBoMA/bisphenol-A-dimethacrylate was studied with the aid of DSC/turbidity measurements, the phase behavior of the initial mixture was investigated. In these measurements bisphenol-A-dimethacrylate was used rather than stilbene-dimethacrylate for reasons that will be explained in the next paragraph. The nematic-isotropic phase transition temperatures T_{NI} of the K15/IBoMA/bisphenol-A-dimethacrylate mixtures as a function of the K15 weight fraction (keeping the IBoMA:bisphenol-A-dimethacrylate constant at 23:1) were determined experimentally according to the method described in Paragraph 6.2.3. The results are

plotted in Figure 6.4. Just below T_{NI} , coexisting nematic and isotropic phases were observed. However, upon further lowering the temperature the transition to the pure nematic phase could not be measured due to the limited contrast of the microscope set-up.

The K15/IBoMA/bisphenol-A-dimethacrylate system is approximated as a binary LC/monomer system. The phase diagram of the initial mixture is therefore a *pseudo*-binary phase diagram. At phase equilibrium the chemical potentials of the monomer ($\Delta\mu_M$) in the isotropic phase (I) and the nematic phase (II) are equal, and the same holds for the chemical potentials of the LC material ($\Delta\mu_{LC}$):

$$\Delta\mu_M^I = \Delta\mu_M^{II} \quad (6.1)$$

$$\Delta\mu_{LC}^I = \Delta\mu_{LC}^{II} \quad (6.2)$$

In the nematic phase (II), the expressions for $\Delta\mu_M$ and $\Delta\mu_{LC}$ are provided by Equations 6.3 and 6.4, respectively (see Chapter 4 for the derivation of the mixing entropy, mixing enthalpy and nematic ordering contributions).

$$\frac{\Delta\mu_M}{k_B T} = \ln \phi_M + \chi \phi_{LC}^2 + 2.27 \frac{T_{NI,LC} \phi_{LC}^2 S^2}{T} \quad (6.3)$$

$$\frac{\Delta\mu_{LC}}{k_B T} = \ln \phi_{LC} + \chi (1 - \phi_{LC})^2 - \ln Z + 2.27 \frac{T_{NI,LC} \phi_{LC}^2 S^2}{T} \quad (6.4)$$

where k_B is the Boltzmann constant, T is the temperature (in K), ϕ_M is the monomer volume fraction, ϕ_{LC} is the LC volume fraction, χ is the monomer-LC Flory-Huggins interaction parameter,¹¹ $T_{NI,LC}$ (K) is the nematic-isotropic phase transition temperature of the pure LC material, Z is a normalization constant, and S is the order parameter (see Chapter 4). The volumes of the monomer and the LC molecule were considered to be equal. The remaining input parameters for the phase separation model are the Flory-Huggins interaction parameter between the monomer and LC (χ) and the nematic-isotropic phase transition temperature of the pure LC material ($T_{NI,LC}$). The expressions for the chemical potentials of the monomer and the LC in the isotropic liquid phase (I) are obtained by omitting the Maier-Saupe terms in Equation 6.3 and 6.4.

In Chapter 5, χ has been estimated as 0.5 at 20°C, based on the solubility parameters of K15, IBoMA and bisphenol-A-dimethacrylate, which were obtained via a method of group contributions.¹² Although this value for χ is only a crude

estimation due to the approximations of the group contribution method, it is a good starting value for the model calculations. Based on the observation that K15 and IBoMA/bisphenol-dimethacrylate are miscible in all ratios, χ must be smaller than 2.¹³ On the other hand, due to the structural dissimilarity between the LC and the monomers, χ is expected to be larger than zero.

With the set of Equations 6.1-6.4 the binodal lines in the phase diagram of the initial LC/monomer mixture have been calculated, see Figure 6.4. In these calculation χ was taken 0.5, independent of the temperature, and the measured nematic-isotropic transition temperature of the pure K15 ($T_{N,LC} = 37^\circ\text{C}$) is used as input for the Maier-Saupe terms in the model. The binodals provide the equilibrium compositions of the isotropic liquid phase and the nematic phase as function of temperature. Above the upper binodal the LC/monomers mixture behaves isotropically (indicated with I). Below the lower binodal the mixture exhibits nematic behavior (indicated with N). In between, the nematic and liquid phase coexist (N+I). It can be seen in Figure 6.4 that the model calculations are in good agreement with the experimental results.

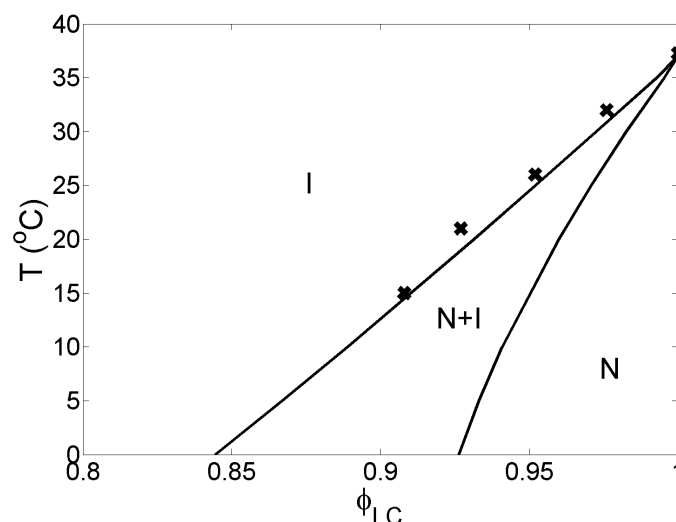


Figure 6.4: Calculated phase diagram of the initial LC-monomer mixture. The binodals (solid lines) provide the equilibrium compositions of the isotropic liquid phase and the nematic phase. The crosses denote the experimentally determined nematic-isotropic phase transition temperatures T_{NI} of K15/IBoMA/bisphenol-A-dimethacrylate mixtures as a function of the K15 wt. fraction.

6.3.2 The phase separation line: Photo-DSC/turbidity measurements and model calculations

With the aid of photo-DSC the photopolymerization rate of the LC/monomers mixtures versus time has been measured, from which the double bond conversion as a function of time was derived. During the photopolymerization the appearance of the sample has been recorded with a microscope set-up in order to determine the *onset of turbidity* i.e. the moment that the sample starts to scatter the incoming light. A turbid sample indicates that the LC/monomers/polymer system has phase separated into

small nematic droplets dispersed in a polymer rich phase. In these experiments stilbene-dimethacrylate has been substituted by bisphenol-A-dimethacrylate, which does not have an overlap with the absorption spectrum of the photo-initiator DMPA at the emission wavelengths of the UV source. This was done in order to obtain a homogeneous irradiation of the sample, and thus a homogeneous conversion throughout the sample. Stilbene-dimethacrylate and bisphenol-A-dimethacrylate have a strong structural similarity (see Figure 6.2), which is illustrated by their comparable molecular weights, the presence of six-membered alkylene spacers connecting the reactive moieties to the aromatic center, comparable solubility parameters and diffusion constants (see Chapter 5). It is therefore assumed that this substitution will hardly the phase separation behavior of the LC/monomers mixture in the photo-DSC/turbidity measurements.

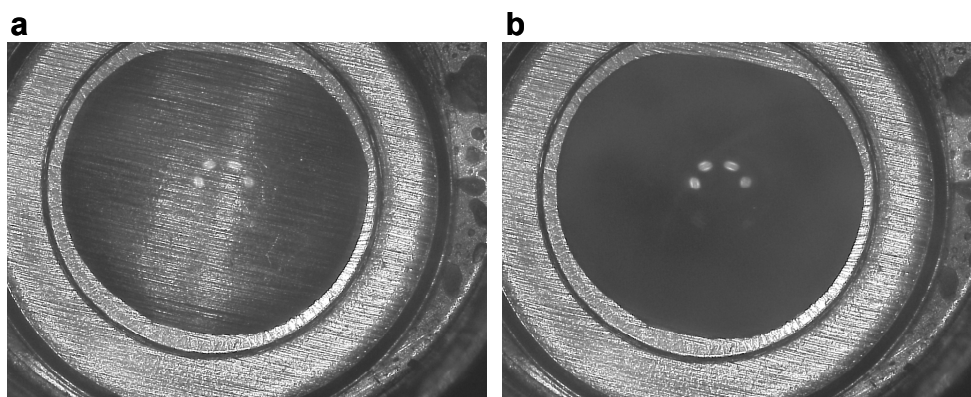


Figure 6.5: a) Image taken of a K15/IBoMA/bisphenol-A-dimethacrylate sample in the photo-DSC before the photopolymerization. b) Image after the polymerization is complete, and phase separation has taken place. Before phase separation the LC/monomers/polymer mixture is transparent and the probe light is reflected at the bottom of the DSC cup. Upon phase separation, the probe light is scattered by the microscopic nematic LC droplets dispersed in the polymer and reflected outside the aperture of the lens of the optical set-up. The four bright spots in the center of the sample originate from reflections of the probe light source at the quartz window above the sample (see also Figure 6.3).

Figure 6.5 shows examples of optical microscope images of a DSC cup containing the K15/IBoMA/bisphenol-A-dimethacrylate mixture taken before and after UV irradiation. Before photopolymerization the probe light is reflected at the bottom of the cup; after photopolymerization the sample has become turbid and appears darker. In Table 6.1 the conversion at the onset of turbidity for K15/IBoMA/bisphenol-A-dimethacrylate mixtures containing different K15 fractions are given for polymerization temperatures of 20°C and 30°C, respectively. The first moment that a given sample was observed to become turbid has been taken as the onset of turbidity. It can be seen in Table 6.1 that the K15/IBoMA/bisphenol-A-dimethacrylate mixtures containing ≥ 55 wt.% K15 exhibited polymerization-induced phase separation. It is remarkable that the phase-separation takes place in the late

stages of the polymerization process. It was found that the final conversion in the mixtures containing ≥ 55 wt.% K15 is approximately 100% (see Chapter 5). Moreover, the onset of phase separation shifts to even higher conversions when the temperature is increased from 20°C to 30°C. When the initial K15 fraction was 50 wt.% or less, no polymerization-induced phase separation was observed. Therefore, it can be concluded that the *solubility limit* of K15 in the copolymer is between 50 wt.% and 55 wt.% at 20°C and 30°C. In other words, the co-polymer can contain an amount of K15 that approximately equals its initial volume.

Table 6.1: Isothermal photopolymerization-induced phase separation: The double bond (C=C) conversion at the onset of turbidity as determined with a modified photo-DSC set up.

K15 (wt.%)	K15/IBoMA/bisphenol-A-DMA *	K15/IBoMA/bisphenol-A-DMA *	K15/IBoMA
	(T = 20°C) C=C conv. (%)	(T = 30°C) C=C conv. (%)	(T = 20°C) C=C conv. (%)
45	Not measured	Not measured	No phase sep.
50	No phase separation	No phase separation	82
55	96	97	88
60	88	95	86
70	83	98	75
80	74	95	50

All mixtures contained 0.5 wt.% DMPA. * The IBoMA:bisphenol-A-dimethacrylate ratio has been kept constant at 23:1 (mol/mol).

In order to plot these experimental data in a ternary diagram the weight fractions of the components have to be converted into volume fractions. For the sake of simplicity the densities of the components have been taken as $1 \text{ g}\cdot\text{cm}^{-3}$ (in fact the densities of the main components K15 and IBoMA are $1.03 \text{ g}\cdot\text{cm}^{-3}$, and $0.98 \text{ g}\cdot\text{cm}^{-3}$, respectively). Therefore, the initial volume fractions of the components are equal to the initial weight fractions. For the calculation of the monomer (and polymer) volume fractions at the onset of phase separation, the following two approximations have been made. First, although the mixture contains four components, the reaction mixture is treated as a ternary mixture containing liquid crystal, monomer and polymer, i.e. the two monomers are treated as having the same molecular weight and volume. Although the molar mass of bisphenol-A-dimethacrylate ($M_w = 565 \text{ g}\cdot\text{mol}^{-1}$) is significantly larger than that of IBoMA ($M_w = 223 \text{ g}\cdot\text{mol}^{-1}$), the error introduced by the approximation is small, since the bisphenol-A-dimethacrylate:IBoMA ratio is only 1:23. The resulting diagrams are therefore *pseudo*-ternary conversion phase diagrams. Second, the *monomer* conversion at the onset of phase separation has been taken

equal to the *double bond* conversion. In Chapter 5 it has been shown that when the bisphenol-A-dimethacrylate:IBoMA molar ratio is sufficiently small, this approximation is justified. The experimental results have been plotted in a pseudo-ternary conversion phase diagram (see Figure 6.6).

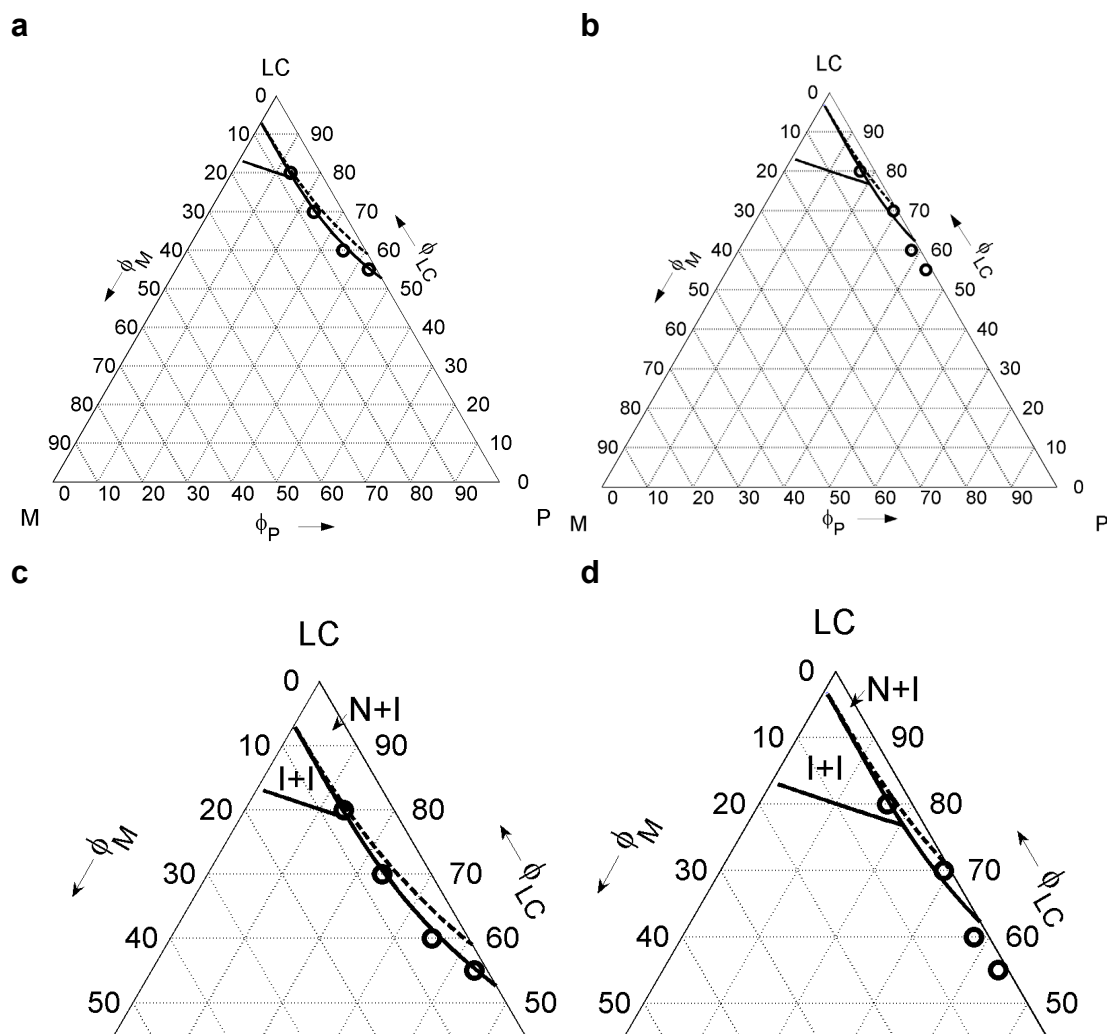


Figure 6.6: Pseudo-ternary conversion phase diagrams showing the experimentally determined conversions at the onset of photopolymerization-induced phase separation of the K15/IBoMA/bisphenol-A-dimethacrylate mixture (circles) at polymerization temperatures of (a) 20 °C and (b) 30 °C. The drawn lines are the results of the model calculations taking $\chi = 0.5$ (dotted line) and $\chi = 0.6$ (solid line). (c) and (d) represent the phase diagrams of 20 °C (a) and 30 °C (b), respectively, zoomed in near the top.

Phase separation lines were calculated with the thermodynamic phase separation model. Phase separation occurs when the polymer rich phase (*I*) and the liquid phase (*II*) are in thermodynamic equilibrium i.e. the chemical potential of the

monomer ($\Delta\mu_M$) as well as the chemical potential of the liquid crystal ($\Delta\mu_{LC}$) have the same value in both phases, see Equations 6.1 and 6.2. $\Delta\mu_M$ and $\Delta\mu_{LC}$ in the liquid phase are given by Equation 6.3 and 6.4. Equation 6.5 and 6.6 provide $\Delta\mu_M$ and $\Delta\mu_{LC}$ in the polymer-rich phase.

$$\frac{\Delta\mu_M}{k_B T} = \ln \phi_M + \phi_P + \chi \phi_{LC}^2 + \varepsilon \rho_{XL} \phi_P \quad (6.5)$$

$$\frac{\Delta\mu_{LC}}{k_B T} = \ln \phi_{LC} + \phi_P + \chi(1 - \phi_{LC})^2 + \varepsilon \rho_{XL} \phi_P \quad (6.6)$$

where ϕ_P is the polymer volume fraction, ε is the fraction of crosslinks that contribute to the elasticity of the polymer network and ρ_{XL} is the fraction of crosslinks.

Again the K15/IBoMA/bisphenol-A-dimethacrylate/co-polymer system is approximated as a ternary LC/monomer/polymer system and the volumes of the monomer, the monomer repeat unit in the polymer and the volume of the LC molecule were considered to be equal. The remaining input parameters for the phase separation model are the temperature T (K), the interaction parameter (χ), the effective crosslink density of the polymer network ($\varepsilon\rho_{XL}$), and the nematic isotropic phase transition temperature of the pure LC material ($T_{NI,LC}$).

The Flory-Huggins interaction parameter χ and the elastic contribution of the polymer network i.e. the value of $\varepsilon\rho_{XL}$, are difficult to determine experimentally. As was mentioned earlier, χ has been estimated as 0.5 at 20°C and 30°C (since for the current system $\chi \sim T^{-1}$, χ is essentially constant within a temperature interval of 10 K around room temperature) To investigate the influence of the bisphenol-A-dimethacrylate crosslinker on the onset of phase separation, the phase separation behavior of the K15/IBoMA/bisphenol-A-dimethacrylate system was compared to that of the K15/IBoMA system. The phase separation was observed to become earlier when the crosslinker was omitted (see Table 6.1). Although this counterintuitive behavior is not well understood, it was concluded that the elastic contribution of the polymer network in this particular system is negligible. Therefore, in the model calculations $\varepsilon\rho_{XL}$ was taken as zero.

The phase separation line of the K15/monomer/polymer system was initially calculated with $\chi = 0.5$ and $\varepsilon\rho_{XL} = 0$, which already gave a good agreement with the experimental results at 20°C and 30°C (see Figures 6.6a,c and 6.6b,d). The calculated phase separation line dissects the ternary diagram into large single-phase region and a small two-phase region in the top right of the diagram where the reaction mixture separates in a polymer-rich phase and a nematic phase. Since the solubility limit

calculated with $\chi = 0.5$ was slightly higher than the experimentally determined solubility limit, but the overall profile of the phase separation line was in agreement with the results from the photo-DSC/turbidity measurements, the phase separation line was recalculated with a slightly higher value for χ , namely $\chi = 0.6$ (and $\varepsilon\rho_{XL} = 0$). This time an even better agreement with the experimentally derived results was obtained, at 20°C as well as at 30°C (see Figures 6.6a,c and 6.6b,d). Again, the calculated phase separation line separates a large single-phase region from a small two-phase region in the top right of the diagram where the reaction mixture separates in a polymer-rich phase and a nematic phase. In addition there is a region in the ternary diagram where the mixture phase separates into a polymer-rich phase and an isotropic LC/monomers phase. The existence of I-I demixing, however, could not be investigated with the current experimental set-up, since scattering of a thin film of isotropic dispersed droplets is limited due to the small index of refraction differences. The existence of I-I demixing could be studied in further detail by conducting photopolymerization-induced phase separation under a polarization microscope following the phase behavior of individual PDLC droplets. Serbutoviez et. al have observed the formation of isotropic droplets at high initial LC fractions ($\phi_{LC} > 0.9$) in a K15/tetraethyleneglycoldiacrylate system with such a measurement set-up.⁸

The calculated phase separation lines show that the solubility limit increases with increasing temperature, which has also been reported for technical PDLC mixtures.¹⁴ Unfortunately, it was not possible to confirm this trend by experiment. For the photopolymerization-induced phase separations performed at 30°C, it was difficult to observe the onset of phase separation very accurately in samples containing volume fractions of K15 close to the solubility limit.

To investigate the influence of χ and $\varepsilon\rho_{XL}$ on the calculated phase separation lines additional simulations have been performed for the K15/IBoMA/bisphenol-A-dimethacrylate/copolymer system. These simulations are discussed in the Appendix.

6.3.3 Polymerization-induced diffusion monitored by confocal Raman microscopy

During the photopolymerization of a 25 μm layer consisting of the K15/IBoMA/stilbene-dimethacrylate/DMPA system under PES conditions, the K15 concentration profiles were measured real time by confocal Raman microscopy. The K15 concentration profiles are proportional to the Raman signal of the $\text{C}\equiv\text{N}$ stretching band (see also Figure 6.2) around 2220 cm^{-1} , which were monitored as function of depth and time. This particular band was selected, since it does not have any overlap with Raman signals originating from the other components in the layer. Moreover, it exhibits a strong Raman signal, which enables integration times of less than 60 s, which is faster than the time scale of the process. Unfortunately, it was not possible to discriminate between the signals originating from the unreacted monomers and the signals originating from the monomer repeat units in the polymer. Therefore no separate depth profiles for the polymer and the monomers could be obtained. The experiments were conducted at room temperature. Some heating of the sample by irradiation of the UV source and the laser spot could not be prevented, but the temperature remained well below 35°C .

Figure 6.7a shows the Raman intensity profile of K15 across the layer thickness at three time intervals during the photopolymerization process of a K15/IBoMA/stilbene-dimethacrylate/DMPA mixture in which the K15 fraction was 50 wt.%. The intensity changes are not dramatic: in the first 300 s the intensity of the K15 signal drops by 20-25% in the top of the layer, while in the bottom of the layer the signal increases with 10-15%. After 300 s, the profiles do not change significantly any more. Variation of the K15:monomers ratio in the initial mixture from 40:60 to 60:40 (wt.:wt.) resulted in approximately the same relative changes in the top and in the bottom. This indicates that varying the initial LC fraction in this range does not significantly influence the K15 diffusion behavior. In a control experiment with the K15/IBoMA/bisphenol-A-dimethacrylate mixture, i.e. in absence of the UV intensity gradient and concomitant polymerization rate gradient across the layer depth, the K15 signal intensity was found to remain constant across the layer depth throughout the polymerization process.

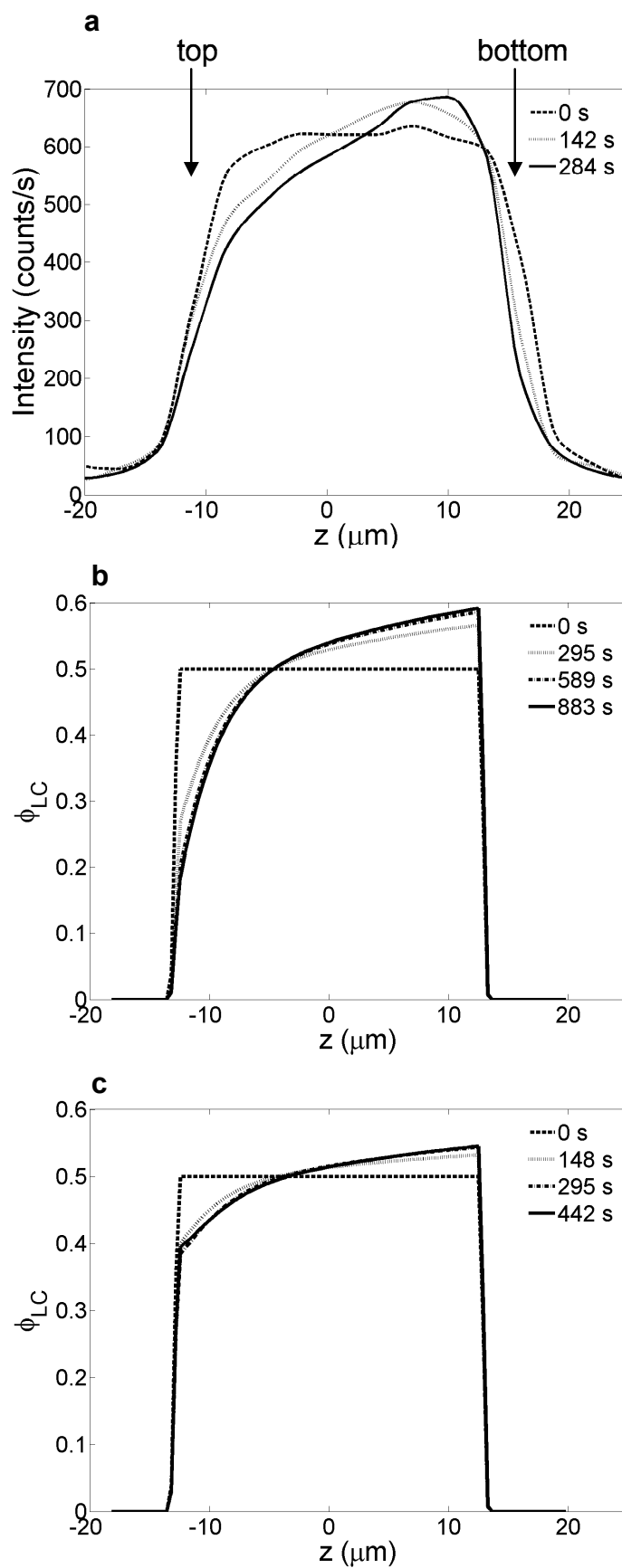


Figure 6.7: a) Evolution of the K15 depth profile measured by confocal Raman microscopy (top: side of the layer facing the UV source). b) Monomer-driven diffusion simulation results. c) LC-driven diffusion simulation results.

6.3.4 Reaction-diffusion model

In order to model the polymerization-induced diffusion in the K15/IBoMA/stilbene-dimethacrylate/polymer mixture, it is again treated as a ternary system. The same approximations as before have been used for the calculations: the densities of the components have been taken as $1 \text{ g}\cdot\text{cm}^{-3}$, the *monomer* conversion has been taken equal to the *double bond* conversion, and the volumes of the monomer, the monomer repeat unit in the polymer and the volume of the LC molecule were considered to be equal. In Chapter 5 the parameter input values and expressions for the reaction diffusion model have been determined. In addition, $\chi = 0.6$ and $\rho_{XL} = 0$ was assumed (see paragraph 6.3.2). The input parameters are listed in Table 6.2.

The reaction-diffusion model, discussed in Chapter 4, provides the monomer, LC and polymer fractions as function of depth in the layer and time. In the model, the layer is divided into segments. In a so-called monomer-driven diffusion simulation, after polymerization during a short defined time-interval the chemical potential of the monomer in each segment is first calculated (via Equation 6.5). Then, in the diffusion step, the monomer is allowed to diffuse during a time-interval of the same length. The resulting monomer volume fractions are calculated with the general diffusion equation in which diffusion is a function of the chemical potential difference between the segments (see Chapter 4). Under the chosen polymerization conditions the monomer is able to diffuse to equilibrium i.e. the monomer chemical potentials in the segments are equal after each diffusion step. Since the polymer is assumed to be immobilized at the position where it is formed and the segment size is taken constant, for a correct material balance the LC flux is taken equal to the monomer flux, but in opposite direction. It should be noted that as a result of these assumptions, with respect to its chemical potentials the LC is not in equilibrium throughout the simulation. In a so-called LC-driven diffusion simulation, after the polymerization step the chemical potential of the LC and the resulting LC flux is first calculated (via Equation 6.6). In that case the monomer flux was subsequently taken equal to the LC flux, but in opposite direction.

Figure 6.7b shows the LC-fraction depth profile as a function of time resulting from the monomer-driven diffusion simulation, while Figure 6.7c shows the results from the LC-driven diffusion simulation. The trends in both calculations, an increasing LC fraction at the bottom and a decreasing LC fraction at the top of the film, correspond to the trends observed in the Raman measurements. Figure 6.8 shows the relative change of the K15 signal as function of time in the bottom and in the top of the layer obtained from the Raman data of the 50 wt.% K15 experiment. Also the relative changes of the LC fraction in the bottom and the top as function of time, calculated with the monomer-driven and the LC-driven diffusion simulations are

plotted. It is noteworthy that the relatively subtle change of the K15 fraction in the bottom of the layer, observed in the Raman measurements, is also predicted by both simulations. With respect to the LC fraction in the top of the layer, the LC driven diffusion simulation is in better agreement with the experimental results.

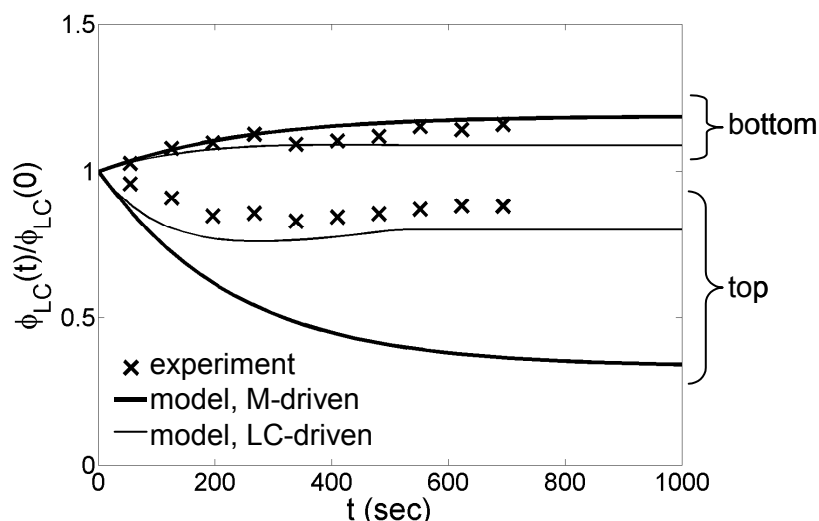


Figure 6.8: The relative change of the K15 signal as function of time in the top and in the bottom of the layer, obtained from the Raman data of the 50 wt.% K15 experiment. The results of the reaction-diffusion model in case of monomer-driven diffusion and LC-driven diffusion are also depicted.

Table 6.2: Input parameters for the reaction diffusion model

	Parameter	Value / calculated via
Layer thickness (μm)	D	25
Incident intensity ($\text{mW}\cdot\text{cm}^{-2}$)	I_0	0.8
Effective intensity gradient ¹ ($\text{Einsteins}\cdot\text{m}^{-2}\cdot\text{s}^{-1}$)	$I_a(z)$	Equation 5.4 (shape: Figure 5.6)
Quantum efficiency photo-initiator	φ_{mi}	0.4
Propagation / termination constants ($\sqrt{\text{l}\cdot\text{mol}^{-1}\cdot\text{s}^{-1}}$)	$\frac{k_p}{\sqrt{k_t}}$	1.5
Interaction parameter	χ	0.6
Mono-vinyl monomer, polymerization kinetics		Equation 4.47
Mono-vinyl monomer, no crosslinks	ρ_{XL}	0
Monomer-driven diffusion, unless stated otherwise; monomer diffusion coefficient ($\text{m}^2\cdot\text{s}^{-1}$)	$D_M = D_{LC}$	Equation 5.10

6.3.5 Photo-enforced stratification: PES model vs. experimental results

The photo-enforced stratification process of K15/IBoMA/stilbene-dimethacrylate has been modeled with the combined PIPS/reaction-diffusion model, i.e. the PES model. The model yields the phase separation line and the polymerization lines which have been plotted in a ternary phase diagram. The phase separation line signifies the distinct compositions of the LC/monomer/polymer mixture for which phase separation will occur, whereas the polymerization lines for various z/d positions in the layer represent the local composition of the mixture as a function of the conversion.

The calculated phase separation line and the polymerization lines in the top and at the bottom of the layer for three different initial LC compositions ($\phi_{LC} = 0.4, 0.5$ and 0.7) have been plotted in a ternary diagram (Figure 6.9a). The diagram illustrates the significance of the initial LC fraction in the LC/monomers mixture. When the initial LC concentration too low (e.g. $\phi_{LC} = 0.4$), none of the polymerization lines intersect the phase separation line and consequently no phase separation takes place. At a high initial LC concentration (e.g. $\phi_{LC} = 0.7$) phase separation takes place almost throughout the entire layer, since most of the polymerization lines cross the phase separation line.

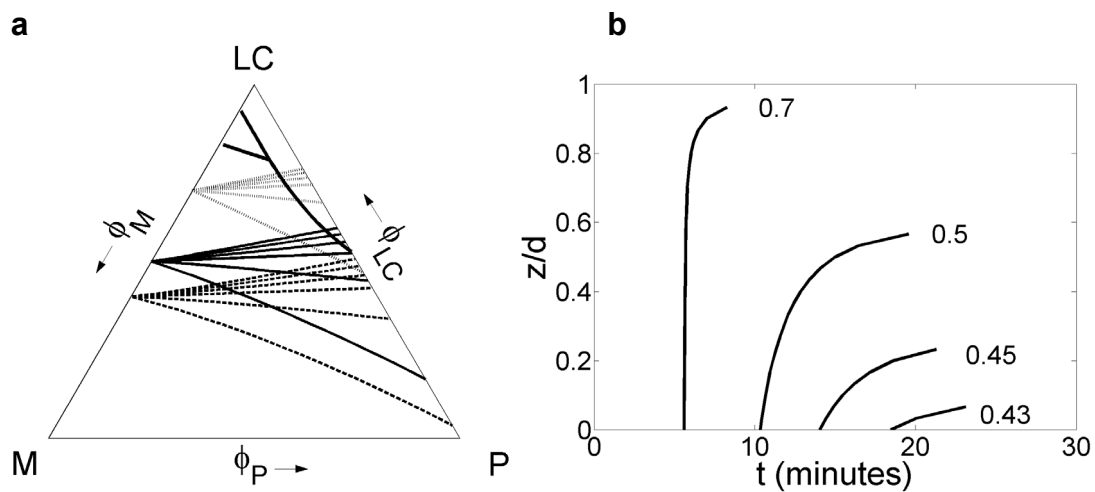


Figure 6.9: a) Ternary phase diagram showing the polymerization lines at six different z -positions in the layer for an initial LC fraction of 0.4, 0.5 and 0.7 (the six polymerization lines at $z = 0 - 25 \mu\text{m}$ with $5 \mu\text{m}$ intervals are calculated with monomer-driven diffusion simulations; the highest polymerization line represents the polymerization in the bottom of the layer). b) The time-of-intersection plot for various initial LC fractions, providing the z/d position where the corresponding polymerization line intersects the phase separation line as a function of time (the LC fraction is indicated near the corresponding intersection curve).

In Figure 6.9b the time-of-intersection plot, which provides the z/d position where the corresponding polymerization line intersects the phase separation line as a function of time, is depicted for various initial LC fractions. The first intersection in time yields the onset of phase separation. It can be seen in Figure 6.9b that the onset of phase separation takes place in the bottom of the layer, independent of the initial LC fraction. Figure 6.10 shows the calculated time to the onset of phase separation τ_{onset} as function of initial LC fraction for the case of monomer-driven diffusion and LC-driven diffusion. The differences between both curves are the result of the assumptions made in the reaction-diffusion model and the actual τ_{onset} will be somewhere within the time interval given by these two extremes: In monomer-driven diffusion, the LC fraction that is expelled towards the bottom is overestimated, resulting in a value of τ_{onset} that is too low, while in LC-driven diffusion the monomer fraction excluded towards the top is underestimated yielding lower LC fractions at the bottom. Consequently, this results in a value of τ_{onset} that is too high. A future improvement of the PES model can possibly be achieved by introducing Stefan-Maxwell equations¹⁵ for the description of the multi-component diffusion. In these equations the effect of the movement of one component of the mixture on the motion of all the other components is taken into account.

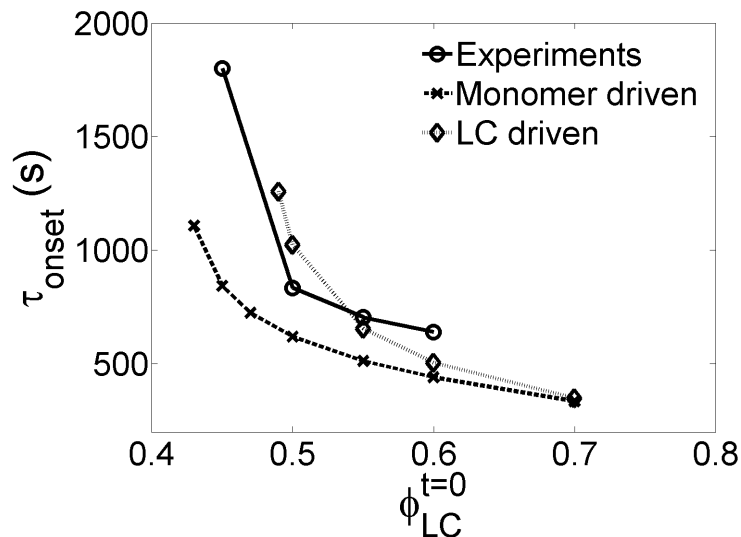


Figure 6.10: Time to the onset of phase separation τ_{onset} for various initial LC fractions calculated by the PES model (monomer- and LC-driven) and measured by in-situ polarization microscopy. For 45wt.% K15 no phase separation was observed during the UV exposure (duration 1800 s) but examination with polarization microscopy revealed that shortly after stopping the irradiation phase separation had occurred. Since the exact time was not established the start of the phase separation was set at 1800 s.

Figure 6.10 also presents the measured τ_{onset} obtained from PES experiments with K15/IBoMA/stilbene-dimethacrylate/DMPA blends containing different K15 fractions. Both model and the experiments show an onset of phase separation coming later at lower LC fractions and a trend to asymptotic behavior for low LC concentrations to infinitely long starting times. The PES model results are in qualitative agreement with the experiments but also almost quantitatively, despite the approximations that have been made in the reaction-diffusion model and the PIPS model.

6.3.6 Morphological phenomena: PES model predictions vs. experimental results

As already mentioned in Chapter 4 the z -interval over which the polymerization lines intersect the phase separation line can be taken as a measure for the probability of PDLC formation in the polymer i.e. micrometer-sized LC droplets randomly distributed in a polymer rich phase. Figure 6.9b shows that at high initial LC fractions ($\phi_{LC} = 0.7$) the starting times of the phase separation are almost equal over the layer thickness. This gives a high probability of PDLC morphology formation. Upon decreasing the initial LC fraction, the region where no intersection and therefore no phase separation will take place becomes larger and larger. Consequently, the chance of PDLC morphology formation in the upper regions of the layer will thereby also decrease. At initial LC fraction $\phi_{LC} = 0.43$ the phase separation is localized in the bottom of the layer. Below this fraction no phase separation takes place. Figure 6.9b shows that close to this lower limit ($\phi_{LC} = 0.43-0.5$) the starting time of the phase separation as well as the shape of the time-of-intersection curves (thus the probability of PDLC formation) depend very strong on the initial LC fraction.

To verify this, the morphology of the polymerized samples was examined with the aid of polarization microscopy and surface profile measurements. Some examples of samples with varying K15 concentrations are depicted in Figure 6.11. Please note that for reasons of accurate knowledge of the initial monomer and LC concentrations the samples were photopolymerized in the absence of the vertical supporting walls made by a first lithographic UV exposure. As explained in Chapter 2 this yields less well-structured LC/polymer morphologies with individual LC domains randomly distributed over the substrate rather than a continuous layer. But the structures are informative enough to draw conclusions on the location of the phase separation. As Figure 6.11 demonstrates all samples with K15 within the 45-60 wt.% range exhibit stratification. Large domains are formed containing monolithically aligned LC at the interface with the alignment layer. The schlieren structure visible in the areas

surrounding the droplets indicate that also LC is present which is not in contact with the alignment layer but located on top of the polymer layer. This is explained by a reverse polymerization gradient near the top interface due to oxygen inhibition. A schematic cross section of the films is depicted in Figure 6.11e.

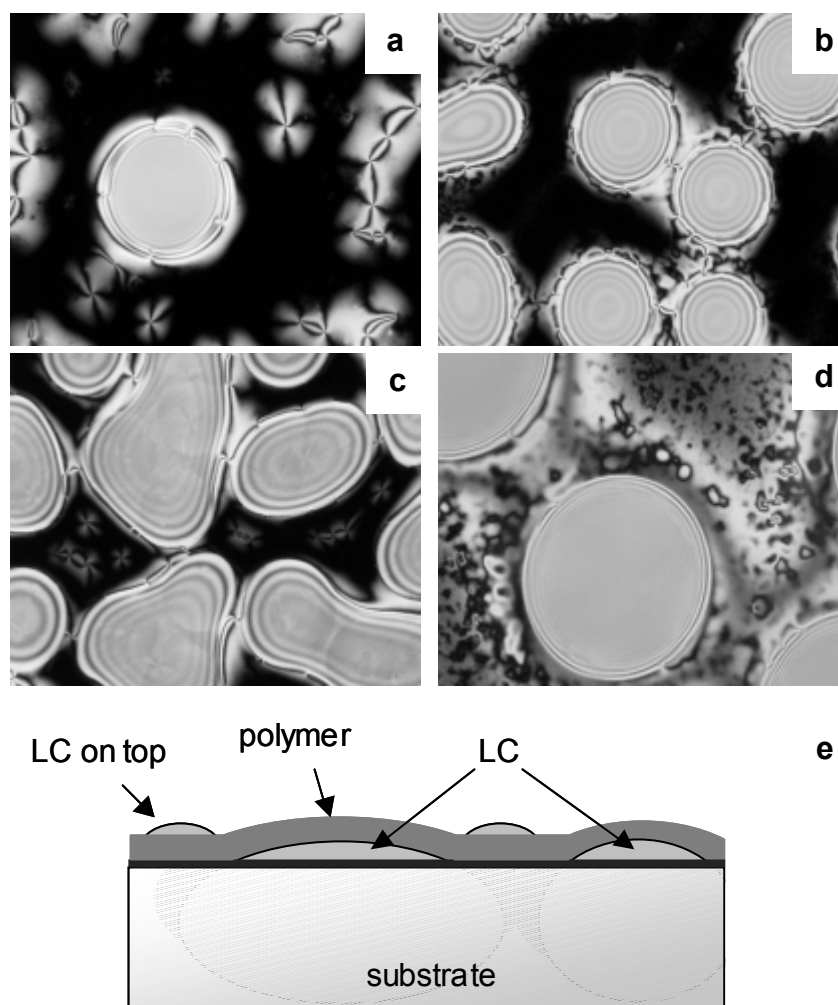


Figure 6.11: Bright state (polarizer axis at 45° with respect to rubbing direction of the alignment layer) of samples containing various initial K15 fractions (observation two days after stratification experiment: a) 45 wt.% K15, b) 50 wt.% K15, c) 55 wt.% K15, d) 60 wt.% K15.. e) A schematic cross-section deduced from microscopy and height profile measurements.

In a next step the polymer films shown in Figure 6.11 were removed from their substrates and subsequently the LC at the surface, both top and bottom, was carefully removed with tissue leaving the LC that is encapsulated by the polymer in place. Figure 6.12 shows the results. The scratches are caused by the rubbing with tissue to remove the LC. At low initial LC concentrations the polymer films are black between crossed polarizers except for some edge effects near the droplet edges. In general this points to the absence of LC confined in droplets. However, at higher initial LC concentrations the films are more opaque. Upon heating above the nematic-

isotropic temperature of K15 all samples became transparent, pointing to the presence of PDLC morphology in the polymer, the amount of microscopic LC droplets formed in the polymer being higher in samples with higher initial LC fractions. The trend observed in these experiments is similar to the trend expected from the shape of the time-of-intersection curves in Figure 6.9b.

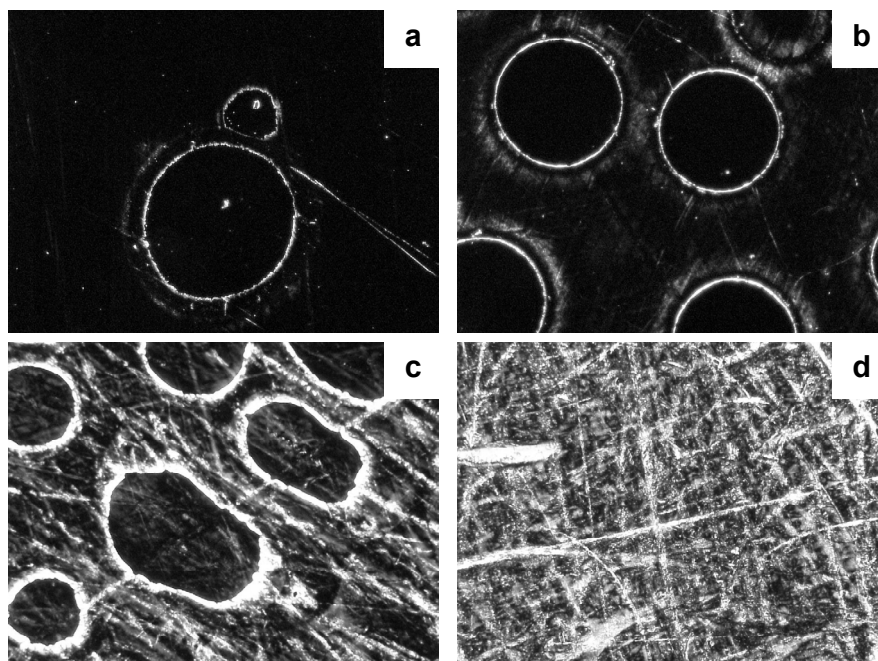


Figure 6.12: Polarization microscope pictures of the polymer topcoat of the samples taken after removal of the LC on both sides of the polymer. a) 45 wt.% K15 sample, b) 50 wt.%, c) 55 wt.% and d) 60 wt.%.

6.4 Conclusions

In this chapter the photo-enforced stratification (PES) model as well as its two basic components, the polymerization-induced phase separation (PIPS) model and the reaction-diffusion model, were compared with experiments. Photo-DSC combined with microscopy enables the location of the onset of turbidity. The postponed onset of phase separation at lower LC concentrations found for the K15-IBoMA-bisphenol-A-dimethacrylate system is in agreement with the calculations. The calculated phase separation lines are quite similar to experimentally determined phase separation lines when the estimated values of the Flory-Huggins interaction parameters between the components, based on solubility parameters calculated via Hoy's system, are inserted and the elastic contribution of the polymer network was neglected. As was corroborated by experiments on K15/IBoMA with and without bisphenol-A-dimethacrylate, the elastic contribution of the polymer network of the

K15/IBoMA/bisphenol-A-dimethacrylate mixture is indeed insignificant. An even better agreement between model and experiment is obtained when the Flory-Huggins interaction parameter is used as adjustable variable. The trends in the K15 depth profile predicted by the monomer-driven- as well as the LC-driven reaction-diffusion model are in agreement with in-situ confocal Raman experiments.

Trends calculated with the resulting PES model correspond to experimental trends. Both model and the experiments show an onset of phase separation coming at higher conversions at lower initial LC fractions and a trend to asymptotic behavior for low LC concentrations to infinitely long starting times.

The model predicts an increased possibility to form PDLC morphology at high initial LC fractions. Investigation of the resulting morphologies after stratification indeed revealed the existence of liquid crystal droplets dispersed in the polymer topcoat.

6.5 Appendix

To illustrate the influence of χ and $\varepsilon\rho_{XL}$ on the phase separation line calculated with the PIPS model, two additional simulations have been performed for the K15/IBoMA/bisphenol-A-dimethacrylate/copolymer system, namely (i) with $\chi = 0$ and $\varepsilon\rho_{XL} = 0$ and (ii) with $\chi = 0$, $\varepsilon = 1$, and ρ_{XL} is a function of the monomer conversion α . Equation (6.7) describes the relationship between the fraction of crosslinks ρ_{XL} and the monomer conversion α (see Chapter 4). Again the system is treated as a ternary system as described above. The $T_{NI,LC}$ was taken as 37° C and the temperature was taken as 20°C.

$$\rho_{XL} = \frac{2 - \alpha - 2\sqrt{1 - \alpha}}{\alpha} \quad (6.7)$$

The results are shown in Figures 6.14 b-c. For comparison, the simulation results for $\chi = 0.6$ and $\varepsilon\rho_{XL} = 0$ are shown again in Figure 6.14a. When χ is taken as zero, it means that the chemical and physical interactions between a monomer (or a monomer repeat unit in the polymer) and an LC molecule are considered to equal to the interactions between two monomers (or two monomer repeat units) and two LC molecules,¹¹ and that thus the heat of mixing is zero (athermal mixing). When $\varepsilon\rho_{XL}$ is taken as zero, it means that the elastic forces in the polymer network are neglected and the polymer is treated as a linear polymer. Figure 6.14b shows the phase separation line calculated for this situation. It can be seen that by taking χ as zero, the compatibility between the

monomer/polymer and K15 is overestimated: the phase separation takes place at much higher conversions compared to the experimentally determined points of the phase separation line and also the solubility limit, i.e. the LC fraction that the fully polymerized material can contain without exhibiting phase separation, is overestimated.

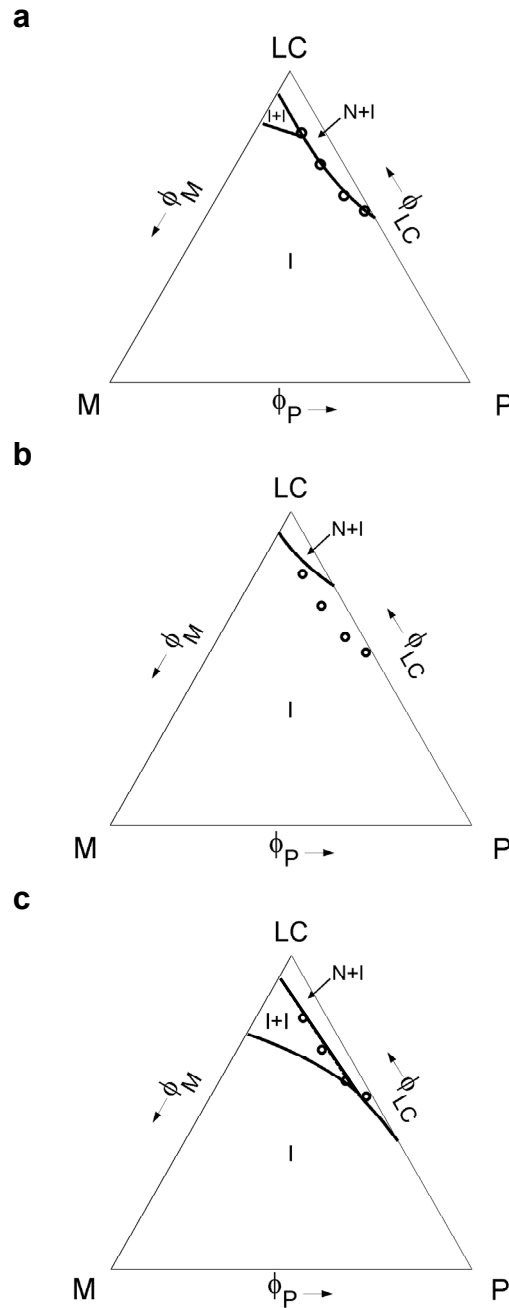


Figure 6.14: Pseudo-ternary conversion phase diagrams calculated for the K15/IBoMA/bisphenol-A-dimethacrylate/copolymer system (at 20° C) for various χ and $\epsilon\rho_{XL}$ combinations, namely (a) $\chi = 0.6$ and $\epsilon\rho_{XL} = 0$, (b) $\chi = 0$ and $\epsilon\rho_{XL} = 0$, and (c) $\chi = 0$, $\epsilon = 1$, and ρ_{XL} is a function of the monomer conversion α (see main text). The open circles in the diagrams represent the experimentally determined compositions of the K15/IBoMA/bisphenol-A-dimethacrylate/copolymer system at the onset of phase separation at 20° C.

In the model, the compatibility can be reduced by taking a positive value for χ . In fact, it was already shown that by taking $\chi = 0.6$, a value that is close to the estimated value of $\chi = 0.5$ based on the calculated solubility parameters of the components in the system, the onset of polymerization-induced phase separation as a function of the initial K15 fraction coincides with the experimentally determined points (see Figure 6.14a.). Another way to decrease the compatibility between the LC material and the polymer in the model is to take the elasticity of the polymer network into account.^{5,16} Figure 6.14c shows the pseudo-ternary conversion phase diagram when the IBoMA/bisphenol-A-dimethacrylate monomer system is treated in the simulation as a pure crosslinker and all the crosslinks contribute to the elasticity of the polymer network. In that case $\varepsilon = 1$, ρ_{XL} is given by Equation 6.7 and $\chi = 0$. Comparison of the resulting phase separation diagram with the phase separation diagram calculated for $\chi = 0.6$ and $\varepsilon\rho_{XL} = 0$ (see Figure 6.14a), shows that a similar phase separation behavior can be obtained for two significantly different starting points: I-I demixing in case of high initial LC fractions, N-I demixing at high conversions for intermediate LC fractions and no phase separation for low LC fractions. The physical consequences of taking a positive value for χ or taking $\varepsilon\rho_{XL}$ into account are different: when χ is larger than zero, the LC/monomer and LC/polymer compatibilities are reduced, while the monomer/polymer compatibility remains unaffected.¹¹ When the value of $\varepsilon\rho_{XL}$ is larger than zero, the LC/polymer and monomer/polymer compatibilities are reduced, while the LC/monomer compatibility remains unaffected. To check whether the chosen input values of χ and $\varepsilon\rho_{XL}$ are physically realistic, additional experiments will be required.

6.6 References and notes

1. Odian, G. *Principles of polymerization*, John Wiley & Sons, New York (1981).
2. Atkins, P. *Physical Chemistry*, Oxford University Press, Oxford (1990).
3. Flory, P.J. *J. Chem. Phys.* **9**, 660 (1941); Huggins, M.L. *J. Chem. Phys.* **9**, 440 (1941).
4. Flory, P.J., and Rehner, J. *J. Chem. Phys.* **11**, 521-526 (1943).
5. Dušek, K. *J. of Pol. Sci.* **16C**, 1289-1299 (1967).
6. Maier, V.W., and Saupe, A. *Z. Naturforsch.* **14a**, 882-889 (1959).
7. Kloosterboer, J.G., Serbutoviez, C., and Touwslager, F.J. *Polymer* **37**, 5937-5942 (1996).

8. Serbutoviez, C., Kloosterboer, J.G., Boots, H.M.J., and Touwslager, F.J. *Macromol.* **29**, 7690-7698 (1996).
9. Mank, A.J.G., Vorstenbosch, I., Penterman, R., Vogels, J.P.A., Klink, S.I., and Broer, D.J. *Appl. Spectrosc.* **59**, 965-975 (2005).
10. Drzaic, P.S. *Liquid Crystal Dispersions*, World Scientific, Singapore (1995).
11. The expressions containing χ in Equations 6.3 and 6.4 have been derived for a ternary LC / monomer (M) / polymer (P) system for which $\chi_{M-LC} = \chi_{LC-P}$ and $\chi_{M-P} = 0$ (see Chapter 4). In these equations χ is equal to χ_{M-LC} and χ_{LC-P} .
12. The solubility parameters have been calculated via Hoy's system: Krevelen, D.W. van, *Properties of Polymers*, Elsevier, Amsterdam, Chapter 7, Table 7.10 (1990).
13. Tompa, H. *Polymer solutions*, Butterworth, London (1956).
14. Smith, G.W., and Vaz, N.A. *Mol. Cryst. Liq. Cryst.* **237**, 243-269 (1993).
15. Bird, R.B., Stewart, W.E., and Lightfoot, E.N. *Transport phenomena*, John Wiley & Sons, New York (1960).
16. Boots, H.M.J., Kloosterboer, J.G., Serbutoviez, C., and Touwslager, F.J. *Macromol.* **29**, 7683-7689 (1996).

Chapter 7

Second generation photo-enforced stratification process

7.1 Introduction

Conventional liquid crystal displays (LCDs) are based on rectangular glass substrates, which is imposed by the current fabrication methods (the so-called cell technology)¹ and related substrate handling. By using the photo-enforced stratification (PES) technology, LCDs are made by a sequence of simple coating processes, and can be applied to rigid glass substrates as well as flexible plastic substrates.² In Chapter 2 it has been shown that a sequence of two different UV exposures of the LC/monomers layer is required to make well-defined structures that form a grid of neighboring LC-filled polymer capsules. The shape of the capsules is defined by the pattern on the mask that is used in the first UV exposure step, during which an array of polymer walls is formed in the LC/monomer layer. During the second UV exposure, which is a flood exposure, the polymer top layer is formed by a process of simultaneous polymerization and phase separation. The phase separation process is spatially controlled by the presence of a UV light absorbing reactive monomer in the layer, such that it ultimately results in two layer-shaped, stratified phases. A functional LCD made by the PES technology was shown in Chapter 2. These initial devices were made on glass substrates, although a single substrate was necessary rather than two substrates required in the current state-of-the-art display manufacturing technologies.

In this chapter, an improved PES technology, especially optimized for manufacturing *plastic* LCDs, is presented. Plastic LCDs are of interest because they widen the scope of applications by improving on robustness and shape factors.³ The innovation of the PES technology involves the direct formation of the liquid crystal-filled capsules (being the heart of the LCD) by a single UV light exposure step. In comparison with the PES process described in Chapter 2, the first UV mask exposure step has been replaced by a surface modification step of the substrate. In this step a

grid pattern of an *adhesion promoter* is printed on the polyimide coated substrate, prior to the coating of the reaction mixture. Exchanging the lithographic UV exposure by printing has two important consequences. It makes the process simpler by avoiding mask alignment, UV exposure under inert atmospheric conditions and accurate control of the required UV dose. But besides that, the resulting LC-filled polymer capsules are mechanically much more robust than their counter parts that were produced by the two-step PES technology, enabling bending without delamination.

7.2 Experimental section

7.2.1 Materials

Isobornyl methacrylate (IBoMA) was purchased from Mitsubishi Chemical (Minato-ku, Tokyo, Japan) and used without further purification. Tripropyleneglycol diacrylate (TPGDA) and hexanediol dimethacrylate (HDDMA) was purchased from Aldrich (Zwijndrecht, Belgium) and used without further purification. The synthesis of 4,4'-di-(6-methacryloyloxyhexyloxy)-3-methylbibenzyl (*stilbene-dimethacrylate*) is described in Ref. 4. E7 was purchased from Merck (Darmstadt, Germany). The photoinitiators Irgacure 651 (Dimethoxyphenylacetophenone, DMPA) and Darocure 4265 (50/50 wt/wt 2-hydroxy-2-methyl-1-phenylpropan-1-one / 2,4,6-trimethylbenzoyl-diphenyl-phosphineoxide) were purchased from Ciba Specialty Chemicals (Basel, Switzerland). Durimide 7505 was purchased from Arch Chemicals (Zwijndrecht, Belgium). Sylgard 184 was purchased from Dow Corning (Midland, MI, USA). The LC/monomers mixture consists of 50 wt.% of K15, 44.5 wt.% of isobornylmethacrylate (IBoMA), 5 wt.% of stilbene-dimethacrylate and 0.5 wt.% of Darocure 4265, see Figure 7.1. For the planarization layer on top of the LC-filled capsules TPGDA was mixed with 2 wt.% Irgacure 651.

Polycarbonate substrate films, 120 μ m-thick and covered with 150 nm Indium-Zinc-Oxide (IZO), type SS120B30, were purchased from Teijin, Tokyo, Japan.

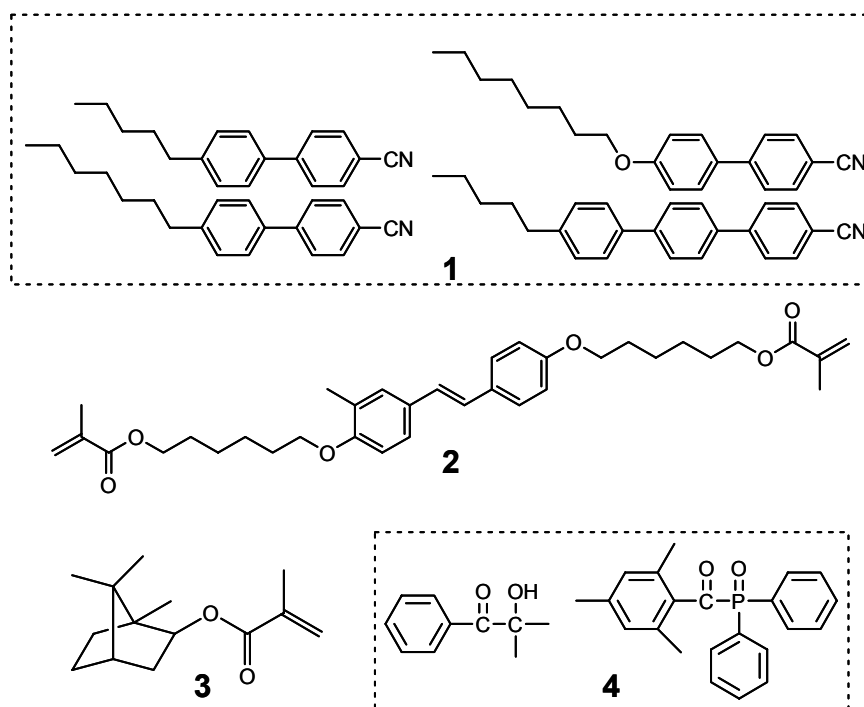


Figure 7.1: 1) The structures of the liquid crystal blend E7 consisting of 3 cyanobiphenyls, 5CB (51 wt.%), 7CB (25 wt.%), 8OCB (16 wt.%) and a cyanoterphenyl, 5CT (8 wt.%). 2) stilbene-dimethacrylate. 3) isobornylmethacrylate (IBoMA). 4) Darocur 4265, which is a mixture of 2-hydroxy-2-methyl-1-phenylpropan-1-one and 2,4,6-trimethylbenzoyl-diphenyl-phosphineoxide in a 50/50 wt./wt. ratio.

7.2.2 Glass substrate preparation

Glass substrates from Corning (Minato-ku, Tokyo, Japan) were prepared for reference experiments (0.7 mm thick) and Raman measurements (0.1 mm thick). The $6 \times 7 \text{ cm}^2$ glass substrates were cleaned by hand with demineralized water and Teepol soap, subsequently rinsed with demineralized water and finally dried in a cold airflow. An AL3046 poly(imide) alignment layer solution (JSR, Tsukiji Chuo-ku, Tokyo, Japan) was deposited on the substrates via a spin coating process on a 20 BM spin coater from B.L.E. Electronic Equipment GmbH, Germany. The spin coat conditions were 5 s at 1000 rpm, followed by 30 s at 4000 rpm. The poly(imide)-covered substrates were subsequently subjected to two heating steps to remove the solvent: 10 minutes at 90°C on a hotplate, and 60 minutes at 180°C in an oven. Finally, the poly(imide) alignment layer was rubbed using a home-made rubbing machine.

7.2.3 Structuring of the alignment layer

The alignment layer was modified by a manual offset printing process. A poly(dimethyl siloxane) (PDMS) stamp was made from Sylgard 184 in a micro machined mould. The stamp pattern is a square grid pattern with grid wall dimensions of $100 \mu\text{m}$ height, $50 \mu\text{m}$ width and a pitch of $500 \mu\text{m}$ (see Figure 7.2).

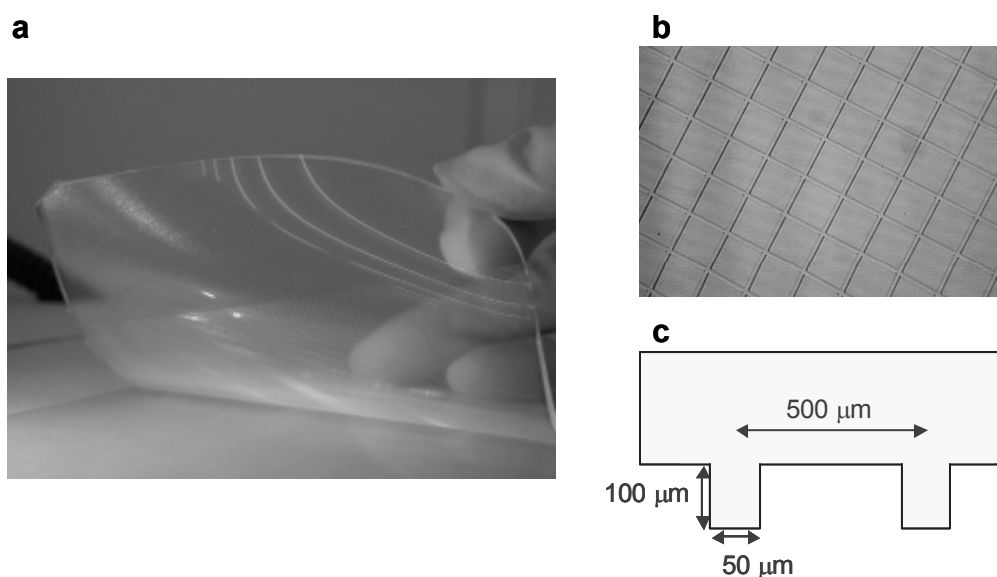


Figure 7.2: a) A photograph of the PDMS stamp, which has been used for the modification of the alignment layer by offset printing of an adhesion promoter. b) Top view magnification of the stamp features. c) A schematic cross section of the stamp.

The methacrylate functionalized poly(amide) (Durimide 7505) formulation (solid content 31 wt.%) that was used as the adhesion promoter was mixed in a 2 : 1 (wt./wt.) ratio with N-methyl pyrrolidone (NMP). For inking of the stamp, the adhesion promoter solution was spin cast on a glass substrate (10s at 500 rpm, and 30s at 3000 rpm) and subsequently transferred to the stamp by placing the stamp on the adhesion promoter solution covered glass substrate. After peeling off the stamp, the stamp with adhesion promoter solution was placed on the sample substrate (covered with the cured and rubbed AL3046 alignment layer). After carefully removing the stamp, the sample substrate was placed on a hotplate (100°C) for 10 minutes. The lines in the resulting square grid pattern of adhesion promoter are 100 - 150 μm wide and in the order of 800 nm thick. The distance between the lines is around 350 - 400 μm.

7.2.4 Doctor blade coating

A thin film of a LC/monomers mixture was applied on the poly(imide)-covered substrate by means of doctor blade coating. An Erichsen 509 MC-1 doctor blade coater (Erichsen, Rueil-Malmaison, France) was used for this purpose. The blade was set to a spacing of 60 μm and the blade velocity to 2.5 mm/s in order to obtain a film of 30 μm thickness. Typically 0.2 ml of the reactive mixture was applied.

7.2.5 UV exposure step

The samples were placed in a stainless steel nitrogen-flushed chamber with a UV transparent glass lid (B270 glass). After placing the sample in the chamber, the system was flushed with nitrogen for 5 minutes prior to the UV exposure (during the exposure there was a constant nitrogen flow through the chamber). The temperature in the chamber was maintained constant at 50°C using a hotplate. The samples were exposed to UV-light for 30 minutes (an array of 4 Philips TL08 lamps positioned at 15 cm ($0.8 \text{ mW}\cdot\text{cm}^{-2}$)). The appearance of the samples during the exposure was followed with a polarization microscope equipped with a camera (see Chapter 3 for details about the set-up).

7.2.6 Confocal Raman microscopy

A confocal LabRam Raman microscope (Jobin Yvon, Lille, France), with a confocal hole of 300 μm and a Zeiss 100x oil immersion objective, was configured for laser excitation at 633 nm. The sample was probed from the backside through the substrate, which for this purpose was chosen to be a 0.1 mm thick glass plate. Signal collection was performed using a Spectrum One CCD detector (1024 pixels, N_2 cooled). For depth profiling a closed-loop piëzo-driven Z-stage (Physik Instrumente, Karlsruhe, Germany) was employed. For a detailed description of the confocal Raman microscopy measurement set-up the reader is further referred to Chapter 3.

7.2.7 Device preparation and electro-optical characterization

The Indium-Zinc-Oxide coating on the polycarbonate film substrate was structured into an interdigitated electrode structure by standard photolithography. The photolithography involves subsequently spin-coating of a photoresist (AZ1518, Clariant, Switzerland) at 2000 rpm for 30 s, UV exposure through a mask (Karl Süss MA-8, $I = 10 \text{ mW}\cdot\text{cm}^{-2}$, $t = 9 \text{ s}$), developing (AZ developer, Clariant, Switzerland), wet chemical etching (etchant: 100 mL 37% HCl + 8 mL 65% HNO_3 + 300 mL water, $t = 40 \text{ s}$) and stripping (Microstrip 2001, Fujifilm, Japan). The resulting interdigitated IZO electrodes have a width of 20 μm and the distance between the electrodes is 20 μm . After the application of a poly(imide) alignment layer on the plastic substrate via spin casting and subsequent curing, the layer was rubbed at an angle of 10 degrees with respect to the electrode axes to obtain a desired in-plane pre-tilt of the LC molecules with respect to the electrical field lines. Subsequently, the alignment layer has been modified by the printing procedure as described in paragraph 7.2.3. After the application of a thin layer of the LC/prepolymer mixture and the UV light-induced formation of the array of LC-filled capsules, an additional tri(propylene glycol) diacrylate (TPGDA) coating was deposited by doctor blade

coating for planarization. The sample was placed in a stainless steel nitrogen-flushed chamber with a UV transparent glass lid (B270 glass) and irradiated with a Philips HPA lamp ($30 \text{ mW}\cdot\text{cm}^{-2}$) for 10 minutes. For the completion of the display, polarizers (TEG 1465-DU, Nitto Denko, Osaka, Japan) were laminated to the front and the back of the stack. The transmission axes of the polarizers were parallel and perpendicular, respectively, to the rubbing direction of the alignment layer. An LDMS Autronic (Autronic-Melchers GmbH, Germany) goniometric set-up was used for the electro-optical characterization of the plastic LCD.

7.3 Results and discussion

7.3.1 The two-step PES process

One of the appealing features of the photo-enforced stratification process is that it can be applied to any substrate ranging from rigid glass substrates to flexible plastic foils. In order to make the combination of the PES technology and flexible substrates feasible, the mechanical integrity of the polymer capsules should be sufficient to cope with potential deformations.⁵ Unfortunately, it soon became apparent that the polymer capsules made by the two-step process suffered from delamination of the polymer walls when force was exerted on the capsules (see Figure 7.3). The delamination can be ascribed to an insufficient adhesion between the poly(BoMA/stilbene-dimethacrylate) copolymer and the poly(imide) alignment layer. A solution to this problem was found in a patterned modification of the alignment layer, which will be described in the remainder of this chapter.

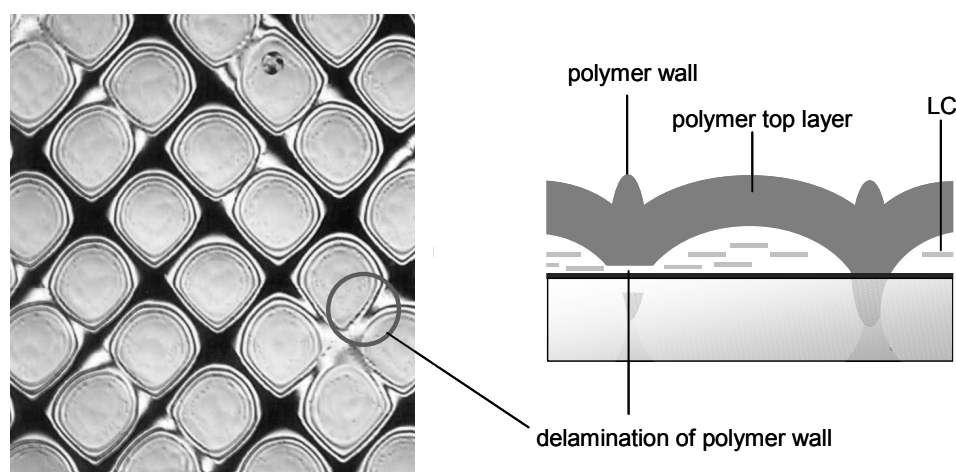


Figure 7.3: A polarization microscope photograph of the LC-filled polymer capsules seen from the top (left), as well as a schematic cross section of neighbouring LC-filled polymer capsules (right) exemplifying the delamination of the polymer walls as a result of mechanical stresses.

7.3.2 The single-step PES process

As was shown in Chapter 2, when a film of E7/IBoMA/stilbene-dimethacrylate/Irgacure 651 coated on a standard AL3046 alignment layer is exposed to UV light, the phase-separated LC droplets do not coalesce into a continuous and flat LC layer. Instead, the resulting morphology is an assembly of flattened LC droplets of random size covered by a continuous polymer layer. Between the droplets the polymer layer is weakly attached to the alignment layer (see Figure 7.4).

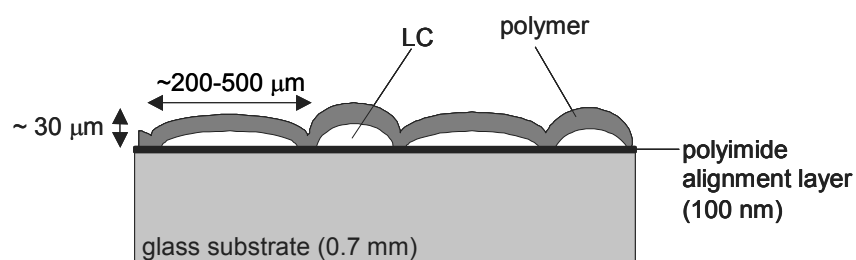


Figure 7.4: Schematic cross-section of a stratified layer resulting from a single step PES process carried out on a poly(imide)-covered substrate without an additional surface modification. The droplets do not coalesce into a continuous and flat LC layer. Note that the dimensions in this drawing are not to scale.

In the two-step PES process the shape of the polymer-capsules is controlled by the mask exposure step that precedes the actual stratification step. In the single-step PES process, the aim is to achieve the capsule shape control *and* to improve the adhesion of the polymer to the substrate with a patterned modification of the alignment layer using an adhesion promoter (see Figure 7.5). With the aid of a rubber stamp made of poly(dimethyl siloxane) (PDMS)⁶ a pattern of a concentrated solution of this adhesion promoter can simply be applied manually on the alignment layer via off-set printing.⁷ By its very nature, the printing step only modifies the selected areas and does not alter or damage the alignment properties of the layer in the unmodified areas.

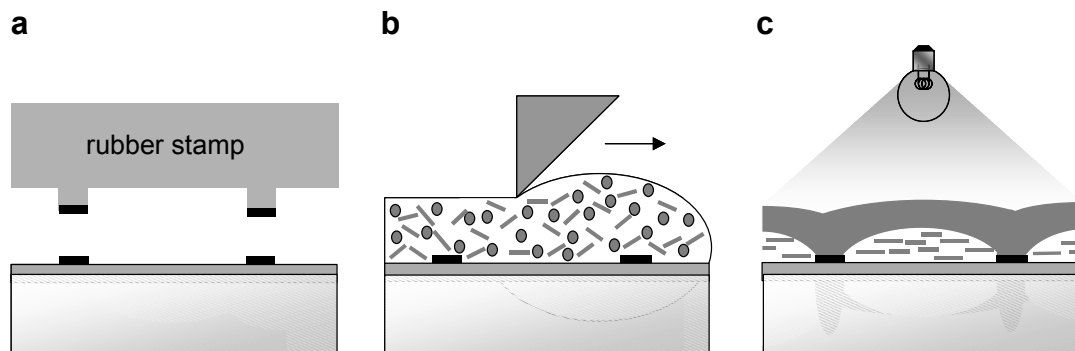


Figure 7.5: The single-step PES process: a) Via offset printing, the alignment layer is locally modified with a grid pattern of an adhesion promoter. The adhesion promoter is a polymer that contains methacrylate side groups that will react with the monomers in the LC/monomer film during the UV exposure. b) The modified alignment layer is coated with the LC/monomer mixture. c) A single UV exposure step results in the formation of the liquid crystal-filled polymer capsules corresponding to the adhesion promoter grid pattern.

The selection criteria for the adhesion promoter are the following. Preferably it is a high molecular weight linear polymer that does not readily dissolve or swell in the E7/IBoMA/stilbene-dimethacrylate mixture. It should adhere firmly to the poly(imide) alignment layer onto which it is printed. To enhance adhesion and to improve structure control, it should contain reactive moieties capable to co-react with the polymerizing methacrylates of the reactive mixture to ensure the formation of covalent bonds between the poly(BoMA-stilbene-dimethacrylate) co-polymer and the printed polymer. The commercially available Durimide 7505 formulation was found to fulfill these requirements. It consists of a solution of a methacrylate side group containing poly(amide) in N-methyl pyrrolidone (NMP). A general structure of this high molecular weight polymer is depicted in Figure 7.6. After coating the substrate with the AL3046 poly(imide) alignment layer, subsequent curing and rubbing with polyester tissue, the solution is offset printed on the substrate.

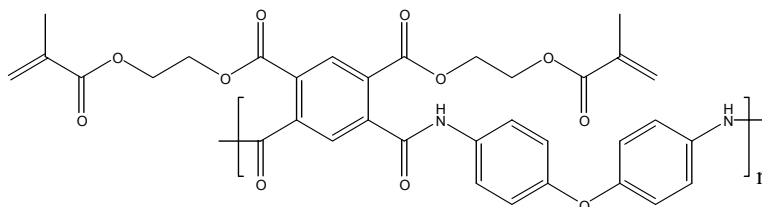


Figure 7.6: Chemical structure of the poly(amide) containing reactive methacrylate side-groups.

After offset printing, the adhesion promoter consists of a square grid pattern of lines of 100 – 150 μm width, somewhat wider than the line pattern of the PDMS mould, see Figure 7.7. The printed lines are approximately 800 nm thick.

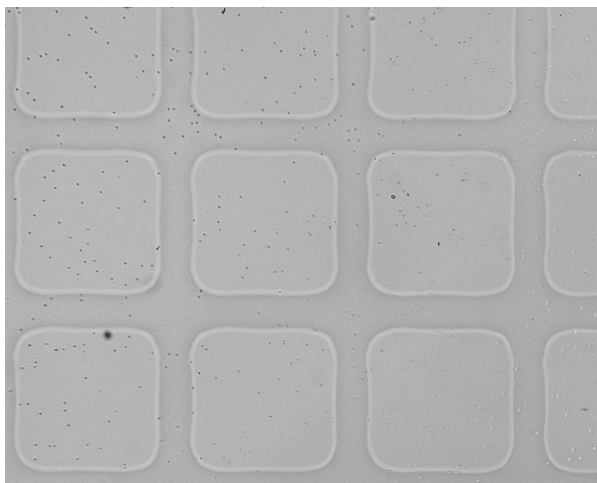


Figure 7.7: Optical microscope photograph of the Durimide 7505 adhesion promoter pattern on the poly(imide)-covered substrate. The width of the adhesion promoter lines is 100 μm and their thickness is 800 nm. The pitch of the grid is 500 μm .

After coating the modified alignment layer with a E7/IBoMA/stilbene-dimethacrylate/Darocure4265 mixture (represented in Figure 7.5b), a single UV exposure directly yielded the array of LC-filled polymer capsules (schematically shown in Figure 7.5c). The required UV intensity gradient across the film thickness was induced by the presence of the stilbene-dimethacrylate monomer in the thin film (see Figure 7.8). As a result of the concomitant photopolymerization rate gradient, the monomers in the film diffuse in the upward direction and at the same time the LC molecules diffuse in the reverse direction. Since the UV light intensity is still considerable near the bottom of the layer (see Figure 7.8b) also here photopolymerization will take place (albeit at a slower rate than in the top of the layer). At the position of the adhesion promoter, the poly(IBoMA-co-stilbene-dimethacrylate) becomes covalently attached to the alignment layer. The strategy was to enhance the local attachment by increasing the polymerization rate at the bottom of the film. Thereto, the photoinitiator Irgacure 651 (used in the two-step PES process) was exchanged for Darocure 4265.

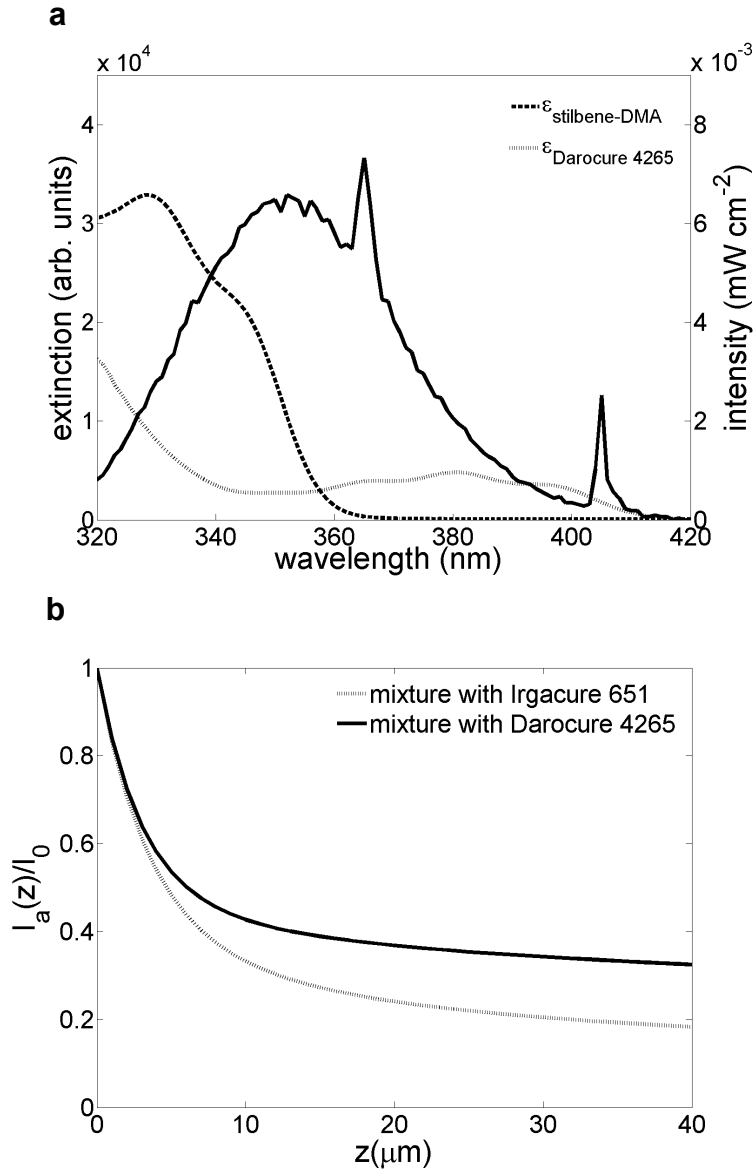


Figure 7.8: a) The emission spectrum of the UV source and the absorption spectra of the stilbene-dimethacrylate compound and the Darocure 4265 photoinitiator. b) The calculated gradient of absorbed light (cf. Chapter 5) for a 30 μm film of the E7/IBoMA/stilbene-dimethacrylate/Darocure4265 mixture at the onset of irradiation. As a reference the gradient of the E7/IBoMA/stilbene-dimethacrylate /Irgacure651 mixture used in previous 2-step PES experiments is also depicted.

The phase separation process has been recorded by means of a polarization microscope equipped with a camera. Snapshots showing some of the intermediate structures formed during the process are depicted in Figure 7.9. At the moment that the phase-separation sets in, pure LC droplets start to grow at the bottom of the film (Figure 7.9a), but only at the positions where the alignment layer has *not* been modified. Subsequently the growing LC droplets coalesce into bigger LC domains (Figures 7.9b-c). During the coalescence in the regions where the adhesion promoter is absent, the formed polymer is ‘pushed’ in the upward direction by the growing LC

domains. As the polymer formed near the adhesion promoter is covalently attached it cannot be exchanged for liquid crystal and remains in place. While this process continues it ultimately results in the desired LC-filled capsules (Figure 7.9d). The peripheral dimensions of the capsules correspond to the pitch of the adhesion promoter pattern.

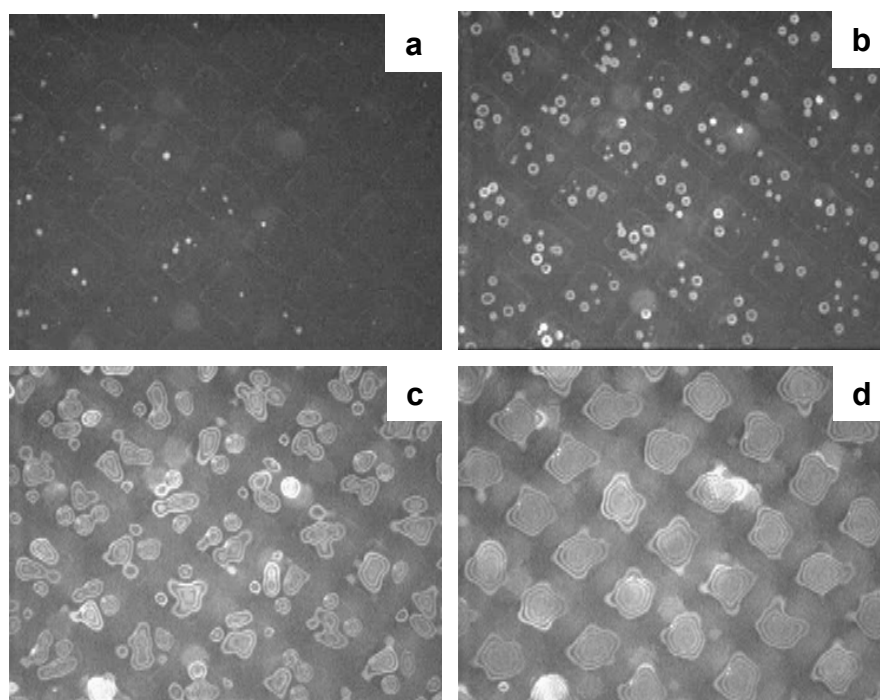


Figure 7.9: Single-step PES process on a substrate patterned with the adhesion promoter, seen from the top after: a) 4.30 minutes, b) 4.40 minutes, c) 8.20 minutes, d) 30 minutes. At the positions where the substrate is not modified with the adhesion promoter the LC droplets formed during UV exposure coalesce into a continuous LC layer.

The formed LC-filled polymer capsules have been investigated further with polarization microscopy and surface profile measurements. The capsules closely resemble the capsules made by the two-step PES process. The main difference can be seen when the surface profiles of both capsules are compared: the polymer walls of the capsules made by the single step PES process do not protrude the polymer top coat, but are indents in the polymer top coat (see Figure 7.10).

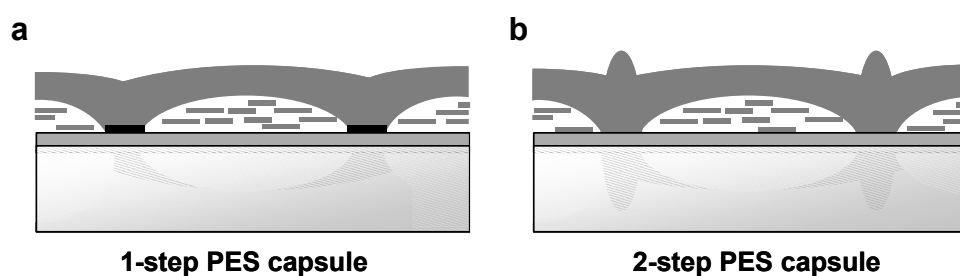


Figure 7.10: Schematic cross sections derived from polarization microscopy and surface profile measurements of the LC-filled polymer capsules. a) capsules made by the 1-step PES process. b) capsules made by the 2-step PES process.

7.3.3 Characterization of the LC-filled polymer capsules after application of the planarization layer: confocal Raman microscopy

To improve further on flatness and robustness of the LC-filled polymer capsules, the single-step PES film is coated by means of a doctor blade with a 30 μm layer of tri(propyleneglycol)diacrylate (TPGDA) that is subsequently cured by photopolymerization. After the application of this topcoat the spatial composition of the LC-filled capsules was analyzed with confocal Raman microscopy⁸ (see Chapter 3 for a detailed description). Figure 7.11a shows a cross-sectional intensity profile of the aromatic C-C bonds of the LC located at 1600 cm^{-1} in the Raman spectrum. This Raman signal cannot be used to determine the LC concentration quantitatively, since some of the components of this multi-component LC mixture preferentially stay dissolved in the polymer with as result that the LC composition in the LC domain as well as in the polymer differs from the initial E7 composition (see Chapter 2). The four components of the LC, the three biphenyl and the terphenyl components (see Figure 7.1), cannot be distinguished independently either as their Raman signals largely overlap. However, the contour plots of the aromatic C-C bonds are still suitable to identify large differences in the depth profiles of the LC. Moreover, the plots elucidate the shape of the structures formed (Figure 7.11c). The high aromatic C-C signals indicate the shape of the LC domain at the bottom of the structure (Figure 7.11a). Figure 7.11b shows the contour plot of stilbene-dimethacrylate, obtained after subtraction of the E7 reference spectrum via the Classical Least Squares approach (CLS, see Chapter 3). Despite the error introduced by ignoring the deviation of the LC compositions in the polymer and LC phase after phase separation with respect to E7, the contour plot gives a clear indication of the shape of the poly(IBoMA-co-stilbene-dimethacrylate) layer. It agrees with the schematic cross-section given in Figure 7.10: The layer follows the shape of the LC domains. In Figure 7.11a can be seen that the

poly(IBoMA-co-stilbene-dimethacrylate) polymer is swollen with LC material. As already has been shown in Chapter 3 this LC material is isotropic. The poly(TPGDA) topcoat can be seen indirectly, since it also contains a small amount of LC. This might be the result of undesired phase separated LC at the outer surface of poly(IBoMA-co-stilbene-dimethacrylate) after the PES step that is subsequently dissolved in the TPGDA monomer after its application and stays dissolved in the poly(TPGDA) after polymerization. In addition, after the curing of the TPGDA, the system may go towards a new equilibrium state in which the LC, initially present in the LC domain and the poly(IBoMA-co-stilbene-dimethacrylate) polymer, is redistributed over the LC domain and the two polymer layers, which will result in a decrease of the LC thickness. The reduced stilbene-dimethacrylate signal in the area above the LC domain (Figure 7.11b) is the result of scattering of the incident laser beam and the Raman excitation light by the nematic LC (see Chapter 3). Above the positions of the adhesion promoter the stilbene-dimethacrylate signal is lower while the LC signals are locally slightly higher. This points to the local presence of micrometer-sized droplets filled with pure LC, similar to PDLC morphologies (cf. Chapter 3).⁹

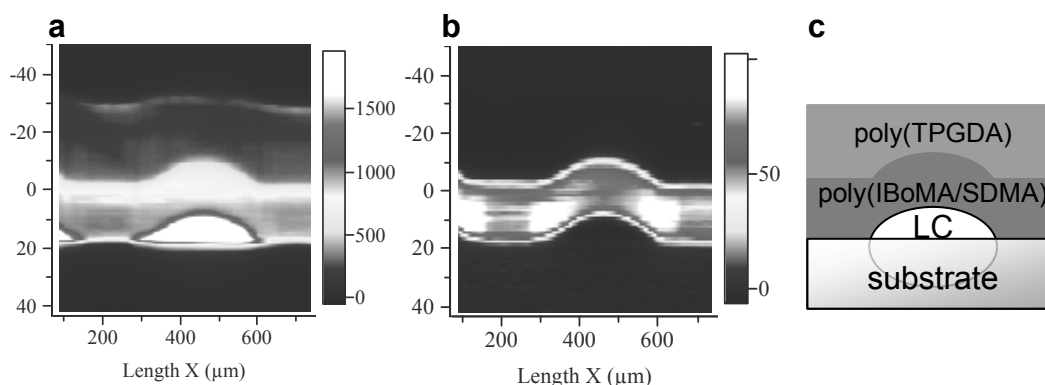


Figure 7.11: Contour plots of a single LC-filled capsule: The aromatic C-C bond of the LC (a) and the central C=C peak of stilbene-dimethacrylate after subtraction of the LC signals with classical least squares (CLS) (b). A schematic drawing of the stack of layers (please note that the drawing is not to scale; the base of the LC domain is $350 \times 350 \mu\text{m}^2$, its height approx. $10 \mu\text{m}$).

7.3.4 Plastic single-step PES LCD demonstrators

An electro-optical demonstrator device, also denoted as ‘Paintable LCD’, is prepared by implementing the 1-step PES process, using the E7/IBoMA/stilbene-dimethacrylate/Darocure4265 system, on a flexible substrate. The substrate has been provided with interdigitated electrodes that, after completion of the display, switch the LC by in-plane electrical fields.¹⁰ After planarization with the poly(TPGDA) layer a sheet polarizer is laminated at each side. The polarizers have a thickness of 130 micrometer each. After completion, the display is cut to its desired form (see Figure

7.12). The resulting plastic LCD is approximately 450 μm thick and shows its robustness by remaining operational during and after bending to a curvature radius of 5 cm.

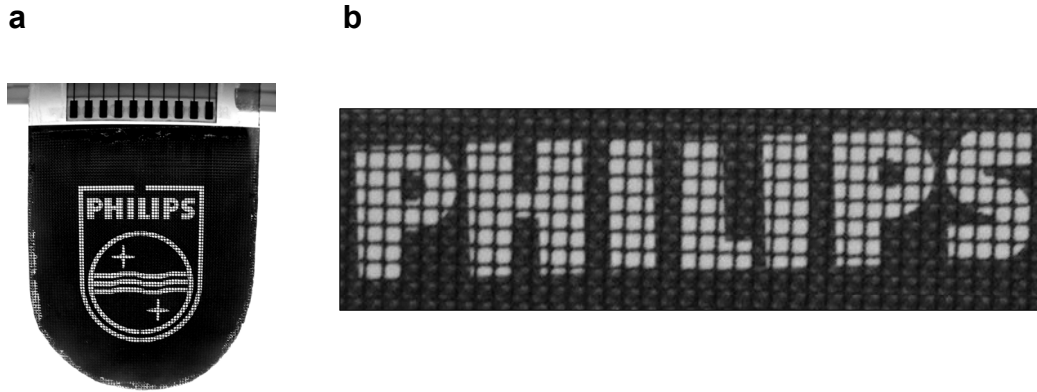


Figure 7.12: a) Photograph of an addressed plastic LCD made by the 1-step PES process. The total thickness of this 'Paintable LCD' is less than 450 micrometer. b) A close-up of the LCD shows the array of LC-filled capsules addressed by the in-plane switching electrode segments underneath.

Figure 7.13 shows the transmission/voltage and transmission/time curves of the plastic LCD in the normally black mode (i.e. the pixels display the dark state at 0V). As expected, the electro-optical behavior of this display is similar to that of the display made by the two-step PES process (cf. Chapter 3). Switching speeds below 50 ms are obtained: $\tau_{\text{on}} = 12$ ms and $\tau_{\text{off}} = 41$ ms (switched between 0-20V, time interval measured between 10%-90% transmission). These are comparable to the speeds obtained with devices made by the two-step PES process (see Chapter 2). The transmission-voltage curve in Figure 7.13 shows that maximum transmission is obtained at 20V. The overall LC director is then at 45° with respect to the transmission axis of the polarizers. The voltage at maximum transmission is 5V higher than in two-step PES example in Chapter 2 due to the larger distance between the interdigitated electrodes (20 μm versus 9 μm). The contrast between the on- and the off-state is approximately 1:10, which is mainly caused by the light leakage in the dark state. This light leakage is contributed to the undesired phase separation of micrometer-sized LC droplets in the polymer layer (PDLC morphologies).

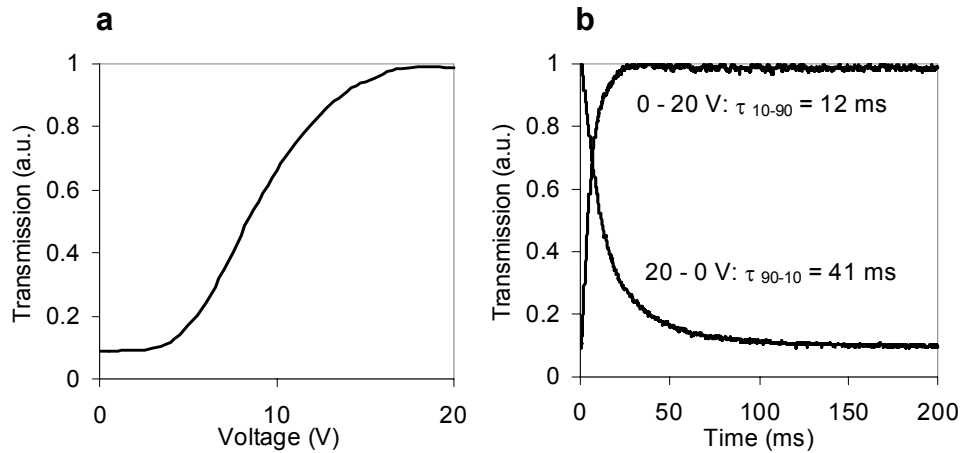


Figure 7.13: a) The transmission/voltage curve of a plastic LCD made by the 1-step PES process. b) The transmission/time curve The LC material (E7) is driven by in-plane switching. The gap between the interdigitated electrodes is $20 \mu\text{m}$.

An attractive feature of the so-called Paintable LCDs is their free form factor i.e. after processing they can be bent and their form can be adjusted such that they can be laminated on curved, non-rectangular surfaces, such as the backside of a phone cover (Figure 7.14). For this typical demonstrator the Paintable LCD, containing seven circle-shaped IPS electrode segments, is laminated on the phone cover with a pressure sensitive adhesive (PSA) film. A color filter printed on a plastic sheet is placed on the inside of the transparent phone cover between the LCD and the backlight.

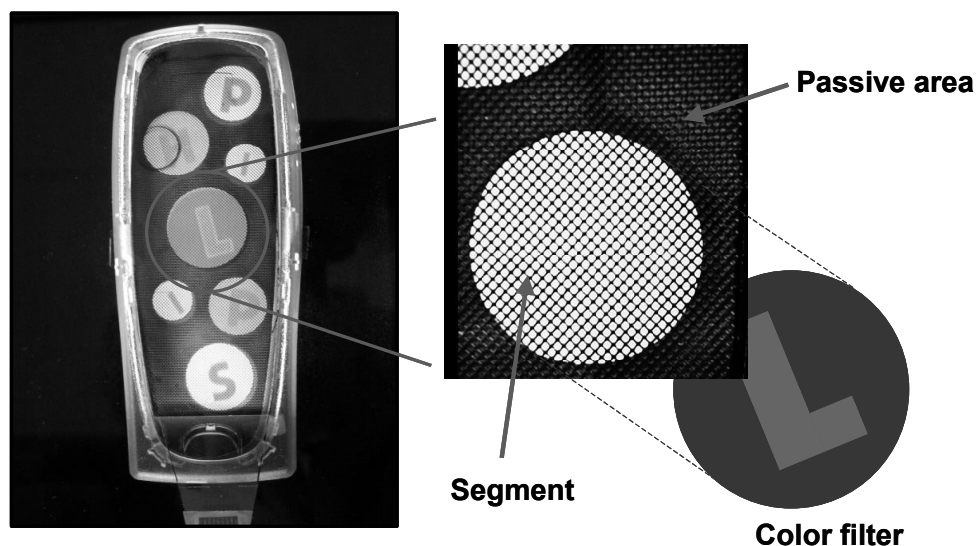


Figure 7.14: Paintable LCD laminated on the backside of a phone cover. The LCD contains seven IPS electrode segments. A color filter printed on a plastic sheet is positioned between the LCD and the backlight, which illuminates the electro-optical stack through the transparent phone cover.

7.4 Conclusions

In this chapter the second generation PES process was presented. A surface modification step with a grid pattern of *adhesion promoter* was introduced replacing the mask exposure step of the first generation two-step PES process. This results in a simpler process, by omitting the mask exposure of a wet layer. Moreover, the resulting LC-filled polymer capsules are mechanically much more robust through the covalent bonds formed with the adhesion promoter. It was demonstrated that the second generation PES process enables the production of plastic LCDs with a free form factor.

7.5 References and notes

1. Morozumi, S. in: *Liquid Crystals: Application and Uses* (Ed. Bahadur, B.), World Scientific, London, 181 (1990).
2. Penterman, R., Klink, S.I., Koning, H. de., Nisato, G., and Broer D.J. *Nature* **417**, 55-58 (2002).
3. Crawford, G.P. *Flexible Flat panel Displays*, John Wiley & Sons, Chichester (2005).
4. Broer, D.J., and Penterman, R. *US patent application*, US6818152 B2 (2002).
5. Bouten, P., Slikkerveer, P., and Letterrier, Y. in: *Flexible flat panel displays* (Ed. Crawford G.P.), John Wiley and Sons, Chichester, 99-120 (2005).
6. Kumar, A., and Whitesides, G.M. *Appl. Phys. Lett.* **63**, 2002-2004 (1993).
7. Darhuber, A.A., Troian, S.M., and Wagner, S. *J. Appl. Phys.* **90**, 3602-3609 (2001).
8. Mank, A.J.G., Vorstenbosch, I., Penterman, R., Vogels, J.P.A., Klink, S.I., and Broer, D.J. *Appl. Spectrosc.* **59**, 965-975 (2005).
9. Drzaic P.S. *Liquid Crystal Dispersions*, World Scientific, Singapore (1995).
10. Oh-e, M., and Kondo, K. *Appl. Phys. Lett.* **67**, 3895-3897 (1995).

Technology assessment

Current flat panel liquid crystal displays are fabricated via cell-technology. This is a batch-wise process that is time consuming and due to the related substrate handling the process is limited to rigid glass substrates with rectangular shapes. The *Paintable LCD* concept allows the preparation of an LCD on a single substrate by the sequential coating and curing of a stack of tailored organic layers. The key process that enables layer stacking on top of the liquid crystal (LC) layer is called *photo-enforced stratification* (PES), which is the subject of this thesis. It comprises the spatially controlled photopolymerization-induced phase separation of an LC blend and a polymer precursor. In the PES process a single thin layer, applied on the bottom substrate via standard coating methods, accurately phase separates in an array of neighboring LC-filled capsules. On top of the polymer capsules, the other necessary optical layers (e.g. polarizer) can be applied. PES enables the use of flexible, plastic substrates, which provides more design freedom with respect to shape of the resulting displays. Moreover, the use of coating processes potentially enables the production of LCDs via roll-to-roll manufacturing processes.¹

A two-step PES process, where the actual stratification step is preceded by a mask step has demonstrated that single-substrate LCDs can be made with switching speeds comparable to current in-plane switching (IPS) LCD panels. In the second generation PES process, pre-treatment of the substrate by printing an adhesion promoting polymer enables a single-step UV exposure to produce the arrays of LC-filled polymer capsules. The adhesion promoting polymer, actually being capable to co-react with the stratifying polymer while being formed, controls the formation and the size of the capsules. The advantages are twofold. Firstly, the processing becomes simpler exchanging a lithographic UV exposure for an offset printing step. Secondly the electro-optical (E/O) switches made are far more stable and resist mechanical deformation. For instance, when processed on plastic substrates they can be bent to small radii (< 5 cm) without failure. A feature of Paintable LCDs that is specially recognized in the display world is the fact the image is retained during the actual bending process of the E/O devices.^{2,3} When current LCDs are mechanically deformed they show image deterioration because of LC flow as a result of a change in the distance between the two substrates. Because of the presence of the capsules, LC flow in PES devices is prohibited and the image is maintained. The improved robustness enables the integration of LCDs at the surface of new products such as mobile phone covers, interactive toys or electronic textile for clothing. Figure T.1 shows examples of potential applications.

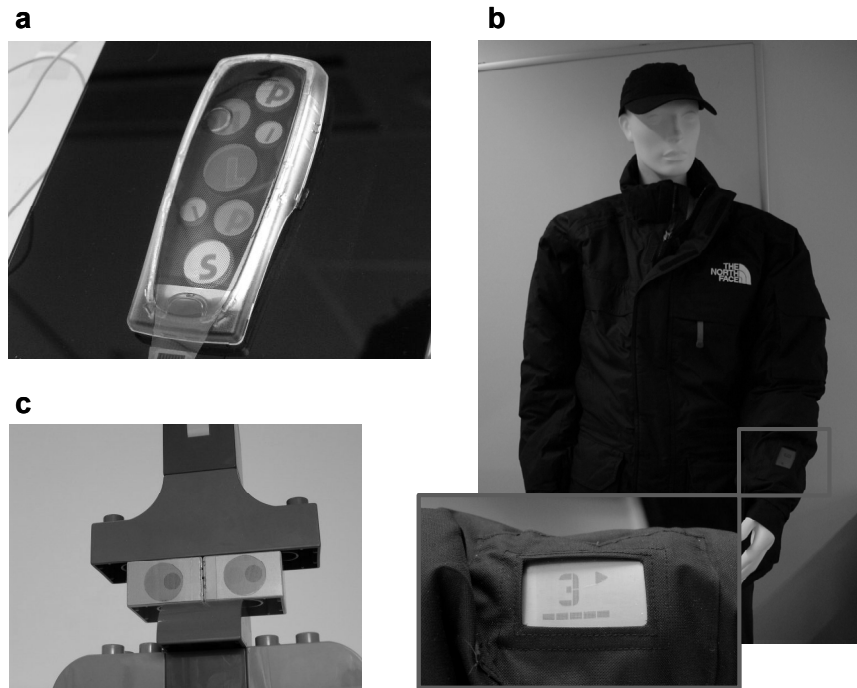


Figure T.1 a) 'Visual ringtone' concept: Paintable LCD integrated on the back of a mobile phone cover. b) Wearable display providing information on the status of a portable disc man. c) Interactive toys: Paintable LCDs applied on LEGO bricks.

Although the PES process has a number of advantages, the E/O performance of this new display type leaves room for improvement. Especially the existence of microscopic LC droplets in the polymer top layer, denoted as PDLC morphology, leads to undesired transmission of light in the off state (dark state) of the device, which decreases the contrast ratio of the display. Values of 1:20 were obtained, which is sufficient for first low-end applications such as the examples mentioned above. It is obvious that for application in high-end monitors and television sets, which currently have contrast ratios exceeding 1:500, the display performance of Paintable LCDs needs to be improved. For the current PES devices IPS is preferred, since other switching modes (e.g. twisted nematic, TN) would require alignment layers and electrodes on both sides of the LC layer. Application of metal electrodes (e.g. Indium-Tin-Oxide) on top of the LC-filled capsules, for example, requires resistance against high process temperatures and etching solvents.

To meet the requirements for mobile phone or automotive applications, the LC/monomer formulation must be developed further by using more complex LC blends that give a larger temperature range of operation and lower switching voltages. The PES model described in this thesis has given insight in the basic principles of the PES process and this will help the optimization of process conditions and new material formulations.

Paintable LCD technology fits well in existing LCD factories, since most of the processing steps are identical: Basically, only the cell making and filling is exchanged for an off-set print step and a set of coating and subsequent UV exposure steps. Moreover, flexible substrates will require the use of carriers on which the substrate is temporarily fixed. Since dedicated equipment for cell-technology is no longer needed, LCD manufacturing becomes available to others in the LCD component supply chain, such as color filter manufacturers that have experience with most of the required processing steps. As already mentioned earlier, the use of coating processes potentially enables the production of LCDs via roll-to-roll manufacturing processes. It should however be noted that these processes are only commercially attractive for large area devices, as for example in signage (advertisement) applications. Signage applications require reflective displays with high daylight contrasts and a low-power consumption. Thereto, the PES process may be combined with cholesteric texture LCs (CTLCS) to yield reflective bistable LCDs. Roll-to-roll processing, however, is still in its developing phase.⁴ Critical for example is the fine patterning of the electrode structures via photolithography and subsequent etching. Also the web coating of other optical components such as coatable polarizers⁵ are still in an early stage.

References

1. Boxtel, M.C.W. *PhD thesis*, Eindhoven University of Technology (2002).
2. Penterman, R., Klink, S.I., Vogels, J.P.A., Huitema, H.E.A., Koning, H. de, and Broer, D.J. in: *Flexible flat panel displays* (Ed. Crawford, G.P.), John Wiley and Sons, Chichester, 99-120 (2005).
3. Vogels, J.P.A., Penterman, R., Klink, S.I., Huitema, H.E.A., Koning, H. de, and Broer, D.J. in: *SID 04 Symp. Digest* **35**, 767-769 (2004).
4. Gregg, A., York, L., Strnad, M. in: *Flexible flat panel displays* (Ed. Crawford, G.P.), John Wiley and Sons, Chichester, 99-120 (2005).
5. Bobrov, Y.A., Cobb, C., Lazarev, P., Bos, P., Bryant, D., and Wonderly, H. in: *SID 00 Symp. Digest*, 1102-1105 (2000).

Summary

To keep pace with customer demand for cost-effective flat panel displays, liquid crystal display (LCD) manufacturing technologies are required that enable the processing of larger substrates with increased production speeds. In cell-technology, currently used in all LCD factories, cells are formed by coupling two substrates, which are subsequently filled with liquid crystal (LC). However, this is a time-consuming process that limits the shape- and substrate choice. New display designs require displays that are curved, optionally flexible, and non-rectangular in shape. This thesis describes the exploration of a new phase separation process that enables the production of *Paintable LCDs*.

Unlike cell-technology, Paintable LCDs are produced on a single-substrate by the sequential coating and curing of multiple organic layers on top of each other. The electro-optical LC layer is confined between the substrate and a polymer sheet with the important feature that the latter is formed during processing. This *in-situ* polymer sheet formation is the result of a spatially-controlled photopolymerization-induced phase separation process. In this process, a film consisting of a mixture of LC and monomers is irradiated with UV light. Due to a photopolymerization rate gradient in the film and a concomitant selective phase separation of LC material at the bottom of the film, the film is transformed into a stratified morphology: a polymer film on top of an LC layer. This concept is referred to as *photo-enforced stratification* (PES). Interdigitated electrodes previously applied on the substrate switch the LC layer. The use of coating processes makes the Paintable LCD technology well suited for application in free form factor displays potentially produced via high-speed roll-to-roll manufacturing processes.

In PES two main physical processes are involved: photopolymerization-induced diffusion and polymerization-induced phase separation. As a result of transversal diffusion of LC and monomers through the film, induced by a vertical gradient in the polymerization rate, the phase separation process is located at the bottom of the film. The phase separation at the bottom of the film leads to the formation of large LC domains randomly distributed over the substrate area, covered by a polymeric topcoat. Characterizations with polarization microscopy and surface profile measurements show that when the stratification step is preceded by a mask exposure step, morphologies are formed that can be described as regular arrays of neighboring LC-filled polymer capsules.

Confocal Raman microscopy measurements on these LC-filled polymer capsules reveal that part of the LC stays isotropically dissolved in the polymer phase. Moreover, it was found that under the current process conditions microscopic LC-

droplets are formed, which are dispersed in the polymer near the polymer-LC interface, comparable to the morphology of PDLC displays (polymer-dispersed liquid crystal displays).

A numerical PES model has been developed based on free radical polymerization rate equations, diffusion equations and the thermodynamics of phase separation. The PES model is a combination of two distinct components: The first component is a reaction-diffusion model that calculates the evolution of the concentration of the liquid crystal (LC), monomer and polymer as a function of depth in the film and time. The second component is a thermodynamic model that describes polymerization-induced phase separation (PIPS). In the model, the contribution of the entropic and enthalpic mixing (Flory-Huggins theory of mixing), elasticity of the polymer network (Flory-Rehner theory) and nematic ordering (Maier-Saupe theory) to the Gibbs free energy are included. The overall PES model is a one-dimensional model, which calculates the location and the time (conversion) at which the phase separation sets in. Moreover, it helps the prediction of trends in the morphologies that will be formed.

In order to compare the model outcomes with the experimental results, the model input parameters have been determined, either by calculations or by experiments on the appropriate LC/monomers systems. The Flory-Huggins interaction parameters between the various components were estimated via the calculated solubility parameters of the components (via a group contribution theory). With the aid of photo-DSC the photopolymerization kinetics was investigated and the diffusion constants the LC and monomer species were measured with the aid of NMR spectroscopy as a function of the conversion.

Both components of the PES model, the reaction-diffusion model and the phase separation model, were independently compared to experiments. With confocal Raman microscopy, the concentration profile of the LC compound was monitored in-situ, during the UV irradiation. The measured changes in the LC concentration profile were found to be similar to the changes calculated by the reaction-diffusion model. Photo-DSC has been combined with in-situ optical microscopy to determine the phase diagram of the investigated LC/monomer/polymer system. The measurements showed that for the investigated system the elastic contribution of the polymer network could be neglected. The theoretical phase diagram, in which the phase separation lines were calculated by taking the mixing contributions and the contribution of nematic ordering of the LC phase into account, are in agreement with the experimental phase diagram. Subsequently, the stratification behavior as a function of the LC fraction in the initial reaction mixture was investigated experimentally. The earlier onset of phase separation as well as an increased formation of PDLC-morphology in the polymer

layer at higher initial LC fraction both agree with trends calculated with the PES model. The PES model and the diffusion-, phase separation- and stratification experiments have led to a better understanding of the PES process in which the position of the onset of phase separation in the layer is controlled by polymerization-induced diffusion.

Besides a better understanding of the physical processes involved in the PES process this research has led to a simplified and improved stratification process in which the arrays of LC-filled polymer capsules are obtained via a single UV exposure step. For this purpose the alignment layer on the bottom substrate is first patterned with an adhesion promoter using offset printing. During the stratification process the polymer top layer locally forms covalent bonds with the adhesion promoter patterns. Besides a simpler manufacturing process, this results in mechanically stable morphologies, which enable the production of flexible, plastic LCDs with a free form factor.

Samenvatting

Door de toenemende vraag naar goedkope platte beeldschermen is er behoefte aan fabricage-technieken voor vloeibaar-kristal beeldschermen (Engels: liquid crystal displays, LCDs) waarmee grotere substraten met hogere snelheden worden verwerkt. In de huidige celtechnologie wordt door de koppeling van twee substraten een cel gevormd die vervolgens wordt gevuld met vloeibaar-kristal (Engels: liquid crystal, LC). Dit is echter een tijdrovend proces dat bovendien de vorm- en substraatkeuze beperkt. Om de ontwerpvrijheid van nieuwe producten te vergroten zijn gebogen, optioneel flexibele beeldschermen met een vrije vormfactor gewenst. In dit proefschrift wordt het onderzoek beschreven naar een nieuw fasescheidingsproces waarmee zogenoemde *Paintable LCD's* kunnen worden gemaakt.

In tegenstelling tot celtechnologie, zoals nu gebruikt in alle LCD fabrieken, worden *Paintable LCD's* op een enkel substraat vervaardigd door de verschillende functionele organische lagen via coatingprocessen laag voor laag op elkaar aan te brengen. Om de electro-responsieve LC-laag compatibel te maken met de verdere procesvoering, wordt het afgedekt door een dunne polymeerlaag die tijdens het proces wordt gevormd. Deze polymeerlaag komt tot stand via een gecontroleerd polymerisatie-geïnduceerd fasescheidingsproces. In dit proces wordt een dunne laag, bestaande uit een mengsel van LC en monomeren, belicht met ultraviolet (UV) licht. Door selectieve fotopolymerisatie wordt deze laag in twee lagen gescheiden: een harde polymere (plastic) laag boven op een LC-laag. Dit concept wordt *photo-enforced stratification* (PES) genoemd. De LC-laag kan worden geschakeld met elektrische velden via kam-elektrodes welke zijn aangebracht op het substraat. Door het gebruik van simpele coatingtechnieken maakt de *Paintable LCD* technologie het mogelijk om in de toekomst zeer dunne, flexibele LCD's via continu-processen te vervaardigen.

In PES worden twee fysische processen gecombineerd: Polymerisatie-geïnduceerde diffusie en polymerisatie-geïnduceerde fasescheiding. Diffusie van LC-materiaal en monomeren, geïnduceerd door een gradiënt in de polymerisatiesnelheid, zorgt er voor dat het fasescheidingsproces in de bodem van de laag plaatsvindt. Het initiëren van de fasescheiding op de bodem resulteert in de vorming van willekeurig over het substraattooppervlak verspreide LC-domeinen, die zijn afgedekt door een polymeerlaag. Uit de karakterisaties met polarisatiemicroscopie en oppervlakteprofielmetingen blijkt dat wanneer deze stratificatiestap vooraf gegaan wordt door een maskerbelichting, regelmatige structuren van aaneengeschakelde polymere capsules gevuld met LC worden gevormd. Confocale Raman-microscopiemetingen tonen echter aan dat een deel van het LC isotroop opgelost blijft

in het polymeer. Bovendien is gevonden dat onder de huidige procescondities nabij het polymeer-LC grensvlak kleine, in het polymeer gedispergeerde, pure LC-druppels worden gevormd, vergelijkbaar met de morfologie in PDLC-schermen (Engels: polymer-dispersed liquid crystal displays).

Er is een numeriek stratificatie model (PES-model) ontwikkeld gebaseerd op de reactiekinetiek van kettingpolymerisatie, diffusie en de thermodynamica van fasescheiding. Het model is een combinatie van twee afzonderlijke componenten. De eerste component is een reactie-diffusiemodel dat de ontwikkeling van de concentratie van het LC, het monomeer en het gevormde polymeer berekent als functie van de positie in de laag en de tijd. De tweede component is een thermodynamisch model dat de polymerisatie-geïnduceerde-fasescheiding beschrijft en waarmee het fase-diagram van het systeem berekend wordt. In het model zijn de bijdrage van entropische en enthalpische menging (Flory-Huggins), de elasticiteit van het polymeer netwerk (Flory-Rehner) en nematische ordening van de LC-fase (Maier-Saupe) aan de verandering van de Gibbs vrije energie toegevoegd. Het totale PES model is een één-dimensionaal model waarmee zowel de plaats als de starttijd van de fasescheiding en de bijbehorende conversie berekend wordt. Bovendien helpt het model bij voorspelling van trends in de gevormde morfologieën.

Om de modeluitkomsten te kunnen vergelijken met experimentele resultaten zijn de benodigde invoerparameters gekwantificeerd, gebaseerd op berekeningen en metingen aan experimentele materiaalsystemen. Zo zijn de Flory-Huggins interactieparameters tussen de verschillende componenten berekend, gebaseerd op schattingen van de oplosbaarheidsparameters via een groepsbijdragetheorie. Met behulp van foto-DSC is de polymerisatie kinetiek onderzocht en de diffusieconstanten als functie van de conversie zijn gemeten met behulp van NMR spectroscopie.

De beide onderdelen van het PES-model, het reactie-diffusiemodel en het fasescheidingsmodel, zijn onafhankelijk van elkaar vergeleken met experimenten. Met confocale Raman microscopie is tijdens de UV-belichting de ontwikkeling van het LC-concentratieprofiel gevolgd. De grootte van de gemeten veranderingen in het concentratieprofiel is vergelijkbaar met de grootte van de veranderingen berekend met het reactie-diffusiemodel. Foto-DSC is gecombineerd met optische microscopie om het fase-diagram van het onderzochte LC/monomeer/polymeer systeem te bepalen. Uit deze metingen is gebleken dat in het onderzochte systeem de elastische bijdrage van het polymeernetwerk nihil is. Het theoretische fase-diagram, waarin de fasescheidingslijnen zijn berekend door in het fasescheidingsmodel de mengbijdragen en de bijdrage van de nematische ordening van de LC-fase mee te nemen, vertoont sterke gelijkenis met het experimentele fase-diagram.

Vervolgens is het stratificatiegedrag als functie van de LC-fractie in het initiële reactiemengsel experimenteel onderzocht. Een vervroegde fasescheiding alsmede een toegenomen vorming van PDLC-morfologie in de polymeerlaag bij een hogere initiële LC-fractie komen overeen met de trends berekend met het PES-model. Het PES-model en de diffusie-, fasescheidings- en stratificatie-experimenten hebben geleid tot een beter begrip van fasescheidingsprocessen waarin de positie bepaald wordt door polymerisatie-geïnduceerde diffusie.

Naast een beter begrip van de fysische processen die aan het PES-proces ten grondslag liggen heeft dit onderzoek geleid tot een vereenvoudigd stratificatieproces waarbij de aaneengeschakelde met LC gevulde polymere capsules worden verkregen via een éénstapsbelichting. Daartoe is eerst het bodemsubstraat gemodificeerd met een adhesiepromotor welke via een offset-printmethode patroonmatig is aangebracht. Tijdens het stratificatieproces vormt de polymere toplaag lokaal covalente bindingen met het adhesiepromotorpatroon. Het resultaat is, naast een vereenvoudigde fabricagewijze, een mechanisch stabiele structuur die het mogelijk maakt buigbare, plastic LCD's te produceren met een vrije vormfactor.

Dankwoord

Ongeveer acht jaar geleden besloot ik, na een opleiding aan het conservatorium gevolgd te hebben, dat een carrière als professioneel saxofonist mij niet gelukkig zou maken. Ik besloot de weg, die ik al eerder was ingeslagen door het behalen van een propaedeuse Technische Natuurkunde aan de Universiteit Twente, te vervolgen en ditmaal aan de Hogeschool Enschede. Dat dit tot een proefschrift zou leiden kon ik toen nog niet vermoeden, maar mede door de inbreng van vele mensen in mijn omgeving heeft het zover kunnen komen. Alle mensen die mij geholpen hebben dit mooie doel te bereiken wil ik daarom van harte bedanken.

Ten eerste wil ik mijn groepsleider Hans Hofstraat bij Philips Research bedanken die vanaf het begin het idee te promoveren enthousiast gesteund heeft.

Ik ben natuurlijk veel dank verschuldigd aan mijn eerste promotor prof. Dick Broer. Dick, jij was initiator en inspirator van het onderzoek en samen met jou heb ik de eerste jaren heel veel progressie kunnen boeken. Hierdoor ontstond het draagvlak voor verdere uitbreiding en verdieping. Door jouw enthousiasme, creativiteit en vertrouwen heb ik veel plezier aan het onderzoek beleefd. Eveneens wil ik prof. Piet Lemstra en Cees Bastiaansen bedanken voor de mogelijkheid om in de SKT groep op de TUE te kunnen promoveren en het doornemen van het concept-proefschrift.

Steve Klink, jij hebt voor mij de afgelopen jaren een grote rol gespeeld. Allereerst als vriend, maar ook als collega en, hoewel niet officieel, als mijn directe begeleider. Jij hebt er mede voor gezorgd dat al het praktische werk van de eerste jaren, op de ‘Roeliaanse’ manier, op meer wetenschappelijke voet werd voortgezet en daarmee ook mijn enthousiasme voor de wetenschap versterkt. Jouw grote kracht is het vasthouden van de rode draad en daarin ben je echt een voorbeeld voor me. Ook wil ik je enorm bedanken voor de steun en de hulp bij het schrijven die je me in de laatste maanden hebt geboden.

Joris Vorselaars, zonder jouw afstudeerstage bij Philips Research had mijn proefschrift er heel anders uit gezien. Dankzij jouw programmeerkunsten hebben we onze modelerings-ideeën omgezet in een mooi numeriek stratificatie-model. Daarbij heb je ook een grote bijdrage geleverd aan het experimentele werk waarmee we het model konden vergelijken. Bedankt voor de fijne samenwerking het afgelopen jaar.

Hans Kloosterboer, jij hebt me veel geleerd over de beginselen van polymerisatie en fasescheiding. We hebben voor ons model natuurlijk kunnen voortbouwen op het prachtige PDLC-werk dat jij met anderen hebt verricht. Bedankt hiervoor en ook voor het becommentariëren van het concept-proefschrift.

Ook wil ik alle leden van het Paintable-LCD-project, of beter gezegd alle ‘Joint StratiFighters’, bedanken. Joost Vogels, Henk de Koning en Jacqueline van

Driel, mede door jullie teamspirit hebben we in de afgelopen jaren verschillende demonstrators gemaakt waarmee we velen hebben geïnteresseerd voor onze technologie. Dit heeft er mede voor gezorgd dat ik zo lang achtereen aan dit onderwerp heb mogen werken.

Johan Lub en Wim Nijssen, bedankt voor de synthese van de grote hoeveelheden '852p' en allerlei varianten daarvan. Door jullie was het mogelijk, via ogenschijnlijk 'kleine' aanpassingen aan de moleculen (in powerpoint-chemie!), het gedrag van het stratificatieproces nauwkeurig te bestuderen.

Verder wil ik de analysegroep op het NatLab bedanken voor alle metingen. Speciaal Arjan Mank en Inge Vorstenbosch voor alle confocale Raman-microscopie-metingen en hun grote bijdrage aan Hoofdstuk 3 in dit proefschrift, Roland van de Molengraaf en Jeroen Pikkemaat voor de diffusiemetingen met behulp van NMR en Gerard van den Heuvel voor de HPLC-metingen.

Ook wil ik hierbij de mensen binnen de afdeling DTS in Philips Research bedanken die hebben bijgedragen. Zonder afbreuk te doen aan de hulp van vele anderen wil ik met name Thijs Bel en Pierre Lemmens voor het etsen van de elektrode-structuren en Frank Kneepkens voor de aanstuurelektronica bedanken.

Christian Lewis and Charlotte Kjellander from the TUE, thank you for helping us starting up the numerical simulation work and the discussions.

Collega's van de groep Hofstraat, leden van het SOAP cluster, bedankt voor de goede sfeer, jullie interesse en hulp bij het onderzoek. René Wegh, je bent een fijne kamergenoot, bedankt voor je hulp, je medeleven en het tolereren van de drukte op het 'JSF hoofdkwartier'.

Pappa en mamma, bedankt voor het stimuleren van mijn interesse in techniek en de goede zorg. Schoonfamilie, heel erg bedankt voor de opvang van Loes en de kinderen toen het nodig was. Cor, jouw motto: 'niet twijfelen, keuze maken en doen!', dat ondermeer tijdens onze vele kluskarweien bij alle verhuizingen zeer effectief bleek, heeft me de afgelopen jaren door moeilijke momenten heen geholpen.

Tenslotte mijn gezin: Gijs, pappa's boekje is af, we gaan weer lekker fietsen op het plein! Lieve Loes, doordat het schrijven van het boekje samenviel met het eerste levenshalfjaar van onze Teun, heeft de afgelopen periode ook een grote inspanning van jou gevegd. Zonder jou was ik niet zover gekomen. Dank je wel.

Roel

Curriculum Vitae

Roel Penterman was born on 25 April 1974 in Delden, The Netherlands. After finishing secondary school (VWO) at Twickel College in Hengelo in 1992 he started to study Technical Physics at the University of Twente (UT), Enschede. In 1994 he left physics for a period of three years (1994-1997) to study saxophone at the Hilversums Conservatorium. In 1997 he went back to Enschede and in 1999 he received his bachelor degree in Technical Physics from the Saxion Hogeschool. He graduated on a project on anode stability in microfocus X-ray tubes, carried out at Philips Analytical in Acht.

In the same year he started his career at Philips Research in the group Polymers and Organic Chemistry. Within the program on liquid crystals and liquid crystal polymers lead by prof. dr. D.J. Broer, his work was focussed on new processes for liquid crystal displays (LCDs). The work that has been carried out on the photo-enforced stratification process to produce so-called Paintable LCDs is reported in this thesis.

Currently, the author is working at Philips Research within the program on new applications in the biomedical field.

